Dissertations, Theses, and Masters Projects   Theses, Dissertations, & Master Projects

2018

Applications of Lattice Qcd to Hadronic Cp Violation

David Brantley
College of William and Mary - Arts & Sciences, dbrantley@lbl.gov

Applications of Lattice QCD to Hadronic CP Violation

David Arthur Brantley

Merced, California

Bachelor of Science, UC Merced, 2013
Master of Science, College of William & Mary, 2015

Dissertation presented to the Graduate Faculty
of The College of William & Mary in Candidacy for the Degree of
Doctor of Philosophy

Department of Physics

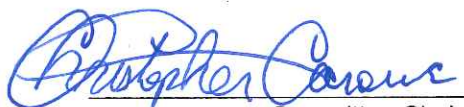College of William & Mary
August, 2018

APPROVAL PAGE

This Dissertation is submitted in partial fulfillment of
the requirements for the degree of

Doctor of Philosophy

David Arthur Brantley

Approved by the Committee July 2018

for André Walker-Loud

Committee Chair
Adjunct Assistant Professor André Walker-Loud, Physics
College of William & Mary

for Konstantinos Orginos

Co-Committee Chair
Professor Konstantinos Orginos, Physics
College of William & Mary

Associate Professor Patricia Vahle, Physics
College of William & Mary

Professor Carl Carlson, Physics
College of William & Mary

for Emanuele Mereghetti

Doctor Emanuele Mereghetti, Physics
Los Alamos National Laboratory

ABSTRACT

Experimental tests of the Standard Model are reaching a precision in which they are probing beyond Standard Model parameter spaces. Increasingly precise experimental tests of the Standard Model (SM) require a concurrent theoretical push to provide ever more precise predictions to interpret experimental results. For example, future direct dark matter detection experiments, searches for Majorana neutrinos, and neutron electric dipole moment searches, all require a fundamental understanding of nuclear physics in the low-energy regime. Nuclear physics emerges from *non-perturbative* dynamics of the fundamental theory of the strong interaction, QCD, at low energies. Lattice QCD is currently our only systematically controllable solution to QCD in the low-energy regime, and coupled with effective field theory, can be used to provide precise physical predictions from QCD. In this thesis, we focused on lattice calculations which have implications for precision tests of the Standard Model.

After a brief introduction to lattice QCD and EFT, we present a lattice computation of the strong isospin breaking contribution to the neutron-proton and cascade mass splitting. We observe non-analytic behavior in the neutron-proton and cascade mass splittings, which is uniquely indicative of chiral dynamics. The neutron-proton mass splitting is related via chiral symmetry to the CP-violating pion-nucleon interactions induced by the QCD $\bar{\theta}$-term, and we provide an estimate of the induced pion-nucleon coupling arising from the $\bar{\theta}$-term.

In the next section, we present the first calculation of the renormalization factors for bilinear operators, and the four quark operator basis induced by new physics, which were computed on the Möbius Domain Wall fermion on gradient flowed HISQ ensembles. We use momentum sources and the RI-SMOM method, using two projection schemes, and use the step scaling procedure to calculate the running of our operators up to a scale of 3 GeV.

In chapter 5, we presented progress in the first lattice QCD calculation of the $\mathcal{CP}$-violating pion-nucleon couplings induced by the quark chromo-electric dipole operators. These long-range pion-nucleon interactions lead to an enhanced nuclear Schiff moment in diamagnetic atoms, and thus play an important role in the interpretation of nuclear EDM experiments. In this work, we use chiral perturbation theory, as well as an unconventional method of calculating nucleon matrix elements on the lattice, to calculate the bare couplings in terms of spectroscopic shifts of the nucleon mass induced by the $\mathcal{CP}$-conserving quark chromo-magnetic dipole operators. We then detail the renormalization procedure to be used to renormalize the chromo-magnetic operator, including subtraction of the power divergent mixing with the scalar operator.

TABLE OF CONTENTS

ACKNOWLEDGMENTS

I would like to thank the numerous people who have helped me through this dissertation. Without their hard work,patience and guidance, this thesis would not have been possible.

I would first like to thank my co-advisor André Walker-Loud for the many years of tireless support, for never giving an inch, and always pushing me to just "do it the right way."

I would also like to thank my advisor Kostas Orginos, whose support has led to so many opportunities for professional growth and career advancement.

I would like to thank Pavlos Vranas, for serving as my LGSP mentor, for the years of professional support and encouragement, and for introducing me to the many opportunities Livermore has to offer.

I would like to thank my group members and collaborators, whose passion for physics, endless intellectual rabbit holes, and most importantly love of coffee, has led to so many fun projects these past couple years.

I would like to thank Jason Chang, Arjun Gambhir, Emanuele Mereghetti, Henry Monge, Amy Nicholson, Enrico Rinaldi, and Evan Berkowitz for the many fun and enlightening conversations.

I would like to thank Michael Buchoff, for the summer internship that led to so many opportunities, for the many coffee bills, and infectious excitement.

I dedicate this thesis to my wife, whose love, support, and great coffee has pushed me through this thesis. I am a much better man, physicist, and father thanks to her. To my sons, Dylan and Zev, who are patient and understanding beyond their years, and have taught me so much about ohana. To my son Avi, when I thought my life couldn't get better, you came in to the world proving me wrong. To my parents, who were always there for me, and have devoted so much time, love, and effort into making me just the right amount of funny. Thank you all.

LIST OF TABLES

LIST OF FIGURES

Chapter 1

Introduction

The universe is observed to contain more baryons than anti-baryons, on the order of one part per billion. All astronomical observations further indicate this asymmetry to be a generic feature of our observable universe. These observations have revealed several features of our universe indicating that the observed asymmetry is not an initial condition, but was generated dynamically via some process (*baryogenesis*) in the early universe [1]. First, if the asymmetry was in fact an initial condition, this implies there is an implausible fine tuning to the order of one extra baryon for every billion anti-baryons. This asymmetry would then have been exponentially diluted during the expansion phase of the universe. Second, if matter and anti-matter were generated in pockets in some out of equilibrium process in the early universe, while still preserving zero net baryon number, there should exist domain walls where matter and anti-matter annihilate and produce gammas. The spectrum of deep space high energy radiation should also contain an equal number of matter and anti-matter. To date, observations from the satellite experiments Alpha Magnetic Spectrometer-02 (AMS-02) and it's predecessors have detected a large dominance of matter over anti-matter in cosmic rays [2]. Furthermore, null observations of complex anti-matter atoms, such as anti-helium, in the cosmic ray flux currently provides no evidence for large scale anti-matter structures such anti-stars [3]. These and other observations suggest that the universe began in a baryon anti-baryon symmetric state.

The current baryon anti-baryon asymmetry can be expressed in two equivalent ways in terms of cosmological parameters

$$\eta \equiv \frac{n_B - n_{\bar{B}}}{n_\gamma} = (6.19 \pm 0.14) \times 10^{-10}$$

$$\Omega_B h^2 \equiv \frac{\rho_B}{\rho_{\text{crit}}} h^2 = 0.0223 \pm 0.0002. \qquad (1.1)$$

η is the baryon to photon ratio, expressed in terms of the number densities of baryons n_B, anti-baryons $n_{\bar{B}}$, and photons n_γ, while $\Omega_B h^2$ is the physical baryon density given in terms of the baryonic fraction of the critical energy density $\rho_B/\rho_{\text{crit}}$, and the h the Hubble parameter [4, 5][1]. The primordial abundances of light nuclei D, ^{3}He, ^{4}He, and ^{7}Li, produced in the early universe is extremely sensitive to the value of η, as reaction rates depend on the baryon number density [6]. The Big Bang Nucleosynthesis (BBN) baryon density, predicted using the above values of η, is then found to be

$$0.021 \leq \Omega_B h^2 \leq 0.024 \ \ (95\% CL). \qquad (1.2)$$

Furthermore, fitting η from the BBN model predictions of light elemental abundances, and comparing the light elemental abundances with Nature, predicts a value of η overlapping with the CMB data [6]. An independent analysis, using Cosmic Microwave Background data from Planck 2015, validates the physical baryon density predicted using the BBN model, yielding $\Omega_B h^2 = 0.0223 \pm 0.0002$. Any complete theory of nature should thus reproduce these observations.

The requirements for the generation of a baryon dominated universe were made precise by Sakharov in 1967, in the form of three conditions [7].

1. Baryon number violation: In order to evolve from $\eta = 0$ to a non-zero value, net baryons must be produced.

2. $\mathcal{C}$ and $\mathcal{CP}$ violation: Any process leading to a net baryon number would neces-

---

[1]Cosmological parameters were taken from the WMAP 9 year, and Planck 2015 data.

sarily distinguish matter from anti-matter. Under $\mathcal{C}$, all internal quantum numbers (e.g. electric charge, isospin, color) are conjugated, changing a particle into an anti-particle. $\mathcal{P}$ parity changes the sign of the spatial components of a field as well as changes it's handedness. $\mathcal{C}$ and $\mathcal{CP}$ violation uniquely distinguishes matter from anti-matter, and thus this process would be distinct from it's $\mathcal{C}$ and $\mathcal{CP}$-conjugate.

3. Out of thermal equilibrium dynamics: This condition is needed in order to preserve the asymmetry generated by condition (1) and (2). Since a particle and it's anti-particle have the same mass, in thermal equilibrium the Boltzmann distribution predicts an equal number particles and anti-particles. Thus any asymmetry generated from (1) and (2) is quickly erased by it's reverse process in equilibrium [8]. Note that this would also erase any initial condition asymmetry.

The Standard Model (SM) of particle physics contains all of the mechanisms necessary for successful baryogenesis, however it is well known that without input from physics beyond the Standard Model (BSM) the observed baryon abundance is not produced [9]. For example, the mass of the Higgs boson is too large to produce a strong first order electroweak phase transition, violating condition (3)[9]. $\mathcal{CP}$ violation within the SM is a consequence of a single $\mathcal{CP}$ violating phase in the CKM matrix, which has been shown to be insufficient to produce the observed baryon to photon ration [10, 11]. Thus successful baryogenesis requires BSM mechanisms for generating out of equilibrium processes, and new sources of $\mathcal{CP}$ violation [12].

The measurement of neutrino oscillations creates another intriguing possibility for baryogenesis. With three generations of massive neutrinos, a $\mathcal{CP}$ violating phase can exist in the neutrino equivalent of the CKM matrix[13]. This $\mathcal{CP}$ violating phase, if non-zero, would provide an extra source of $\mathcal{CP}$-violation in the extended SM. Recent results from the T2K experiment measuring the $\mathcal{CP}$-violating neutrino phase δ_{CP} excludes $\mathcal{CP}$-conservation at $\sim 2\sigma$ [14, 15]. This $\mathcal{CP}$-violating phase, if it is not 0 or $\pm\pi$, would result in a difference in the oscillations of neutrinos and anti-neutrinos that is measurable[16]. This

preliminary result comes after analysis of the near and far detector event data comparing to expected electron neutrino and anti-neutrino events[17]. The T2K result is suggestive of $\mathcal{CP}$-violation in the lepton sector, however the detector has collected roughly 30% of expected total protons-on-target, and the analysis, especially for anti-neutrino events, suffers from low statistics [17]. Furthermore, subsequent results from the NOνA experiment do not rule out a $\mathcal{CP}$-conserving value of δ_{CP}, indicating $\mathcal{CP}$-violation in the lepton sector deserves much further scrutiny before any conclusion may be reached [18] . Next generation experiments DUNE and T2HK may have the required sensitivity to detect a $\mathcal{CP}$-violating δ_{CP}, so the true value of this parameter may be resolved by next generation experiments [19, 20].

Since neutrinos are neutral, this presents the possibility that they are their own antiparticle e.g. are Majorana fermions. Such a possibility is forbidden in the charge sector, since $U(1)_{em}$ forbids mixings of fermions of the same charge[9]. Such Majorana interactions would violate lepton number, and the classical baryon plus lepton number symmetry of the SM (B - L is still conserved at the quantum level)[12]. It is well known however, that B + L number is violated by anomalies in the SM [21] which induce non-perturbative gauge field configurations which act as a source for B + L violation. Such *sphaleron* processes are highly suppressed at low temperature, however at temperatures above the electroweak phase transition ($\sim$ 100 GeV) the sphaleron processes are in thermal equilibrium [21]. This implies that any L violating process (since B - L is conserved) generates an excess baryon number through the sphaleron process, and provides a *Leptogenesis* mechanism for the observed baryon asymmetry[12]. An experimental observation of the process of neutrino-less double beta decay ($0\nu\beta\beta$), which violates lepton number by two through the exchange of (usually light) Majorana neutrinos, would confirm the Majorana nature of neutrinos, and provide support for a leptogenesis origin of matter. Note that many scenarios require the addition of heavy right handed neutrinos through the "seesaw" mechanism, which naturally explains the small scale of the light neutrino masses [12].

Assuming the BSM degrees of freedom are heavy[2], then integrating out the heavy dynamics at the electroweak scale induces effective higher (than four) dimensional interactions involving SM fields present at the electroweak scale [1, 22]. After electroweak symmetry breaking, these higher dimensional operators take the form four quark, three gluon, dipole moment, etc... operators which are suppressed by two powers of the heavy new physics scale Λ_{BSM} [23]. This suppression by a heavy scale allows us to apply the EFT framework further, tracking their induced interactions among mesons and baryons below the hadronic scale $\sim \mathcal{O}(1)$ GeV. Using this framework, experimental observations of processes such as proton decay, permanent neutron electric dipole moments, and neutrino-less double beta decay, may then be linked directly to their BSM sources. In practice, interpretation of experimental results in this manner relies upon precision matrix elements at low energy scales from the fundamental theory of quarks and gluons, QCD. In the next chapter we review the important aspects of QCD, as well as it's discretized solution, lattice QCD.

_____

[2]This is not an unreasonable supposition. Baryogenesis suggests that new degrees of freedom are active above the electroweak scale $\mathcal{O}(100)$ GeV, however the lack of observation in nuclear experiments suggests their effects at hadronic scales are highly suppressed.

Chapter 2

QCD and Effective Field Theory

2.1 QCD

Quantum Chromodynamics (QCD) is the fundamental theory of the strong interaction, and describes the dynamics of quarks and gluons. Quarks, which are fermions, transform under the fundamental representation of $SU(3)$ and carry a single color index. Gluons, which carry two color indices and transform under the adjoint representation of $SU(3)$, are the 8 boson color force carriers of QCD. The transformation properties of quarks and gluons are determined by the requirement that QCD be invariant under local $SU(3)$ color transformations. QCD contains at most eight parameters that must be measured: the quark masses, an emergent scale Λ_{QCD}, and the $\bar{\theta}$ term. After adding in the the electroweak force, all of nuclear physics is in principle derivable from QCD.

The QCD lagrangian, including a possible $\mathcal{CP}$ violating θ term, is given by

$$\mathcal{L}_{QCD} = \sum_f \bar{q}_f(i\slashed{D} - m_f)q_f - \frac{1}{4}G^a_{\mu\nu}G^{\mu\nu}_a - \bar{\theta}\frac{g_s^2}{64\pi^2}\epsilon^{\mu\nu\alpha\beta}G^a_{\mu\nu}G^a_{\alpha\beta}. \tag{2.1}$$

The quark fields of flavor f are q_f, while the covariant derivative $D_\mu = \partial_\mu - ig_s A_\mu$ describes the dynamics of the quark field and their coupling to the gluons. The dynamics and self interactions of the gluons are contained in the term quadratic in the field strength $G_{\mu\nu} = \partial_\mu A_\nu - \partial_\nu A_\mu - i[A_\mu, A_\nu]$. The final term contributes to $\mathcal{CP}$ violation in the Standard

6

Model, and is proportional to the (reduced) QCD vacuum angle $\bar{\theta}$. A priori, this parameter is expected to be $\mathcal{O}(1)$, however experiments measuring the permanent electric dipole moment of Ultracold neutrons places an upper bound on this value to be $\mathcal{O}(10^{-10})$ [6, 24]. This is known as the strong $\mathcal{CP}$ problem, and remains unresolved.

A possible solution to the strong CP problem, known as the Peccei-Quinn (PQ) mechanism, generates a zero $\bar{\theta}$ angle dynamically by positing a spontaneously broken global $U(1)_{PQ}$ chiral symmetry [25–27]. The broken $U(1)_{PQ}$ symmetry generates a Nambu-Goldstone boson, the axion, which is an as of yet unobserved dark matter candidate [28–30]. The $U(1)_{PQ}$ invariant Lagrangian with the addition of the axion field $a(x)$ is[27]

$$\mathcal{L} = \mathcal{L}_{SM} - \bar{\theta}\frac{g_s^2}{64\pi^2}\epsilon^{\mu\nu\alpha\beta}G_{\mu\nu}^a G_{\alpha\beta}^a - \frac{1}{2}\partial_\mu a \partial^\mu a + \mathcal{L}_{int} - \xi\frac{a}{f_a}\frac{g_s^2}{64\pi^2}\epsilon^{\mu\nu\alpha\beta}G_{\mu\nu}^a G_{\alpha\beta}^a, \qquad (2.2)$$

which after $U(1)_{PQ}$ is spontaneously broken settles on the minimum of the axion potential

$$\langle a \rangle = -\frac{f_a}{\xi}\bar{\theta}, \qquad (2.3)$$

and the "effective" $\bar{\theta}$ term dynamically relaxes to zero.

The challenge with extracting first principle results from QCD comes from the same property that binds quarks and gluons into hadrons: namely that QCD is confining. In QCD, the color potential between quarks gets larger with distance, while at short distance the quarks become asymptotically free. This mechanism was hypothesized as a means of explaining the experimental observation that all hadrons were colorless $SU(3)$ singlet states, despite the theory having massless force carrier particles[1]. Though confinement has never been proven mathematically, a hint of it can be seen by looking at the variation of the strong coupling $\alpha_s(\mu^2) = \frac{g_s^2(\mu^2)}{4\pi}$ with energy scale. This leads to the well known

---

[1]This discovery by David Gross, David Politzer and Frank Wilczek lead them to win the 2004 Nobel Prize.

logarithmic differential equation

$$\mu^2 \frac{d\alpha_s}{d\mu^2} = \beta(\alpha_s) = -\alpha_s^2(\beta_0 + \beta_1\alpha_s + \beta_2\alpha_s^2 + ...),$$ (2.4)

with $\beta(\alpha_s)$ known as the QCD β-function. A solution is found via a perturbative expansion of $\beta(\alpha_s)$, with the first two universal (scheme independent) orders β_0 and β_1 shown in equation (2.5) [31].

$$\beta_0 = \frac{1}{4\pi}\left[\frac{11}{3}N_c - \frac{2}{3}N_f\right] \quad , \quad \beta_1 = \frac{1}{(4\pi)^2}\left[\frac{34}{3}N_c^2 - \frac{38}{3}N_f\right]$$ (2.5)

Figure 2.1a shows an example of the scale dependence of the strong coupling α_s as a function of renormalization scale μ^2 for fixed number of quark flavors. As the scale is lowered, the coupling between quarks and gluons becomes stronger, and results that depend on a perturbative expansion in terms of α_s break down. There is yet no rigorous proof of confinement for QCD with dynamical quarks, and a proper solution is related to the existence of a mass gap which is one of the as of yet unsolved Millennium Prize Problems [32]. Note the negative sign in the beta functions comes from the gauge field (N_c) contribution in Eq. (2.5). Only non-abelian gauge theories exhibit this type of behavior, which arises from self interactions of the gauge fields (gluons) such as that shown in Figure 2.1b (E.g. it is well known that Quantum Electrodynamics does not exhibit asymptotic freedom).

In lattice QCD, one can formulate the static (heavy) quark potential in terms of gauge invariant Wilson loops, which leads to a static quark potential of the form [33–35]

$$V(r) = A + \frac{B}{r} + \sigma r.$$ (2.6)

The term σr arises from the large coupling limit (and large Euclidian time) of the Wilson loop, and shows the confining behavior expected at large distances and couplings. σ is called the string tension, and is roughly $\sqrt{\sigma} \approx 0.45$ GeV [36].
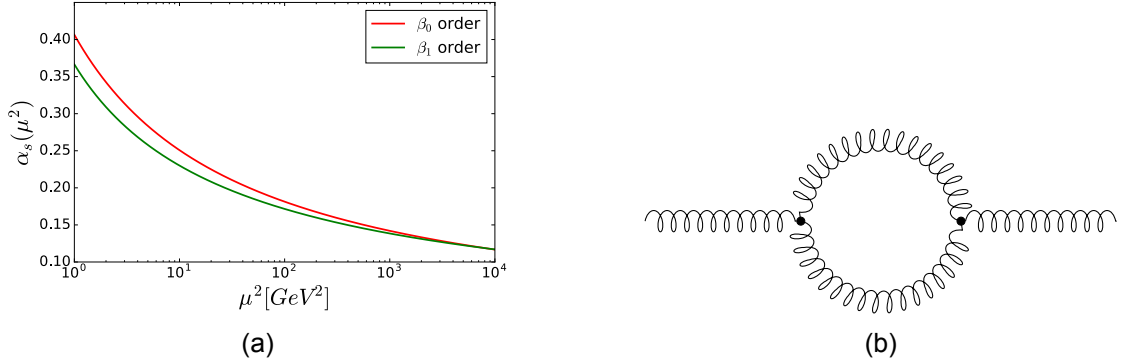
Figure 2.1: Figure 2.1a QCD renormalized coupling as a function of renormalization scale μ^2 for $N_f = 4$ active quark flavors. Figure 2.1b Example of the types of diagrams contributing to the gluon self energy at one loop that are used in determining β_0.

The non-trivial properties of QCD at low energies, namely confinement and asymptotic freedom, require that results at nuclear physics energy scales ($\mu^2 \sim 1$ GeV^2) come from a non-perturbative solution of the theory. While many clever methods have been developed to derive results from QCD non-perturbatively[2], the most well tested and systematically improvable method is Lattice QCD. When combined with Effective Field Theory, precise physical prediction from QCD are possible [40]. In the next sections we review the general aspects of both approaches, as well as specifics that will be useful for the work done in this thesis.

2.2 Lattice QCD

We give a very brief introduction to the basic principles of lattice QCD.

It is well established that all of quantum mechanics may be formulated in a path integral representation[41–45]. In this formulation, calculations involving quantum mechanical fields and operators are instead replaced by a functional integration over all possible field configurations weighted by the classical action. The principal object in this representation is the partition function, which represents the vacuum to vacuum transition amplitude

---

[2]See for example [37–39].

9

$\langle\Omega|\Omega\rangle$. The QCD partition function without a $\bar{\theta}$ term is given in Eq. (2.7),

$$\mathscr{Z}_{QCD} = \int \mathcal{D}[\Phi(x)] e^{iS_g[A_\mu(x)] + i\int d^4x \sum_f \bar{q}_f(i\slashed{D} - m_f)q_f(x)} \qquad (2.7)$$

where $\Phi(x)$ is shorthand for all of the fields in our theory, S_g is the Yang-Mills gauge action, and the fermion action is left explicit. With the addition of source terms, and proper gauge fixing conditions, all n-point correlation functions may be generated by taking functional derivatives of the above expression, without reference to perturbation theory. For example, the expectation value of an operator $\mathcal{O}$ may be found by evaluating Eq. (2.8).

$$\langle\Omega| \mathcal{O}[\Phi(x)] |\Omega\rangle = \frac{1}{\mathscr{Z}_{QCD}} \int \mathcal{D}[\Phi(x)] e^{iS_{QCD}[\Phi(x)]} \mathcal{O}[\Phi(x)] \qquad (2.8)$$

As written, direct calculation of (2.8) is numerically intractable, involving an infinite dimensional integral with a highly oscillatory weight factor. Numerical integrability can be realized by a combined Wick rotation and discretization prescription. The Wick rotation analytically continues our time parameter into the complex plane, such that $t \to i\tau$, while we discretize our spacetime points such that $\Lambda = \{(\mathbf{n}, n_t) | \mathbf{n} \in \Lambda_3, n_t \in 0, 1, ... N_T - 1\}$. Under this prescription, the weight factor is now strictly real and positive, and decays exponentially away from the minimum[3]. The finite, but large dimensional integral may then be approximated using stochastic techniques in finite computational time. Furthermore, the necessarily finite lattice spacing and box size regulate our theory, with the UV regulator given by the inverse inter-lattice point spacing a, and the IR regulator given by the box size L.

---

[3] The weight factor is real and positive in the absence of a chemical potential for the quarks. For a discussion of the quark chemical potential, see e.g. [46, 47]. The fermion sign problem also makes it a challenge to perform calculations in the presence of $\mathcal{CP}$-violating operators directly added to our Lagrangian, as these terms are generally imaginary and thus importance sampling of the path integral fails [46, 48].

After imposing proper boundary conditions[4], the expectation value takes the form

$$\langle \Omega | \, \mathcal{O}[\Phi(x)] \, | \Omega \rangle_E = \frac{1}{\mathcal{Z}_E} \sum_{x \in \Lambda} \mathcal{D}[\Phi(x)] e^{-S_E[\Phi(x)]} \mathcal{O}[\Phi(x)]. \tag{2.9}$$

S_E is some discretization of the Euclidian QCD action, generically depending in some non-trivial manner on the discretization scale a, but with a well defined limit $\lim_{a \to 0} S_E \to S_{QCD}^E$.

The discretization of fermions on the lattice induces non-local contact terms between quarks, for which a link variable $U_\mu(x) \in SU(N_c)$ (a gauge transporter) must be included to preserve gauge invariance. The gauge dependence in our discretized action is thus most naturally framed in terms link variables, which are related to our gauge fields $U_\mu(x) = \exp\{iaA_\mu(x)\}$. In lattice calculations we thus replace integration over $\mathcal{D}[A(x)]$ with integration over the link variables $\mathcal{D}[U]$. This amounts to integrating over the group manifold of $SU(N_c)$.

Since the discretized Euclidian formulation above is quadratic in the quark fields, this allows us the estimate the integral using *Monte Carlo* techniques. It is convenient to first integrate our action over the fermion fields, yielding a fermion determinant for each flavor that is dependent on the gauge field. Expectation values of operators are now calculated via an average over stochastic samples of the probability distribution

$$dP(U) = \frac{1}{\mathcal{Z}_E} e^{-S_g[U]} \det[\slashed{D} + m_q]. \tag{2.10}$$

Gluon dynamics are captured by the gauge part of the action, S_g, while the fermion determinant $\det[\slashed{D} + m_q]$ (shorthand for N_f determinants) contains the quark dynamics. In true dynamical calculations, the determinant must be included as part of the probability distribution if we are to properly account for quark loops in the sea[5]. Once samples of

---

[4]If we interpret above as a finite temperature Euclidian field theory, then the temperature is proportional to the inverse temporal extent of our lattice, and we must impose anti-periodic boundary conditions on our fermion fields in order that the trace in the partition function is properly taken. In all other cases we take periodic boundary conditions.

[5]Inclusion of the determinant in gauge generation is non-trivial, see e.g. [49, 50].

$dP(U)$ are generated, expectation values are found by taking an average over configurations

$$\langle \mathcal{O} \rangle \approx \frac{1}{N} \sum_{n=1}^{N} \mathcal{O}(U_n) + \mathcal{O}(1/\sqrt{N}), \qquad (2.11)$$

with the stochastic error scaling as $\mathcal{O}(1/\sqrt{N})$ for perfectly uncorrelated samples. Assuming our sampling is ergodic, the $N \to \infty$ limit of the expectation value becomes exact.

Through judicious choice of interpolating fields, we create states with the continuum quantum numbers of interest that have overlap with our physical states in lattice simulations. For example, the operator $\bar{d}(x)\gamma_5 u(x)$, where u and d are up and down quark fields, and γ_5 is the fifth gamma matrix, has the same valence flavor structure of the π^- as well as correct the quantum numbers $J^{PC} = 0^{-+}$. This operator will excite the pion, as well as any other state with the same quantum numbers and flavor structure. The two point correlation function arising from this interpolator is

$$\begin{aligned}
\langle \mathcal{O}_{\pi^-}(x)\bar{\mathcal{O}}_{\pi^-}(0) \rangle &= \frac{1}{\mathcal{Z}_E} \int \mathcal{D}[\Phi(x)] e^{-S_{QCD}^E[\Phi(x)]} \bar{u}\gamma_5 d(x)\bar{d}\gamma_5 u(0) \\
&\approx -\frac{1}{N} \sum_{n=1}^{N} \text{tr}[\gamma_5 S_d(x|0)\gamma_5 S_u(0|x)](U_n),
\end{aligned} \qquad (2.12)$$

where Wick's Theorem has been used to generate all possible contractions of our interpolators.

Generating gauge fields involves computing the fermion determinant, a highly non-local object, and computationally expensive. Calculation of the determinant scales with lattice parameters differently depending on the discretization and algorithm used. Domain Wall Fermion gauge field computations, for example, are known to scale at least as $L^5 m_\pi^{-3} a^{-7}$ [51]. Given the polynomial scaling of cost as calculations become more physical, calculations are typically done on an ensemble of parameters that allow results to be extrapolated to the physical point, ideally accounting for all systematics. The underlying theoretical framework enabling such an extrapolation in a physically motivated, and systematically improvable manner is Effective Field Theory (EFT) and is the subject

of the next section.

2.3   Effective Field Theory

In the physical description of a system, irrelevant parameters or degrees of freedom can obfuscate results and physical intuition. Generically, if the description of a system contains a natural separation of scales, then in some limit one may remove structure from the theory which contributes less than a desired ϵ to results. A classical example would be special relativity in the limit where $c \to \infty$. The Lorentz transformation relating two sets of coordinate systems S and S' whose origins coincide at $t = t' = 0$, and whose relative velocity is v along the x axis as measured by S is given by [52]

$$
\begin{aligned}
ct' &= \gamma \left(ct - \beta x \right) \\
x' &= \gamma \left(x - \beta ct \right),
\end{aligned}
\tag{2.13}
$$

where

$$
\begin{aligned}
\beta &= v/c \\
\gamma &= \frac{1}{\sqrt{1 - \beta^2}}.
\end{aligned}
\tag{2.14}
$$

For velocities which are small relative to the speed of light,

$$
\gamma \approx 1 - \frac{1}{2}\beta^2 + \mathcal{O}(\beta^4)
\tag{2.15}
$$

our Lorentz transformation approaches unity and we recover our Galilean result. The small expansion parameter for this system is β, and is the ratio of the small to large scale in the system. We may also systematically improve our accuracy by including more orders in the expansion. For typical velocities in human experience $\beta \sim \mathcal{O}(10^{-7})$ and we may safely ignore relativistic effects. Other examples involving a separation of scales are multipole approximations, classical limit of the path integral, and the gravitational potential near the surface of the Earth.

The generalization of the idea above to Quantum Field Theories requires more work, but the underlying physical principle is similar, and is given by the "folk theorem" written down by Steven Weinberg [22]:

> If one writes down the most general possible Lagrangian, including *all* terms consistent with assumed symmetry principles, and then calculates matrix elements with this Lagrangian to any given order of perturbation theory, the result will simply be the most general possible S-matrix consistent with analyticity, perturbative unitarity, cluster decomposition, and the assumed symmetry principles.

What makes an EFT so useful is the separation of large and small scales, allowing irrelevant parameters or degrees of freedom to decouple from our description of the system. The relevant degrees of freedom are then ordered term by term in the Lagrangian in an expansion in ϵ, generally the ratio of the small to large scale, to some desired accuracy. Each term comes with an accompanying *a priori* unknown low energy constant (LEC), that must be determined by matching to the underlying theory, or to experiment. Once determined, the Lagrangian may then be used to calculate other processes in the region of validity.

Here we see manifest the separation of scales. The long distance physics is encoded in the relevant degrees of freedom of the expansion in ϵ, while the short distance physics is integrated into the LECs.

In the case of nuclear systems, quarks and gluons form an inefficient description of nuclear processes, while the low energy states of QCD, the pions and nucleons, are the more natural degrees of freedom. The pions (and to a lesser degree the kaons) have a large spectral gap with the $\rho(770)$ and the $\omega(782)$, and it is thus natural to posit that the ρ sets a heavy scale Λ, while the pion sets a soft scale Q, suggesting an expansion in terms of Q/Λ. In order to make this description in terms of pions(and kaons) an EFT, and

not a phenomenology, we must connect the degrees of freedom at the soft scale to the symmetries of the fundamental theory, QCD.

The fermion part of the Minkowski space QCD Lagrangian is

$$\mathcal{L}_f = \bar{q} \left(i\slashed{D} - m_q \right) q, \tag{2.16}$$

where $\bar{q} = \left(\bar{u}, \bar{d}, \bar{s}, ... \right)$ and m_q is the diagonal quark mass matrix. Sorting our light and heavy quarks[6] based on our heavy scale Λ [6, 40]

$$\begin{matrix} m_u = 0.00236(24) \text{ GeV} & & m_c = 1.286(30) \text{ GeV} \\ m_d = 0.00503(26) \text{ GeV} & \ll 1 \text{ GeV} \le & m_b = 4.190(21) \text{ GeV} \\ m_s = 0.09390(110) \text{ GeV} & & m_t = (156 - 173) \text{ GeV}, \end{matrix} \tag{2.17}$$

we ignore, or "integrate out", the heavy quark dynamics as being above our heavy scale Λ, and just consider the symmetries of the light quarks. The chiral projection operators

$$\begin{aligned} P_R &= \frac{1}{2} \left(1 + \gamma_5 \right) \\ P_L &= \frac{1}{2} \left(1 - \gamma_5 \right), \end{aligned} \tag{2.18}$$

project out the left and right handed chiral components of spinors. Applying these projection operators on our light QCD Lagrangian, we find

$$\mathcal{L}_f = \bar{q}_L i\slashed{D} q_L + \bar{q}_R i\slashed{D} q_R - \bar{q}_R m_q q_L - \bar{q}_L m_q q_R. \tag{2.19}$$

The quark mass matrix m_q mixes the left and right handed components of our spinors, and explicitly breaks the $SU(N_f)_L \times SU(N_f)_R \times U(1)_V$ global symmetry of the kinetic term[7]. The light quark masses are light enough however, that this explicit breaking is

---

[6]The most precise determinations of the up, down, strange, charm, and bottom quark masses come from lattice calculations [6, 40]. The up, down, strange, charm, and bottom quark masses quoted in this work are given in the renormalization scheme and scale of reference [40] for 2+1+1 flavors of quarks, while the top quark mass is taken from the PDG review [6]. The interested reader may refer to [53] for a state of the art calculation of the quark masses.

[7]Classically we would expect the above kinetic terms to be invariant under a full $U(N_f)_L \times U(N_f)_R$ symmetry, however the $U(1)_A$ symmetry is broken at the quantum level by the chiral anomaly. The remaining unbroken symmetry is then $SU(N_f)_L \times SU(N_f)_R \times U(1)_V$.

small, and can be accounted for perturbatively[8].

If chiral symmetry was broken only by a small explicit mass term, we would expect hadrons composed of our light quarks to form into nearly mass degenerate multiplets with dimensionalities of the irreducible representations of the $SU(N_f)_L \times SU(N_f)_R \times U(1)_V$ symmetry of the chiral QCD Lagrangian [54]. Such multiplets should have nearly degenerate negative parity partners, e.g. such that the nucleon N (P = +1) would be nearly degenerate with the negative parity partner N^*. Nature does not however provide such degenerate multiplets, and indeed $m_N \sim .94$ GeV $< m_{N^*} \sim 1.5$ GeV [6]. Furthermore, the existence of nearly massless multiplets in the meson spectrum (pions and kaons), despite having no even parity degenerate multiplet, suggests the existence of a *spontaneously* broken chiral symmetry.

The mass spectra of the ρ mesons form a degenerate isospin multiplet that indicates the vector subgroup of $SU(N_f)_L \times SU(N_f)_R$ is still a good symmetry[55]. Nature thus gives evidence that the global chiral symmetry is then spontaneously broken down to the vector subgroup $SU(N_f)_V \times U(1)_V$ [9]. The Goldstone theorem then allows the generation of $N_f^2 - 1$ Nambu-Goldstone bosons in the process (one for each broken generator), with relatively small masses due the explicit breaking of chiral symmetry from the quark mass matrix [28, 29, 57]. The quark mass matrix leads to a non-zero divergence of the axial and vector QCD currents, however due to the small scale generated by the quark masses we may include them as a perturbation to the "exact" chiral symmetry of the QCD Hamiltonian, leading to Chiral Perturbation Theory [57, 58].

---

[8]This supposition, and thus the validity of an EFT modeled after this symmetry, is naively expected to hold so long as the mass scale of the heaviest quark included in the theory is small relative to the heavy scale. Including two light quarks, and using our heavy scale Λ, the light scale is roughly 1 - 2 % of the heavy, while including the strange yields 10 - 20 %.

[9]Under certain assumptions, Vafa and Witten [56] showed that the global vector-like symmetries of QCD cannot be spontaneously broken.

2.3.1 Chiral Perturbation Theory

In this section we describe the relevant aspects of the low energy Effective Field Theory for the pseudo Nambu-Goldstone bosons of our broken chiral symmetry, χPT.

As a consequence of spontaneous symmetry breaking, we expect that the broken generators of our global symmetry G are associated with a spin-0 particle for each X^a which does not annihilate the vacuum

$$X^a \ket{0} \neq 0, \tag{2.20}$$

while those generators which do annihilate the vacuum form a subgroup H of G[28, 29, 59, 60]. For N_f flavors, the group of X^a is isomorphic to $SU(N_f)$, and we expect our Goldstone bosons to be described by an $SU(N_f)$ valued field $\Sigma(x)$.

The Σ field is composed of our broken generators

$$\Sigma = \exp\left(\frac{2i\phi}{f}\right) \qquad \text{and} \qquad \phi = \sum_i \lambda_i \phi_i(x), \tag{2.21}$$

where λ_i is an element of the lie algebra of the broken group, and $\phi_i(x)$ is a Goldstone boson field. $f \approx 130$ MeV is a low energy constant fixed by the canonical normalization of our fields, and is related to the pion decay constant. Since Σ parameterizes the fluctuations about our vacua, it must transform in G as

$$\Sigma \xrightarrow{G} L\Sigma R^\dagger. \tag{2.22}$$

Including the quark masses can be achieved using *spurion* analysis, e.g. we pretend that the quark matrix transforms in an invariant manner under G

$$m_q \quad \xrightarrow{G} \quad Rm_qL^\dagger. \tag{2.23}$$

At the end of our calculation we may then set m_q = diag(m_u,m_d,...) to explicitly break

chiral symmetry down to the vector subgroup. The most general lowest order Lagrangian consistent with our underlying symmetries and including our quark masses is now

$$\mathcal{L}_{eff}^{(2)} = \frac{f^2}{8} \text{tr}\left[\partial_\mu \Sigma \partial^\mu \Sigma^\dagger\right] + \frac{f^2 B_0}{4} \text{tr}\left[\Sigma m_q^\dagger + m_q \Sigma^\dagger\right]. \tag{2.24}$$

f and B_0 are low energy constants (LECs) determined by the underlying theory (QCD), and must be determined from non-perturbative matching calculations. B_0 is related to the chiral condensate in the chiral limit

$$B_0 = \lim_{m_q \to 0} \frac{|\langle\Omega|\bar{q}q|\Omega\rangle|}{f^2}. \tag{2.25}$$

From here on we work in $SU(3)$ chiral perturbation theory, in which we have three light flavors of quarks. The ϕ matrix in $SU(3)$ is

$$\phi = \sum_i t^i \phi_i(x) = \begin{bmatrix} \frac{\pi^0}{\sqrt{2}} + \frac{1}{\sqrt{6}}\eta & \pi^+ & K^+ \\ \pi^- & -\frac{\pi^0}{\sqrt{2}} + \frac{1}{\sqrt{6}}\eta & K^0 \\ K^- & \bar{K}^0 & -\frac{2}{\sqrt{6}}\eta \end{bmatrix}. \tag{2.26}$$

where $t^i = \lambda^i/2$ with λ^i the ith Gell-Mann matrix. Expanding the Σ about the ground state, we find for the leading order (LO) Lagrangian [58]

$$\mathcal{L}^{(2)} \approx \partial_\mu \pi^+ \partial^\mu \pi^- + \partial_\mu K^+ \partial^\mu K^- + \partial_\mu \bar{K}^0 \partial^\mu K^0 + \frac{1}{2}\partial_\mu \pi^0 \partial^\mu \pi^0 + \frac{1}{2}\partial_\mu \eta \partial^\mu \eta$$

$$+B_0 \left(m_u + m_d\right) \pi^+ \pi^- + B_0 \left(m_u + m_s\right) K^+ K^- + B_0 \left(m_d + m_s\right) \bar{K}^0 K^0 \tag{2.27}$$

$$+B_0 \bar{m} \pi^0 \pi^0 + \frac{1}{3} B_0 \left(\frac{m_u}{2} + \frac{m_d}{2} + 2m_s\right) \eta\eta + \frac{1}{\sqrt{3}}\left(m_u - m_d\right)\pi^0 \eta + ...,$$

plus interaction terms, from which we determine our LO pion, kaon and eta masses. The interaction terms give rise to self energy corrections to our LO masses which are suppressed by a factor of $\left(M_x^2/(4\pi f)^2\right)^n$, where M_x^2 is a quantity the same *order* as the squared meson masses [10]. The scale factor $4\pi f \approx m_\rho$ is naturally identified with our

---

[10] Note also that in the chiral limit the interactions between our now Nambu-Goldstone bosons vanish in the limit of zero external momenta, as we should expect [54].

heavy chiral symmetry breaking scale, and naturally sets the scale for our chiral expansion[11].

In keeping with the correct power counting [22], the $\mathcal{O}(\frac{M_x^2}{(4\pi f)^2})$ (NLO) meson masses must include loop contributions from $\mathcal{L}^{(2)}$ above, as well as tree level contributions from the NLO Lagrangian $\mathcal{L}^{(4)}$. Writing down all terms of $\mathcal{O}(p^4, p^2 m_q, m_q^2)$ composed of derivatives of our Σ fields and quark mass terms, the $\mathcal{L}^{(4)}$ Lagrangian is [58]

$$
\begin{aligned}
\mathcal{L}_{eff}^{(4)} =& L_1 \, \text{tr}\Big[\partial_\mu \Sigma^\dagger \partial^\mu\Big]^2 + L_2 \, \text{tr}\Big[\partial_\mu \Sigma^\dagger \partial_\nu \Sigma\Big] \, \text{tr}\Big[\partial^\mu \Sigma^\dagger \partial^\nu \Sigma\Big] + L_3 \, \text{tr}\Big[\partial^\mu \Sigma^\dagger \partial_\mu \Sigma \partial^\nu \Sigma^\dagger \partial_\mu \Sigma\Big] \\
&+ 2B_0 L_4 \, \text{tr}\Big[\partial^\mu \Sigma^\dagger \partial_\mu \Sigma\Big] \, \text{tr}\Big[m_q^\dagger \Sigma + m_q \Sigma^\dagger\Big] + 2B_0 L_5 \, \text{tr}\Big[\partial^\mu \Sigma^\dagger \partial_\mu \Sigma \left(m_q^\dagger \Sigma + \Sigma^\dagger m_q\right)\Big] \\
&+ 4B_0^2 L_6 \, \text{tr}\Big[m_q^\dagger \Sigma + m_q \Sigma^\dagger\Big]^2 + 4B_0^2 L_7 \, \text{tr}\Big[m_q^\dagger \Sigma - m_q \Sigma^\dagger\Big]^2 \\
&+ 4B_0^2 L_8 \, \text{tr}\Big[m_q^\dagger \Sigma m_q^\dagger \Sigma + m_q \Sigma^\dagger m_q \Sigma^\dagger\Big],
\end{aligned}
$$

$$(2.28)$$

where we've introduced the dimensionless LECs $L_1, ..., L_8$. The power of EFT lies in the universality of these LECs. Since we've constructed the most general Lagrangian consistent with our symmetries, once the LECs are fixed by some process, we may then compute *other* quantities of interest using the same fixed Lagrangian. The same generality however becomes unwieldy at higher orders, where the number of LECs for $\mathcal{L}^{(6)}$ increases by an order of magnitude with respect to the $\mathcal{L}^{(4)}$ [62].

Neglecting electromagnetic contributions, at NLO the meson masses now become

---

[11]This gives the correct power counting scheme for Meson Chiral Perturbation Theory [22, 61].

[58]

$$
\begin{aligned}
M_\pi^2 =& B_0 \left(m_u + m_d\right) \{1 + \frac{M_\pi^2}{16\pi^2 f^2} \ln\left(\frac{M_\pi^2}{\mu^2}\right) - \frac{1}{3} \frac{M_\eta^2}{16\pi^2 f^2} \ln\left(\frac{M_\eta^2}{\mu^2}\right) \\
&+ \frac{16 B_0}{f^2} \left(m_u + m_d\right) \left(2 L_8^r - L_5^r\right) \\
&+ \frac{32 B_0}{f^2} \left(m_u + m_d + m_s\right) \left(2 L_6^r - L_4^r\right)\} \\
M_K^2 =& B_0 \left(\frac{m_u}{2} + \frac{m_d}{2} + m_s\right) \{1 + \frac{2}{3} \frac{M_\eta^2}{16\pi^2 f^2} \ln\left(\frac{M_\eta^2}{\mu^2}\right) \\
&+ \left(\frac{m_u}{2} + \frac{m_d}{2} + m_s\right) \frac{16 B_0}{f^2} \left(2 L_8^r - L_5^r\right) \\
&+ \frac{32 B_0}{f^2} \left(m_u + m_d + m_s\right) \left(2 L_6^r - L_4^r\right)\},
\end{aligned}
\tag{2.29}
$$

where $M_\pi^2 = \frac{1}{2}\left(M_{\pi^+}^2 + M_{\pi^0}^2\right)$ and $M_K^2 = \frac{1}{2}\left(M_{K^+}^2 + M_{K^0}^2\right)$. Away from the isospin limit, the non-zero light quark mass difference $2\delta \equiv m_d - m_u$ induces a splitting of the kaon masses proportional to the isospin breaking

$$
\begin{aligned}
\Delta M_K^2 = \left(M_{K^0}^2 - M_{K^+}^2\right) =& 2 B_0 \delta \{1 + \frac{2}{3} \frac{M_\eta^2}{16\pi^2 f^2} \ln\left(\frac{M_\eta^2}{\mu^2}\right) \\
&+ \frac{M_K^2}{M_K^2 - M_\pi^2} \left(\frac{M_\eta^2}{16\pi^2 f^2} \ln\left(\frac{M_\eta^2}{\mu^2}\right) - \frac{M_\pi^2}{16\pi^2 f^2} \ln\left(\frac{M_\pi^2}{\mu^2}\right)\right) \\
&+ \left(m_u + m_d + 2 m_s\right) \frac{16 B_0}{f^2} \left(2 L_8^r - L_5^r\right) + \frac{32 B_0}{f^2} \left(m_u + m_d + m_s\right) \left(2 L_6^r - L_4^r\right)\}
\end{aligned}
\tag{2.30}
$$

while for the pions the splitting is proportional to δ^2 and thus neglected.

2.3.2 Heavy Baryon Chiral Perturbation Theory

In order to include interactions with baryons in chiral theory, we use Heavy Baryon Chiral Perturbation Theory ($HB\chi PT$) [63][12]. Here we do not come close to a pedagogical intro-

---

[12] An analogous approach to χPT in constructing a chiral baryon theory fails, as the nucleon mass $m_N \sim$ 1 GeV introduces a new scale which is of $\mathcal{O}(1)$ with respect to our chiral symmetry breaking scale. This new scale is also of $\mathcal{O}(1)$ with respect to $4\pi f$, killing any hope of establishing a consistent power counting scheme.

duction, but only give some salient features relevant to this work. The interested reader may dive deeper in [54, 63, 64].

In the Heavy Baryon formalism, we separate the heavy baryon mass from the four momentum of the initial and final baryon states. The heavy components of our baryon field may then be integrated out similar to heavy degrees of freedom [64].This enables us to study small fluctuations about the heavy mass parameter. The process is equivalent to a non-relativistic reduction of our theory, and in that spirit we define the momentum of our baryon to be

$$p^\mu = mv^\mu + k^\mu, \tag{2.31}$$

where v^μ is the four velocity of our baryon, and k^μ is a small off-shell momentum $|k^\mu| \ll m$. Typically one uses the rest velocity $v^\mu = (1, 0, 0, 0)$, but other choices are possible. In a given frame defined by v^μ, our baryon is then described by a two component field $N_v(x)$ which is the projection

$$N_v(x) = \frac{1 + \slashed{v}}{2} e^{imv \cdot x} N(x). \tag{2.32}$$

This projection modifies the Dirac Lagrangian to produce a massless Dirac equation for $N_v(x)$, with corrections suppressed by powers of the nucleon mass

$$\bar{N}_v(x) iv \cdot \partial N_v(x) + \sum_{n=1}^{\infty} \frac{1}{(2m)^n} \hat{\mathcal{L}}^n. \tag{2.33}$$

For the case of $v^\mu = (1, 0, 0, 0)$ the parameterization (2.31) gives

$$iv \cdot \partial \quad \rightarrow \quad v \cdot k = -\frac{k^2}{2m} = k_0 = E - m \ll m. \tag{2.34}$$

Higher order corrections bring down more powers of $v \cdot k$ suppressed by the baryon mass (or equivalently $4\pi f$).

21

2.3.2.1 LO Pion Nucleon Lagrangian

Working in $SU(2)$ χPT the LO relativistic πN Lagrangian was derived in [65]

$$\mathcal{L}_{\pi N}^{(1)} = \bar{N}\left(i\not{D} - m_N + \frac{g_A}{2}\gamma^\mu\gamma_5 u_\mu\right)N, \tag{2.35}$$

where N = (p, n), and the chiral covariant derivative

$$D_\mu = \partial_\mu + \Gamma_\mu \tag{2.36}$$

contains a vector current Γ_μ which leads to interactions with an even number of pion fields

$$\Gamma_\mu = \frac{1}{2}\left(\xi^\dagger\partial_\mu\xi + \xi\partial_\mu\xi^\dagger\right). \tag{2.37}$$

We've introduced the field ξ which is related to our Σ field $\xi^2 = \Sigma$. The axial vector couples an odd number of pion fields to the nucleon

$$u_\mu = i\left(\xi^\dagger\partial_\mu\xi - \xi\partial_\mu\xi^\dagger\right). \tag{2.38}$$

Applying our heavy baryon reduction on the LO Lagrangian above we find

$$\mathcal{L}^{\hat{(1)}}{}_{\pi N} = \bar{N}_v\left(iD_0 - \frac{g_A}{2}\vec{\sigma}\cdot\vec{u}\right)N_v + \sum_{n=1}^{\infty}\frac{1}{(2m)^n}\mathcal{L}^{\hat{(n)}}{}_{\pi N} \tag{2.39}$$

where the higher order corrections are suppressed as expected. The mass terms may be included via spurion analysis

$$M = \frac{1}{2}\left(\xi^\dagger m_q\xi^\dagger + \xi m_q^\dagger\xi\right). \tag{2.40}$$

Formally, we may also include the Δ resonances in the above heavy baryon description if we are to accurately capture the dynamics. The Δ nucleon mass splitting is small

(~ 293 MeV) compared to our heavy scale Λ_χ, and thus the Δ dynamics should not be reabsorbed into the LECs of our LO Lagrangian. Dropping the v subscript as we will be working exclusively with the light component, the full LO free Lagrangian including Δ degrees of freedom is [66–68]

$$
\begin{aligned}
\hat{\mathcal{L}^{(1)}}_{\text{free}} =& \bar{N}\left(iv \cdot D + 2\alpha_M M + 2\sigma_M \operatorname{tr}(M)\right) N \\
& -\bar{T}^\mu\left(iv \cdot D - \Delta - 2\gamma_M M + 2\bar{\sigma}_M \operatorname{tr}(M)\right) T_\mu,
\end{aligned}
\tag{2.41}
$$

from which one finds the LO nucleon and delta masses

$$
\begin{aligned}
m_p^{(1)} &= 2\alpha_M m_u + 2\sigma_M \operatorname{tr}(m_q) \\
m_n^{(1)} &= 2\alpha_M m_d + 2\sigma_M \operatorname{tr}(m_q) \\
m_T^{(1)} &= \frac{2}{3}\gamma_M m_T - 2\bar{\sigma}_M \operatorname{tr}(m_q).
\end{aligned}
\tag{2.42}
$$

Chapter 3

Strong Isospin Breaking in the Baryon Spectrum

This section is based on [68]. In response to referee comments, we are currently calculating additional loop contributions to the baryon mass splittings which are relevant to the physical extrapolation. We are also making a more modest claim about the evidence of a chiral log from "definitive" to "strongly supported".

3.1   Introduction

Strong nuclear interactions exhibit a near perfect symmetry between protons and neutrons.Today, we understand this symmetry as a manifestation of the approximate $SU(2)$ -flavor symmetry between the *up* and *down* quarks. In the absence of electromagnetism, this approximate symmetry allows us to think of the up and down quarks as being two flavors with the same common mass m_l, ie the isospin limit. In lattice QCD calculations, the isospin approximation is routinely used, and has been shown to precisely reproduce the observed hadron spectrum as well as other spectroscopic quantities [40, 69]. In χPT, isospin symmetry manifests itself as a mass degenerate multiplet of pions (or nucleons), which well approximates it's natural counterparts since the mass splitting between quarks

in Nature $2\delta = m_d - m_u$ remains small compared to typical hadronic scales [54].

Violation of $SU(2)$ symmetry is perturbatively small, but has profound consequences upon our understanding of the universe. Isospin breaking leads to a tiny relative splitting between the nucleon masses ($\sim 0.07\%$), which allows for the neutron to undergo the weak β-decay process. The primordial abundance of hydrogen and helium after big-bang nucleosynthesis is exquisitely sensitive to the magnitude of isospin breaking, due to the sensitivity of the weak-reaction rates of nucleons on the nucleon mass splitting. Varying the size of isospin breaking by only 1%, for example, is inconsistent with the observed abundance of primordial nuclei at the two-sigma level [70]. Explicit isospin breaking in QCD interactions arises due to the difference between up and down quark masses, and leads to charge symmetry breaking phenomena, see Ref. [71] for an overview. Isospin is additionally broken by the quark electric charges, and the Coulomb repulsion between protons has a significant influence on the nuclear landscape, from the stability of the Sun to neutron-rich exotic nuclei and fission. The physical value of the neutron-proton mass difference results from the competition of electromagnetism and isospin breaking effects, and thus a precise determination of the isospin breaking contribution from the Standard Model could have grand implications for the big-bang nucleosynthesis prediction of the observed abundance of primordial light nuclei.

Connecting isospin breaking in the Standard Model to that in nuclear physics is theoretically challenging due to the strongly coupled nature of low-energy QCD. Lattice QCD may be used to stochastically estimate the QCD correlation functions, however control of lattice systematics requires calculations at multiple lattice spacings, volumes, and input quark masses. To maximize the impact of such non-trivial resource requirements, the results need to be coupled to and understood within the broader field of nuclear physics. An essential tool to attain this is effective field theory (EFT) [22]. The EFT description of low-energy QCD is chiral perturbation theory (χPT) [57, 72, 73], which is formulated in terms of pion degrees of freedom as an expansion about the chiral limit. EFTs are constructed by including all operators consistent with the symmetries of the theory. While the

25

form of these operators is dictated by symmetries, the values of the coefficients, known as low-energy constants (LECs), are *a priori* unknown. LECs must be determined by comparing derived formula to experimentally measured quantities, or by matching with numerical results from LQCD. In particular, LQCD affords the ability to determine LECs of the quark-mass dependent operators, a feat which is considerably challenging or even impossible when comparing with experimental results alone. The true power of χPT is to economize on LQCD calculations, as the determination of LECs from QCD permits systematic EFT predictions for other quantities.

The efficacy of an EFT is determined by the size of its expansion parameters, which must be sufficiently small to organize contributions from the multitude of operators. The expansion parameter for two-flavor χPT is given by $\varepsilon_\pi = m_\pi^2/\Lambda_\chi^2$, where $\Lambda_\chi \sim 1$ GeV is a typical hadronic scale, and m_π is the mass of the pion. This small parameter provides for a rapidly converging expansion for pion masses up to a few hundred MeV [74]. If one also considers dynamical strange matter, then kaon and eta degrees of freedom are relevant. The convergence of $SU(3)$ χPT is not as good as that of $SU(2)$ due, in part, to the number of virtual mesons propagating in loop diagrams, and the size of the expansion parameter $\varepsilon_K = m_K^2/\Lambda_\chi^2$. Heavy matter fields, such as nucleons and mesons containing a heavy quark, can also be incorporated in the EFT. This requires care, however, as the large mass scale can enter loop corrections and spoil the EFT power counting [65]. A well-known solution to this problem is that of heavy baryon χPT (HBχPT) [63, 75], in which the theory is expanded about the infinite mass limit of the baryon, in a similar spirit to heavy-quark EFT [76].

The hallmark prediction of χPT is the non-analytic behavior of quantities with respect to the pion mass. Often this behavior is logarithmic, and referred to generically as "chiral logs." Because the square of the pion mass is proportional to the quark mass at leading order (LO) in χPT, these chiral logs are non-analytic in the light quark masses. Such effects cannot be produced by a simple power-series expansion about the chiral limit, and are crucial predictions for QCD in the non-perturbative regime. Conclusive evidence for the

26

predicted quark-mass dependence will expose *chiral dynamics* in low-energy QCD correlation functions, and further establish confidence in LQCD techniques. Such evidence has been observed in properties of light [74, 77] and heavy [78] mesons and hadrons with a heavy (charm or bottom) quark [79]; but, to date, there has been no conclusive demonstration for such behavior in properties of baryons composed of light quarks. Suggestive evidence for the presence of non-analytic light quark mass dependence in the baryon spectrum was presented in Ref. [80] using various linear combinations of octet and decuplet baryon masses. In this work, we present, for the first time, strongly supported evidence for a chiral log in the strong isospin splitting of the nucleon. This evidence constitutes an important foundational step for broadening the reach of LQCD calculations when combined with χPT.

We begin with a description of the lattice calculation, our analysis strategies, and a determination of the lattice scale in Sec. 3.2. We use the kaon spectrum to determine the LQCD input value of $2\delta \equiv m_d - m_u$ that reproduces the physical value of the isovector light quark mass. In Sec. 3.3, we present our results for the isovector nucleon mass as a function of $m_d - m_u$ and m_π, and demonstrate the presence of non-analytic light quark mass dependence. To solidify this observation, we also present results for the isovector cascade mass. As the cascade also forms an isospin doublet, $SU(2)$ χPT describing the cascade spectrum is largely identical in form to that of the nucleon, with only the numerical values of the LECs altered. Phenomenologically, we know the cascade axial coupling is approximately 5 times smaller than that of the nucleon. This in turn implies that the coefficient of the chiral logarithm is approximately 10 times weaker in the cascade splitting than the nucleon, which is observed in the numerical results. We then briefly discuss the implications for the QCD θ-term in Sec. 3.4, before concluding in Sec. 3.5.

27

3.2 Details of the Lattice Calculation

The calculations presented in this work are performed on the Hadron Spectrum Collaboration (HSC) anisotropic clover-Wilson ensembles [81, 82]. The HSC ensembles exist for a variety of light quark masses and volumes but just a single lattice spacing with fixed renormalized anisotropy $\xi = a_s/a_t = 3.5$.

We show the space-time dimensions in terms of lattice sites, and bare quark parameters of the datasets used in Tab. 3.1. The configurations were generated using an improved anisotropic gauge action comprised of combined plaquette and rectangle terms as described in [83]. The action simulated two degenerate light quarks of mass m_l and a single flavor for the strange quark with mass m_s, using the $O(a)$ improved Sheikoleslami Wohlert [84] action also known as the Wilson-Clover, or simply "Clover" action. The fermion action also utilized so called "Stout" smeared gauge links [85]. Two levels of smearing were performed, with a stout smearing weight of $\rho = 0.22$. The gauge link smearing was performed only in the spatial directions. The anisotropy parameters and clover coefficients were tuned non-perturbatively, employing the Schrödinger Functional method as discussed in [81].

The configurations were generated using the Hybrid Monte Carlo [86] algorithm, utilizing the Chroma code [87]. The single-flavor strange quark term was simulated by Rational Hybrid Monte Carlo [88]. A variety of algorithmic tuning techniques were used to optimize the configuration generation process, including use of even-odd preconditioning, utilizing an anisotropic time-step in the molecular dynamics, splitting the molecular dynamics integration into several time-scales both in the sense of mass preconditioning [89] of the light quark determinant, and in the same spirit, by splitting the gauge action into spatial and temporal parts and evolving the temporal gauge action with its larger forces on a finer timescale. Finally, the second order "minimum norm" integrator of Omelyan [90, 91] was employed with an attempt to tune its parameter λ to minimize the integration truncation errors. The form of the actions and a majority of the gauge generation technique opti-

mizations are described in detail in [82], with the exception of some additional tuning for the larger lattices (e.g. further tuning the integrator parameters) that were carried out after that publication.

	ensemble			m_π	m_K	N_{cfg}	N_{src}	$a_t\delta$	$a_t m_s^{val}$
L/a_s	T/a_t	$a_t m_l$	$a_t m_s$	MeV	MeV				
16	128	-0.0830	-0.0743	490	629	207	16	{0.0002,0.0004,0.0010}	{-0.0743,-0.0728,-0.0713}
32	256	-0.0840	-0.0743	421	588	291	10	{0.0002,0.0004,0.0010}	{-0.0743,-0.0728,-0.0713}
32	256	-0.0860	-0.0743	241	506	802	10.5	{0.0002}	{-0.0743,-0.0728,-0.0713}

Table 3.1: Summary of LQCD ensembles used in this work. We provide approximate values of the pion and kaon masses at the unitary point after our scale setting procedure 3.2.2. The number of configurations N_{cfg} and average number of random sources N_{src} as well as the values of the strong isospin breaking parameter $2\delta = m_d - m_u$ used in the valence sector are provided. In order to control the scale setting, we also use several partially quenched values of the valence strange quark mass.

The two-point correlation functions of the ground-state hadrons are constructed for this work in a standard fashion. We generate several gauge-invariant Gaussian-smeared sources [92] on each gauge configuration with random space-time locations [93]. From each source, we solve for the $light$ and $strange$ quark propagators. For efficient solves, we utilize the deflated `eigcg` inverter [94] on CPU machines and the `QUDA` library [95] with multi-GPU support [96] on GPU enabled machines. A point sink or gauge-invariant smeared sink is then applied to each quark propagator to construct PS (point-smeared) or SS (smeared-smeared) correlation functions.

In order to induce strong isospin breaking, we follow the suggestion of Ref. [97] and spread the valence up and down quark masses symmetrically about the degenerate light quark mass

$$m_u^{val} = m_l - \delta \,, \qquad\qquad m_d^{val} = m_l + \delta \,. \qquad\qquad (3.1)$$

Because the valence and sea quark masses are not equal, this is a partially quenched (PQ) LQCD calculation with induced PQ systematics which must be removed through the use of PQ χPT [67, 98–104]. In Ref. [97], it was shown in some detail this choice of *symmetric isospin* breaking significantly suppresses the unitarity violating PQ effects.

Most importantly, it was demonstrated that the *errors* from PQ do not enter isospin-odd quantities, such as $m_n - m_p$ until $\mathcal{O}(\delta^3)$, well beyond the current precision of interest. In Table 3.1, we list the ensembles used in this work, as well as the pion and kaon masses in MeV, as determined from our scale setting in Sec. 3.2.2. We further list the number of sources and the values of $a_t \delta$ used in this work. In order to fully control the scale setting, we also vary the valence strange quark mass $a_t m_s^{val}$. We found the tuned value of $a_t m_s = -0.0743$ results in a strange quark mass slightly lighter than the physical one, see Sec. 3.2.2. The quality of the correlation functions we compute on these HSC ensembles are very good as can be inferred from the higher-statistics calculations on the same ensembles in Refs. [82, 93]. In this article, we only show the new isospin breaking results not presented previously.

3.2.1 Stochastic and systematic uncertainties of the ground-state spectrum

In order to determine the stochastic and systematic uncertainties of the ground-state hadron spectrum, we employ a fitting strategy that is an evolution of that described in Ref. [105]. Either multi-exponential (multi-cosh) fits or the Matrix Prony (MP) method is used to fit the baryon (meson) correlation functions [93]. A large set of reasonable choices of fit window, MP window, etc. are chosen and swept over, resulting in $\mathcal{O}(100)$ different fit choices for each correlation function. Each fit is performed with a seeded bootstrap to preserve the correlations between various hadron correlation functions computed on the same ensembles, and to ensure the same number of stochastic results across all ensembles, resulting in $N_{bs} = 500$ statistical samples for each quantity. We also perform standard least-squares fits for all the fits in this systematic loop to assess the quality of each fit. For each fit, a weight is constructed as

$$w_i = \frac{Q_i}{\sigma_{E,i}^2} \tag{3.2}$$

where $\sigma_{E,i}$ is the stochastic uncertainty determined for the ground-state energy, and the quality of fit is defined

$$Q = \int_{\chi^2_{min}}^{\infty} d\chi^2 \mathcal{P}(\chi^2, d),$$ (3.3)

with

$$\mathcal{P}(\chi^2, d) = \frac{1}{2^{d/2}\Gamma\left(\frac{d}{2}\right)}(\chi^2)^{\frac{d}{2}-1}e^{-\chi^2/2}$$ (3.4)

being the probability distribution function for χ^2 with d degrees of freedom. To assess the fitting systematic uncertainty, the fits from the systematic sweep are re-sampled with weight to generate $N_{sys} = 500$ different systematic fits for each correlation function. By re-sampling with weight, the resulting flat systematic distribution faithfully represents the weighted distribution of the original fits and allows us to enforce an equal number of systematic samples for every correlation function on every ensemble.

In order to properly preserve the correlations amongst various quantities computed on the same ensemble, for example the nucleon isospin splitting at different values of $a_t\delta$, care must be taken to resample the systematic distributions in a correlated manner. For example, the multi-exponential/MP fits for $m_n - m_p$ are aligned such that the choice of t_{min}, t_{max}, n_{exp}, etc. are the same for each value of $a_t\delta$ on a given ensemble. The weight factor is then taken as the average of the weights from each value of $a_t\delta$, such that the seeded weighted re-sampling always chooses the fits from each $a_t\delta$ in equal proportion, thus preserving the correlation between the samples. If this careful alignment is not performed, the resulting χ^2-minimum in the subsequent chiral extrapolations becomes at least an order of magnitude too small, as the correlations become "washed out".

The use of the full covariance matrix is critical in the subsequent analysis due to the correlations amongst results computed on the same sea-quark ensembles but with different values of the valence quark mass parameters.

$a_t m_l$	$a_t m_s$	$a_t m_s^{val}$	$a_t m_{\pi^\pm}$	$a_t m_{K^\pm}$	$a_t m_{K^0}$	$a_t m_\Omega$	l_Ω	s_Ω
-0.0830	-0.0743	-0.0743	0.0801(4)(1)	0.1028(3)(1)	0.1038(3)(1)	0.301(3)(2)	0.0707(15)(9)	0.1646(36)(22)
-0.0830	-0.0743	-0.0728	–	0.1064(3)(1)	0.1073(3)(1)	0.307(3)(2)	0.0680(14)(8)	0.1739(35)(21)
-0.0830	-0.0743	-0.0713	–	0.1098(3)(1)	0.1107(3)(1)	0.313(3)(2)	0.0656(12)(8)	0.1825(35)(21)
-0.0840	-0.0743	-0.0743	0.0689(1)(2)	0.0963(1)(1)	0.0972(1)(1)	0.293(2)(2)	0.0553(7)(8)	0.1627(19)(24)
-0.0840	-0.0743	-0.0728	–	0.1000(1)(1)	0.1009(1)(1)	0.299(2)(2)	0.0530(6)(7)	0.1722(19)(23)
-0.0840	-0.0743	-0.0713	–	0.1035(1)(1)	0.1044(1)(1)	0.305(2)(2)	0.0509(5)(6)	0.1810(19)(52)
-0.0860	-0.0743	-0.0743	0.0393(1)(1)	0.08276(6)(7)	0.08383(6)(6)	0.275(1)(1)	0.0205(2)(1)	0.1629(13)(7)
-0.0860	-0.0743	-0.0728	–	0.08691(7)(5)	0.08791(7)(5)	0.282(1)(1)	0.0195(1)(1)	0.1725(13)(6)
-0.0860	-0.0743	-0.0713	–	0.09086(7)(5)	0.09182(7)(5)	0.289(1)(1)	0.0186(1)(1)	0.1816(13)(6)

Table 3.2: Computed values of the hadron spectrum in lattice units and the corresponding values of l_Ω and s_Ω. These results are computed with the smallest value of $a_t \delta = 0.0002$.

3.2.2 Scale setting

In order to relate dimensionless quantities computed on the lattice to physical quantities comparable to experiment, a lattice scale must be determined. There is ambiguity in choosing a scale-setting method, but all choices must result in the same continuum limit. This ambiguity becomes more relevant when one has just a single lattice spacing, as in the present work. We choose the omega baryon mass, m_Ω, to set the scale in this work. Using a hadronic scale allows for a direct comparison with experimental quantities, after electromagnetic corrections have been accounted for. The omega baryon has mild light-quark mass dependence as it is composed of only strange valence quarks. This also results in a rapidly convergent $SU(2)$ chiral extrapolation for m_Ω [106].

As the lattice ensembles were generated with a strange quark mass near its physical value, only a simple interpolation in the strange mass is needed. In order to perform the necessary light and strange quark mass extrapolations to determine the scale, we utilize the two ratios of hadronic quantities [82]

$$l_\Omega \equiv \frac{m_\pi^2}{m_\Omega^2}, \qquad\qquad s_\Omega \equiv \frac{2m_K^2 - m_\pi^2}{m_\Omega^2} . \qquad\qquad (3.5)$$

At LO (leading order) in χPT we have the relations

$$m_\pi^2 = 2Bm_l \tag{3.6}$$

$$m_K^2 = B(m_l + m_s) \tag{3.7}$$

where we quote the isospin-averaged kaon mass. In order to capture the strange-quark mass dependence, we compute the spectrum with 3 different values of the valence strange quark mass, with values provided in Table 3.1. The omega baryon mass can then be determined for each choice of parameters and fit as a function of l_Ω and s_Ω. For the unitary points, one has the simple parameterization

$$m_\Omega = m_0 + c_l^{(1)} l_\Omega + c_s^{(1)} s_\Omega + ... \tag{3.8}$$

where the (...) denote terms higher order in l_Ω and s_Ω. We can use PQχPT for the decuplet baryons [107] to make an *Ansatz* for the dependence on $a_t m_s^{val}$. Using the LO χPT expressions for the meson masses, one has

$$m_\Omega^{PQ} = m_0^{PQ} + c_l^{(1)} \left(l_\Omega + \frac{1}{2} s_\Omega^{sea} \right) + c_s^{(1)} s_\Omega^{val} \tag{3.9}$$

where $m_0 = m_0^{PQ} + \frac{1}{2} c_l^{(1)} s_\Omega^{sea}$. Written in this way, the fit parameters $c_l^{(1)}$ and $c_s^{(1)}$ are found to agree between the unitary and PQ theories.

The calculated values of $a_t m_\Omega$ are extrapolated to the physical point as functions of l_Ω, s_Ω^{val} and s_Ω^{sea} using the above parameterizations. Denoting quantities at the physical point with a $*$ (e.g. $l_\Omega^* = m_\pi^{2\,phys} / m_\Omega^{2\,phys}$), we can determine an ensemble independent scale

$$a_t^* \equiv \frac{a_t m_\Omega(l_\Omega^*, s_\Omega^*)}{m_\Omega^{phys}}. \tag{3.10}$$

The parameter space of l_Ω and s_Ω used in this work is depicted in Figure 3.1 and listed in Table 3.2.
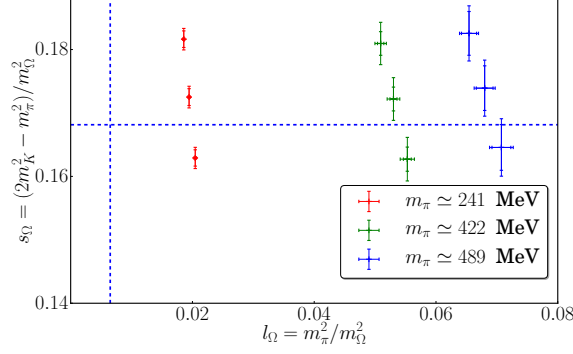
Figure 3.1: Parameter space of l_Ω and s_Ω used in this work. The vertical and horizontal dashed lines denote the physical values of l_Ω and s_Ω with electromagnetic corrections subtracted.

In this work, we are interested in the strong isospin-breaking corrections to $m_n - m_p$. We therefore define the physical point in the absence of electromagnetic corrections. Unless the electromagnetic corrections to m_Ω are unnaturally large (greater than several MeV), these corrections are sub-percent and well within our total uncertainty budget, and therefore we choose to neglect them. The strong isospin breaking in the pion spectrum is $\mathcal{O}(\delta^2)$ and assumed to be small [40]. Further, the electromagnetic corrections to the π^0 are suppressed [108]. We therefore take the QCD value of m_π in the absence of electromagnetism as defined by m_{π^0}. The FLAG [40] estimate of the electromagnetic self-energy corrections to the kaon spectrum can be used to define the QCD value of the isospin-averaged kaon mass $m_K^{QCD} = 494$ MeV (the uncertainties on these QCD input values are well within our total uncertainty). The physical point is then defined in this work as $m_\Omega^{phys} \equiv m_\Omega^{PDG}$ and

$$l_\Omega^* \equiv \frac{m_{\pi^0}^2}{m_\Omega^{2,PDG}} = 0.0065 \,,$$

$$s_\Omega^* \equiv \frac{2m_K^{2,QCD} - m_{\pi^0}^2}{m_\Omega^{2,PDG}} = 0.1681 \,. \tag{3.11}$$

In Figures 3.2a and 3.2b, we depict the values of $a_t m_\Omega$ vs. l_Ω and s_Ω. One observes linear dependence of $a_t m_\Omega$ in both l_Ω and s_Ω, consistent with the LO expressions
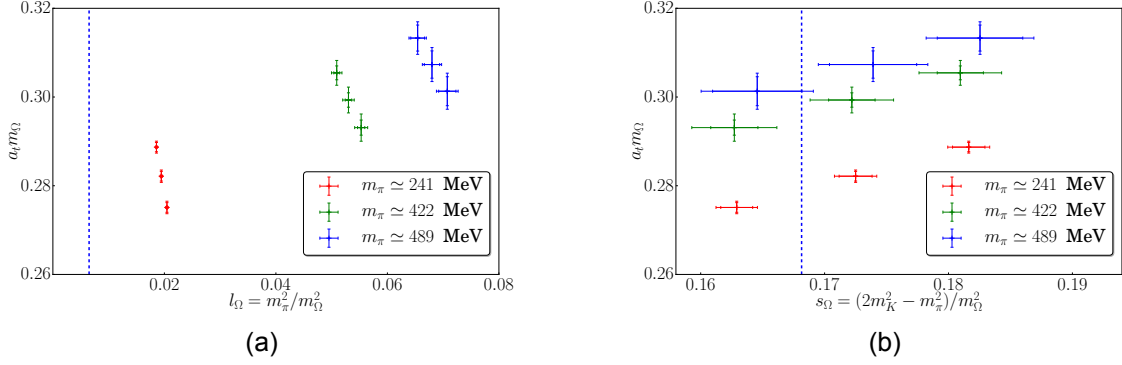
Figure 3.2: The l_Ω and s_Ω dependence of $a_t m_\Omega$. The dashed vertical lines denote the physical value of l_Ω^* and s_Ω^*.

PQ	$a_t m_0$	$c_l^{(1)}$	$c_s^{(1)}$	χ^2	dof	Q	$a_t m_\Omega^{phys}$	a_t[fm]	a_t^{-1}[MeV]
no	0.139(07)(04)	0.50(13)(8)	0.77(2)(01)	0.39	4	0.98	0.2721(35)(18)	0.0320(4)(2)	6145(80)(40)
yes	0.099(19)(23)	0.50(14)(7)	0.77(3)(11)	0.38	4	0.98	0.2736(38)(56)	0.0322(4)(7)	6111(85)(94)

Table 3.3: Scale setting extrapolation using Eqs. (3.8) and (3.9).

in Eqs. (3.8) and (3.9). Using the results listed in Table 3.2, the omega mass is determined as a function of l_Ω and s_Ω. Both the unitary and PQ formula fit the data well with the following caveat: a fully correlated fit to all data, including errors in the independent variables, produces an unexpectedly large χ^2 despite having small residuals, normalized by the extrapolated uncertainty. Removing the two heaviest valence strange quark masses, $a_t m_s = \{-0.0728, -0.0713\}$, in the two heaviest sea ensembles from the fit produces a much better χ^2, while losing none of the predictive power of the fit, even for the points not included. Using these quantities for the fit, we tabulate our fit results in Table 3.3. We find the unitary and PQ fits results are perfectly consistent, with the PQ fit having a factor of 2 larger systematic uncertainty. We take the PQ fit as our determination of the scale:

$$\frac{1}{a_t^*} = 6111 \pm 85 \pm 94 \text{ MeV}, \tag{3.12}$$

where the first uncertainty is statistical and the second is systematic. The statistical and systematic uncertainties can be individually determined by taking the complete statistical-systematic covariance matrix constructed from the $N_{bs} \times N_{sys}$ samples, and first averaging over the systematic or statistical fluctuations, respectively.

35

3.2.3 The kaon spectrum and determination of δ

In order to determine the QCD contribution to the nucleon isovector mass, we must first determine the physical value of δ. At LO in χPT, the kaon masses are

$$m^2_{K^\pm} = B(m_s + m_u)\,, \qquad\qquad m^2_{K^0} = B(m_s + m_d)\,. \tag{3.13}$$

A calculation of $\Delta m^2_K \equiv m^2_{K^0} - m^2_{K^\pm} = 2B\delta$ allows for this determination. The electromagnetic contributions to this kaon splitting must be subtracted. We use the value of the strong isospin splitting provided in the FLAG report

$$\Delta m^2_K \Big|_{QCD} = 5930 \text{ MeV}^2\,. \tag{3.14}$$

$a_t m_l$	$a_t m_s$	m_π [MeV]	$a_t \delta$	$(a_t \Delta m_K)^2$
-0.0860	-0.0743	241	0.0002	0.000178(03)
-0.0840	-0.0743	421	0.0002	0.000189(02)
-0.0830	-0.0743	490	0.0002	0.000196(05)
-0.0840	-0.0743	421	0.0004	0.000378(03)
-0.0830	-0.0743	490	0.0004	0.000392(06)
-0.0840	-0.0743	421	0.0010	0.000947(05)
-0.0830	-0.0743	490	0.0010	0.000980(12)

Table 3.4: Kaon mass splitting versus δ and m_π on the various ensembles.

The values of the kaon mass splitting computed in this work are provided in Table 3.4. The kaon splitting exhibits a slight pion-mass dependence, indicating the presence of NLO (next-to-leading order) corrections. We do not observe any $a_t m_s^{val}$ dependence. Starting from the work of Gasser and Leutwyler [58], we can integrate out the strange quark contribution to Δm^2_K to arrive at the NLO formula

$$\Delta m^2_K = 2B\delta \left[1 + \alpha(\mu)m^2_\pi - \frac{m^2_\pi}{(4\pi f)^2} \ln\left(\frac{m^2_\pi}{\mu^2}\right) \right]\,. \tag{3.15}$$

In this expression, $\alpha(\mu)$ is an unknown LEC and f is the pion decay constant in the chiral

limit with the normalization $f_\pi = 130$ MeV and we set $\mu = 770$ MeV.[1] In our χPT analysis, we use the FLAG $N_f = 2+1$ determination of $f = 122.6$ MeV as input to the fits. This expression describes the data well as observed in our analysis results collected in Table 3.5.

$a_t B$	α	χ^2/dof	Q	$a_t\delta^*[10^{-4}]$
0.411(6)(5)	13.5(3)(3)	2.25/5	0.81	1.87(2)(2)

Table 3.5: Extrapolation of Δm_K^2 using Eq. (3.15) and the determination of $a_t\delta^*$. Notice, we treat the scale dependence of the LEC α implicitly, because we work at the standard renormalization scale $\mu = 770$ MeV throughout.

We solve for the value of $a_t\delta$ that reproduces the physical QCD kaon splitting, Eq. (3.14), finding

$$a_t\delta^* = 1.87(2)(2) \times 10^{-4} \,, \tag{3.16}$$

where the first and second uncertainties arise from the stochastic and systematic uncertainties, respectively. The extrapolation and determination of $a_t\delta^*$ are depicted in Figure 3.3. Interestingly, we can use the value of $a_t B$ determined in this fit to estimate the bare vacuum condensate, $\Sigma = BF^2$, with $F = 86.6$ MeV as the pion decay constant in the $F_\pi = 92.2$ MeV normalization. Using our lattice scale, Eq. (3.12), we obtain the bare value

$$\mathring{\Sigma}^{1/3} = 266(4)(1) \text{ MeV}\,, \tag{3.17}$$

which is very similar to the FLAG average [40]. As we have not performed the necessary renormalization, this is a qualitative comparison. However, it seems to imply the isovector quark-mass renormalization is close to unity.
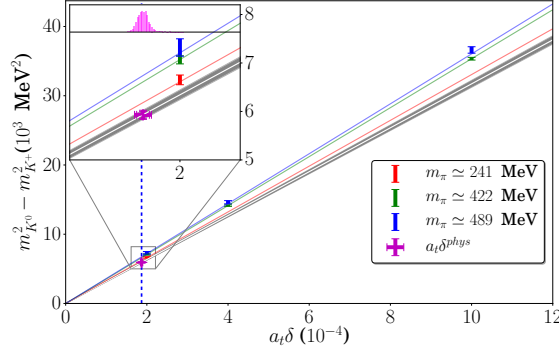
Figure 3.3: Plot of strong isospin splitting Δm_K^2 versus lattice values for δ. The gray band is the predicted value of $\Delta m_K^2(\delta, m_\pi = m_\pi^{phy})$ while the colored lines are the central values for the corresponding pion masses. The magenta point is the distribution of $a_t\delta^{phys}$.

$a_t m_l$	$a_t m_s$	$m_\pi/$MeV	$a_t\delta$	$a_t\delta M_N^\delta/(a_t\delta)$	$a_t\delta M_\Xi^\delta/(a_t\delta)$
-0.0860	-0.0743	241	0.0002	2.31(08)(09)	4.66(12)(19)
-0.0840	-0.0743	421	0.0002	2.34(04)(05)	4.29(05)(10)
-0.0840	-0.0743	421	0.0004	2.34(04)(05)	4.31(05)(10)
-0.0840	-0.0743	421	0.0010	2.33(04)(05)	4.30(05)(10)
-0.0830	-0.0743	490	0.0002	2.15(05)(07)	3.83(08)(04)
-0.0830	-0.0743	490	0.0004	2.15(05)(07)	3.83(08)(04)
-0.0830	-0.0743	490	0.0010	2.14(05)(07)	3.83(08)(04)

Table 3.6: The nucleon ($a_t\delta M_N^\delta$) and cascade ($a_t\delta M_\Xi^\delta$) mass splittings, normalized by $a_t\delta$ for different values of $a_t\delta$ and m_π on the various ensembles.

3.3   Isovector Nucleon Mass and Chiral Logarithms

We now turn to the nucleon mass splitting. We define the isovector masses to be the positive quantities

$$\delta M_N^\delta \equiv m_n - m_p\,, \qquad\qquad \delta M_\Xi^\delta \equiv m_{\Xi^-} - m_{\Xi^0}\,. \qquad\qquad (3.18)$$

In Table 3.6, we list the numerical values of the nucleon and cascade mass splittings determined in this work. If Figure 3.4, we display sample effective mass plots of the nucleon and cascade isovector masses. These values can be converted to MeV using the scale Eq. (3.12) and the physical value of $a_t\delta^*$, Eq. (3.16).

---

[1]In this and all subsequent χPT analyses, we work at the standard χPT renormalization scale $\mu = 770\,$MeV and treat an μ-dependence of LECs implicitly.
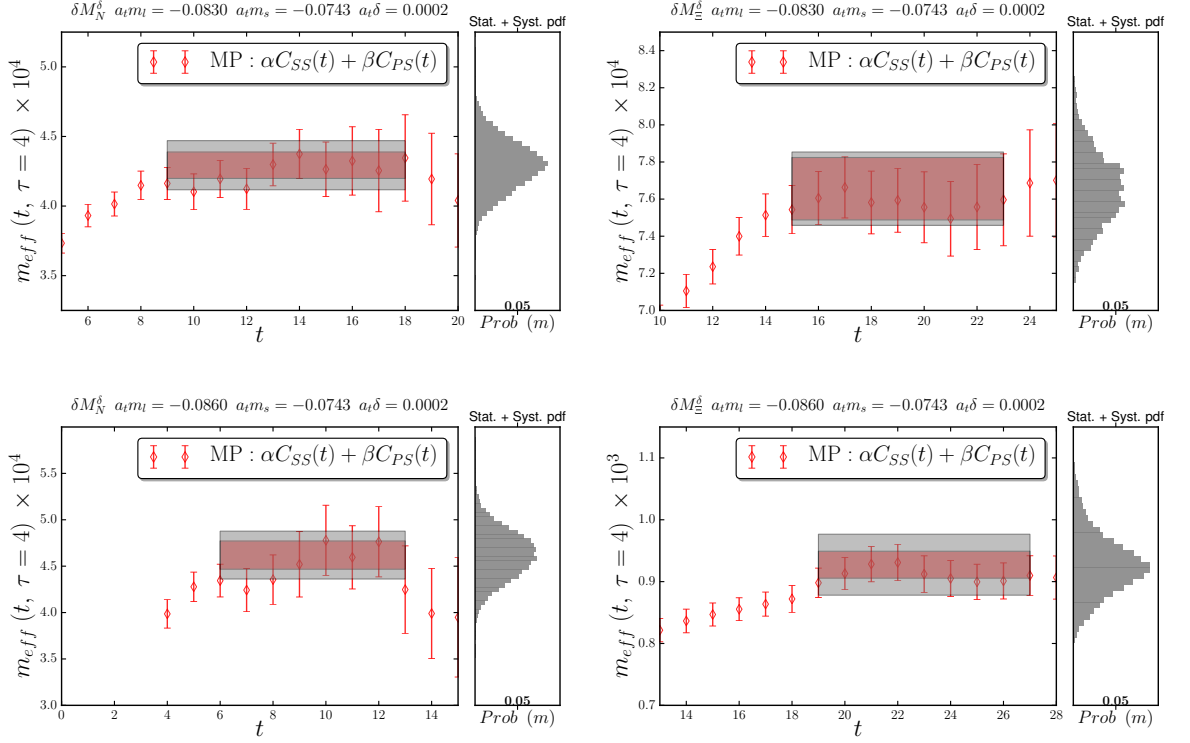
Figure 3.4: Sample effective masses of the nucleon and cascade isovector correlation functions. The resulting ground-state mass splitting determined from Matrix Prony and multi-exponential fits is displayed as a horizontal band over the region of times considered.

At LO in the chiral expansion, we write the heavy baryon Lagrangian [63] with the conventions of Ref. [67], with the replacement $\alpha_N = -4\alpha_M$ of that work,

$$
\mathcal{L}_N^{(LO)} = \bar{N}iv \cdot DN - \bar{T}^\mu iv \cdot DT_\mu + \Delta\bar{T}^\mu T_\mu
$$
$$
- \frac{\alpha_N}{2}\bar{N}\mathcal{M}N + 2\gamma_M\bar{T}^\mu\mathcal{M}T_\mu \tag{3.19}
$$

where $\mathcal{M} = \frac{1}{2}(\xi^\dagger m_q\xi^\dagger + \xi m_q^\dagger\xi)$. We similarly construct the $SU(2)$ Lagrangian for the Ξ, Ξ^* system, following Ref. [106], but keep the normalization similar to that in Ref. [67] instead

of using the extra $1/(4\pi f)$ in the LO operators,

$$\mathcal{L}_{\Xi}^{(LO)} = \bar{\Xi} iv \cdot D\Xi - \bar{\Xi}^{*,\mu} iv \cdot D\Xi_{\mu}^* + \Delta_{\Xi^*\Xi} \bar{\Xi}^{*,\mu} \Xi_{\mu}^*$$

$$- \frac{\alpha_{\Xi}}{2} \bar{\Xi} \mathcal{M} \Xi - 2\alpha_{\Xi^*} \bar{\Xi}^{*,\mu} \mathcal{M} \Xi_{\mu}^* \qquad (3.20)$$

The present choice of normalization is such that the LO isovector masses are proportional to δ, with the slopes $\delta M_{N,\Xi}^{\delta} = \alpha_{N,\Xi}\delta$. The NLO contributions that scale as m_π^3 for the isoscalar mass exactly cancel in the isovector mass, provided one utilizes the symmetric PQ isospin breaking, Eq. (3.1), or includes isospin breaking in the sea quarks with a unitary calculation. The first non-vanishing corrections arise at NNLO (next-to-next-to-leading order), originating from the self-energy corrections due to virtual pion loops. These long-range corrections depend logarithmically on the pion mass; and, provided they have a large coefficient, cannot be well parameterized by a low-order power-series expansion about the chiral limit. It is precisely this non-analytic behavior that signals the influence of chiral dynamics in QCD observables.

At NNLO in the $SU(2)$ chiral expansion, the expression for the nucleon mass splitting, including partial quenching effects, is given by [97]

$$\delta M_N^{\delta} = \delta \left\{ \alpha_N \left[1 - (6g_A^2 + 1) \frac{m_\pi^2}{(4\pi f_\pi)^2} \ln\left(\frac{m_\pi^2}{\mu^2}\right) \right] + 4g_{\pi N\Delta}^2 \left(\frac{20}{9}\gamma_M - \alpha_N \right) \frac{\mathcal{J}(m_\pi, \Delta, \mu)}{(4\pi f_\pi)^2} \right.$$
$$\left. + \beta(\mu) \frac{2m_\pi^2}{(4\pi f_\pi)^2} + \frac{\alpha_N \Delta_{PQ}^4}{2m_\pi^2 (4\pi f_\pi)^2}(4 - 3g_0^2) \right\}. \quad (3.21)$$

In this expression, all finite contributions are absorbed into the LECs which stem from local operators. The quantity $\alpha_N \delta$ is the LO contribution to δM_N^{δ} and similarly, the LO contribution to the delta-resonance isospin splitting is proportional to $\gamma_M \delta$, e.g.

$$m_{\Delta^+} - m_{\Delta^{++}} = \frac{4}{3}\gamma_M \delta. \qquad (3.22)$$

The axial couplings g_A and $g_{\pi N\Delta}$ are well known phenomenologically. At this order in the

chiral expansion, g_A can be either the nucleon axial charge or its chiral limit value, with the difference being of higher order than NNLO. The quantity $\Delta \equiv m_\Delta - m_N$ is the delta-nucleon mass splitting, which is $\Delta \simeq 293$ MeV at the physical pion mass. $\mathcal{J}(m_\pi, \Delta, \mu)$ is a non-analytic function appearing above, defined as [67][2]

$$\mathcal{J}(m, \Delta, \mu) = 2\Delta\sqrt{\Delta^2 - m^2}\, \ln\left(\frac{\Delta - \sqrt{\Delta^2 - m^2 + i\varepsilon}}{\Delta + \sqrt{\Delta^2 - m^2 + i\varepsilon}}\right) + m^2 \ln\left(\frac{m^2}{\mu^2}\right) + 2\Delta^2 \ln\left(\frac{4\Delta^2}{m^2}\right).$$

(3.23)

For $m > \Delta$, we can use the equality between log and arctan to express this function with all positive and real arguments:

$$\sqrt{\Delta^2 - m^2}\, \ln\left(\frac{\Delta - \sqrt{\Delta^2 - m^2 + i\varepsilon}}{\Delta + \sqrt{\Delta^2 - m^2 + i\varepsilon}}\right) = 2\sqrt{m^2 - \Delta^2}\, \arctan\left(\sqrt{\frac{m^2}{\Delta^2} - 1}\right). \quad (3.24)$$

In Eq. (3.21), the last contribution arises from the PQ effect but comes with no new LECs. The simplification of this PQ effects occurs because of the symmetric splitting of the valence quark masses about the degenerate sea quark mass, Eq. (3.1), with the definition [97]

$$\Delta_{PQ}^2 = 2B\delta. \quad (3.25)$$

For this choice of PQ LQCD, the same quantity which controls the isospin breaking effects also controls the PQ effects. Lastly, g_0 is the singlet axial coupling which can be reliably estimated phenomenologically.

We would like to assess the various contributions to δM_N^δ arising in Eq. (3.21). At LO in χPT, $\Delta_{PQ}^2 = \Delta m_K^2$, Eq. (3.15), so the size of the PQ corrections can be readily estimated. Normalizing the PQ correction by the LO term, and using our computed values of Δm_K^2

---

[2]Compared with the more standard definition of $\mathcal{J}'$, found for example in Refs. [107, 109], following Ref. [67], we define $\mathcal{J}(m, \Delta, \mu) = \mathcal{J}'(m, \Delta, \mu) - \mathcal{J}'(0, \Delta, \mu)$ with a suitable absorption of analytic pion mass terms in the LECs.

from Table 3.4 as estimates for Δ_{PQ}^2, we find

$$\epsilon_{PQ} \equiv \frac{\delta M_N^{\delta,PQ}}{\delta M_N^{\delta,LO}} = \frac{(4-3g_0^2)\Delta_{PQ}^4}{2m_\pi^2(4\pi f_\pi)^2} \lesssim 5 \cdot 10^{-4}, \tag{3.26}$$

for all values of the parameters used in this work. The bound is derived from the lightest pion mass, where this effect is the largest. This is consistent with the observation that our results in Table 3.6 show no sign of quadratic $a_t\delta$ dependence. Thus, the PQ effects can be safely ignored as they are much smaller than our other uncertainties.

3.3.1 χ-extrapolation of δM_N^δ

We begin with the simplest extrapolation using only the nucleon and pion degrees of freedom, for which the quark-mass dependence is given by

$$\delta M_N^\delta = \delta \left\{ \alpha_N \left[1 - \frac{m_\pi^2}{(4\pi f)^2}(6g_A^2 + 1) \ln\left(\frac{m_\pi^2}{\mu^2}\right) \right] + \beta(\mu)\frac{2m_\pi^2}{(4\pi f)^2} \right\}. \tag{3.27}$$

In this work, we have not computed the pion decay constant or the nucleon axial coupling. While the pion decay constant has a relatively large pion-mass dependence, it is known that the nucleon axial coupling has a very mild pion-mass dependence. For a recent review including g_A, see Ref. [110]. Whether we take f to be the chiral-limit value of f_π, the physical value or pion-mass dependent, the differences are all higher order than NNLO. For our central values, we take $f = f_\pi^{phy} = 130.4$ MeV. Because we are interested in identifying the presence of the chiral logarithm in Eq. (3.27), we try setting the nucleon axial coupling to its physical value $g_A = 1.2723$ and also letting it float as a free parameter in the minimization. It is worth noting that fits to the isoscalar nucleon mass, with g_A left a free parameter, return values consistent with 0 or significantly smaller than the measured value [111]. This is due, in part, to the dramatic pion-mass dependence observed in LQCD spectrum calculations in which the nucleon mass scales linearly in the pion mass [112, 113].

In the first extrapolation analysis we perform, we set $g_A = 1.2723$. With this value, Eq. (3.27) predicts a strong pion-mass dependence due to the large coefficient in front of the logarithm, $6g_A^2 + 1$. The resulting fit is tabulated in Table 3.7 and depicted in Figure 3.5, and produces the value

$$\delta M_N^\delta = 2.28(11)(3)(5) \text{ MeV}. \qquad (3.28)$$

The first uncertainty is from combined statistical and systematic uncertainties in the correlator analysis. The second uncertainty is from the value of $a_t \delta^*$ we determine, Eq. (3.16), and the third uncertainty is from our scale setting analysis, Eq. (3.12). As is evident from the quality of fit, this extrapolation is strongly favored by our numerical results. The strong curvature arises from the competition between the logarithm and the local counter-term β in Eq. (3.27). This very rapid pion-mass dependence is precisely what cannot be accounted for easily in a power-series expansion about $m_\pi = 0$, but is easily accommodated using the extrapolation formula predicted by χPT. A detailed study of power-series expansion fits shows that the size of the higher-order terms are as large or larger than the lower-order terms, and the result is unstable with respect to the inclusion of higher-order terms.

α_N	β	g_A	$\chi^2/$dof	Q	$a_t \delta M_N^\delta$ MeV
1.64(09)	-5.2(1.3)	fixed	2.73/5	0.74	2.28(11)(3)(5)
1.67(47)	-5.1(2.3)	1.24(56)	2.72/4	0.61	2.29(32)(3)(5)
with other LQCD results					
1.81(24)	-4.7(1.9)	1.08(33)	2.87/5	0.72	2.39(16)(3)(5)

Table 3.7: Chiral extrapolation of δM_N^δ using Eq. (3.27) with g_A input (fixed) or free to float in the minimization. The last set of results include input from other LQCD calculations as described in Sec. 3.3.1.2.

3.3.1.1 Support for a large χ-log coefficient in the LQCD results

From the perspective of exposing non-analytic light quark-mass dependence, the most interesting prospect in our analysis is to relax the input of g_A and see what value the numerical results favor. In the subsequent analysis, we let g_A float and only input the value
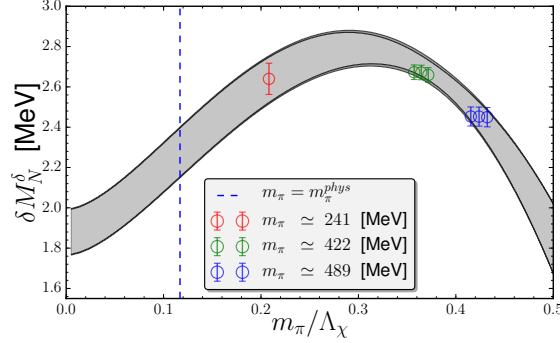
Figure 3.5: The nucleon mass splitting δM_N^δ versus m_π/Λ_χ where $\Lambda_\chi = 2\sqrt{2}\pi f$. The numerical results show statistical uncertainties only. The multiple values at the two heavier pion masses arise from the three values of $a_t\delta$ used in this work and are split for clarity. These values have been converted to MeV and scaled to the physical quark mass splitting $a_t\delta^*$, Eq. (3.16).

of f_π, which we take to be the physical pion decay constant, as above. The resulting fit results are provided in Table 3.7. As demonstrated by this analysis, the numerical results strongly favor a large coefficient of the χ-logarithm, with a value of nucleon axial coupling

$$g_A = 1.24(56).$$ (3.29)

While there is a large uncertainty on the axial coupling, it is very encouraging that the numerical results for the isovector mass prefer a large value, as this is the coefficient of the χ-logarithm. This is in sharp contrast to the numerical analysis of the isoscalar nucleon mass [111], where floating g_A results $g_A \lesssim 0.4$. This observation quantitatively justifies for the first time our choice to input the value of $g_A = 1.2723$ to our analysis.

3.3.1.2 Including other LQCD input

There are only a handful LQCD calculations of δM_N^δ [114–120], with only Refs. [117–119] controlling the continuum limit and just Refs. [118, 119] also fully controlling the chiral extrapolation. The results from these three publications, with all quoted uncertainties added in quadrature are $\delta M_N^\delta[117] = 2.9(.60)$ MeV, $\delta M_N^\delta[118] = 2.28(.26)$ MeV, and

$\delta M_N^\delta[119] = 2.52(.29)$ MeV. To test the unconstrained χ-extrapolation, we take a weighted average of these results with weights $w_i = 1/\sigma_i^2$ and include the result

$$\delta M_N^{\delta,\text{other LQCD}} = 2.43 \pm 0.18 \text{ MeV} , \tag{3.30}$$

with the results of this work in a fit allowing g_A to be determined by the combined set of LQCD results. This results in a final extrapolation of (see Table 3.7)

$$g_A = 1.08(.33) ,$$
$$\delta M_N^\delta = 2.39(16)(3)(5) \text{ MeV} . \tag{3.31}$$

This shows our results are already in perfect agreement with predictions from other LQCD calculations, and still supportive of a large coefficient of the chiral logarithm with a value of g_A consistent with the experimental value.

3.3.1.3 Influence of heaviest pion mass on the χ-log

One may worry that the largest pion mass data strongly influences the fit and induces the curvature. To test this, we drop the heaviest pion mass results from the analysis, resulting in the fit depicted in Figure 3.6. As is evident, the resulting fit is in perfect agreement, but less precise, indicating the heaviest pion mass results align with the predicted χPT formula, and only serve to improve the precision of the analysis. The resulting nucleon mass splitting in this case is $\delta M_N^\delta = 2.28(15)(03)(05)$ MeV, to be compared to Eq. (3.28).

3.3.1.4 Δ-full extrapolation

The last chiral extrapolation systematic we explore is whether the numerical results are sensitive to the delta-resonance contributions. For $m_\pi \gtrsim 290$ MeV, the delta-resonance becomes stable as $m_N + m_\pi > m_\Delta$ in this pion-mass regime. The delta degrees of freedom are also strongly coupled to the nucleon with $g_{\pi N\Delta} \simeq 1.5$. For these reasons, there
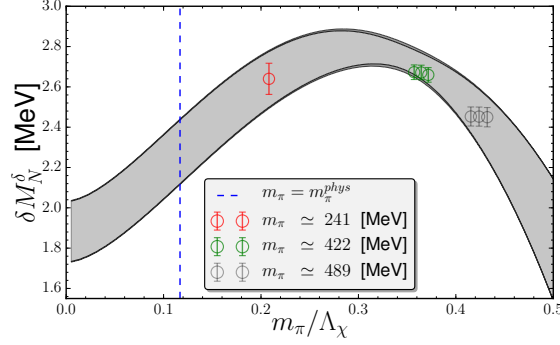
Figure 3.6: Analysis of δM_N^δ excluding the heaviest pion mass results.

is an expectation that these contributions will be important to include explicitly. Neglecting the delta degrees of freedom is equivalent to integrating them out using a small expansion parameter of $\epsilon_\pi^\Delta = m_\pi/\Delta$, which is clearly not small for LQCD calculations with pion masses heavier than physical.

$a_t m_l$	$a_t m_s$	m_π [MeV]	$a_t \delta$	Δ [MeV]	$\Delta_{\Xi^*\Xi}$ [MeV]
-0.0860	-0.0743	241	0.0002	330(12)(12)	244(06)(06)
-0.0840	-0.0743	421	0.0002	318(12)(06)	257(06)(06)
-0.0840	-0.0743	421	0.0004	318(12)(06)	257(06)(06)
-0.0840	-0.0743	421	0.0010	318(12)(06)	263(06)(06)
-0.0830	-0.0743	490	0.0002	244(24)(18)	232(12)(06)
-0.0830	-0.0743	490	0.0004	244(24)(18)	232(12)(06)
-0.0830	-0.0743	490	0.0010	244(24)(18)	232(12)(06)

Table 3.8: The delta-nucleon ($a_t\Delta$) and cascade ($a_t\Delta_{\Xi^*\Xi}$) mass splittings determined in this work, for different values of $a_t\delta$ and m_π on the various ensembles.

In order to assess whether our numerical results support the inclusion of the delta degrees of freedom, we perform several different analyses. In each assessment, we use the extrapolation formula

$$\delta M_N^\delta = \delta \Bigg\{ \alpha_N \left[1 - (6g_A^2 + 1)\frac{m_\pi^2}{(4\pi f_\pi)^2} \ln\left(\frac{m_\pi^2}{\mu^2}\right) \right] + 4g_{\pi N\Delta}^2 \left(\frac{20}{9}\gamma_M - \alpha_N \right) \frac{\mathcal{J}(m_\pi, \Delta, \mu)}{(4\pi f_\pi)^2} + \beta(\mu)\frac{2m_\pi^2}{(4\pi f_\pi)^2} \Bigg\}. \quad (3.32)$$

To perform the analysis, we also determine or estimate the values of $\Delta = m_\Delta - m_N$ and γ_M using the delta correlation functions. The values of Δ are collected in Table 3.8 and the isospin splittings $m_{\Delta^-} - m_{\Delta^0}$ in Table 3.9. From Eq. (3.22), we see only the product $\gamma_M \delta$ is renormalization scheme and scale independent and as we are working with bare values of δ. Thus, we find estimate the unrenormalized LEC

$$\mathring{\gamma}_M = 1.68(3) \,. \tag{3.33}$$

Given the similarity of our estimate of the condensate $\mathring{\Sigma}$, Eq. (3.17) with that in the FLAG report [40], we expect this to be a good approximation of the renormalized LEC.

$a_t m_l$	$a_t m_s$	m_π [MeV]	$a_t \delta$	$m_{\Delta^-} - m_{\Delta^0}$ [MeV]	$m_{\Xi^{*-}} - m_{\Xi^{*0}}$ [MeV]
-0.0860	-0.0743	241	0.0002	–	3.09(14)(24)
-0.0840	-0.0743	421	0.0002	2.80(05)(12)	2.86(04)(08)
-0.0840	-0.0743	421	0.0004	5.56(10)(24)	5.72(09)(15)
-0.0840	-0.0743	421	0.0010	13.6(23)(55)	14.2(02)(04)
-0.0830	-0.0743	490	0.0002	2.52(06)(08)	2.68(06)(12)
-0.0830	-0.0743	490	0.0004	5.05(13)(15)	5.36(12)(24)
-0.0830	-0.0743	490	0.0010	12.7(03)(04)	13.3(03)(05)

Table 3.9: The Δ baryon mass splitting used in the determination of γ_m e.g. Eq. (3.22). The Ξ^* baryon mass splitting is used to determine α_{Ξ^*} as in Eq. (3.36). As the Δ baryon is unstable at the lightest pion mass, no fit was taken from this ensemble.

When assessing the contribution of these new terms, we always take $g_A = 1.2723$ because that is consistent with our unrestricted analysis in Sec. 3.3.1.1. The leading large-N_c relation between g_A and $g_{\pi N \Delta}$ provides the estimate [121, 122] (our normalization of g_A follows Refs. [67, 80])

$$g_{\pi N \Delta} = \frac{6}{5} g_A + \mathcal{O}\left(\frac{1}{N_c}\right) \,. \tag{3.34}$$

We perform the analysis of our results using Eq. (3.32) augmented with Bayesian constrained fits with several generous values of a Gaussian prior width.[3] The results are

---

[3]There has been a recent interest in using Bayesian analysis methods for determining LECs in EFTs [123–

collected in Table 3.10. All fits have a good fit-statistic and the predicted values of δM_N^δ are largely insensitive to these modifications. However, we observe that the extracted uncertainty on the $g_{\pi N\Delta}$ axial coupling tracks the size of the prior width indicating the numerical results provide no guidance for the delta contributions. The strongest conclusion one can draw from this analysis is that the numerical results are not inconsistent with the contributions from the delta degrees of freedom, but there is no quantitative support for them.

$\tilde{g}_{\pi N\Delta}$	α_N	β	$\hat{g}_{\pi N\Delta}$	δM_N^δ MeV
1.50(25)	1.79(10)	-16(3)	1.51(25)	2.40(12)(4)(5)
1.50(50)	1.78(12)	-15(6)	1.46(47)	2.39(14)(4)(5)
1.50(∞)	1.66(32)	-6(22)	0.49(4.47)	2.29(28)(4)(5)

Table 3.10: Chiral extrapolation of δM_N^δ using Eq. (3.32) with a Bayesian constraint on $g_{\pi N\Delta}$. The prior width given to the augmented χ^2 is denoted $\tilde{g}_{\pi N\Delta}$ and $\hat{g}_{\pi N\Delta}$ is the resulting posterior value. For any small finite prior width, the coupling is just determined by the prior, Eq (3.34).

3.3.1.5 δM_Ξ^δ and the lack of χ-logarithmic behavior

The cascade also forms an isodoublet, like the nucleon. At low-energies, the $SU(2)$ χPT theory for the Ξ will be identical in form to that of the nucleon with only numerical values of the LECs being different, as reflected in Eqs. (3.19) and (3.20). Including virtual corrections from the resonant spin-3/2 Ξ^* states breaks the exact mapping of Eq. (3.21) to the Ξ, Ξ^* system, as the Ξ^* form an iso-doublet while the Δ states form an iso-quartet. Accounting for these differences, the full expression for the iso-vector Ξ mass becomes

$$\delta M_\Xi^\delta = \delta \left\{ \alpha_\Xi \left[1 - (6g_{\pi\Xi\Xi}^2 + 1)\frac{m_\pi^2}{(4\pi f_\pi)^2} \ln\left(\frac{m_\pi^2}{\mu^2}\right) \right] + g_{\pi\Xi\Xi^*}^2 \left(4\alpha_{\Xi^*} - 3\alpha_\Xi\right) \frac{\mathcal{J}(m_\pi, \Delta_{\Xi^*\Xi}, \mu)}{(4\pi f_\pi)^2} \right.$$
$$\left. + \beta_\Xi(\mu)\frac{2m_\pi^2}{(4\pi f_\pi)^2} \right\}. \quad (3.35)$$

126].

48

This expression can be determined from Ref. [127] by matching $SU(3)$ onto $SU(2)\,\chi$PT [106]. We use the LO contribution to the Ξ^* isospin splitting to determine α_{Ξ^*}, e.g.

$$m_{\Xi^{*-}} - m_{\Xi^{*0}} = -4\alpha_{\Xi^*}\delta,\qquad(3.36)$$

with the data collected in Table 3.9. This allows an estimation of the unrenormalized LEC

$$\mathring{\alpha}_{\Xi^*} = -0.58(2)\,.\qquad(3.37)$$

$\tilde{g}_{\pi\Xi\Xi}$	$\tilde{g}_{\pi\Xi\Xi^*}$	$\hat{g}_{\pi\Xi\Xi}$	$\hat{g}_{\pi\Xi\Xi^*}$	α_Ξ	β_Ξ	$\delta M_\Xi^{\mathring{\delta}}$ MeV
$\Delta_{\Xi\Xi^*} = 213.5$ MeV						
0.240(02)	0.882(09)	0.240(02)	0.882(09)	4.59(22)	-2.6(14)	5.37(24)(8)(5)
0.240(05)	0.882(18)	0.240(05)	0.882(18)	4.59(23)	-2.6(15)	5.37(24)(8)(5)
0.240(12)	0.882(44)	0.240(12)	0.882(44)	4.59(22)	-2.6(15)	5.37(24)(8)(5)
0.240(24)	0.882(88)	0.240(24)	0.885(88)	4.59(23)	-2.6(19)	5.37(25)(8)(5)
$\Delta_{\Xi\Xi^*} = \Delta_{\Xi\Xi^*}^{LQCD}$ MeV						
0.240(02)	0.882(09)	0.240(02)	0.882(09)	4.70(24)	-2.3(15)	5.50(25)(8)(5)
0.240(05)	0.882(18)	0.240(05)	0.882(18)	4.70(24)	-2.3(16)	5.50(25)(8)(5)
0.240(12)	0.882(44)	0.240(12)	0.882(44)	4.70(24)	-2.3(17)	5.50(25)(8)(5)
0.240(24)	0.882(88)	0.240(24)	0.884(88)	4.70(24)	-2.3(20)	5.50(26)(8)(5)

Table 3.11: Chiral extrapolation of δM_Ξ^δ using Eq. (3.35) with Bayesian constrained fits. The prior values are denoted as $\tilde{g}_{\pi\Xi\Xi}$ while the posteriors are denoted as $\hat{g}_{\pi\Xi\Xi}$.

Phenomenologically, we know the Ξ axial charge is much smaller than the nucleon axial charge. Similarly, the axial transition coupling is suppressed [106],

$$g_{\pi\Xi\Xi} \simeq 0.24\,,\qquad\qquad g_{\pi\Xi\Xi^*} \simeq \frac{g_{\pi N\Delta}}{\sqrt{3}} \simeq 0.87\,.\qquad(3.38)$$

Comparing the coefficient of the chiral-log term arising from the $\Xi - \pi$ virtual state, we estimate that this logarithmic m_π contribution is $\mathcal{O}(10)$ times smaller than in δM_N^δ. We observe the pion-mass dependence of δM_Ξ^δ is much milder than that of the nucleon, see Figure 3.7. However, the contribution from the $\Xi^* - \pi$ virtual corrections is not as suppressed.

In order to assess the contributions from the Ξ^* states, we therefore perform an analysis using Bayesian priors on both axial couplings, $g_{\pi\Xi\Xi}$ and $g_{\pi\Xi\Xi^*}$. We explore setting prior widths that are 1, 2, 5 and 10% of the phenomenological values in Eq. (3.38). We use both the experimental $\Delta_{\Xi^*\Xi}$ splitting as well as those determined in this work, see Table 3.8. The results of these analyses are collected in Table 3.11 and a representative extrapolation is depicted in Figure 3.7. As with the nucleon isovector mass, we find the uncertainty on $g_{\pi\Xi\Xi}$ and $g_{\pi\Xi\Xi^*}$ scales with the prior width we set. However, we also observe the resulting value of δM_Ξ^δ is stable as we increase the prior width. We therefore take the results with 5% prior widths on the axial couplings. There is a systematic associated with using the experimental value of $\Delta_{\Xi^*\Xi}$ and the values determined in this work, which is nominally higher order. For our final prediction, we therefore split this difference as a systematic

$$\delta M_\Xi^\delta = 5.44(24)(8)(5)(7) \text{ MeV}, \tag{3.39}$$

where the uncertainties are the fitting statistical/systematic uncertainty, the uncertainty from $a_t\delta^*$, the scale-setting uncertainty and finally the uncertainty from $\Delta_{\Xi^*\Xi}$.
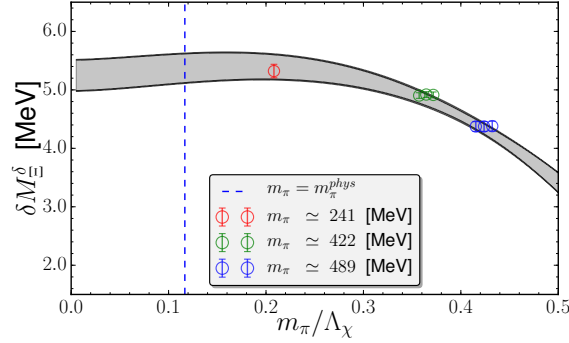
Figure 3.7: The mass splitting δM_Ξ^δ [MeV] versus m_π with $g_{\pi\Xi\Xi}$ and $g_{\pi\Xi\Xi^*}$ constrained with 5% prior widths. The numerical results show statistical uncertainties only. The multiple values at the two heavier pion masses arise from the three values of $a_t\delta$ used in this work and are split for visual clarity.

3.3.1.6 χ-logarithms in the isovector nucleon mass

Taken all together, we find the evidence presented here to be conclusive evidence for the presence of non-analytic light quark mass dependence in the nucleon spectrum:

- strong pion-mass dependence is observed which cannot be accounted for with a power-series expansion about $m_\pi = 0$, Figure 3.5 but perfectly predicted and accounted for with χPT;

- the observed pion-mass dependent curvature is not sensitive to the inclusion of the heaviest pion mass data, Figure 3.6;

- relaxing the coefficient of the χ-log to freely vary results in the large value of g_A consistent with the experimental value, Eq. (3.29);

- the lack of observation of strong pion-mass dependence in the cascade isovector mass, which is in accordance with expectations predicted by χPT, Figure 3.6.
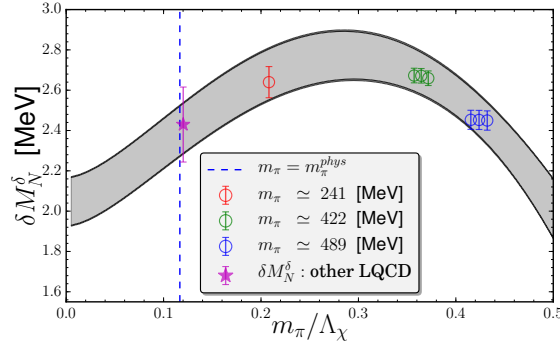
Figure 3.8: The mass splitting δM_N^δ [MeV] versus m_π with g_A and $g_{\pi N \Delta}$ constrained with 5% prior widths. The numerical results show statistical uncertainties only. The multiple values at the two heavier pion masses arise from the three values of $a_t \delta$ used in this work and are split for visual clarity. The (magenta) star is the weighted average of other LQCD results, Eq. (3.30), not included in this analysis.

To be conservative, for our final determination of δM_N^δ, we use a fit including both nucleon and delta intermediate states, Eq. (3.32). We use our prior knowledge of g_A and $g_{\pi N \Delta}$ from experiment to allow these couplings to float in the numerical minimization,

but we apply reasonable prior widths to their central values via an augmented χ^2 with Gaussian priors. We explore the sensitivity of the extrapolated value of δM_N^δ to the size of the prior widths on these axial couplings with 1, 2, 5 and 10% widths. As with δM_Ξ^δ, we use both the value of $\Delta = m_\Delta - m_N$ from experiment, and determined in this work, Table 3.8 as a further extrapolation systematic. The results of this study are presented in Table 3.12. The posterior uncertainties on the axial couplings track the prior widths, however, the resulting value of δ_M^δ is not sensitive to this variation. We observe dependence on the values of Δ, which we take as an extrapolation systematic. Our final prediction for the strong contribution to the isovector nucleon mass is

$$\delta M_N^\delta = 2.32(12)(4)(5)(8) \text{ MeV},\qquad(3.40)$$

where the uncertainties are the fitting statistical/systematic uncertainty, the uncertainty from $a_t\delta^*$, the scale-setting uncertainty and finally the uncertainty from Δ. A representative fit is provided in Figure 3.8.

$\tilde{g}_A$	$\tilde{g}_{\pi N\Delta}$	$\hat{g}_A$	$\hat{g}_{\pi N\Delta}$	α_N	β	δM_N^δ MeV
			$\Delta = 293$ MeV			
1.27(01)	1.53(02)	1.27(01)	1.53(02)	1.80(09)	-15.9(08)	2.40(11)(4)(5)
1.27(03)	1.53(03)	1.27(03)	1.53(03)	1.80(09)	-15.9(09)	2.40(12)(4)(5)
1.27(06)	1.53(08)	1.28(06)	1.53(08)	1.80(10)	-16.0(14)	2.40(12)(4)(5)
1.27(13)	1.53(15)	1.29(12)	1.52(15)	1.79(14)	-16.0(24)	2.40(13)(4)(5)
			$\Delta = \Delta_{LQCD}$ MeV			
1.27(01)	1.53(02)	1.27(01)	1.53(02)	1.67(12)	-15.2(12)	2.23(14)(3)(5)
1.27(03)	1.53(03)	1.27(03)	1.53(03)	1.67(12)	-15.2(12)	2.23(12)(3)(5)
1.27(06)	1.53(08)	1.26(06)	1.51(08)	1.67(13)	-15.0(16)	2.23(12)(3)(5)
1.27(13)	1.53(15)	1.24(13)	1.48(15)	1.68(15)	-14.2(26)	2.24(15)(3)(5)

Table 3.12: Chiral extrapolation of δM_N^δ using Eq. (3.32) with Bayesian constrained fits. Here $\tilde{g}_{\pi N\Delta}$ is the prior width given to the augmented χ^2 and $\hat{g}_{\pi N\Delta}$ is the resulting fit value. For any small finite prior width, the coupling is just determined by the prior, Eq (3.34).

3.4 Implications for the QCD θ-term

$\mathcal{CP}$ (Charge-Parity) violation from the QCD $\bar{\theta}$ term is intimately related to the quark masses [128–130]. Via the $U(1)_A$ anomaly, the $\bar{\theta}$ term can be rotated into a complex quark-mass term, which, after performing additional non-anomalous $SU(N_f)$ rotations needed to align the vacuum of the theories with and without $\mathcal{CP}$-violation, is isoscalar and proportional to the light quark reduced mass m_*. In SU(2), $m_* = (1/m_u + 1/m_d)^{-1}$ and the quark-mass operator can be expressed as

$$\mathcal{L}_m = -\bar{m}\bar{q}q + \delta\,\bar{q}\tau_3 q + m_*\bar{\theta}\bar{q}i\gamma_5 q - \bar{m}\bar{q}q + \delta\bar{q}\tau_3 q + \frac{\bar{m}}{2}\left(1 - \frac{\delta^2}{\bar{m}^2}\right)\bar{\theta}\bar{q}i\gamma_5 q, \qquad (3.41)$$

where $2\bar{m} = m_u + m_d$. The observation of Ref. [130] is that the QCD $\bar{\theta}$ term and the quark mass difference are related by an $SU(2)_L \times SU(2)_R$ rotation, and this implies that chiral symmetry relates the matrix elements of the isoscalar $\bar{\theta}$ term between n_N nucleon and n_π pions to those of the isovector quark-mass term with n_N nucleons and $n_\pi - 1$ pions. These relations are particularly robust for the leading interactions induced by $\mathcal{L}_m$ in the χPT Lagrangian [127, 131].

The pseudoscalar mass term in Eq. (3.41) induces isospin invariant, TV (time-reversal violating) pion-baryon couplings,

$$\mathcal{L} = -\frac{\bar{g}_0}{\sqrt{2}f_\pi}\bar{N}\tau \cdot \pi N - \frac{\bar{g}_{0\,\Xi}}{\sqrt{2}f_\pi}\bar{\Xi}\,\tau \cdot \pi\Xi + \dots, \qquad (3.42)$$

where $\dots$ includes terms with multiple pions, which are fixed by chiral symmetry, and TV couplings of the Σ and Λ, which we will not discuss. The coupling of greatest phenomenological interest is $\bar{g}_0$, which determines the leading non-analytic contributions to the nucleon EDM (electric dipole moment) [130] and the momentum dependence of the nucleon EDFF (electric dipole form factor) [132, 133]. Furthermore, $\bar{g}_0$ dominates the nucleon-nucleon TV potential induced by the QCD $\bar{\theta}$ term, and, consequently, the $\bar{\theta}$ term contribution to the EDM of ^{3}He, and of diamagnetic atoms, such as ^{199}Hg and ^{129}Xe.

Chiral symmetry implies that, for $\mathcal{CP}$-violation induced by the QCD $\bar\theta$ term, the nonperturbative information entering $\bar{g}_0$ and $\bar{g}_{0\Xi}$ is determined by the quark mass contribution to nucleon and cascade mass splittings [130, 131]

$$\bar{g}_0(\bar\theta) = \delta M_N^\delta \frac{\bar{m}}{2\delta} \left(1 - \frac{\delta^2}{\bar{m}^2}\right)\bar\theta\,,$$

$$\bar{g}_{0\Xi}(\bar\theta) = \delta M_\Xi^\delta \frac{\bar{m}}{2\delta} \left(1 - \frac{\delta^2}{\bar{m}^2}\right)\bar\theta. \qquad (3.43)$$

These relations were derived at LO in χPT, but it has been showed that they are respected by all loop corrections of $\mathcal{O}(\varepsilon_\pi)$, and violated only by finite counterterms [127].

Our extraction of the nucleon and cascade mass splittings allows for a precise determination of $\bar{g}_0$ and $\bar{g}_{0\Xi}$. We find

$$\frac{\bar{g}_0}{\sqrt{2}f_\pi} = (14.7 \pm 1.8 \pm 1.4) \cdot 10^{-3}\,\bar\theta, \qquad (3.44)$$

$$\frac{\bar{g}_{0\Xi}}{\sqrt{2}f_\pi} = (34.4 \pm 4.0 \pm 3.5) \cdot 10^{-3}\,\bar\theta, \qquad (3.45)$$

where we used the FLAG averages for $\delta/\bar{m}$ at the physical point, $\delta/\bar{m} = 0.37 \pm 0.03$ [40]. The first error in Eqs. (3.44) and (3.45) comes from the lattice errors on the mass splittings and $\delta/\bar{m}$, combined in quadrature. The second error is an estimate of the $\mathcal{O}(\varepsilon_\pi)$ corrections to Eq. (3.43), which, following Ref. [127], we conservatively estimate to be at the 10% level.

The pion-nucleon coupling $\bar{g}_0$ determines the non-analytic dependence of the neutron EDM on the pion mass [130]. At NLO in χPT [130, 133, 134]

$$d_n = \bar{d}_n(\mu) + \frac{eg_A\bar{g}_0}{8\pi^2 f_\pi^2}\left(\log\left(\frac{\mu^2}{m_\pi^2}\right) - \frac{\pi m_\pi}{2m_N}\right) \qquad (3.46)$$

where $\bar{d}_n(\mu)$ is a counterterm needed to absorb the scale dependence of the chiral loop, and a very similar expression holds for the EDM of the Ξ baryon. Recent LQCD calculations of the nucleon EDM induced by the QCD $\bar\theta$ term [48, 135, 136] do not yet show

evidence of this non-analytic behavior. As the precision improves and calculations at pion masses closer to the physical point are performed, it will be important for LQCD to confirm, or, maybe more interestingly, refute the behavior predicted by Eq. (3.46).

In addition, our calculation predicts the slope of the nucleon EDFF. Defining $S_B = -dF_B(\vec{q}^2)/d\vec{q}^2$, where F_B is the EDFF of the baryon B and $\vec{q}$ indicates the photon three-momentum, at the physical pion mass we find

$$S_n = (0.69 \pm 0.08) \cdot 10^{-4}\, \bar{\theta}\, e\, \mathsf{fm}^3 \tag{3.47}$$

$$\tag{3.48}$$

$$\frac{g_{\pi\Xi\Xi}S_n}{g_A S_{\Xi^-}} = \frac{\delta M_N^\delta}{\delta M_\Xi^\delta}\frac{1 - \frac{5\pi m_\pi}{4m_N}}{1 - \frac{5\pi m_\pi}{4m_\Xi}} = 0.30 \pm 0.02, \tag{3.49}$$

where we used the NLO χPT expression of the EDFF [131, 134]. While these predictions are of little phenomenological interest, since there are no plans to measure the momentum dependence of the nucleon or Ξ EDFF, they provide an important benchmarks to check the validity of current and future LQCD calculations of baryonic EDMs.

3.5 Conclusions

While we are not able to perform the continuum limit of our results, we estimate the discretization effects to be 0.07 MeV for δM_N^δ and 0.16 MeV for δM_Ξ^δ with the assumption of either $\mathcal{O}(a_s^2)$ of $\mathcal{O}(\alpha^2 a_s)$ contributions.

We perform precise lattice QCD calculations of the ground state isovector spectrum by utilizing a symmetric breaking of isospin in the valence sector about the degenerate sea-quark mass. These results strongly support non-analytic light-quark mass dependence in the baryon spectrum. The quantity which prominently displays this non-analytic behavior is the isovector nucleon mass splitting. The evidence includes the observation of rapidly changing pion mass dependence in this quantity, which cannot be simply understood with a well behaved power-series expansion about the chiral limit. The presence of the non-

analytic χ-log is robust to several systematic variations, including letting the coefficient of the χ-log float as a free parameter. We also observe the isovector Ξ spectrum has a milder pion mass dependence, lending significant confidence in our understanding low-energy QCD through the confirmation of non-analytic pion-mass dependence predicted by χPT.

We also provide an estimate for the $\bar{\theta}$ term contribution to $\mathcal{CP}$-violating pion-nucleon interactions, which contribute to the nucleon EDM.

Chapter 4

Renormalization of Quark Bilinear and Four Quark Operators for New Physics

Selected results from this work have appeared in [137], however the results not given in [137] await final independent verification.

4.1 Introduction

Quantities that are "measurable," such as the pion mass, proton mass, $m_s \bar{s}s$, are renormalization scheme and scale independent. Therefore, these results from analysis of QCD correlation functions can be directly used to extrapolate to the continuum, infinite volume, and physical pion mass limit. In general, this does not hold for composite operators or the quark masses, for example. These quantities are renormalization scheme and scale dependent, therefore calculations of these quantities must be renormalized. It is also useful to convert them to $\overline{\text{MS}}$, to connect with literature using perturbative renormalization.

To make this obvious, consider for a moment a physical observable $P(g(a), a, m(a))$ which has a well defined continuum limit, e.g. $\lim_{a \to 0} P(g(a), a, m(a)) \to P_0$. Scheme and

57

scale independence requires that this observable satisfy the (simplified) Callan-Symanzik equation

$$\frac{dP}{d\ln a} = \left(\frac{\partial}{\partial \ln a} + \frac{\partial g}{\partial \ln a}\frac{\partial}{\partial g} + \frac{\partial m}{\partial \ln a}\frac{\partial}{\partial m} \right) P = 0. \tag{4.1}$$

Any change in the lattice scale a must be compensated for by a simultaneous shift in the coupling $g(a)$ or the mass $m(a)$ such that any scale dependence is canceled. The second term in (4.1) leads to the familiar QCD β-function, from which we find that the coupling g depends on the lattice spacing, and vica versa. Thus bare correlation functions which are scheme and scale *dependent*, and which are computed on ensembles of lattices with different scales a but with other quantities held fixed (such as pion mass, volume, etc...), correspond to different values of the renormalized coupling, and thus different energy scales. To take the correct continuum limit, we therefore must renormalize our results to a common energy scale first, and then evaluate the corresponding limits. Note that the running of the strong coupling with lattice scale $\lim_{a\to 0} g(a) \to 0$ implies our theory becomes asymptotically free towards the continuum limit, motivating the use of the small a expansion of lattice perturbation theory.

Intuitively, different discretization prescriptions of Euclidian QCD correspond to different regularization schemes, and thus renormalization factors must be recomputed on each lattice discretization used. This is made rigorous in lattice perturbation theory, as distinct discretization prescriptions lead to a unique set of counter-terms in the small a expansion, giving rise to distinct finite contributions to the renormalization factors. More so, if a trivializing algorithm is applied to the gauge field, then the renormalization factors must be computed at each non-zero smoothing time of the algorithm used[1]. Lastly, different discretization prescriptions break continuum symmetries in unique ways, leading to possible power divergent (in $1/a$) mixings with lower dimensional operators that must be subtracted off non-perturbatively before the continuum limit is taken, as will be discussed later.

---

[1]See [138] for common algorithms, and [138] for the algorithm used in this work.

Systematic problems with the perturbative renormalization method, namely poor convergence and the rapid proliferation of diagrams, led to the development a non-perturbative method of computing renormalization factors by imposing renormalization conditions directly on Green's functions computed in lattice QCD. The idea of imposing renormalization conditions directly on lattice Green's functions was first rigorously set down by Martinelli *et. al* [139], where it was applied to the case of quark bilinear operators (e.g. $\bar{q}\Gamma q$). This method is known as the Regularization Independent, or Rome-Southampton method. The Rome-Southampton method has since been used successfully to extract the bilinear renormalization factors from a variety of lattice actions, including mixed actions [140–145], as well as more complicated composite operators such as the four quark $\Delta F = 2$ operators necessary for BSM neutral kaon mixing and BSM heavy physics contributions to neutrino-less double beta decay[137, 146, 147]. In this work we use the RI/SMOM variant of this method, where RI stands for *Regularization Independent*, a desirable property as the scheme should not depend on the specific lattice regularization used, while SMOM refers to they type of kinematics imposed on the vertex of interest. Matching to $\overline{\text{MS}}$ is then done in continuum perturbation theory, with typical conversion factors known to the two or three loop level [146].

In this work, we detail the first determination of the renormalization factors necessary to renormalize the quark bilinear and four quark operators determined on the lattice ensembles of references [137, 138, 148, 149]. These factors were used to renormalize the nucleon axial coupling in references [148, 149], as well as the effective heavy physics contributions to neutrino-less double beta decay in reference [137]. Future calculations of the bilinear matrix elements in the nucleon and pion using these lattice ensembles will also use the renormalization factors computed in this work.

4.2 Lattice Ensembles

This work uses mixed action Möbius Domain Wall fermions solved on HISQ ensembles with dynamical light, strange, and charm quarks. Gradient (Wilson) flow smoothing of the gauge configurations was used to remove large UV fluctuations of the gauge fields, and to further suppress residual chiral symmetry breaking due to the finite L_5 (see section 5.5). The result is an approximate restoration of chiral symmetry in the valence sector, with residual chiral symmetry breaking term m_{res} an order of magnitude smaller than the lightest light quark mass. The valence and sea parameters for the lattice ensembles used in this work are shown in Table 4.1.

HISQ gauge configuration parameters							valence parameters					
abbr.	N_{cfg}	volume	$\sim a$ [fm]	$\sim m_{\pi_5}$ [MeV]	m_l/m_s	$\sim m_{\pi_5}L$	L_5/a	aM_5	b_5	c_5	$am_l^{\text{val.}}$	$m_{\text{res}} \times 10^4$
a15m350	10	$16^3 \times 48$	0.15	350	0.255	4.2	12	1.3	1.5	0.5	0.0206	9.380
a15m310	10	$16^3 \times 48$	0.15	310	0.2	3.8	12	1.3	1.5	0.5	0.01580	10.12
a15m220	10	$24^3 \times 48$	0.15	220	0.1	4.0	16	1.3	1.75	0.75	0.00712	5.770
a15m130	10	$32^3 \times 48$	0.15	130	0.036	3.2	24	1.3	2.25	1.25	0.00216	2.539
a12m350	10	$24^3 \times 64$	0.12	350	0.255	5.1	8	1.2	1.25	0.25	0.01660	7.559
a12m310	10	$24^3 \times 64$	0.12	310	0.2	4.5	8	1.2	1.25	0.25	0.01260	8.250
a12m220	10	$32^3 \times 64$	0.12	220	0.1	4.3	12	1.2	1.5	0.5	0.00600	3.970
a12m130	10	$48^3 \times 64$	0.12	130	0.036	3.9	20	1.2	2.0	1.0	0.00195	1.641
a09m310	10	$32^3 \times 96$	0.09	310	0.2	4.5	6	1.1	1.25	0.25	0.00951	2.430
a09m220	10	$48^3 \times 96$	0.09	220	0.1	4.7	8	1.1	1.25	0.25	0.00449	1.652

Table 4.1: HISQ gauge configurations and valence sector parameters.

4.3 Background

The Rome-Southampton method imposes renormalization conditions non-perturbatively, directly on quark and gluon Green functions, with given off shell states, in a fixed gauge at large virtuality [139]. Landau gauge fixing conditions are used, and momenta are chosen such that the "window condition"

$$\Lambda_{QCD}^2 << p^2 << \left(\frac{\pi}{a}\right)^2 \tag{4.2}$$

is met. The lower condition (large virtuality) ensures that we are well within the perturbative regime, while the upper ensures that finite lattice spacing effects are under control.

We use momentum source propagators, solved using the `MOMENTUM_VOLUME_SOURCE` routine in the `Chroma` software suite, to achieve $\mathcal{O}(V)$ statistical precision over point source techniques. Using volume sources, it's possible to achieve $\mathcal{O}(.5\%)$ statistical precision with as few as ten configurations [150]. For each momentum, we solve

$$\sum_x D(y, x)G(x, p) = e^{ip \cdot y}\delta_{\alpha\beta}\delta_{ab} \tag{4.3}$$

for the momentum source propagator $G(x, p)$. The full momentum space propagator is then found by Fourier transformation

$$\sum_x e^{-ip' \cdot x}G(x, p) = G(p', p). \tag{4.4}$$

The un-amputated vertex of the operator $\mathcal{O}$ of interest is then constructed from the momentum source propagators.

The choice of kinematics has a strong impact on the control of non-perturbative effects in our renormalization factors. In this work we use the non-exceptional momentum conditions (SMOM conditions), which have been shown to suppress non-perturbative infrared effects by a factor of $1/p^6$ [140]. We choose momentum conditions which allow a non-zero momentum transfer through the vertex at a fixed momentum scale (4.5), while ensuring that discretization errors aren't mixed by using only $\mathcal{H}(4)$ equivalent momenta along a fixed unit vector. The SMOM kinematic conditions read [140]

$$p_1^2 = p_2^2 = (p_1 - p_2)^2 = q^2 = \mu^2. \tag{4.5}$$

We choose p_1 and p_2 such that $p_1 = n(1, 1, 0, 0)$ and $p_2 = n(0, 1, 1, 0)$ and vary n to change the renormalization scale μ.

4.4 Bilinear Operators

For the case of the quark bilinear operators, $j = \bar{q}\Gamma q$, we form the un-amputated vertex by inserting our bilinear current between two off shell quark states (in Landau gauge) with momenta chosen to satisfy the SMOM conditions

$$V_\Gamma(p_2, p_1) = \langle p_2 | j_\Gamma(p_2, p_1) | p_1 \rangle. \tag{4.6}$$

Γ is in the set $\{1, \gamma_5, \gamma_\mu, \gamma_\mu\gamma_5, \sigma_{\mu\nu}\}$ with the shorthand identifiers $\{S, P, V, A, T\}$.
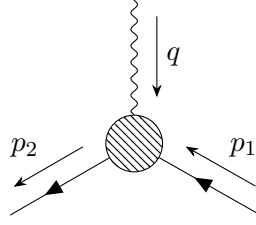
(a) Graphical representation of the SMOM kinematic conditions used for the bilinear factors used in this work. p_1 and p_2 are chosen such that the Rome-Southampton window condition is satisfied.

The un-amputated vertex in momentum space is then given by (4.7), where the antiquark propagator is given by $\bar{G}(p_2, p_2) = \sum_x \left(\gamma_5 e^{-ip_2 \cdot x} G(x, p_2)\gamma_5\right)^\dagger$. The momentum flow of a typical diagram used in the renormalization of the quark bilinear operators is shown in Figure 4.1a.

$$V_\Gamma(p_2, p_1) = \langle \sum_x \left(\gamma_5 e^{-ip_2 \cdot x} G(x, p_2)\gamma_5\right)^\dagger \Gamma \left(e^{-ip_1 \cdot x} G(x, p_1)\right) \rangle = \langle \bar{G}(p_2, p_2)\Gamma G(p_1, p_1) \rangle \tag{4.7}$$

The amputated vertex function is then found by amputating the external legs after averaging over an ensemble

$$\Pi_\Gamma(p_2, p_1) = \langle \bar{G}(p_2, p_2) \rangle^{-1} \langle \bar{G}(p_2, p_2)\Gamma G(p_1, p_1) \rangle \langle G(p_1, p_1) \rangle^{-1}. \tag{4.8}$$

We project our amputated vertex to the correct Lorentz structure to construct the projected

amputated vertex

$$\Lambda_\Gamma(p_2, p_1) = \mathcal{P}_\Gamma \Pi_\Gamma(p_2, p_1), \tag{4.9}$$

on which we impose our renormalization conditions. Renormalization conditions require that the renormalized projected amputated bilinear Green's function takes it's tree level value at the non-exceptional kinematic point. At the SMOM kinematic point, p_2 and p_1 dependence can be traded for renormalization scale dependence from the relation (4.5), and thus our renormalization conditions require

$$\Lambda_\Gamma^r(p_2, p_1) = \Lambda_\Gamma^r(\mu) = \frac{Z_\Gamma(\mu)}{Z_q(\mu)} \Lambda_\Gamma(\mu) = T_\Gamma. \tag{4.10}$$

In this work we normalize our projected amputated vertices by the tree level values such that the projected amputated vertex is the inverse of the renormalization factors. Suitable extrapolations to the chiral limit, and interpolations to the correct momentum transfer $q^2 = \mu^2$ for each lattice ensemble, are then found by fitting the normalized projected amputated vertex, or the Z_q and Z_m factors themselves.

The renormalization conditions on the projected amputated vertex are exact in the chiral continuum limit, however our lattice amputated projected vertices also contain dependence on the light (and strange) quark masses as well as finite lattice spacing artifacts. To remove these contaminations we first must extrapolate to the chiral limit, as well as interpolate our data to a common renormalization scale μ, such that an $a \to 0$ limit of the renormalized operator $Z_\Gamma(\mu, a)\langle \mathcal{O}_\Gamma(a) \rangle$ is well defined. In practice, we observe that the quark mass dependence of our renormalization factors is very mild[2].

We consider a general ansatz motivated by the expected running of the operators as a function of momentum and quark mass

$$\Lambda(p, am_q) = \left(1 + \sum_i a_i \, (am_q)^i\right) \left(b_0 + \sum_{j \in \{-4, -2, \dots 2, 4 \dots\}} b_j p^j\right) + \sum_l c_l p^l, \tag{4.11}$$

---

[2]The exceptions are the scalar and pseudo-scalar vertices, which suffer from a well known pion pole contamination [151].

where am_q is the quark mass in lattice units ($am_l + am_{\text{res}}$), while p is the momentum in physical units. The form takes into account the running of the operator itself, non-perturbative contamination, and discretization errors[152]. We include $f(c_l, p^l)$, where l is a positive even integer, on general grounds that the fit ansatz need not be perfectly factorize-able.

4.4.0.1 Step Scaling

The window condition (4.2) turns out to be quite restrictive in practice. To control perturbative errors in the matching to $\overline{\text{MS}}$, a high renormalization scale of 3 GeV is generally used. For coarse lattices, for example the a15 in our work[3] , large discretization errors at the upper end of the Rome-Southampton window become uncontrollable well before this matching scale is reached. The renormalization factors themselves have no well defined continuum limit, and thus unless the matching scale is lowered we would be forced to use only finer lattice spacing in our work.

An alternative strategy was proposed by the RBC-UKQCD collaboration, which uses information from the running of our renormalization factors at different lattice spacings to raise the scale of our coarser lattices beyond the limit of the Rome-Southampton window for the coarse lattice [153]. As a solution to the Callan-Symanzik equation for a given operator, the running has a well-defined continuum limit, and thus a continuum extrapolation of the running of each operator is well defined [154]. Assuming the continuum limit of the running has been properly taken, no additional discretization errors are introduced in mapping from the lower scale to the higher, and the continuum limit of the renormalized operator may be taken in a controlled manner.

For each lattice spacing in Table 4.1, we construct the (lattice spacing dependent) step scaling function

$$\Sigma_\Gamma(\mu_2, \mu_1, a) = Z_\Gamma(\mu_2, a) Z_\Gamma^{-1}(\mu_1, a) \tag{4.12}$$

---

[3]This notation is shorthand for the a ~ 0.15 fm lattice spacing ensembles used in this work.

using the chiral limit values of the momentum interpolated running of our renormalization factors. The momentum interpolation and chiral extrapolation is accomplished by fitting (4.11) in a combined momentum and quark mass fit to all renormalization factors for a given lattice spacing. The step scaling is then constructed by taking the ratio of the chiral momentum interpolated renormalization factors for a given μ_1 and μ_2 as shown (4.12). For the finer lattice spacings a09 and a12 we use as our low scale μ_1 = 2 GeV, and step scale to a maximum high scale of μ_2 = 3 GeV. The coarsest lattice spacing hits the upper window well before 3 GeV, so we take the maximum high scale for the a15 step scaling to be μ_2 = 2.5 GeV. We interpolate a range of μ_2 values between the low scale and the maximum high scale, which gives the step scaling at each lattice spacing as a function of momentum.

The momentum and lattice spacing dependence of the step scaling functions is then parameterized in two ways. The first method parameterizes the running and lattice spacing dependence of the scaling function by a polynomial in p and a^2

$$\Sigma(\mu_2, \mu_1, a) = \left(1 + \sum_i \alpha_i \left(a^2\right)^i\right) \left(\beta_0 + \sum_j \beta_j \mu_2^j\right) + \sum_l \chi_l \mu_2^l, \qquad (4.13)$$

which is then fit to all three lattice spacing dependent step scaling functions simultaneously. The resulting continuum limit is found by taking $a \to 0$ of the best fit function

$$\sigma_\Gamma(\mu_2, \mu_1) \equiv \lim_{a \to 0} \Sigma_\Gamma(\mu_2, \mu_1, a). \qquad (4.14)$$

The second method uses a polynomial in a^2 in a constrained "fit" of the lattice spacing dependence of the step scaling functions at each value of μ_2. The continuum limit is simply the a^0 term of the polynomial fit at each final momentum μ_2. The two methodologies above are checked against each other and give consistent continuum limits.
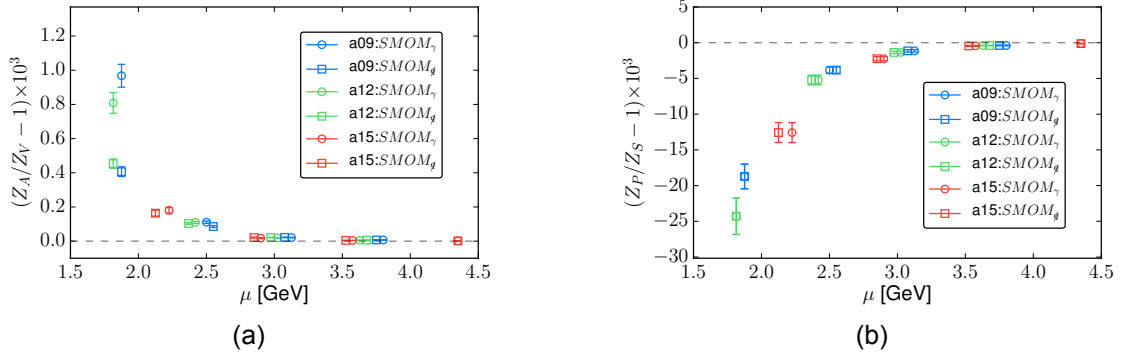
Figure 4.2: Difference between the chiral expectation and lattice quantities for the ~ 310 MeV pion mass ensembles. For large momenta, the axial and pseudo-scalar renormalization factors obey the expected chiral relation to one part in one million for the axial and vector factors, even away from the chiral limit. Points are displaced along the x-axis for clarity.

4.4.1 Projection Schemes

The use of non-exceptional kinematics allows some freedom in choosing the projection operator used in the vector and axial vector renormalization conditions. We use two projection schemes, γ-scheme and $\not{q}$-scheme. The $\not{q}$-scheme has the advantage that conversion formulae to $\overline{\text{MS}}$ contain less theoretical error, e.g. for a given order $\mathcal{O}(\alpha_s^n)$ the correction from the next higher order $\mathcal{O}(\alpha_s^{(n+1)})$ is smaller for $\not{q}$-scheme than for γ-scheme. The projectors used in the two schemes are shown in Table 4.2.

Γ	γ-scheme	$\not{q}$-scheme
A	$\gamma_\mu \gamma_5$	$\not{q}\gamma_5 q_\mu / q^2$
V	γ_μ	$\not{q} q_\mu / q^2$

Table 4.2: γ and $\not{q}$ vector and axial vector projectors.

If chiral symmetry is preserved in our lattice results, we expect (from the chiral ward identities) $Z_A = Z_V$ and $Z_S = Z_P$. Figure 4.2 shows the difference between the expected chiral symmetry value and the lattice quantities, which for momenta of interest shows chiral symmetry is well respected. This is due to the synergistic combination of valence Domain Wall Fermions, which have good chiral symmetry in the large L_s limit, and the

Wilson flow. We will use the approximate chiral symmetry to determine the quark mass and wave function renormalization in the next section.

abbr.	$\mathring{g}_V$
a15m400	0.998(01)
a15m350	0.997(01)
a15m310	1.001(02)
a15m220	1.000(04)
a15m130	0.994(35)
a12m400	1.016(01)
a12m350	1.016(01)
a12m310	1.021(02)
a12m220	1.015(02)
a12m130	1.020(08)
a09m400	1.023(01)
a09m350	1.024(02)
a09m310	1.024(01)
a09m220	1.022(02)

Table 4.3: Values of the bare $\mathring{g}_V$ used to find Z_V.

4.4.2 Vector and Axial

The local vector current is conserved in the continuum, but at non-zero lattice spacing receives non-trivial renormalization [155]. This running may be determined using the conserved vector current, or by calculating the forward matrix element of the (non-conserved) vector current between judicious chosen states [155]. We use the vector charge of the nucleon, $\mathring{g}_V$, which is renormalized to be 1, to find the renormalization factor Z_V. The values of $\mathring{g}_V$ were determined in another work [149], and used here to set the renormalization factor $Z_V = 1/\mathring{g}_V$. The values of Z_V and $\mathring{g}_V$ used in the extrapolation are shown in Table 4.3, and an example extrapolation to the chiral limit for the a15 lattice ensembles is given in Figure 4.3a.

The data is fit well with either a linear function of the light quark mass or a constant, with the resulting extrapolations to the chiral limit agreeing within error. We choose the linear fit to be conservative, as it has the larger extrapolation error. The resulting chiral

limit values of $\mathring{g}_V$, and Z_V, are shown in Table 4.4. With the chiral limit values of Z_V

(a)

(b)
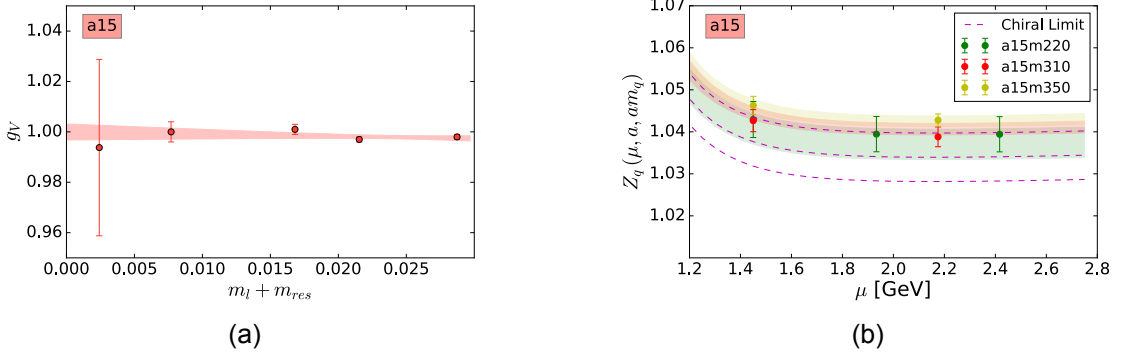
Figure 4.3: (4.3a) Extrapolation of the a15 ensemble g_V data to the chiral limit. The shaded band denotes the reproduced fit data from the fitted function. (4.3b) The combined momentum and quark mass dependence fit of the wave function renormalization factor for the a15 ensemble. The dashed line denotes the chiral limit, while the shaded bands once again give the reproduced fit data from the fitted function.

scale	Z_V^a	g_V^a	χ^2/dof [dof]	P-value
a15	1.0000(31)	1.0000(31)	0.53 [2]	0.59
a12	0.9829(22)	1.0174(23)	2.03 [3]	0.11
a09	0.9770(20)	1.0235(21)	1.03 [3]	0.38

Table 4.4: Chiral limit values of the vector coupling, and Z_V. The a superscript refers to the residual lattice spacing dependence of these quantities.

obtained, it is now advantageous to exchange the Z_q dependence of our bilinear (and four quark) renormalization factors for Z_V. This eliminates the running of Z_q in our momentum interpolations of the Z_Γ factors. The extrapolation plots for all ensembles are given in Appendix B.1.

For completeness sake, we perform the step scaling analysis on the axial renormalization factor in the γ-scheme. The data behaves as expected from Figure 4.2a, with the running of Λ_A/Λ_V fit well with a momentum independent constant plus a small quark mass and momentum dependent perturbation. The step scaling from 2 to 3 GeV for the axial vector operator is equal to one well within error. We thus take $Z_A = Z_V$ in both $\slashed{q}$ and γ scheme.

4.4.3   Quark Mass and Wave Function Renormalization

The quark mass and wave function renormalization may be determined using the $\mathring{g}_V$ (Z_V) values, and by exploiting the good chiral symmetry of our lattice. In both the $\slashed{q}$ and γ schemes, the quark wave function renormalization can be found via the axial and vector amputated vertices

$$Z_q(\mu) = Z_V \frac{\Lambda_V(\mu) + \Lambda_A(\mu)}{2}. \tag{4.15}$$

Since we don't have perfectly matched momenta between our lattice ensembles, we must first interpolate to a common scale μ. After converting our momenta to physical units, using the MILC lattice scales determined in [156], we then perform a combined quark mass and momentum fit. We use 200 bootstrap resamples of 8 configurations each to construct our covariance matrix. We find the chiral extrapolation for Z_q to be mild, and the fit function reproduces the fitted data precisely. Figure 4.3b shows an example fit for the a15 ensemble.

The quark mass renormalization may be found likewise via the scalar and pseudo-scalar vertices

$$Z_m(\mu) = \frac{\Lambda_S(\mu) + \Lambda_P(\mu)}{2Z_q(\mu)}. \tag{4.16}$$

The extrapolation to the chiral limit of (4.16) must be carefully taken, as the pseudo-scalar vertex contains a well known pion pole, leading to divergence in the chiral limit[151]. This pole arises from the coupling of the pseudo-scalar vertex to the one pion state, leading to a momentum dependent pion pole contribution[151]. The mixing is non-perturbative, and must be subtracted before any chiral limit of the quark mass renormalization factor (or pseudo-scalar vertex) is taken. We find the pion pole contribution to the mass renormalization factor to be much milder compared to the pseudo-scalar vertex in the next section. An example is shown in Figure 4.4a.
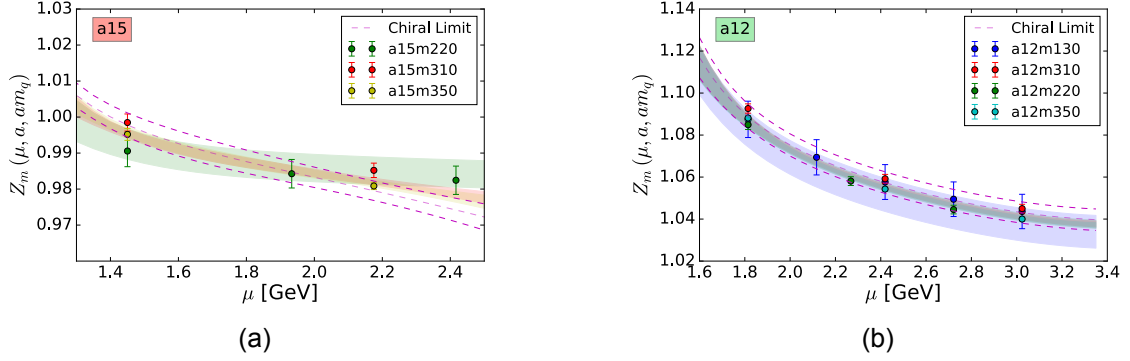
Figure 4.4: Reproduced data points from the best fit of (4.11) to the Z_m renormalization factors. The influence of the pion pole is mild at these quark masses, and appears further suppressed for finer lattice spacings.

4.4.3.1 Step Scaling of Z_q and Z_m

Given the running of our renormalization factors a lá (4.11), we construct the step scaling functions according to (4.12). With three lattice spacings, we include in the parameterization up to quadratic order in a^2. The step scaling functions for Z_q and Z_m and resulting continuum extrapolation are shown in Figure 4.5. Using the continuum step scaling func-
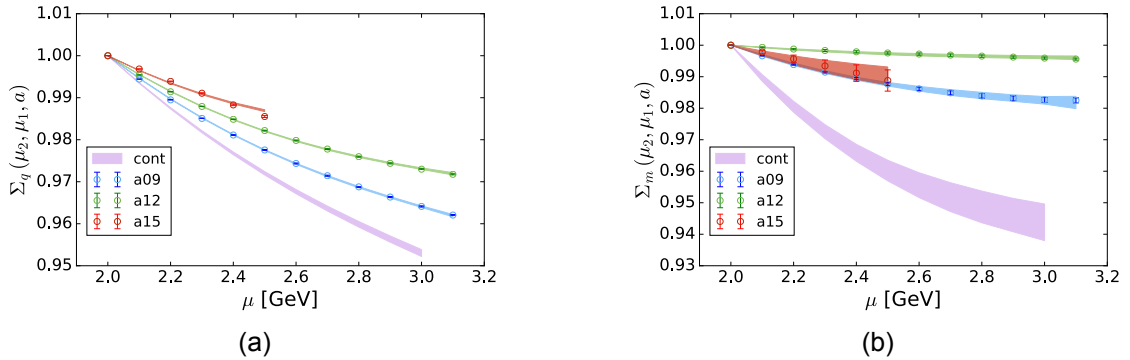
Figure 4.5: Reproduced data, and continuum limit, of the quark mass and wave function step scaling functions in the $\not{q}$-scheme.

tion, we raise the renormalization factors of all ensembles from 2 to 3 GeV

$$Z^a_{(q,m)}(\mu_2) = \sigma_{(q,m)}(\mu_2, \mu_1) Z^a_{(q,m)}(\mu_1). \tag{4.17}$$

The full set of renormalization factors at 2 GeV, step scaling functions, and final value at 3 GeV are given in Appendix B.1 . We quote the final values at 3 GeV only in Table4.5.

scale	$\slashed{q}$-scheme		γ-scheme	
	Z_q^a [3 GeV]	Z_m^a [3 GeV]	Z_q^a [3 GeV]	Z_m^a [3 GeV]
a15	1.0450(58)	0.9280(58)	1.0218(57)	0.9476(50)
a12	1.0437(80)	0.9502(61)	1.0048(30)	0.9740(74)
a09	1.0342(41)	0.9767(63)	0.9995(39)	1.0076(59)

Table 4.5: Chiral limit values of the quark mass and wave function renormalization in $\slashed{q}$ and γ-schemes at $\mu = 3$ GeV.

4.4.4   Scalar, Pseudoscalar and Tensor

Figure 4.2b indicates that the scalar and pseudo-scalar factors should be roughly equal at high scales, however fitting each factor separately introduces a large fitting systematic due to the presence of the pion pole. To reduce the influence of this systematic, we fit the running of the scalar factor, as well as the ratio Λ_S/Λ_P, which has a well defined chiral limit. In practice this method reduces the fitting systematic, and gives better results for scalar and pseudo-scalar factors. The fit to Λ_S/Λ_P for the a12 ensemble is shown in Figure 4.6b, along with the accompanying fit to the scalar factor. After interpolation, we multiply by the scalar factor to recover Z_P. The analysis of the scalar, pseudo-scalar, and tensor factors then proceeds in a similar manner to the wave function renormalization.

scale	$\slashed{q}$-scheme			γ-scheme		
	Z_S^a	Z_P^a	Z_T^a	Z_S^a	Z_P^a	Z_T^a
a15	1.045(21)	1.073(31)	1.0043(64)	1.018(25)	1.052(34)	0.9871(61)
a12	1.035(20)	1.071(31)	1.0187(30)	1.001(24)	1.042(34)	0.9969(37)
a09	1.016(20)	1.041(30)	1.0360(28)	0.975(24)	1.004(32)	1.0074(44)

Table 4.6: Chiral limit values of the scalar, pseudo-scalar, and tensor renormalization factors in $\slashed{q}$ and γ-schemes at $\mu = 3$ GeV. The scalar and pseudo-scalar factors have an added fitting systematic.
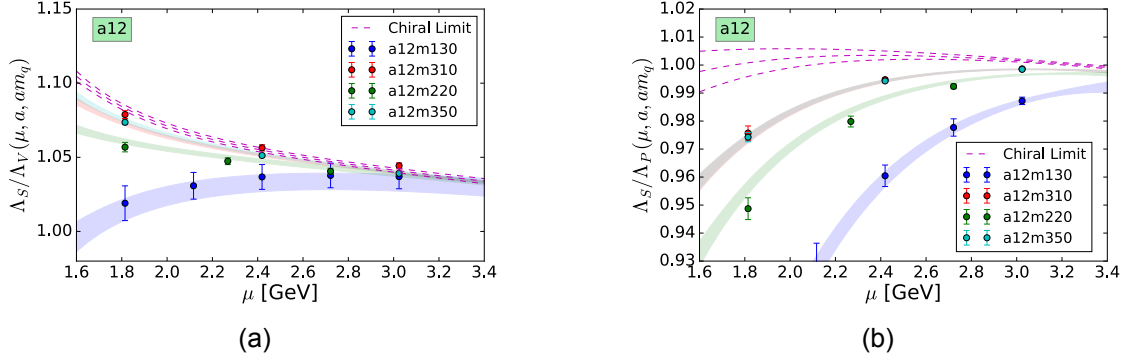
Figure 4.6: Reproduced data, and chiral limit, of the scalar renormalization factor and the ratio of the scalar and pseudo-scalar factors in the γ-scheme.

4.4.5 Systematics

The use of volume sources allows high statistical precision, using very few configurations due to averaging over the entire spacetime volume [150]. It is well known however, that physically expected properties, such as gauge invariance of observables, arise only under an average of gauge configurations [157]. This raises the question of whether we have sufficiently sampled enough configurations to converge to the true mean of the distribution. To answer this question, we compare the distribution of our most precisely determined quantity using 10 configurations, to the same quantity sampled from 100 configurations. We use the coarsest lattice spacing a $\sim .15$ fm, where we naively expect the greatest influence of discretization artifacts, and select a momentum within the range of interest 2 GeV $< \mu <$ 3 GeV. Figure 4.7a shows the distribution of Z_A/Z_V with 10 and 100 configurations, and shows no statistically significant difference after increasing our statistics by a factor of 10.

In non-Abelian gauge theories, it is well known that the Landau gauge fixing condition is incomplete [158, 159]. Given any Landau fixed gauge field $A_\mu(x)$, there is another $A'_\mu(x)$ which satisfies the same gauge fixing conditions $\partial_\mu A^a_\mu = \partial_\mu A'^a_\mu = 0$. The existence of these Gribov copies poses an additional systematic to any gauge fixed quantity, as each gauge fixed Monte Carlo sample may lie along a different gauge orbit [160]. This
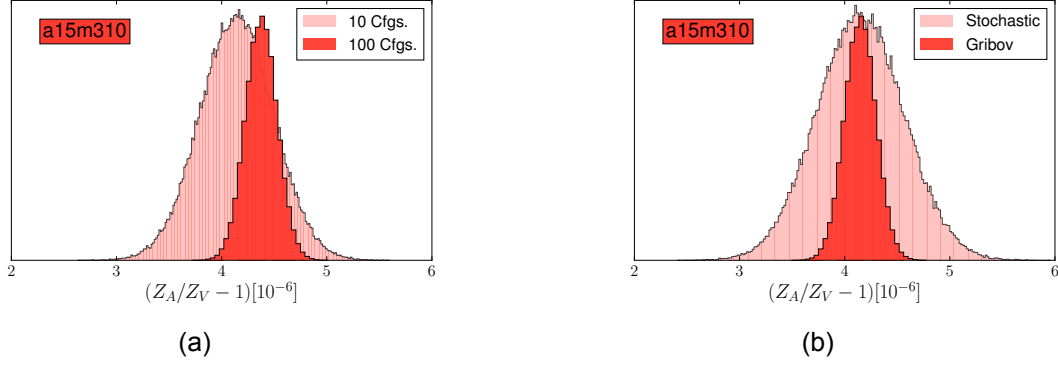
Figure 4.7: Gribov ambiguity, and statistical convergence, of Z_A/Z_V. The data is taken at a momentum ~ 3 GeV.

has sparked a number of innovations in order to try and control this problem, including expensive global optimization methods, new restricted actions, and the "mother-daughter" method [33, 161, 162].

The most economical solution is to generate Gribov copies using the mother-daughter method [33], where a random gauge transformation is first applied to our lattice gauge field

$$U_\mu(x) \to U'_\mu(x) = r(x)U_\mu(x)r^\dagger(x+\mu), \tag{4.18}$$

where $r(x) = e^{w(x)}$ and $w(x)$ is a (randomly generated) traceless anti-hermitian matrix. The new gauge field $U'_\mu(x)$ is then gauge fixed by finding the $g(x)$ that minimizes the functional

$$F[g] = \mathsf{Re}\{\sum_{x,\mu} \mathsf{tr}\Big[g(x)U_\mu(x)g^\dagger(x+\mu)\Big]\}. \tag{4.19}$$

We generate 50 such random perturbations for our smallest β lattice (coarsest lattice spacing), which is expected to have the largest density of Gribov copies [163]. The variance of the distribution of Gribov copies is observed to be sub dominant to Monte Carlo error for all renormalization factors considered at momenta of interest 4.7b. This agrees with similar studies done using different lattice discretizations [33, 164].

4.5 Four Quark Operators

At leading order in the EFT expansion, three processes contribute to $0\nu\beta\beta$ lepton number violation mediated by heavy physics: $\pi\pi ee$, $NN\pi ee$, and the $NNNNee$ contact interaction[165]. A subset of the induced quark-lepton operators (after integrating out the heavy physics) contributes to each of these processes, and is in general dependent on the type of underlying particle theory responsible for generating the low energy contact interactions [165]. In this work, we consider the parity even component of the quark-lepton operators that mix under renormalization of the $\pi\pi ee$ contact interaction. The resulting renormalized $\pi\pi ee$ operators first appeared in [137]. This basis is related via Fierz transformation[4] to a color diagonal basis

$$
\begin{aligned}
\mathcal{Q}_1 &= \left(\bar{u}\gamma^\mu\left(1-\gamma_5\right)d\right)\left[\bar{u}\gamma_\mu\left(1-\gamma_5\right)d\right] \\
\mathcal{Q}_2 &= \left(\bar{u}\gamma^\mu\left(1-\gamma_5\right)d\right)\left[\bar{u}\gamma_\mu\left(1+\gamma_5\right)d\right] \\
\mathcal{Q}_3 &= \left(\bar{u}\left(1-\gamma_5\right)d\right)\left[\bar{u}\left(1+\gamma_5\right)d\right] \\
\mathcal{Q}_4 &= \left(\bar{u}\left(1-\gamma_5\right)d\right)\left[\bar{u}\left(1-\gamma_5\right)d\right] \\
\mathcal{Q}_5 &= \frac{1}{4}\left(\bar{u}\sigma_{\mu\nu}\left(1-\gamma_5\right)d\right)\left[\bar{u}\sigma^{\mu\nu}\left(1-\gamma_5\right)d\right],
\end{aligned}
\tag{4.20}
$$

for which perform our renormalization, with the final color mixed answer of [137] found by applying the inverse transformation. The color diagonal basis has been used to renormalize BSM contributions to $K-\bar{K}$ mixing (with different flavor replacement in equation (4.20)), and the renormalization factors have been calculated on a number of lattice discretizations [140, 156, 166, 167]. Keeping only the parity even components of (4.20), we impose the SMOM conditions on our off shell Green's function

$$
V_i(\mu) = \langle\bar{u}(-p_1)d(p_2)|\,\mathcal{Q}_i(\mu)\,|u(p_1)\bar{d}(-p_2)\rangle,
\tag{4.21}
$$

with the kinematic configuration shown in 4.8a.

---

[4]See Appendix A.2.
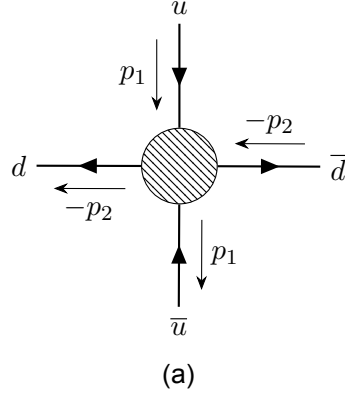
Figure 4.8: SMOM conditions for four quark vertex.

For each operator Q_i we construct the Green's function (we define $\tilde{x}_i = x_i - x$)

$$
\begin{aligned}
&[V_i(\mu)]^{\alpha\beta;\delta\gamma}_{ab;cd} \\
&= \sum_{x,x_1,x_2,\dots,x_4} \langle 0| \, u_a^\alpha(x_4) \bar{d}_b^\beta(x_3) \left[Q_i(x)\right] u_c^\delta(x_2) \bar{d}_d^\gamma(x_1) \, |0\rangle \, e^{-ip_1\cdot\tilde{x}_1 + ip_2\cdot\tilde{x}_2 - ip_1\cdot\tilde{x}_3 + ip_2\cdot\tilde{x}_4},
\end{aligned}
\tag{4.22}
$$

where the Greek indices denote spin and Roman denote color. Since this basis contains no color mixed components, the vertex factorizes into components (summing over $x_1, \dots, x_4$)

$$
\begin{aligned}
[V_i(\mu)]^{\alpha\beta;\delta\gamma}_{ab;cd} = \\
2\sum_x \langle \left[\bar{G}(x,p_2)\Gamma^1_{(i)}G(x,p_1)\right]^{\alpha\beta}_{ab} \left[\bar{G}(x,p_2)\Gamma^2_{(i)}G(x,p_1)\right]^{\delta\gamma}_{cd} \rangle \\
- 2\sum_x \langle \left[\bar{G}(x,p_2)\Gamma^1_{(i)}G(x,p_1)\right]^{\alpha\gamma}_{ad} \left[\bar{G}(x,p_2)\Gamma^2_{(i)}G(x,p_1)\right]^{\delta\beta}_{cb} \rangle,
\end{aligned}
\tag{4.23}
$$

where the $\Gamma^{1,2}_{(i)}$ depend on the spin and color structure of the given Q_i. For the parity even component of Q_1 for example, we have

$$
\left(\Gamma^1_{(1)}\right)^{\alpha\beta}_{ab} \otimes \left(\Gamma^2_{(1)}\right)^{\delta\gamma}_{cd} = (\gamma^\mu)^{\alpha\beta}\,\delta_{ab} \otimes (\gamma_\mu)^{\delta\gamma}\,\delta_{cd} + (\gamma^\mu\gamma_5)^{\alpha\beta}\,\delta_{ab} \otimes (\gamma_\mu\gamma_5)^{\delta\gamma}\,\delta_{cd}.
\tag{4.24}
$$

75

The amputated vertex is then constructed by amputating the external legs

$$(\Pi_i(\mu))_{\bar{a}\bar{b};\bar{c}\bar{d}}^{\bar{\alpha}\bar{\beta};\bar{\gamma}\bar{\delta}} = \langle \bar{G}^{-1}(p_2)_{\bar{a}a}^{\bar{\alpha}\alpha} \rangle \langle \bar{G}^{-1}(p_2)_{\bar{c}c}^{\bar{\gamma}\gamma} \rangle \, [V_i(\mu)]_{ab;cd}^{\alpha\beta;\delta\gamma} \, \langle G^{-1}(p_1)_{b\bar{b}}^{\beta\bar{\beta}} \rangle \langle G^{-1}(p_1)_{d\bar{d}}^{\delta\bar{\delta}} \rangle. \quad (4.25)$$

Renormalization conditions are imposed on the amputated projected vertex such that the renormalized amputated projected vertex equals it's tree level value at the SMOM kinematic point. Given a projection scheme $\mathcal{P}_j$ for operator j, the amputated projected vertex matrix element is defined to be

$$\Lambda_{ij}(\mu) = \mathcal{P}_j \Pi_i(\mu) = [\mathcal{P}_j]_{ab;cd}^{\alpha\beta;\delta\gamma} \, [\Pi_i(\mu)]_{ba;dc}^{\beta\alpha;\gamma\delta} \,. \quad (4.26)$$

The renormalization conditions then require at $q^2 = \mu^2$

$$\frac{Z(\mu)}{Z_q^2(\mu)} \Lambda(\mu) = F, \quad (4.27)$$

where F is the matrix of tree level values. We construct F using the tree level amputated vertex Π_i for operator i and projector $\mathcal{P}_j$ as

$$\mathcal{P}_j \Pi_i^{\text{tree}} = F_{ij}. \quad (4.28)$$

As in the case of the bilinear renormalization factors, we normalize our amputated projected vertices such that they equal the inverse of the renormalization factors, e.g

$$\Lambda \to \Lambda F^{-1}. \quad (4.29)$$

4.5.1 Projection Scheme

We use two projection schemes, one which uses the Lorentz structure of the operator itself to project out the correct spin and color components, and another which takes advantage of the non-zero momentum transfer afforded by the SMOM kinematics. We use

the appropriate vector bilinear projector for each scheme to remove the Z_q dependence, e.g. for the first we use the γ scheme Z_V/Z_q and the second we use $\slashed{q}$ scheme Z_V/Z_q. For the γ scheme, we use the projectors

$$[\mathcal{P}_1^\gamma]_{ab;cd}^{\alpha\beta;\delta\gamma} = (\gamma^\mu)^{\alpha\beta}\,\delta_{ab} \otimes (\gamma^\mu)^{\delta\gamma}\,\delta_{cd} + (\gamma^\mu\gamma_5)^{\alpha\beta}\,\delta_{ab} \otimes (\gamma^\mu\gamma_5)^{\delta\gamma}\,\delta_{cd}$$

$$[\mathcal{P}_2^\gamma]_{ab;cd}^{\alpha\beta;\delta\gamma} = (\gamma^\mu)^{\alpha\beta}\,\delta_{ab} \otimes (\gamma_\mu)^{\delta\gamma}\,\delta_{cd} - (\gamma^\mu\gamma_5)^{\alpha\beta}\,\delta_{ab} \otimes (\gamma_\mu\gamma_5)^{\delta\gamma}\,\delta_{cd}$$

$$[\mathcal{P}_3^\gamma]_{ab;cd}^{\alpha\beta;\delta\gamma} = \delta^{\alpha\beta}\delta_{ab} \otimes \delta^{\delta\gamma}\delta_{cd} - (\gamma_5)^{\alpha\beta}\,\delta_{ab} \otimes (\gamma_5)^{\delta\gamma}\,\delta_{cd} \tag{4.30}$$

$$[\mathcal{P}_4^\gamma]_{ab;cd}^{\alpha\beta;\delta\gamma} = \delta^{\alpha\beta}\delta_{ab} \otimes \delta^{\delta\gamma}\delta_{cd} + (\gamma_5)^{\alpha\beta}\,\delta_{ab} \otimes (\gamma_5)^{\delta\gamma}\,\delta_{cd}$$

$$[\mathcal{P}_5^\gamma]_{ab;cd}^{\alpha\beta;\delta\gamma} = \frac{1}{2}\,(\sigma^{\mu\nu})^{\alpha\beta}\,\delta_{ab} \otimes (\sigma^{\mu\nu})^{\delta\gamma}\,\delta_{cd}.$$

For the $\slashed{q}$ scheme, we follow reference [146], in defining the new projection operators via the replacement $\gamma_\mu \to \slashed{q}/q$. The $\slashed{q}$ scheme is then given by

$$\left[\mathcal{P}_1^{\slashed{q}}\right]_{ab;cd}^{\alpha\beta;\delta\gamma} = \frac{1}{q^2}\{(\slashed{q})^{\alpha\beta}\,\delta_{ab} \otimes (\slashed{q})^{\delta\gamma}\,\delta_{cd} + (\slashed{q}\gamma_5)^{\alpha\beta}\,\delta_{ab} \otimes (\slashed{q}\gamma_5)^{\delta\gamma}\,\delta_{cd}\}$$

$$\left[\mathcal{P}_2^{\slashed{q}}\right]_{ab;cd}^{\alpha\beta;\delta\gamma} = \frac{1}{q^2}\{(\slashed{q})^{\alpha\beta}\,\delta_{ab} \otimes (\slashed{q})^{\delta\gamma}\,\delta_{cd} - (\slashed{q}\gamma_5)^{\alpha\beta}\,\delta_{ab} \otimes (\slashed{q}\gamma_5)^{\delta\gamma}\,\delta_{cd}\}$$

$$\left[\mathcal{P}_3^{\slashed{q}}\right]_{ab;cd}^{\alpha\beta;\delta\gamma} = \frac{1}{q^2}\{(\slashed{q})^{\alpha\beta}\,\delta_{ad} \otimes (\slashed{q})^{\delta\gamma}\,\delta_{cb} - (\slashed{q}\gamma_5)^{\alpha\beta}\,\delta_{ad} \otimes (\slashed{q}\gamma_5)^{\delta\gamma}\,\delta_{cb}\} \tag{4.31}$$

$$\left[\mathcal{P}_4^{\slashed{q}}\right]_{ab;cd}^{\alpha\beta;\delta\gamma} = \frac{1}{p_1^2 p_2^2 - (p_1 \cdot p_2)^2}\{(p_1^\mu\,(\sigma^{\mu\nu}P_L)\,p_2^\nu)^{\alpha\beta}\,\delta_{ad} \otimes \left(p_1^\rho\left(\sigma^{\rho\psi}P_L\right)p_2^\psi\right)^{\delta\gamma}\,\delta_{cb}\}$$

$$\left[\mathcal{P}_5^{\slashed{q}}\right]_{ab;cd}^{\alpha\beta;\delta\gamma} = \frac{1}{p_1^2 p_2^2 - (p_1 \cdot p_2)^2}\{(p_1^\mu\,(\sigma^{\mu\nu}P_L)\,p_2^\nu)^{\alpha\beta}\,\delta_{ab} \otimes \left(p_1^\rho\left(\sigma^{\rho\psi}P_L\right)p_2^\psi\right)^{\delta\gamma}\,\delta_{cd}\},$$

where P_L is the usual left chiral projection operator $P_L = 1/2\,(1 - \gamma_5)$. Note that for $\left[\mathcal{P}_3^{\slashed{q}}\right]$ and $\left[\mathcal{P}_4^{\slashed{q}}\right]$, we Fierz rearranged the operators.

Having defined our projection operators, the tree level matrices F^γ and $F^{\slashed{q}}$ may be constructed by applying our projectors onto the tree level amputated projected vertices. The tree level amputated vertex is trivial

$$\Pi_{(i)}^{\text{tree}} = 2\left(\Gamma_{(i)}^1\right)_{ab}^{\alpha\beta} \otimes \left(\Gamma_{(i)}^2\right)_{cd}^{\delta\gamma} - 2\left(\Gamma_{(i)}^1\right)_{ad}^{\alpha\gamma} \otimes \left(\Gamma_{(i)}^2\right)_{cb}^{\delta\beta}, \tag{4.32}$$

which is found by inserting tree level propagators in the evaluation of (4.25). For the γ scheme with three colors, the tree level amputated projected yields

$$\frac{F^\gamma}{F_V^{\gamma 2}} = \frac{1}{48^2} \begin{pmatrix} 3072 & 0 & 0 & 0 & 0 \\ 0 & 2304 & -384 & 0 & 0 \\ 0 & -384 & 576 & 0 & 0 \\ 0 & 0 & 0 & 480 & 288 \\ 0 & 0 & 0 & 288 & 2016 \end{pmatrix}, \tag{4.33}$$

while for the $\not{q}$ scheme we find

$$\frac{F^{\not{q}}}{F_V^{\not{q}2}} = \frac{1}{12^2} \begin{pmatrix} 768 & 0 & 0 & 0 & 0 \\ 0 & 576 & 192 & 0 & 0 \\ 0 & -96 & -288 & 0 & 0 \\ 0 & 0 & 0 & 72 & 24 \\ 0 & 0 & 0 & 120 & 168 \end{pmatrix}. \tag{4.34}$$

The γ and $\not{q}$ tree level amputated projected vector vertex has been normalized to be 48 and 12 respectively.

The chiral mixing structure is dictated by the transformations of our operators under $SU(2)_L \times SU(2)_R$ (or $SU(3)_L \times SU(3)_R$ for BSM Kaon physics) [165]. If chiral symmetry is exact, then we expect $\mathcal{Q}_1$ to renormalize multiplicatively as an $(5,1) \oplus (1,5)$ under $SU(2)_L \times SU(2)_R$, while $\mathcal{Q}_2$ mixes with $\mathcal{Q}_3$ and $\mathcal{Q}_4$ mixes with $\mathcal{Q}_5$. Since chiral symmetry is well conserved on our lattices, we expect this mixing structure to be well approximated. We observe that the off block diagonal mixing elements (that should be zero if chiral symmetry is exact) are orders of magnitude smaller than the block diagonal elements, and extrapolate to zero when taking the chiral limit of our renormalization matrix. Chiral symmetry violating mixings may thus be safely ignored in the ensuing analysis.

4.5.2 Amputated Projected Fits and Step Scaling

The analysis of the four quark amputated projected vertices now mimics the bilinear analysis of section 4.4. We fit each matrix element using the fit ansatz (4.11) to interpolate each matrix element to a common scale μ. We then construct our step scaling matrix $\Sigma(\mu_2, \mu_1, a)$ according to equation (4.12) for each lattice spacing. The continuum step

scaling is then used to raise the scale of our renormalization matrix to 3 GeV. Plots show-
ing the fit of each matrix element are given in Appendix B.1, while 4.9 shows an example
step scaling parameterization and resulting continuum limit in both γ and $\not{q}$ schemes.
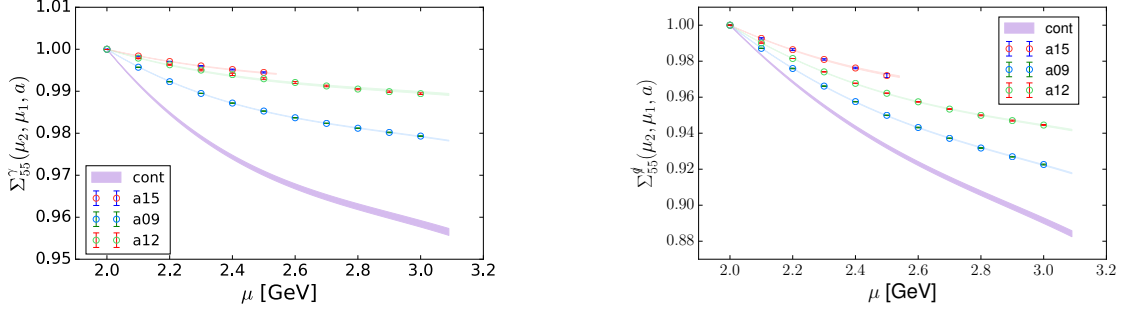
Figure 4.9: SMOM step scaling for matrix element Λ_{55}/Λ_V^2. The left most figure corre-
sponds to the γ scheme, while the right most plot gives the $\not{q}$ scheme.

To reduce bias, we average over two independent determinations of the renormaliza-
tion factors at 2 GeV. We check that the step scaling factors from 2 to 3 GeV derived using
the independent analyses agree within error. For the γ-scheme factors, we use two meth-
ods of constructing the continuum step scaling matrix. The first method parameterizes the
running and lattice spacing dependence of the three lattice step scaling matrices, while
the other takes the continuum limit momentum point by momentum point. We take half
the difference of the central values between the two continuum results as a systematic.
The averaged 2 GeV renormalization factors, step scaling matrix, and resulting 3 GeV
matrices are given in Appendix B.1.

Using the step scaling matrix, we raise the scale of our 2 GeV renormalization factors
to find

$$
Z^{\gamma,a15}(\mu = 3\,\text{GeV}) = \begin{pmatrix} 0.9408(63) & 0 & 0 & 0 & 0 \\ 0 & 0.9835(68) & 0.0212(30) & 0 & 0 \\ 0 & 0.0185(20) & 1.0519(81) & 0 & 0 \\ 0 & 0 & 0 & 1.037(11) & -0.0178(34) \\ 0 & 0 & 0 & -0.0115(83) & 0.9341(75) \end{pmatrix} \tag{4.35}
$$

$$
Z^{\gamma,a12}(\mu = 3\,\text{GeV}) = \begin{pmatrix} 0.9118(43) & 0 & 0 & 0 & 0 \\ 0 & 0.9535(48) & 0.0261(29)) & 0 & 0 \\ 0 & 0.0142(20) & 0.9922(61) & 0 & 0 \\ 0 & 0 & 0 & 0.9794(92) & -0.0137(34) \\ 0 & 0 & 0 & -0.0197(81) & 0.9132(60) \end{pmatrix} \tag{4.36}
$$

79

$$Z^{\gamma,a09}(\mu = 3\,\text{GeV}) = \begin{pmatrix} 0.9018(39) & 0 & 0 & 0 & 0 \\ 0 & 0.9483(44) & 0.0538(28) & 0 & 0 \\ 0 & 0.0118(20) & 0.9369(55) & 0 & 0 \\ 0 & 0 & 0 & 0.9321(86) & -0.0112(34) \\ 0 & 0 & 0 & -0.0470(78) & 0.9220(57) \end{pmatrix} \tag{4.37}$$

in the γ scheme. The procedure for transforming these renormalization matrices to the color mixed basis are given in Appendix A.2. The $\displaystyle{\not{q}}$ factors likewise may be constructed from (4.27) using the $\displaystyle{\not{q}}$ projectors (4.31).

$$Z^{\not{q},a15}(\mu = 3\,\text{GeV}) = \begin{pmatrix} 0.9620(61) & 0 & 0 & 0 & 0 \\ 0 & 0.9892(63) & 0.0219(33) & 0 & 0 \\ 0 & 0.0211(11) & 1.0886(74) & 0 & 0 \\ 0 & 0 & 0 & 1.0844(98) & -0.0174(14) \\ 0 & 0 & 0 & -0.0714(44) & 0.9897(66) \end{pmatrix} \tag{4.38}$$

$$Z^{\not{q},a12}(\mu = 3\,\text{GeV}) = \begin{pmatrix} 0.9345(43) & 0 & 0 & 0 & 0 \\ 0 & 0.9594(44) & 0.0272(32) & 0 & 0 \\ 0 & 0.0190(11) & 1.0394(54) & 0 & 0 \\ 0 & 0 & 0 & 1.0325(69) & -0.01736(54) \\ 0 & 0 & 0 & -0.0598(37) & 0.9684(48) \end{pmatrix} \tag{4.39}$$

$$Z^{\not{q},a09}(\mu = 3\,\text{GeV}) = \begin{pmatrix} 0.9304(38) & 0 & 0 & 0 & 0 \\ 0 & 0.9547(40) & 0.0531(31) & 0 & 0 \\ 0 & 0.0201(11) & 1.0016(48) & 0 & 0 \\ 0 & 0 & 0 & 1.0013(64) & -0.01530(46) \\ 0 & 0 & 0 & -0.0763(38) & 0.9900(45) \end{pmatrix} \tag{4.40}$$

4.5.3 Gribov Contamination

As in the case of the bilinear vertices, we investigate the influence of Gribov ambiguity on our four quark renormalization matrix. The results of our analysis are shown in Figure 4.10, for two different β at a physical momentum ~ 3 GeV. The Gribov ambiguity is sub-dominant to the Monte Carlo sampling error for all matrix elements.

4.6 Conclusion

We have computed for the first time the renormalization factors necessary to renormalize the operators $\{1, \gamma_5, \gamma_\mu, \gamma_\mu\gamma_5, \sigma_{\mu\nu}\}$ computed on the gradient flowed Domain Wall fermion on HISQ ensembles used in references [137, 138, 148, 149]. Renormalization matrices were also computed for the effective four quark operator basis induced by heavy physics contributions to $0\nu\beta\beta$. The axial and vector renormalization factors were used to renormalize the first percent level determination of the nucleon axial coupling [149], while the four
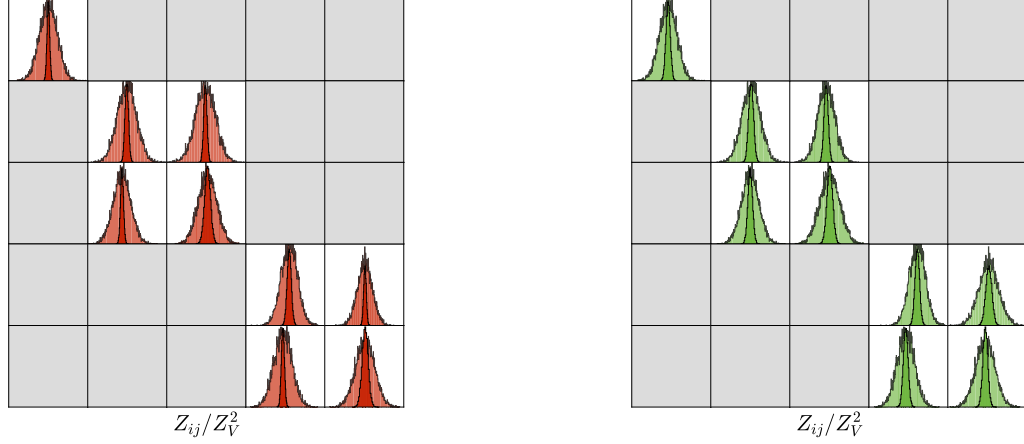
Figure 4.10: Relative widths of Gribov and Monte Carlo sampling distributions for a12m310 (green) and a15m310 (red) ensembles. The darker shade corresponds to the Gribov distribution, and the lighter to the Monte Carlo sample distribution.

quark renormalization matrices were necessary for the first LQCD calculation of hadronic matrix elements for short-range operators contributing to $0\nu\beta\beta$ [137]. These renormalization factors may be used to renormalize any matrix element in the above set, which uses the mixed action configuration detailed in [138] with t_{gf} = 1.0.

The renormalization factors of the axial and vector vertices, as well as the scalar and pseudoscalar, were found to be equal to a high degree at our renormalization scales of interest (2 to 3 GeV). These renormalization factors are predicted to be equal to each other by the chiral Ward-Takahashi identities [144], and the aforementioned agreement is indicative of the approximate restoration of chiral symmetry afforded by the combined use of the gradient flow and Möbius Domain Wall valence fermions. The use of local vector and axial vector currents, instead of the conserved versions [168], gives the vector and axial vector vertices a finite renormalization, however in our work the ratio still satisfies the Ward identity expectation, even if they are not formally related via Ward identities [169]. Likewise the four quark renormalization matrices exhibit good chiral symmetry by reproducing the expected block diagonal form. The off block diagonal components of our renormalization matrices are orders of magnitude smaller than the diagonal, and

extrapolate to zero in the chiral limit.

The step scaling procedure was used to compute the renormalization factors for our coarsest lattice spacing at an energy scale of 3 GeV [153]. This energy scale is beyond the upper limit of the "window condition" (4.2) for the coarsest a15 ensemble, however using the information from all three lattice spacings, we used the corresponding continuum limit of the running to raise the renormalization scale of our factors for all three lattice spacings simultaneously from 2 to 3 GeV. This allows us to use all three lattice spacings in our continuum extrapolation, while taking advantage of the reduced theoretical error in matching from RI to $\overline{\text{MS}}$ offered by the high matching scale.

Two sources of systematic error were investigated. To check whether we've sufficiently sampled our gauge fields to have converged on the true mean of the distribution, we computed the sample distributions of our renormalization factors for 10 configurations, and for 100 configurations. The two distributions are shown to be in almost perfect agreement, aside from a reduced width from the increased number of samples. The Gribov uncertainty due to our Landau gauge fixed conditions is also investigated. We take 50 samples of renormalization factors which were found after a random gauge transformations before gauge fixing in order to sample the space of equivalent minima of our gauge fixing functional. It was found that the Gribov uncertainty due to the Landau gauge fixed conditions was sub-dominant to statistical error in all cases.

The research presented in this chapter is being prepared for a publication to be submitted to Physical Review D.

Chapter 5

CPV Pion Nucleon Couplings

The work in this chapter is ongoing, and is extended from previously published ideas in [170–172].

5.1   Introduction

Permanent electric dipole moments (EDMs) of particles, nuclei, atoms and molecules provide stringent constraints on beyond Standard Model sources of $\mathcal{CP}$, and $\mathcal{T}$-violation. The Standard Model predictions for current EDMs of interest, the electron and neutron EDMs, arise from 3 or more loop processes involving a single $\mathcal{CP}$-violating phase in the CKM matrix[173]. In the case of the neutron EDM (nEDM), the predicted SM contribution is 6 orders of magnitude below current experimental upper limits [173, 174]. In extensions of the Standard Model, the nEDM can arise from one loop processes involving new $\mathcal{CP}$-violating interactions [175]. SUSY predictions of the nEDM for example, give an nEDM of $10^{-25} - 10^{-28}$ e-cm [174, 175], which is already constrained based on current experimental upper bounds. Planned experiments will reduce the current experimental upper bound of the neutron EDM, $|d_n| < 3 \times 10^{-26}$ e-cm, by up to two orders of magnitude over the next few years [23, 24], and could provide strong constraints on possible BSM sources of $\mathcal{CP}$-violation. A non-zero measurement of an EDM of the electron or neutron

in the next-generation of experiments will thus be an unambiguous signal of new physics. The interpretation of a non-zero measurement of an EDM is an outstanding theoretical challenge, with current theoretical calculations subject to order of magnitude or more uncertainties [175].

For the case of heavy BSM physics, effective field theory may be used to parameterize the effect of high energy BSM physics in terms of low-energy effective interactions, with the UV physics "hidden" in the low energy couplings (LECs) of the effective theory [1, 22, 176]. For the case of the nucleon electric dipole moment, BSM physics induces effective $\mathcal{CP}$-violating pion-nucleon interactions, whose strength is given by the $\mathcal{CP}$-violating pion-nucleon couplings $\bar{g}_i$ [177]. A direct calculation of the $\bar{g}_i$ couplings requires a solution of QCD in the low-energy (strong coupling) regime. Lattice QCD calculations in the presence of higher dimensional $\mathcal{CP}$-violating operators is untenable, as the additional operators are complex and the fermion sign problem becomes manifest [46, 48]. Instead, we exploit the chiral symmetry relation between the dimension 6 quark chromo-electric and quark chromo-magnetic operators, which relates the $\mathcal{CP}$-violating pion-nucleon couplings to spectroscopic shifts induced by the chromo-magnetic operators [170]. Such relations have been successful for the case of the $\bar{\theta}$-term, which relates the $\bar{\theta}$ term contribution to the isovector mass of the nucleon, and is free from large theoretical errors due to $SU(3)$ flavor breaking corrections through NNLO [130]. Likewise the chiral matching relations for $\bar{g}_0$ and $\bar{g}_1$ have been shown to be free from large theoretical errors through NNLO [170].

In this work, we use lattice QCD to compute the five spectroscopic quantities necessary to use our chiral matching conditions relating the $\mathcal{CP}$-violating pion-nucleon couplings to spectroscopic shifts in the nucleon and pion. We utilize the method of reference [172] to calculate the linear response of the pion and nucleon spectrum to the addition of our operators, which is simply the operator of interest inserted on the nucleon or pion. The calculation of the required matrix elements on the lattice has been of interest [178–186], however this is the first time they will be used in the matching relations relating nucleon spectroscopic shifts to the $\mathcal{CP}$-violating LECs $\bar{g}_i$. Given the large theoretical uncertain-

ties present in current calculations of these quantities [175], an $\mathcal{O}(20\%)$ determination of these couplings from lattice QCD would represent a significant improvement for the field.

5.2 Motivation

One of the Sakharov Conditions necessary for successful baryogenesis is the combined violation of $\mathcal{CP}$ symmetry [7]. Baryogenesis scenarios typically require new CP-violating physics to thaw at a scale above that of electroweak symmetry breaking. If these new physics processes involve the exchange of a heavy particle, e.g. Left-Right Symmetric models, Supersymmetry etc..., then this motivates an EFT description of BSM physics in terms of SM fields present at the electroweak scale. In this case, at the electroweak scale, the BSM physics induces effective higher dimensional operators composed of electroweak scale SM fields which are suppressed by powers of the BSM scale Λ_{BSM}. In addition to the SM CKM and $\bar{\theta}$ terms, the $\mathcal{CP}$-violating Lagrangian at the weak scale may be factored as[1]

$$\mathcal{L}_{CPV} = \mathcal{L}_{CKM} + \mathcal{L}_{\bar{\theta}} + \mathcal{L}_{CPV}^{eff}, \tag{5.1}$$

where

$$\mathcal{L}_{CPV}^{eff} = \frac{1}{\Lambda_{BSM}^2} \sum_i C_i^{(6)} \mathcal{O}_i^{(6)}. \tag{5.2}$$

The $C_i^{(6)}$ are Wilson coefficients for the dimension 6 operators which encode the UV physics of our full high energy theory, and must be calculated by matching onto the full theory. An exhaustive list of such operators to this order (excluding the neutrino sector) may be found in [175]. Since higher order terms beyond dimension 6 are suppressed by further powers of Λ_{BSM}, we expect that the leading order BSM induced operators at dimension 6 should give the dominant physics contributions at low energies. We may further match hadronic scale operators through the QCD scale ($\sim$ 1 GeV) via a set of low

---

[1]The only allowed dimension 5 operator consistent with SM symmetries is the neutrino mass term. The neutrino sector is also highly intriguing as a source of additional mechanisms for $\mathcal{CP}$-violation, but such considerations are beyond the scope of this work, see e.g. [12]. The next highest dimensional operators allowed are at dimension 6.

energy parameters (LECs) involving interactions of pions, nucleons, photons and electrons using Effective Field Theory. This process is represented diagrammatically for the chromo-electric and chromo-magnetic operators of interest in Figure 5.1a.
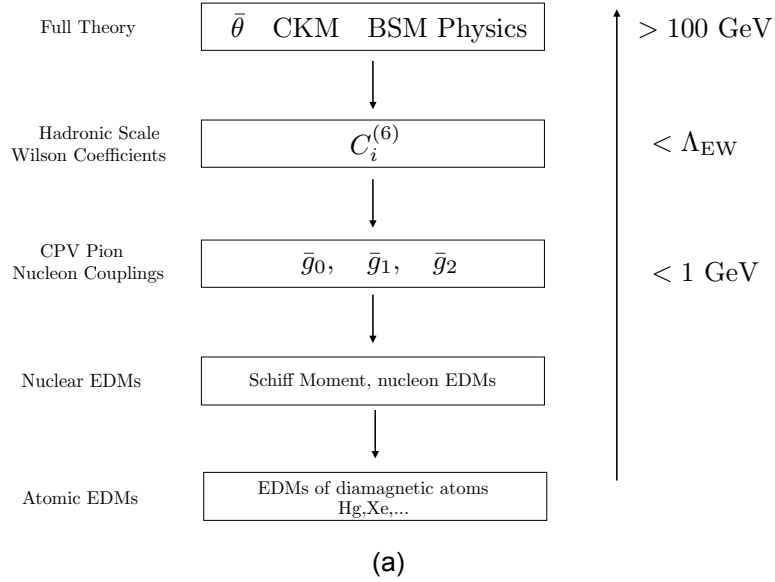
Full Theory	$\bar{\theta}$ CKM BSM Physics	> 100 GeV
Hadronic Scale Wilson Coefficients	$C_i^{(6)}$	$< \Lambda_{\mathrm{EW}}$
CPV Pion Nucleon Couplings	$\bar{g}_0,$ $\bar{g}_1,$ $\bar{g}_2$	< 1 GeV
Nuclear EDMs	Schiff Moment, nucleon EDMs	
Atomic EDMs	EDMs of diamagnetic atoms Hg,Xe,...	

(a)

Figure 5.1: At the electroweak scale BSM contributions are parameterized in terms of an EFT expansion of higher dimensional operators with theory dependent Wilson coefficients. For the case of the dimension 6 chromo-magnetic operator, the effective expansion below the hadronic scale produces $\mathcal{CP}$-violating pion nucleon interactions which may be enhanced in large diamagnetic nuclei due to the enhanced nuclear Schiff moment.

Noting the CPT Theorem [187], a physical system which is not invariant under $\mathcal{CP}$ should likewise be odd under time-reversal $\mathcal{T}$. If the induced $\mathcal{CP}$-violating operators contribute to interactions among SM particles, we expect these interactions to give rise to $\mathcal{T}$-violating physics. In the nucleon, $\mathcal{CP}$-violating interactions among quarks and gluons are expected to give rise to a $\mathcal{T}$-violating permanent electric dipole moment of the nucleon [174]. This is the low-energy consequence of the underlying high energy $\mathcal{CP}$-violating source shown in Figure 5.1a. In general, the EDM of particles and quantum systems have become a major focus of modern research for several reasons [23]:

1. EDMs provide a direct experimental probe of $\mathcal{CP}$-violation, which arises in the Stan-

dard Model (SM) and Beyond Standard Model (BSM) physics.

2. The $\mathcal{CP}$-violating and $\mathcal{T}$-violating interactions giving rise to the EDM may be cleanly distinguished from the large strong and electromagnetic backgrounds.

3. As discussed in the introduction, $\mathcal{CP}$-violation is a required condition for the baryon asymmetry of the universe. The SM contributions have been well documented and are orders of magnitude below current experimental bounds. The EDM thus provides a sensitive probe of BSM $\mathcal{CP}$-violating physics at the electroweak scale [173, 188].

In this work we focus on the permanent electric dipole moment of the nucleon, however the EDMs of other particles, such as the electron, are interesting for similar reasons [189].

Focusing on the quark chromo-magnetic (qCMDM) and quark chromo-electric (qCEDM) induced hadronic operators $\bar{q}\tilde{d}_{CM}\sigma^{\mu\nu}G_{\mu\nu}q$ and $\bar{q}\tilde{d}_{CE}i\gamma_5\sigma^{\mu\nu}G_{\mu\nu}q$, these operators induce $\mathcal{CP}$-violating interactions between nucleons and pions at the nuclear scale [170]

$$\mathcal{L} = \frac{\bar{g}_0}{2F_\pi}\bar{N}\vec{\tau}\cdot\vec{\pi}N - \frac{\bar{g}_1}{2F_\pi}\pi_0\bar{N}N - \frac{\bar{g}_2}{2F_\pi}\pi_0\bar{N}\tau^3 N + ... \tag{5.3}$$

$\bar{g}_i$ are the $\mathcal{CP}$-violating pion-nucleon couplings which depend on the hadronic scale couplings $\tilde{d}_{CM}$ and $\tilde{d}_{CE}$, and F_π is the pion decay constant. These pion-nucleon interactions lead to long-range $\mathcal{CP}$-violating contributions to the nucleon EDM [177].

At leading order, the EDM of a single nucleon contains contributions from short range operators which depend on the fundamental source of CP-violation [176]. These short range contributions are modified by long-range loop contributions induced by the $\mathcal{CP}$-violating pion-nucleon Lagrangian (5.3). These loop contributions, which depend on the CP-violating pion-nucleon couplings, cannot be separated from the short range contributions in a model independent manner [175]. Model dependent estimates of the short distance contributions exist, however they are subject to large theoretical uncertainties[175, 176]. Taken together, this implies that an experimental measurement of the EDM of a sin-

gle nucleon cannot give complete information about the underlying source of $\mathcal{CP}$-violation [175].

In diamagnetic atoms, such as ^{199}Hg, the unpaired neutron leads to an enhancement of the nuclear Schiff moment from both the EDM of the unpaired nucleon, as well as the long-range $\mathcal{CP}$-violating pion-nucleon interactions[23]. Indeed, the $\mathcal{T}$-odd pion-nucleon contributions dominate the EDMs of the constituent nuclei, making the computation of the CP-violating pion-nucleon interactions as important as those of the nucleon EDMs [170, 190]. Furthermore, nuclear and atomic structure calculations of ^{225}Ra indicate it may be orders of magnitude more sensitive to an EDM generated in the nucleus due to it's large octupole deformed nucleus and large atomic number [191–193]. Combining EDM measurements of the nucleon, with those of a large diamagnetic atom such as ^{225}Ra, presents the possibility for separating the fundamental sources of $\mathcal{CP}$-violation in the event of a non-zero nEDM measurement.

Another possibility, proposed in [194], is to use a combined measurement of the nucleon and light nuclei EDM to partially untangle the underlying source of $\mathcal{CP}$-violation. Investigating EDMs in light nuclei have an advantage over heavy nuclei in that there are rigorous theoretical tools for extracting analytical results, and the use of costly and theoretically error prone many body nuclear simulations may be avoided [176, 194]. Furthermore, calculations using EFT with non-perturbative operator product expansion (OPE), as well as perturbative meson exchange calculations, show that in the presence of a qCEDM the neutral pion exchange dominates the EDM of the deuteron [176, 194]. This implies that a deuteron EDM significantly larger than the nEDM signals the presence of the qCEDM contribution. Including EDM measurements of other light nuclei, such as the helion and triton, allows further information to be extracted by relative comparisons among the EDMs. For example, if the dominant contribution to the light nuclei EDMs comes from the quark

EDM, then the EDMs of the constituent nucleons dominate, and we expect [176]

$$d_{2_H} \sim d_n + d_p$$
$$d_{3_{He}} + d_{3_H} \sim 0.84(d_n + d_p) \tag{5.4}$$
$$d_{3_{He}} - d_{3_H} \sim 0.94(d_n - d_p).$$

The interpretation of an nEDM measurement relies on knowledge of the long-range pion-nucleon couplings in equation (5.3), which are fundamentally determined by QCD at low energies. Due to recent experimental advances, and increased computational resources, there has been a spike in lattice calculations of several $\mathcal{CP}$-violating sources contributing to the nEDM. For example, reference [195] calculated the $\mathcal{CP}$-odd form factor in the presence of the θ term and Weinberg three gluon operator [195], while references [183, 185] determined the qCEDM contribution to the $\mathcal{CP}$-violating form factor. Reference [68] used chiral symmetry to relate the isovector nucleon mass to the $\bar{g}_0$ contributions from the QCD $\bar{\theta}$-term. For a more thorough review of recent calculations, see reference [183].

Current information on the size of the $\mathcal{CP}$-violating pion-nucleon couplings come from chiral considerations/naive dimensional analysis, and QCD sum rules[175]. These values are subject to large theoretical errors, for example the predicted value for the isovector coupling $\bar{g}_1/F_\pi \sim 9$ - 62 [175]. It is an outstanding theoretical challenge to determine these couplings to the required precision to be useful in interpreting future nEDM measurements. Matching conditions exist, which relate the $\mathcal{CP}$-violating pion-nucleon couplings to simple spectroscopic CP-conserving quantities well suited to be computed on the lattice [170]. In the next section we review the relevant theory behind these matching relations, and afterwards discuss how their computation on the lattice was carried out.

5.3 Review of Chiral Matching Forms

The bulk of this section is a review of [170].

The most relevant higher dimensional operators induced by BSM physics are the quark electric dipole moments (qEDMs), the chromo-electric dipole moments (qCEDMs), the Weinberg three gluon operator, and several four quark operators. The chiral Lagrangian in $SU(2)$ accounting for the above dimension 6 operators was developed in reference [177]. In this work we focus on the qCEDM operators, as they are expected to give large contributions to the long-range CP-violating pion-nucleon interactions, and their computation is significantly easier than the other effective operators. Chiral symmetry considerations allow the qCEDM operators to be related to their CP-conserving qCMDM chiral partners. To that end, the most general hadronic scale Lagrangian including the $\bar{\theta}$-term, qCEDM and qCMDM operators is [170, 171]

$$
\begin{aligned}
\mathcal{L} =& \bar{q} i \slashed{D} q - \bar{q} M q + \bar{q} i \gamma_5 q m_* \left(\bar{\theta} - \bar{\theta}_{ind} \right) + r \bar{q} i \gamma_5 \tilde{d}_{CE} q \\
& - \frac{g_s}{2} \bar{q} \sigma^{\mu\nu} G_{\mu\nu} \left(\tilde{d}_{CM} + \tilde{d}_{CE} i \gamma_5 \right) q,
\end{aligned}
\tag{5.5}
$$

where $q = (u, d, s)$, $M = \text{diag}(m_u, m_d, m_s)$, $\bar{\theta}$ is the QCD theta term, and $\tilde{d}_{CE} = \left(\tilde{d}_u, \tilde{d}_d, \tilde{d}_s \right)$ and $\tilde{d}_{CM} = (\tilde{c}_u, \tilde{c}_d, \tilde{c}_s)$ are the quark chromo-electric and chromo-magnetic couplings[2]. The r parameter is the ratio of the vacuum condensates

$$
r = \frac{1}{2} \frac{\langle \Omega | \bar{q} g_s \sigma^{\mu\nu} G_{\mu\nu} q | \Omega \rangle}{\langle \Omega | \bar{q} q | \Omega \rangle}
\tag{5.6}
$$

and will be vital in determining the CP-violating couplings.

From (5.5) we see the dipole terms break chiral symmetry in the same pattern as the quark masses, and likewise induce non-derivative couplings to the pions in the low energy effective theory. The effect of these chiral symmetry breaking operators may be understood using spurion techniques, and requiring that the mass and dipole terms transform

---

[2]This is the Lagrangian that one arrives when the $\bar{\theta}$ term is rotated into a complex mass term using an anomalous $U(1)_A$ rotation and after vacuum alignment [170, 196]. The $\bar{\theta}_{ind}$ term is included to account for the possibility of the PQ mechanism.

as

$$M + i\left[m_*\left(\bar{\theta} - \bar{\theta}_{ind} \right) + r\tilde{d}_{CE} \right] \to R\left(M + i\left[m_*\left(\bar{\theta} - \bar{\theta}_{ind} \right) + r\tilde{d}_{CE} \right] \right) L^\dagger$$
$$\tilde{d}_{CM} - i\tilde{d}_{CE} \to R\left(\tilde{d}_{CM} - i\tilde{d}_{CE} \right) L^\dagger, \tag{5.7}$$

where R,L are elements of the $SU(N_f)_{L,R}$. Restricting ourselves to the two lightest flavors, we introduce the fields Σ and ξ

$$\Sigma = \xi^2 = \exp\left(\frac{i\phi}{F_0} \right), \tag{5.8}$$

which are the Σ and ξ fields of chapter 2 with a different convention for the pion decay constant ($F_\pi = f_\pi / \sqrt{2}$). Defining our spurion fields analogously to the mass term in χPT

$$\chi = 2B\left(M + i\left[m_*\left(\bar{\theta} - \bar{\theta}_{ind} \right) + r\tilde{d}_{CE} \right] \right)$$
$$\tilde{\chi} = 2\tilde{B}\left(\tilde{d}_{CM} - i\tilde{d}_{CE} \right) \tag{5.9}$$
$$\chi_\pm = \xi^\dagger \chi \xi^\dagger \pm \xi \chi^\dagger \xi \qquad\qquad \tilde{\chi}_\pm = \xi^\dagger \tilde{\chi} \xi^\dagger \pm \xi \tilde{\chi}^\dagger \xi,$$

one finds in analogy to the Gell-Mann-Oakes-Renner relation for the mass term, the new condensate $\tilde{B}$ is related to the mixed vacuum condensate

$$B = -\frac{\langle \Omega | \bar{q}q | \Omega \rangle}{F_0^2}$$
$$\tilde{B} = -\frac{\langle \Omega | \bar{q}g_s\sigma^{\mu\nu}G_{\mu\nu}q | \Omega \rangle}{2F_0^2}. \tag{5.10}$$

Denoting the traceless component of χ as $\chi_{t\!/\!r} = \left(\chi - \frac{1}{2}\,\text{tr}[\chi] \right)$, the LO spurion contributions are

$$\mathcal{L}_{\text{eff}}^\chi = \frac{F_0^2}{4}\left(\text{tr}\left[\Sigma^\dagger \chi + \Sigma \chi^\dagger \right] + \text{tr}\left[\Sigma^\dagger \tilde{\chi} + \Sigma \tilde{\chi}^\dagger \right] \right)$$
$$\left(c_1\,\text{tr}[\chi_+] + \tilde{C}_1\,\text{tr}[\tilde{\chi}_+] \right) \bar{N}N + \bar{N}\left(c_5\,[\chi_+]_{t\!/\!r} + \tilde{C}_5\,[\tilde{\chi}_+]_{t\!/\!r} \right) N, \tag{5.11}$$

where $]barN = (\bar{p}, \bar{n})$ is the nucleon doublet, and $c_1, \tilde{C}_1, c_5, \tilde{C}_5$ are unknown LECs. From (5.11) it's clear the qCMDM operators lead to shifts in the leading order pion and nucleon

masses proportional to the isoscalar and isovector qCMDM couplings $\tilde{c}_0$, $\tilde{c}_3$. One finds

$$m_\pi^2 = 2\left(B\bar{m} + \tilde{B}\tilde{c}_0\right)$$

$$\delta m_N = -8B\left(\bar{m}\epsilon c_5 - \tilde{c}_3 r \tilde{C}_5\right) \tag{5.12}$$

$$\Delta m_N = -8B\left(\bar{m}c_1 - \tilde{c}_0 r \tilde{C}_1\right),$$

where δm_N, Δm_N, and ϵ are the isovector nucleon mass $m_n - m_p$, nucleon mass shift $(m_n + m_p)/2 - m_N(m_\pi^2 = 0)$, and isovector quark mass $2\bar{m}\epsilon = m_d - m_u$.

Matching (5.11) onto the CP-violating pion-nucleon Lagrangian equation (5.3), the matching relations[3]

$$\bar{g}_0 = \tilde{d}_0\left(\frac{d}{d\tilde{c}_3} + r\frac{d}{d(\bar{m}\epsilon)}\right)\delta m_N$$

$$\tag{5.13}$$

$$\bar{g}_1 = -2\tilde{d}_3\left(\frac{d}{d\tilde{c}_0} - r\frac{d}{d\bar{m}}\right)\Delta m_N$$

emerge. These relations are not exact, but receive corrections at N²LO in chiral perturbation theory [170]. We may use the Feynman-Hellman theorem to evaluate our relations (5.13) in terms of our QCD Lagrangian equation (5.5), treating the higher dimensional terms as perturbations. The result is a relation between our CP-violating couplings and matrix elements of the nucleon

$$\bar{m}\epsilon\left(\frac{d}{d(\bar{m}\epsilon)}\delta m_N\right) = \bar{m}\epsilon\langle p|\,\bar{q}\tau^3 q\,|p\rangle$$

$$\bar{m}\left(\frac{d}{d\bar{m}}\Delta m_N\right) = \bar{m}\langle p|\,\bar{q}q\,|p\rangle$$

$$\tilde{d}_0\left(\frac{d}{d\tilde{c}_3}\delta m_N\right)\bigg|_{\tilde{c}_3=0} = \frac{\tilde{d}_0}{2}\langle p|\,g_s\bar{q}\sigma^{\mu\nu}G_{\mu\nu}\tau^3 q\,|p\rangle \tag{5.14}$$

$$\tilde{d}_3\left(\frac{d}{d\tilde{c}_0}\Delta m_N\right)\bigg|_{\tilde{c}_0=0} = \frac{\tilde{d}_3}{2}\langle p|\,g_s\bar{q}\sigma^{\mu\nu}G_{\mu\nu}q\,|p\rangle\,.$$

---

[3]If the PQ mechanism is absent, $\bar{g}_0$ receives an additive contribution proportional to $\bar{\theta} - \bar{\theta}_{\text{ind}}$.

5.4 Review of the Feynman-Hellmann Method for Calculating Matrix Elements

Formally, to use our relations (5.13), one must perform spectroscopic calculations of the nucleon mass shifts (5.12) in the background of our higher dimensional operators in (5.5), as well as nucleon sigma terms. To lowest order in the small source expansion, this is simply the linear response of our theory to the higher dimensional operators as perturbation. To perform this calculation on the lattice, we use the technique of [172] to calculate the linear response of our theory to the addition of our higher dimensional operators, which we review here.

In essence this corresponds to calculating our matrix element of interest summed over all spacetime insertion points. Due to this sum over insertion times, this method leads to an $\mathcal{O}(t)$ statistical improvement over sequential source methods[197, 198], and has been used in a high precision determination of the nucleon axial coupling [149]. We review the relevant details of this technique used in this work, as well as recently developed extensions that address certain shortcomings of the technique.

In continuum Euclidian field theory, a two point correlation function computed in the presence of an external current is given by

$$C_\lambda(t) = \langle\lambda|\,\mathcal{O}(t)\mathcal{O}^\dagger(0)\,|\lambda\rangle = \frac{1}{\mathcal{Z}_\lambda}\int \mathcal{D}[\Phi]e^{-S-S_\lambda}\mathcal{O}(t)\mathcal{O}^\dagger(0) \tag{5.15}$$

where Φ is shorthand for all fields in our theory, S_λ is an external source corresponding to a bilinear current density

$$S_\lambda = \lambda \int d^4x\, j(x), \tag{5.16}$$

and the partition function in the presence of our external source is

$$\mathcal{Z}_\lambda = \int \mathcal{D}[\Phi]e^{-S-S_\lambda}. \tag{5.17}$$

In the limit that the coupling λ goes to zero, our external source smoothly decouples from the theory, and we recover

$$C(t) = \lim_{\lambda \to 0} C_\lambda(t)$$

$$\mathcal{Z} = \lim_{\lambda \to 0} \mathcal{Z}_\lambda \qquad (5.18)$$

$$|\Omega\rangle = \lim_{\lambda \to 0} |\lambda\rangle \,.$$

In interpolating operator $\mathcal{O}^\dagger(0)$ creates a tower of states out of the vacuum at $t = 0$ with specified quantum numbers, and the $\mathcal{O}(t)$ destroys these states. Due to the finite size of our lattice, the correlation function (without our external source) may be spectrally decomposed as a finite temperature field theory

$$C(t) = \frac{1}{\mathcal{Z}} \int \mathcal{D}[\Phi] e^{-S} \mathcal{O}(t) \mathcal{O}^\dagger(0) = \frac{\sum_\beta \langle \beta| \, e^{-HT} \mathcal{O}(t) \mathcal{O}^\dagger(0) \, |\beta\rangle}{\sum_\beta \langle \beta| \, e^{-HT} \, |\beta\rangle}, \qquad (5.19)$$

where H is the Hamiltonian, β are eigenstates of the Hamiltonian, and the temporal extent of the lattice T plays the role of the inverse temperature. In the zero temperature and long Euclidian time limit, the ground state dominates the above spectral decomposition

$$\lim_{t \to \infty} C(t) = \frac{Z_0^0 Z_0^\dagger}{2E_0} e^{-E_0 t}, \qquad (5.20)$$

from which we may find our ground state energy from the effective mass

$$m_{\text{eff}}(t, \tau) = \frac{1}{\tau} \ln \left(\frac{C(t)}{C(t + \tau)} \right) \to \frac{E_0 \tau}{\tau}. \qquad (5.21)$$

This motivates looking at the linear response of the effective mass to a non-zero external source parameter[4] λ, in analogy to the Feynman-Hellmann Theorem

$$\frac{\partial}{\partial \lambda} m_\lambda^{\text{eff}}(t, \tau) \bigg|_{\lambda=0} = \frac{1}{\tau} \left(\frac{\partial_\lambda C_\lambda(t)}{C_\lambda(t)} - \frac{\partial_\lambda C_\lambda(t + \tau)}{C_\lambda(t + \tau)} \right) \bigg|_{\lambda=0}, \qquad (5.22)$$

---

[4]In this work a constant λ is used, though generalizations are possible.

94

where $\partial_\lambda C_\lambda(t)$ is found by applying the derivative at the level of the path integral

$$
\begin{aligned}
\frac{\partial}{\partial \lambda} C_\lambda(t)\bigg|_{\lambda=0} &= \frac{\partial}{\partial \lambda} \frac{1}{\mathcal{Z}_\lambda} \int \mathcal{D}[\Phi] e^{-S-S_\lambda} \mathcal{O}(t) \mathcal{O}^\dagger(0)\bigg|_{\lambda=0} \\
&= -\frac{\partial_\lambda \mathcal{Z}_\lambda}{\mathcal{Z}}\bigg|_{\lambda=0} C(t) + \frac{1}{\mathcal{Z}} \int \mathcal{D}[\Phi] e^{-S} \int d^4 x' j(x') \mathcal{O}(t) \mathcal{O}^\dagger(0) \qquad (5.23) \\
&= -C(t) \int dt' \langle \Omega | \mathcal{J}(t') | \Omega \rangle + \int dt' \langle \Omega | T\{\mathcal{O}(t) \mathcal{J}(t') \mathcal{O}^\dagger(0)\} | \Omega \rangle .
\end{aligned}
$$

Note that the first term corresponds to the vacuum expectation value (VEV) of our current, and is canceled in the derivative effective mass even for a non-zero VEV.

Applying the spectral decomposition in time-momentum space to the expression (5.23), and neglecting the VEV, we find four contributions (including contact terms) which may be parameterized as

$$
N(t) = \sum_n \left[(t-1) z_n g_{nn} z_n^\dagger + d_n \right] e^{-E_n t} + \sum_{n \neq m} z_n g_{nm} z_m^\dagger \frac{e^{-E_n t} e^{\frac{\Delta_{nm}}{2}} - e^{-E_m t} e^{-\frac{\Delta_{nm}}{2}}}{e^{-\frac{\Delta_{nm}}{2}} - e^{\frac{\Delta_{nm}}{2}}},
$$

$$(5.24)$$

where we've defined

$$
\begin{aligned}
z_n &\equiv \frac{Z_n}{\sqrt{2E_n}} \\
g_{nm} &\equiv \frac{\langle n | \mathcal{J}(0) | m \rangle}{\sqrt{4E_n E_m}}
\end{aligned}
\qquad (5.25)
$$

and d_n which contains the time independent contributions from outside our region of interest ($t < t' < 0$). This parameterization leads to the form

$$
C(t) = \sum_n z_n^0 z_n^\dagger e^{-E_n t} \qquad (5.26)
$$

for the two point function, which in combination with (5.24) above, may be used to fit the derivative effective mass

$$
\frac{\partial}{\partial \lambda} m_\lambda^{\text{eff}}(t, \tau)\bigg|_{\lambda=0} = \frac{1}{\tau} \left(\frac{N(t+\tau)}{C(t+\tau)} - \frac{N(t)}{C(t)} \right). \qquad (5.27)
$$

Using the spectral decompositions, it's easy to show that in the long time limit, the deriva-

tive effective mass (5.27) approaches our matrix element of interest

$$\left.\frac{\partial}{\partial\lambda}m_\lambda^{\text{eff}}(t,\tau)\right|_{\lambda=0} \xrightarrow[t\to\infty]{} g_{00}. \tag{5.28}$$

The signal of interest is linearly enhanced as the source-sink separation time t is increased, while excited states decay exponentially. Furthermore, the increase in statistics allows us to fit earlier in Euclidian time, which leads to a cleaner parameterization of excited state contamination. If one is interested in the matrix elements of nucleons, this enhancement leads to more usable data before the correlator signal is swamped by noise. For nucleons, the signal-to-noise of the two point correlator decays exponentially in time[5]

$$\frac{\text{S}}{\text{N}} \sim \frac{e^{-m_N t}}{\sqrt{e^{-3m_\pi t}}} = e^{-\left(m_N - \frac{3}{2}m_\pi\right)t}, \tag{5.29}$$

with the signal-to-noise decaying faster in Euclidian time as the chiral limit is approached[199, 200]. Through the advantages offered using this method, a fully controlled high precision calculation of the nucleon axial coupling g_A was performed with percent level uncertainty [148, 149].

For mesons, the above equations need modification. This is due to interference from the backwards propagating state, which becomes exponentially less suppressed as the Euclidian time approaches the temporal boundary[6]. One accounts for this by using a symmetric version of the effective mass which takes the backwards propagating state into account

$$m_{\text{cosh}}^{\text{eff}}(t,\tau) = \cosh^{-1}\left(\frac{C(t+\tau) + C(t-\tau)}{2C(t)}\right). \tag{5.30}$$

The linear response of $m_{\text{cosh}}^{\text{eff}}(t,\tau)$ to an external source gives the matrix element of interest

---

[5]Using similar arguments, when A nucleons are included in the correlation function, the signal to noise decays exponentially faster as $e^{-A\left(m_N - \frac{3}{2}m_\pi\right)t}$.

[6]In the limit of an infinite temporal length, or equivalently zero temperature, such states could not be thermally excited out of the vacuum and our meson interpolation operators would only produce the desired states.

in a symmetric form

$$\frac{\partial}{\partial\lambda}m_{\text{cosh},\lambda}^{\text{eff}}(t,\tau)\bigg|_{\lambda=0} = \frac{1}{\tau\sqrt{S^2(t,\tau) - 4C^2(t)}}\left(\partial_\lambda S_\lambda(t,\tau) - \frac{S(t,\tau)\partial_\lambda C_\lambda(t)}{C(t)}\right)\bigg|_{\lambda=0}$$

(5.31)

where

$$S(t,\tau) = C(t+\tau) + C(t-\tau).$$ (5.32)

The exact details of the spectral decomposition in the case of mesons will be given in a forthcoming publication [201].

For the case of a π^+ correlation function ($\mathcal{O}_{\pi^+}(x) = \bar{u}\gamma_5 d(x)$ creates a π^+ at x)

$$C_{\pi^+}(y,x) = \frac{1}{\mathcal{Z}}\int\mathcal{D}[\Phi]e^{-S}\bar{\mathcal{O}}_{\pi^+}(y)\mathcal{O}_{\pi^+}(x) = -\,\text{tr}[\gamma_5 S_u(y|x)\gamma_5 S_d(x|y)],$$ (5.33)

where $S_u(y|x)$ is the up quark propagator from x to y. Applying $\partial_\lambda C_\lambda(y,x)|_{\lambda=0}$ for an external current $j(x') = \bar{u}\Gamma u(x')$ at the level of the correlation function

$$\begin{aligned}
\frac{\partial}{\partial\lambda}C_{\pi^+}(y,x)\bigg|_{\lambda=0} &= \frac{1}{\mathcal{Z}}\int\mathcal{D}[\Phi]e^{-S}\bar{\mathcal{O}}_{\pi^+}(y)\int d^4x'\, j(x')\mathcal{O}_{\pi^+}(x) \\
&= -\sum_{x'}\text{tr}\left[\gamma_5 S_u(y|x')\Gamma S_u(x'|x)\gamma_5 S_d(x|y)\right] \\
&= -\,\text{tr}\left[\gamma_5 S_u^\Gamma(y|x)\gamma_5 S_d(x|y)\right],
\end{aligned}$$ (5.34)

we find the derivative correlation function is found by replacing one of our propagators $S_u(y|x)$ with a *Feynman-Hellmann* (FH) propagator $S_u^\Gamma(y|x)$ for the current Γ. This is shown graphically in 5.2a. The sum over all spacetime insertion points allows greater statistical accuracy per configuration compared to sequential source methods, however one must do an inversion for each matrix element (Γ) and each momentum desired. Once created however, the FH propagator may be used in any hadron correlation function one wishes to construct as the sink is fixed during the contraction phase exactly analogous to the two point function. We can avoid explicitly solving the anti-quark FH propagator off of the sink position so long as the anti-quark FH propagator is γ_5-hermitian (up to a sign), ie
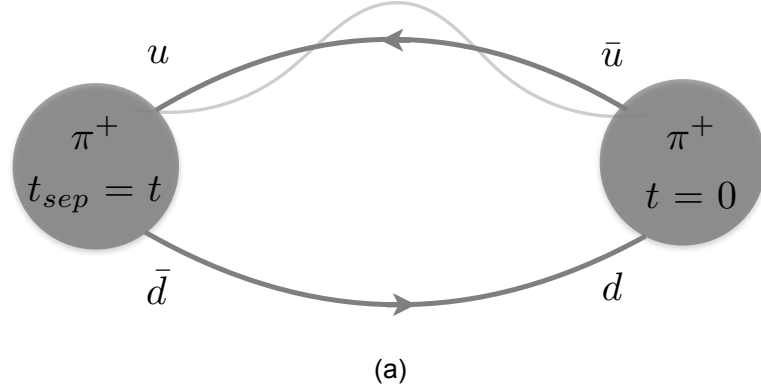
(a)

Figure 5.2: The derivative correlation function is constructed by replacing one our quark lines with a Feynman-Hellmann propagator (wavy line). For inserting on the u-quark in the π^+ the forward propagator becomes the FH propagator.

the quark propagator satisfies

$$\gamma_5 S \gamma_5 = S^\dagger. \tag{5.35}$$

5.4.1 Constructing the qCMDM

In order to calculate the isoscalar and isovector qCMDM operators, we construct the lattice gluon gauge field strength tensor $G_{\mu\nu}$ in the manner of [202, 203]. The lattice equivalent of $G_{\mu\nu}$ is constructed as the sum of 1×1 plaquettes

$$P_{\mu\nu} = \frac{1}{8} \sum_p [W_{p,\mu\nu} - W^\dagger_{p,\mu\nu}]_{tfr}, \tag{5.36}$$

with $W_{p,\mu\nu}$ defined in terms of the lattice link variables as [203]

$$
\begin{aligned}
W_1 &= U_\mu(x) U_\nu(x+\mu) U^\dagger_\mu(x+\nu) U^\dagger_\nu(x) \\
W_2 &= U_\nu(x) U^\dagger_\mu(x-\mu+\nu) U^\dagger_\nu(x-\mu) U_\mu(x-\mu) \\
W_3 &= U^\dagger_\mu(x-\mu) U^\dagger_\nu(x-\mu-\nu) U_\mu(x-\mu-\nu) U_\nu(x-\nu) \\
W_4 &= U^\dagger_\nu(x-\nu) U_\mu(x-\nu) U_\nu(x-\nu+\mu) U^\dagger_\mu(x).
\end{aligned}
\tag{5.37}
$$

98

We use the notation $[A]_{tr}$ to denote the traceless representation, e.g. for the case of SU(3) color $[A]_{tr} = A - (1/3)\,\mathrm{tr}_c(A)$. The plaquettes used in constructing $P_{\mu\nu}$ are shown in Figure 5.3a, and expressed in equation (5.37). To build the chromo-magnetic term, we
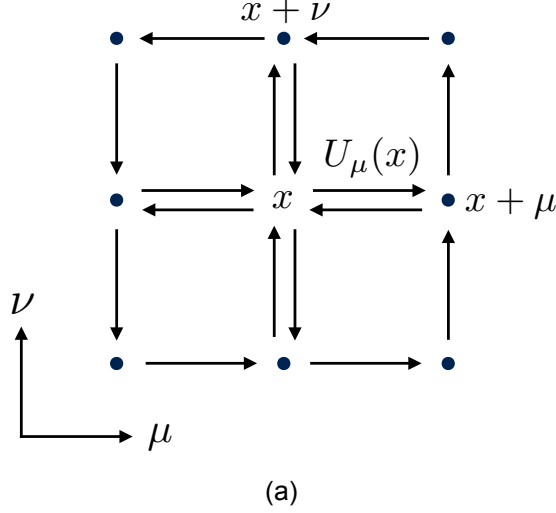

(a)

Figure 5.3: Lattice equivalent of the field strength tensor up to $\mathcal{O}(a^2)$ corrections. The sum of plaquettes localized about x yields the continuum field strength tensor in the limit $a \to 0$.

then contract the Lorentz indices of $P_{\mu\nu}$ with the Dirac tensor $\sigma^{\mu\nu}$ to construct a lattice object with spin and color components at each spacetime point. We use the standard lattice Dirac matrix conventions of the Degrand-Rossi basis, the details of which are in Appendix A.1.

The iso-vector qCMDM operator ($\tilde{c}_3$) is free from disconnected contributions, which cancel exactly in the isospin limit. The iso-scalar operator retains these contributions however, which must be computed as they are *a priori* large N_c suppressed, but should be computed for full control. The two types of contributions to the iso-scalar qCMDM matrix element in the nucleon is shown in Figure 5.4. The disconnected contributions contribute to the derivative effective mass through the derivative correlation function (5.23), and are summed over all possible quark loop positions correlated with the proton through the sea. The contributions between the source and sink are desired, while the rest are contam-

inations that are parameterized in the fitting procedure. We compute the disconnected contributions to the iso-scalar operators using the methods of section 5.5.1.
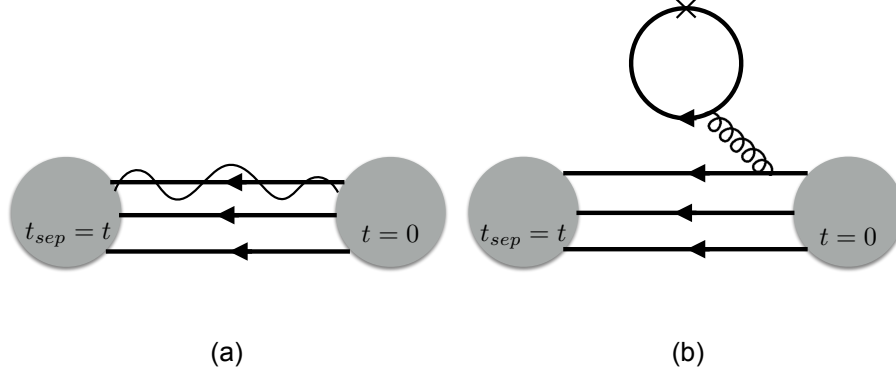

Figure 5.4: Connected and disconnected diagrams contributing to the qCMDM and scalar iso-scalar matrix elements. The connected contribution has the FH propagator replacing one of the quark lines, while the disconnected contribution is correlated with the nucleon through the sea. The cross denotes matrix element insertion.

$$t_{sep} = t \qquad\qquad t = 0$$

5.5 Bare Matrix Elements

Since gauge field generation is done independently of the construction of the correlation functions, see for example 2.12, the quark propagators $S(y|x)$ need not have the same pole mass as those used in generating the gauge fields. Even more exotic, the propagators used in the construction of correlation functions need not even be from the same discretization of the S_{QCD}^{E}. The use of a different discretization for the sea and valence fermions is motivated by the cost of computing gauge configurations. This *mixed action* (MA) setup must be used judiciously however, as choosing different discretized Dirac operators for the sea and valence quarks leads to the violation of unitarity and the Optical Theorem[204]. In this work we calculate static quantities using valence fermions which preserve chiral symmetry [7], which have been shown to give good results using a mixed

---

[7]We use Domain Wall Fermions, which formally has approximate chiral symmetry at finite fifth dimension L_5, however the chiral symmetry violating effects in this work are shown to be below statistical precision.

action setup [149, 205]. Furthermore our MA is tuned such that unitarity is recovered as $a \to 0$.

We use Möbius Domain Wall fermions[206–208] solved on the MILC Collaborations 2+1+1 flavor dynamical Highly Improved Staggered Quark (HISQ) ensembles (see also chapter 4) [209, 210]. The gauge configurations come in three different pion masses $m_\pi \sim \{130, 220, 310\}$ MeV, while two larger pion masses $m_\pi \sim \{350, 400\}$ MeV were generated by the CalLat collaboration to better control the pion mass dependence. The subset of ensembles used in this work are shown in Table 5.1, with plans to generate data further towards the chiral limit in the near future.

The HISQ action has leading order discretization effects starting at $(\alpha_S a^2, a^4)$ [211], while the multiple levels of smearing leads to a reduction in taste-symmetry[8] violations [210]. The gluons are simulated using a tadpole-improved, one-loop Symanzik improved gauge action, which has leading discretization errors starting at $(\alpha_S^2 a^2, a^4)$. If a valence action (used to construct correlation functions) is used that respects chiral symmetry, then the leading order discretization errors are at least $\mathcal{O}(a^2)$ [9]. Furthermore, a chiral valence action significantly suppresses chiral symmetry violation from the sea action, since the sea quark contributions occur at most at the loop level [148, 214].

HISQ gauge configuration parameters							valence parameters							
abbr.	N_{cfg}	volume	$\sim a$ [fm]	$\sim m_{\pi_5}$ [MeV]	m_l/m_s	$\sim m_{\pi_5} L$	N_{src}	L_5/a	aM_5	b_5	c_5	$am_l^{\text{val.}}$	σ_{smr}	N_{smr}
a15m400	1000	$16^3 \times 48$	0.15	400	0.334	4.8	8	12	1.3	1.5	0.5	0.0206	3.0	30
a15m350	1000	$16^3 \times 48$	0.15	350	0.255	4.2	16	12	1.3	1.5	0.5	0.0206	3.0	30
a15m310	1960	$16^3 \times 48$	0.15	310	0.2	3.8	8	12	1.3	1.5	0.5	0.01580	3.0	30
a12m400	1000	$24^3 \times 64$	0.12	400	0.334	5.8	8	8	1.2	1.25	0.25	0.02190	3.0	30
a12m310	1053	$24^3 \times 64$	0.12	310	0.2	4.5	8	8	1.2	1.25	0.25	0.01260	3.0	30
a09m400	1201	$32^3 \times 96$	0.09	400	0.2	4.5	8	6	1.1	1.25	0.25	0.0160	3.5	45
a09m310	784	$32^3 \times 96$	0.09	310	0.2	4.5	8	6	1.1	1.25	0.25	0.00951	7.5	167

Table 5.1: HISQ gauge configurations and valence sector parameters.

[8]In naively discretizing the fermion action, one creates not one fermion, but 16 degenerate fermion "doublers" corresponding to the extra poles in the fermion propagator at momenta of order $\mathcal{O}(\pi/a)$ [33]. In a discretization prescription which retains doublers, each fermion "flavor" has doubled versions called 'tastes'. A single hard gluon may induce interactions among different tastes, resulting in unphysical taste-symmetry violation [212]. The HISQ action uses layers of smearing to reduce these interactions [212, 213].

[9]This is because the only $\mathcal{O}(a)$ term that respects the symmetries of QCD is the clover term $\bar{q}\sigma^{\mu\nu}G_{\mu\nu}q$ which explicitly breaks chiral symmetry.

The Domain Wall action has a finite fifth dimension L_5, where the left and right chiral modes are bound to opposite ends of the fifth dimensional extent [215–217]. The gluon action is copied trivially on each fifth dimensional slice, and thus the fifth dimensional fermion term contains only kinetic contributions[138]. At finite L_5, the massive modes decay exponentially through the fifth dimension, however zero modes decay less benignly as a power law. This induces a residual chiral symmetry breaking m_{res}, which modifies the quark masses such that (for the light quarks) $m_q = m_l + m_{res}$ where m_l is the input light quark mass.

For values of the parameters $b_5 - c_5 = 1$, and $b_5 + c_5 \sim 2 - 4$, the Möbius formulation[10]

$$D^{\text{Möbius}}(M_5) = \frac{(b_5 + c_5)\, D^{\text{Wilson}}(M_5)}{2 + (b_5 - c_5)\, D^{\text{Wilson}}(M_5)} \equiv \alpha D^{\text{Shamir}}(M_5) \qquad (5.38)$$

leads to further suppression of the residual chiral symmetry breaking for fixed L_5 [208].

$$m_{\text{res}} \sim e^{-\alpha L_5}. \qquad (5.39)$$

To further reduce residual chiral symmetry breaking, we use the gradient flow algorithm to smooth the UV fluctuations of our gauge field. The gradient flow algorithm is a non-perturbative evolution of our fields towards the classical minimum of our gauge action as a function of a new parameter, the *flow time* [218, 219]. For the moderate flow time used in this work, $t_{gf} = 1.0$, it has been shown that the gradient flow highly suppresses the zero mode contributions to m_{res}, such that $m_{\text{res}} < 0.1 \times m_l^{\text{dwf}}$, while keeping the new gradient flow induced scale $l_{\text{gf}} \sim \sqrt{8t_{\text{gf}}}\, a$ small [138]. In addition to the gradient flow, we apply two types sink smearing to our quark propagators to optimize our signal.

We use the strategy of reference [172], and perform a simultaneous fit to our four correlation functions in a fully constrained manner[11]. The energy and overlap priors are

---

[10]We use the formulation of reference [208], though others are possible.

[11]Constrained curve fitting is well developed, and has been used in lattice QCD correlator analysis successfully, see e.g. [220, 221].

set using the two point function (5.26), while the d_n factors of (5.24) are found from the derivative correlation function at $t = 1$. We then simultaneously fit the two and three point functions, varying the minimum fit time t_{min} until a region of stability as a function of t_{min} and number of included states is found. We use the `lsqfit` Python package[222], which has built in capability for constrained and unconstrained fits, and has been successfully used in high precision analysis projects [149, 220].
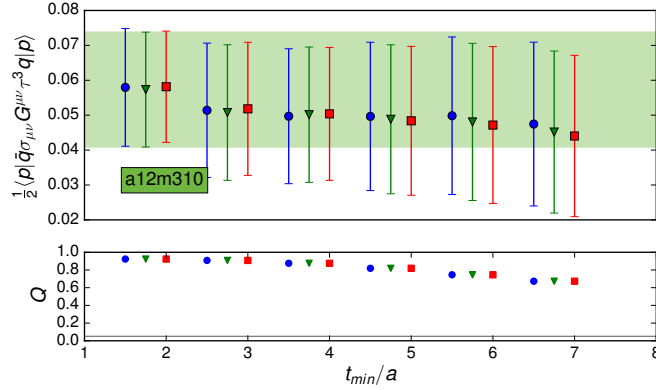
Figure 5.5: Stability analysis of the ground state matrix element as a function of smallest source sink separation time. The multi-colored points correspond to increasing number of states, which are displaced for clarity at each t_{min}. We only accept fits that are above the minimum Q-value cut of 0.05.

We fit the two iso-scalar and two iso-vector operators of equation (5.14) using the spectral decomposition (5.24). We use at least two exponentials, allowing us to further control excited state contamination that occurs at small source sink separation times, and pull our fit closer to the source. Several fits show stability at source sink separations as far back as $t_{\mathrm{min}} = 2$, allowing us to parameterize and remove the majority of the excited state contaminants. Dependence of our results on the maximum source sink separation is found to be much suppressed compared t_{min}, and the central values of the chosen constrained fits are found to agree within error of a two state unconstrained fit.

Figure 5.6 shows the results of our analysis procedure for the two and three point correlators. The fitted function reconstructs the data well (gray band through gray points), while the black and white points show that the multi-exponential fit removes the domi-
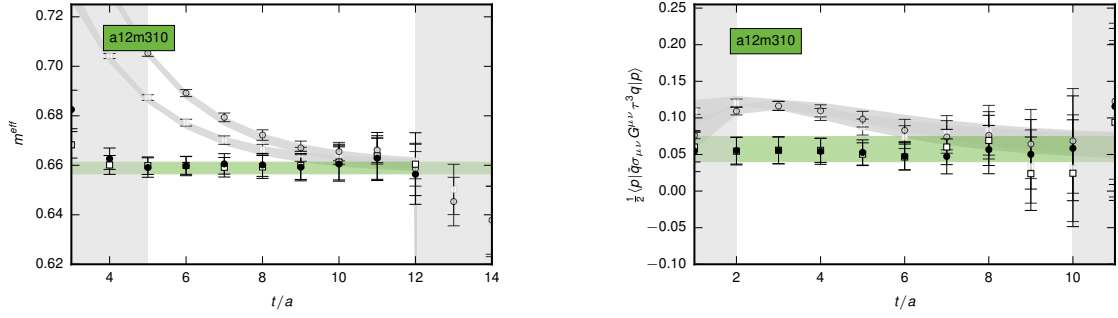
Figure 5.6: Correlation functions of the a12m310 two and three point functions. The gray data points are the raw correlation function data, while the gray bands are reconstructed data using the best fit parameters. The black and white data points correspond to the gray data after subtraction of the fitted excited state contributions. The colored band corresponds to the fitted ground state.

nant excited contamination. The ground state matrix element is then cleanly pulled from the resulting subtracted signal. Results for the bare matrix elements, as well as other parameters needed for the continuum and chiral extrapolation[12] are shown in Table 5.2.

ensemble	ϵ_π	$m_\pi L$	a/w_0	α_S	$\tilde{c}_3$	$\tilde{c}_0$	$\bar{m}\epsilon$	$\bar{m}$
a15m400	0.30374(53)	4.8451(49)	0.8804(3)	0.58801	0.019(14)	4.41(44)	0.466(31)	8.9(1.2)
a15m350	0.27411(50)	4.2359(47)	0.8804(3)	0.58801	-0.029(22)	5.05(47)	0.567(62)	9.9(1.9)
a15m310	0.24957(36)	3.7772(48)	0.8804(3)	0.58801	-0.087(32)	6.01(48)	0.233(56)	12.9(1.6)
a12m400	0.29841(52)	5.8428(39)	0.7036(5)	0.53796	0.087(11))	5.10(62)	0.590(33)	10.0(1.4)
a12m310	0.24485(50)	4.5282(41)	0.7036(5)	0.53796	0.065(15)	3.51(46)	0.519(55)	9.3(1.5)
a09m400	0.29818(53)	5.7965(46)	0.5105(3)	0.43356	0.1313(82)	2.99(46)	0.741(28)	9.6(1.1)
a09m310	0.24619(44)	4.5035(38)	0.5105(3)	0.43356	0.105(20)	2.68(84)	0.55(11)	9.4(1.5)

Table 5.2: Results for the bare matrix elements, as well as other parameters needed for the continuum and chiral extrapolation. We use the couplings to differentiate the various matrix elements, e.g. $\tilde{c}_3$ is the iso-vector qCMDM.

5.5.1 Calculation of the r Parameter

The r parameter of (5.13) is the ratio of two vacuum expectation values (5.6), which formally requires the trace of the all-to-all propagator with the insertion of our matrix elements

$$r = \frac{1}{2}\frac{\langle\Omega|\,\bar{q}\sigma^{\mu\nu}G_{\mu\nu}(x)\,|\Omega\rangle}{\langle\Omega|\,\bar{q}q\,|\Omega\rangle} = \frac{1}{2}\frac{\text{tr}[\sigma^{\mu\nu}G_{\mu\nu}(x)S_f(x|x)]}{\text{tr}[S_f(x|x)]}, \qquad (5.40)$$

---

[12]These quantities were determined in another work [149]

where $S_f = D_f^{-1}$ is the quark propagator for flavor f. On the lattice, direct calculation of the all-to-all propagator is prohibitively expensive, requiring $\mathcal{O}(N_c * N_s * V)$ inversions per gauge configuration. The prohibitive cost of computing the trace of the inverse of a large sparse matrix has motivated a large breadth of work dedicated to estimating the trace to a given precision, and has applications in many fields beyond lattice QCD [223–225]. We use the Monte Carlo method using $\mathbb{Z}_4$ noise ($\pm 1, \pm i$ uniformly distributed) to estimate (5.40), along with the Hierarchical Probing improvement [226, 227].

The basic Monte Carlo method is the Hutchinson Trace, which estimates the trace by averaging over matrix quadratures [228, 229] using random vectors $z_{(i)}$ which satisfy

$$
\begin{aligned}
\frac{1}{n} \sum_{i=1}^{n} \langle z_{(i)}(x) | z_{(i)}(x') \rangle &\approx \delta_{xx'} + \mathcal{O}\left(\frac{1}{\sqrt{n}}\right) \\
\frac{1}{n} \sum_{i=1}^{n} \left| z_{(i)}(x) \right\rangle &\approx \mathcal{O}\left(\frac{1}{\sqrt{n}}\right).
\end{aligned}
\tag{5.41}
$$

From each random vector we solve

$$
D^{\alpha a \beta b}(x, t | x', t') \phi_{(i)}^{\beta b}(x', t') = z_{(i)}^{\alpha a}(x, t)
\tag{5.42}
$$

to get our solution vector $\phi^{(i)}$ from which we construct our trace estimate

$$
\text{tr}\left[\Gamma D^{-1}\right] \approx \frac{1}{n} \sum_{i=1}^{n} z_{(i)}^{\dagger} \Gamma \phi_{(i)},
\tag{5.43}
$$

where the trace is over spin and color indices. To construct the r element above, we then sum over all spacetime to construct the full vacuum expectation value. If one is interested in disconnected contributions, we instead correlate the quark loop with the proton.

The Hierarchical Probing (HP) method is an improvement upon the basic MC algorithm above. The HP method generates reusable probing vectors that take advantage of the decay structure of a matrix (if it exists) in such a way that the convergence to the true trace is improved by removing the largest off diagonal elements. Since off-diagonal elements

are responsible for the variance in the trace estimation in (5.41), this method has been shown to significantly speed up the variance reduction in our trace estimator [226, 227]. Once the probing vectors have been generated, the method become stochastic, and the trace estimation proceeds similarly to (5.43).

The results of calculating the r element in the vacuum are shown in Figure 5.7. To maintain correlations with our connected matrix elements, we calculate the trace using 32 HP (or $\mathbb{Z}_4$) vectors per configuration. In the vacuum, the trace is determined very precisely as shown in the figure below.
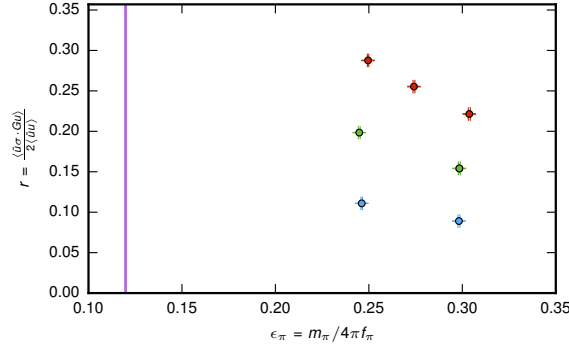
Figure 5.7: Bare (no renormalization) ratio of the vacuum expectation values of the quark chromo-magnetic operator and the quark scalar operator as a function of pion mass. The points are color coded based on ensemble, blue is a09, green is a12, and red is a15. The magenta band denotes the physical limit.

5.5.2 Improved Algorithms

The Feynman-Hellmann method as presented above suffers from the disadvantage that one needs to compute a propagator for every matrix element and momentum desired. For high precision single matrix element studies, the method offers an additional boost in statistics, and so the increased cost incurred by the inversions may be warranted. For studies that involve more than one matrix element, or if one wishes to investigate form factors which involve many momentum points, the method becomes prohibitively expensive. The cost can be mitigated using a new strategy, where we use the same noise vectors solved for computing the disconnected components and the r element tied together in

106

such a way that we construct an FH propagator. This allows one to generate new momenta and matrix elements for which the cost to scales roughly as that of performing a contraction.

$$\sum_i |z_i\rangle\langle z_i| \, \Gamma$$

$$\frac{1}{N}\sum_i^N |z_i\rangle\langle z_i| \approx 1$$

Sink

Source

Figure 5.8: Construction of the stochastic Feynman-Hellmann propagator from a noise basis. A Feynman-Hellmann source propagator is tied together with the stochastic propagators by insertion of a δ function.

The process is shown diagrammatically in Figure 5.8. The method relies on the averaging over noise vectors producing a resolution of the identity. The end result of the above contraction is an FH propagator that may be used to generate three point correlations in the usual manner. The stochastic FH method has been tested against the exact FH method for the matrix elements used in this work, with results generically following 5.9.
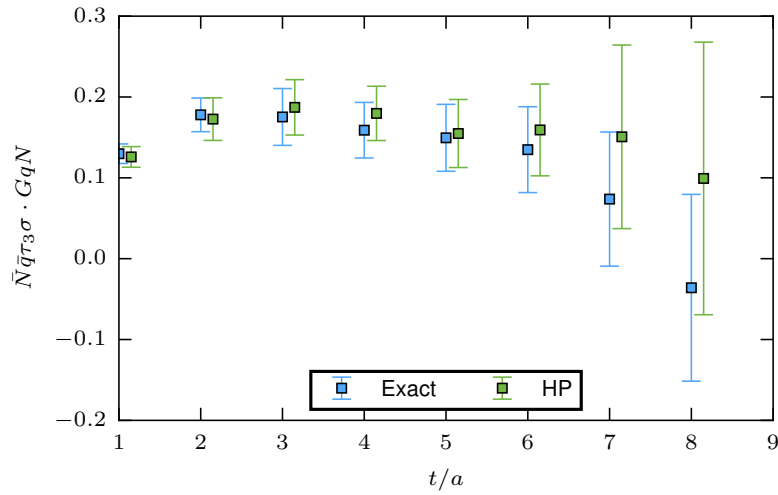
Figure 5.9: Comparison of stochastic FH method to exact FH method for the qCMDM iso-vector operator using 32 vectors each for 113 configurations.

We use the stochastic FH method to produce the scalar current insertions for the a12m400 ensemble.

5.6 Renormalization

This section is mostly derived from notes in conversation with Emanuele Mereghetti on the renormalization of the qCMDM operator. We are currently exploring two options in computing renormalization coefficients for the qCMDM (the scalar was determined in RI-SMOM in chapter 4).

On the lattice, if one uses a lattice discretization which respects chiral symmetry at finite lattice spacing[13], such as Domain Wall Fermions[208, 215–217] or Overlap Fermions[230–234] then there are no dimension-4 operators the qCMDM (or qCEDM) can mix with [235, 236].

If chiral symmetry is exact, and neglecting electromagnetic contributions, the qCMDM operator mixes with a number equal dimensional operators as well the dimension 3 scalar current. The minimal set of dimension 5 operators that mix with the qCMDM is given by

$$
\begin{align}
\mathcal{O}_1 &\equiv C = \bar{\psi}\sigma^{\mu\nu} g G_{\mu\nu} t^a \psi, \tag{5.44} \\
\mathcal{O}_2 &\equiv \partial^2 S = \partial^2 (\bar{\psi} t^a \psi), \tag{5.45} \\
\mathcal{O}_5 &\equiv mGG = \text{Tr}[\mathcal{M} t^a] G^b_{\mu\nu} G^{b\,\mu\nu}, \tag{5.46} \\
\mathcal{O}_8 &\equiv (m^2 S)_1 = \frac{1}{2}\bar{\psi}\left\{\mathcal{M}^2, t^a\right\}\psi, \tag{5.47} \\
\mathcal{O}_9 &\equiv (m^2 S)_2 = \text{Tr}[\mathcal{M}^2]\bar{\psi} t^a \psi, \tag{5.48} \\
\mathcal{O}_{10} &\equiv (m^2 S)_3 = \text{Tr}[\mathcal{M} t^a]\bar{\psi}\mathcal{M}\psi,, \tag{5.49}
\end{align}
$$

where we use the notation of [235]. If our renormalization pattern is determined in a gauge fixed renormalization scheme, such as the Rome-Southampton method, then there are

---

[13]Meaning that the Dirac operator satisfies the Ginsparg-Wilson equation which allows us to define chiral rotations on the lattice at finite a with the correct naive continuum limit.

additional dimension 5 operators allowed by the more general BRST symmetry. These operators vanish via the equations of motion, and thus we adopt the shorthand notation

$$\psi_E \equiv (iD^\mu\gamma_\mu - \mathcal{M})\psi\,, \qquad\qquad D_\mu = \partial_\mu - igA^a_\mu t^a \qquad (5.50)$$

$$\bar\psi_E \equiv -\bar\psi\,(i\overleftarrow{D}^\mu\gamma_\mu + \mathcal{M})\,, \qquad\qquad \overleftarrow{D}_\mu = \overleftarrow{\partial}_\mu + igA^a_\mu t^a\,. \qquad (5.51)$$

where $\mathcal{M} = \mathrm{diag}(m_u, m_d, m_s)$ is the quark mass matrix. The "nuisance" operators allowed by BRST symmetry are given by

$$\mathcal{O}_{11} \equiv S_{EE} = \bar\psi_E t^a \psi_E, \qquad\qquad (5.52)$$

$$\mathcal{O}_{12} \equiv (\partial \cdot V)_E = i\partial_\mu \left(\bar\psi\gamma^\mu t^a\psi_E - \bar\psi_E t^a\gamma^\mu\psi\right), \qquad\qquad (5.53)$$

$$\mathcal{O}_{13} \equiv V_\partial = \bar\psi t^a(i\overrightarrow{\partial})\psi_E + \bar\psi_E(-i\overleftarrow{\partial})t^a\psi, \qquad\qquad (5.54)$$

$$\mathcal{O}_{15} \equiv (mS_E)_1 = \frac{1}{2}\left(\bar\psi\left\{\mathcal{M}, t^a\right\}\psi_E + \bar\psi_E\left\{\mathcal{M}, t^a\right\}\psi_E\right), \qquad\qquad (5.55)$$

$$\mathcal{O}_{16} \equiv (mS_E)_2 = \mathrm{Tr}[\mathcal{M}t^a]\left(\bar\psi\psi_E + \bar\psi_E\psi\right), \qquad\qquad (5.56)$$

$$\mathcal{O}_{17} \equiv (mDG) = \mathrm{Tr}[\mathcal{M}t^a]\left(D^{bc}_\mu G^b_{\mu\nu}\right)A^{\nu c}. \qquad\qquad (5.57)$$

In addition to the above operators, the lattice qCMDM operator has a power divergent mixing with the dimension 3 operator $\mathcal{O}^{(3)} \equiv S = \bar{q}t^a q$. Defining the subtracted qCMDM operator above as $C \equiv C_L - Z^{53}S_L$, we must first determine Z^{53} on the lattice and subtract off the divergence before any continuum limit is taken.

The bare operator is related to the renormalized in a given scheme via

$$\mathcal{O}^{(0)}_i = Z_{ij}\mathcal{O}_j, \qquad\qquad (5.58)$$

where the bare operator is denoted $\mathcal{O}^{(0)}_i$. The renormalized operators are then found by taking the inverse of our matrix $Z^{-1}_{ij}\mathcal{O}^{(0)}_j = \mathcal{O}_i$. The mixing structure of our operators is given in Table 5.3. Note that many of the operators in our basis have mixings proportional to the quark mass, and thus small. This may allow one to truncate the basis if the

neglected terms are small compared to the statistical precision of our calculation. The renormalization conditions for our operators have been determined in the modified RI-SMOM conditions of reference [235], as well as the one-loop conversion coefficients to $\overline{\text{M}S}$.

	C	$\partial^2 S$	mGG	$(m^2S)_1$	$(m^2S)_2$	$(m^2S)_3$	S_{EE}	$\partial \cdot V_E$	V_∂	$(mS_E)_1$	$(mS_E)_2$	(mDG)
C	X	X	X	X	X	X	X	X	X	X	X	X
$\partial^2 S$		X										
mGG			X			X				X	X	X
$(m^2S)_1$				X								
$(m^2S)_2$					X							
$(m^2S)_3$						X						
S_{EE}							X	X	X	X	X	X
$\partial \cdot V_E$							X	X	X	X	X	X
V_∂							X	X	X	X	X	X
$(mS_E)_1$							X	X	X	X	X	X
$(mS_E)_2$							X	X	X	X	X	X
(mDG)							X	X	X	X	X	X

Table 5.3: Mixing structure of the dimension-5 operators, with "x" representing non-zero entries.

Alternatively, to avoid the "nuisance" operators in the gauge fixed scheme, we are investigating the gauge invariant "X-Space" renormalization scheme of [237–239]. This scheme imposes renormalization conditions on correlation functions of flavor non-singlet quark bilinears of the form

$$\langle \mathcal{O}_\Gamma(x)\mathcal{O}_\Gamma(0)\rangle \tag{5.59}$$

where

$$\mathcal{O}_\Gamma(x) = \bar{q}\Gamma q(x) \tag{5.60}$$

and Γ is one of the 16 Dirac γ matrices. The renormalization conditions of reference

[237, 239] impose non-perturbatively, in coordinate space and in the chiral limit

$$\lim_{a\to 0}\langle\mathcal{O}_\Gamma(x)\mathcal{O}_\Gamma(0)\rangle\bigg|_{x^2=x_0^2} = \langle\mathcal{O}_\Gamma(x_0)\mathcal{O}_\Gamma(0)\rangle^{\text{free}}_{\text{cont}},\tag{5.61}$$

such that the renormalized operator is $\mathcal{O}_\Gamma(x, x_0) = Z_\Gamma(x_0)\mathcal{O}_\Gamma(x)$ at the renormalization point x_0. The renormalization point x_0 naturally must satisfy the window condition

$$a << x_0 << \Lambda_{QCD}^{-1}\tag{5.62}$$

to keep discretization and non-perturbative effects small. The renormalization scale is then naturally defined as

$$\mu = \frac{1}{\sqrt{x_0^2}}.\tag{5.63}$$

This method has been used to renormalize the standard bilinear operators on a number of lattice discretizations including Möbius Domain wall [240, 241], and comparisons to other renormalization schemes have found good agreement [239]. Furthermore, the generalization of the step scaling procedure is straightforward, and has been done in [242, 243]. We pick a single lattice direction in position space x (or average over equivalent directions giving the same $|x^2|$) and then vary the magnitude of the vector to raise the renormalization scale. The running from a low to high scale is then found to be [243]

$$\sigma_\Gamma[\mu_2, \mu_1] = \sigma_\Gamma[x_0, nx_0] = \lim_{a\to 0}\Sigma_\Gamma(x_0, nx_0) = \frac{Z_\Gamma(x_0, a)}{Z_\Gamma(nx_0, a)}.\tag{5.64}$$

The renormalization conditions of (5.61) will not work for qCMDM operator, as the field strength is zero in free field. We propose a modification to the renormalization conditions, such that our correlation function, in coordinate space and in the chiral limit, equals it's tree level value at the renormalization point x_0.

$$\lim_{a\to 0}\langle\mathcal{O}_\Gamma(x)\mathcal{O}_\Gamma(0)\rangle\bigg|_{x^2=x_0^2} = \langle\mathcal{O}_\Gamma(x_0)\mathcal{O}_\Gamma(0)\rangle^{\text{tree}}_{\text{cont}}\tag{5.65}$$

111

This condition is similar in flavor to the RI-SMOM conditions, and in principle allows the composite bilinear $\bar{q}\sigma_{\mu\nu}G^{\mu\nu}q(x)$ to be renormalized using this method. To use this modification, one must compute the tree level correlation function in position space, which for the scalar current is one-loop, but for the qCMDM is a two-loop calculation. The computation of the scalar current is already known in the literature [244], and plans are underway to calculate the two-loop qCMDM current.

Considering just the qCMDM and scalar current, this method generates a matrix of correlation functions

$$\mathcal{O}(x) = \begin{pmatrix} \langle \mathcal{O}_C(x)\mathcal{O}_C(0) \rangle & \langle \mathcal{O}_C(x)\mathcal{O}_S(0) \rangle \\ \langle \mathcal{O}_S(x)\mathcal{O}_C(0) \rangle & \langle \mathcal{O}_S(x)\mathcal{O}_S(0) \rangle \end{pmatrix} \tag{5.66}$$

from which our divergent mixing may be removed after applying our renormalization conditions (5.65). Code has been written to compute the matrix of correlators, and preliminary data has been generated.

5.7 Remaining Work

Though considerable progress has been made, the work is incomplete until the following are complete:

- The bare matrix elements of the qCMDM and scalar operator are renormalized to a common scale μ for each lattice spacing. This includes removing the power divergent mixing of the qCMDM with the scalar. Code has been written, and data generated, for the X-Space renormalization scheme above that awaits analysis.

- A chiral and continuum extrapolation is performed to extract physical results. The theoretical forms enabling the chiral continuum extrapolation have been determined in [170], and can be applied after renormalization.

5.8 Conclusion

The search for the nEDM is an active experimental and theoretical field, with great potential for constraining BSM models in the next decade. Current null-measurements have already constrained SUSY predictions for the nEDM [175, 183], while future experiments will reduce increase experimental sensitivity by up to two orders of magnitude in the near future[23]. Interpretation of a future non-zero nEDM measurement relies on constraining the possible CP-violating sources which contribute to the nEDM. Several methods have been proposed, which use concurrent measurements of the nEDM as well as the EDM of light or heavy nuclei, to isolate possible BSM contributions [23, 176, 194]. In addition to short-range contributions, the EDMs of the neutron and nuclei contain (possibly dominant) contributions from long-range CP-violating pion-nucleon interactions, whose couplings are determined by QCD in the low-energy regime [175]. Current theoretical knowledge of the CP-violating couplings comes from chiral symmetry/naive dimensional analysis and QCD sum rules, and is subject to large theoretical uncertainties [175]. Given the present level of theoretical uncertainty, a determination of these couplings to the $\mathcal{O}(20\%)$ level would be an advance for the field.

Under constraints from chiral symmetry, the CP-violating pion-nucleon couplings are related to spectroscopic shifts of the pion and nucleon masses induced by the CP-conserving quark chromo-magnetic operators [170]. In this work, we show progress towards the first determination of the CP-violating pion-nucleon couplings $\bar{g}_0$ and $\bar{g}_1$ from lattice QCD. We used the linear response of the effective mass to the addition of our CP-conserving operators (5.14) to precisely calculate the four matrix elements in the nucleon, including disconnected diagrams. These operators show good signal in the nucleon, however the qCMDM suffers from a power divergent mixing with the quark scalar operator. It is expected, from the form of the chiral matching relations equation (5.13), that this power divergence is approximately canceled when taking the appropriate combination of terms [170]. Preliminary calculations show a possible reduction in the power divergence for the

bar $\bar{g}_0$ and $\bar{g}_1$ terms, however proper renormalization, including removing the power divergent mixing, is needed to confirm these expectations. Assuming all correlations are maintained after renormalization, an extraction of our pion-nucleon coupling to $\mathcal{O}(20\%)$ will be possible.

A non-trivial amount of time was devoted to the development of code `Lalibe` used to run these calculations, which will become publicly available with the next year. We also extended the work of reference [172] to include the linear response of the meson spectrum to the addition of a bilinear source, which will appear in a subsequent publication [201], and will be used to test certain expectations from the soft-pion theorem relating matrix elements in the vacuum to those in the pion [170]. Lastly, code has been written to perform the X-space renormalization necessary to properly renormalize the qCMDM operator, and theoretical matching calculations are under way.

Chapter 6

Concluding Remarks

Experimental tests of the Standard Model are reaching a precision in which they are probing beyond Standard Model parameter spaces [23]. Increasingly precise experimental tests of the Standard Model (SM) require a concurrent theoretical push to provide ever more precise predictions to interpret experimental results. For example, future direct dark matter detection experiments [245, 246], searches for Majorana neutrinos [247–249], and nEDM searches [250–252], all require a fundamental understanding of nuclear physics in the low-energy regime. Nuclear physics emerges from *non-perturbative* dynamics of the fundamental theory of the strong interaction, QCD, at low energies [253]. Lattice QCD is currently our best solution to QCD in the low-energy regime, and coupled with effective field theory, can be used to provide precise physical predictions from QCD. In this thesis, we focused on lattice calculations which have implications for precision tests of the Standard Model.

In chapter 3, we used precise spectroscopic calculations of the baryon spectrum in the presence of strong isospin breaking ($2\delta = (m_d - m_u) \neq 0$) to extract the quark mass difference contribution to the neutron-proton mass splitting from lattice QCD. The physical value of the neutron-proton mass splitting is the result of competition between the electromagnetic and strong contributions, and thus a precise determination from QCD is necessary to cleanly separate the two (or more) contributions[6]. What's more, the observed

primordial abundance of helium in the universe is exquisitely sensitive to $\delta m_N = m_n - m_p$, and thus sensitive to the amount of isospin breaking in the SM. A precise prediction of this quantity from the SM would contribute to an excellent test of our understanding of Nature, as our big-bang nucleosynthesis models are sensitive to every known physical interaction [6]. We also observe strong evidence of non-analytic behavior in the baryon spectrum, which is a unique feature of the low-energy effective field theories describing pions and nucleons [54]. This lends support to our understanding of low-energy QCD. Through chiral matching conditions, which relate the neutron-proton mass splitting to the $\mathcal{CP}$-violating pion-nucleon coupling arising from a non-zero $\bar{\theta}$-term, we find an estimate for the pion-nucleon coupling $\frac{\bar{g}_0}{\sqrt{2}f_\pi} = (14.7 \pm 1.8 \pm 1.4) \cdot 10^{-3}\,\bar{\theta}$, and the derivative of the $\mathcal{CP}$-violating form factor $S_n = (0.69 \pm 0.08) \cdot 10^{-4}\,\bar{\theta}\,e\,\mathsf{fm}^3$.

Chapter 4 detailed the computation of renormalization factors necessary to renormalize bilinear and four quark matrix elements computed on lattice ensembles of current and future interest [138]. These renormalization factors were necessary for the first percent level determination of the nucleon axial coupling [149], as well as the first lattice determination of hadronic operators contributing to $0\nu\beta\beta$ induced by heavy physics [137]. We used the RI/SMOM method, which has been shown to give better suppression of chiral symmetry breaking artifacts at typical renormalization scales [140]. The bilinear renormalization factors were found to satisfy the Ward-identity expectations [144] to a high degree of accuracy, indicating that our program of using Möbius Domain Wall fermions on gradient flowed gauge fields has been successful in approximately restoring chiral symmetry. Two possible sources of systematic error were explored, and found to be negligible. The renormalization factors computed in this work will be necessary for future projects.

In chapter 5 we presented progress in the first lattice QCD calculation of the $\mathcal{CP}$-violating pion-nucleon couplings induced by the quark chromo-electric dipole moment. Given the current state of estimates of these couplings from QCD sum rules and NDA, we seek a determination of the $\mathcal{CP}$-violating couplings $\bar{g}_0$ and $\bar{g}_1$ to the $\mathcal{O}(20\%)$ level. Using chiral matching conditions similar to those of chapter 3 for the $\bar{\theta}$-term, we match or

$\mathcal{CP}$-violating couplings to spectroscopic shifts in the nucleon spectrum arising from the $\mathcal{CP}$-conserving quark chromo-magnetic dipole operators. We present preliminary bare results, calculated using the method of reference [172], for all 5 matrix elements needed to construct our matching relation. The chromo-magnetic operator has a power divergent mixing with the scalar operator, and we detail two renormalization prescriptions which we will use to renormalize the chromo-magnetic operator, including subtraction of the power divergent mixing. It is expected that the power divergent mixing will be approximately canceled in the specific combinations used to construct our matching relations [170], however a proper renormalization is necessary to verify this expectation. An $\mathcal{O}(20\%)$ determination of the $\mathcal{CP}$-violating couplings would be a significant advance for the field, and in the case of large nuclei, be sub-leading in precision to nuclear many-body theoretical uncertainties [175].

Appendix A

A.1 Gamma Matrix Conventions

In constructing our propagators and correlation functions, we use the gamma matrix conventions of the `Chroma` software

$$\{\gamma^\mu, \gamma_\nu\} = 2\delta_{\mu\nu} \qquad , \qquad \gamma_\mu^\dagger = \gamma_\mu$$

$$\sigma_{\mu\nu} = \tfrac{i}{2}[\gamma_\mu, \gamma_\nu].$$

(A.1)

All propagators are solved with the spin components in Degrand-Rossi basis,

$$\gamma_1 = \begin{pmatrix} 0 & i\sigma_1 \\ -i\sigma_1 & 0 \end{pmatrix} \;\; , \;\; \gamma_2 = \begin{pmatrix} 0 & -i\sigma_2 \\ i\sigma_2 & 0 \end{pmatrix} \;\; , \;\; \gamma_3 = \begin{pmatrix} 0 & i\sigma_3 \\ -i\sigma_3 & 0 \end{pmatrix}$$

(A.2)

$$\gamma_4 = \begin{pmatrix} 0 & I \\ I & 0 \end{pmatrix},$$

with the Pauli matrices defined in the usual way. In constructing our baryon correlation functions, we rotate to the Dirac basis using the unitary rotation operator defined in `Chroma`

$$\frac{1}{\sqrt{2}} \begin{pmatrix} i\sigma_2 & i\sigma_2 \\ -i\sigma_2 & -i\sigma_2 \end{pmatrix}$$

(A.3)

such that spin matrices in Dirac basis are

$$\Gamma^D = U^\dagger \Gamma^{DR} U$$

(A.4)

A.2 Fierz Transformations and the Four Quark Renormalization Basis

A.2.1 Euclidian Dirac Conventions and Fierz Transformations

The choice of convention is arbitrary, but must be consistent. For example if we choose $\sigma_{\mu\nu} = 1/2[\gamma_\mu, \gamma_\nu]$, or $\sigma_{\mu\nu} = i/2[\gamma_\mu, \gamma_\nu]$, this changes the tree level matrix we must calculate to determine the renormalization matrix. The 16 Euclidian Dirac 4 x 4 matrices which form a complete basis are denoted $\Gamma = \{S, P, V, A, T\} = \{\mathbb{I}, \gamma_5, \gamma_\mu, \gamma_\mu\gamma_5, \sigma_{\mu\nu}\}$. In the following analysis, we use the conventions in Euclidian space:

$$\gamma_5 = \gamma_1\gamma_2\gamma_3\gamma_4$$
$$\sigma_{\mu\nu} = \frac{1}{2}[\gamma_\mu, \gamma_\nu] \tag{A.5}$$

$$\{\gamma_\mu, \gamma_\nu\} = 2\delta_{\mu\nu} \quad , \quad \gamma_\mu^\dagger = \gamma_\mu \quad , \quad \gamma_5^\dagger = \gamma_5 \tag{A.6}$$

A Fierz transformation is a transformation in Dirac space of the type

$$\Gamma_{\alpha\beta} \otimes \Gamma_{\gamma\delta} \to \Gamma_{\alpha\delta} \otimes \Gamma_{\gamma\beta}$$

. Devising appropriate rules for these types of transformations is our goal. Recall that the Dirac Gamma matrices defined above form a complete set of anti-commuting 4 x 4 matrices in spin space. Thus we may expand any 4 x 4 matrix in this basis. The Dirac matrix orthogonality relation implies (raised/lowered Dirac indices do not matter in Euclidian space, but old habits die hard)

$$\text{tr}(\Gamma^a\Gamma_b) = 4\delta_b^a \tag{A.7}$$

which allows us to expand any 4 x 4 matrix A as

$$A = A_a \Gamma^a \qquad , \qquad A_a = \frac{1}{4} \text{tr}(A\Gamma^a). \tag{A.8}$$

Component wise, we have

$$A_{ij} = \delta_{ik} A_{kl} \delta_{lj} = \frac{1}{4} A_{kl} \Gamma^a_{lk} \Gamma^a_{ij} \tag{A.9}$$

which naturally leads to an identity that we will use to derive the Fierz relations

$$\delta_{ik} \delta_{lj} = \frac{1}{4} \Gamma^a_{lk} \Gamma^a_{ij} \tag{A.10}$$

which after some algebra yields the Fierz Identities

$$\Gamma^a_{ik} \Gamma^b_{lj} = \frac{1}{16} \text{tr}\left(\Gamma^a \Gamma_c \Gamma^b \Gamma_d \right) \Gamma^d_{ij} \Gamma^c_{lk}. \tag{A.11}$$

We are interested in the transformation matrix between the Fierz transformed basis of (A.16) and the original basis (A.17). Our matrix elements are parity even, so we only consider the parity conserving parts of the Fierz transformations of $\{S \otimes S, P \otimes P, V \otimes V, A \otimes A, T \otimes T\}$. We'll denote the Fierz transformed operators $\{(S \otimes S)^F, (P \otimes P)^F, (V \otimes V)^F, (A \otimes A)^F, (T \otimes T)^F\}$. The Fierz Identities for anticommuting fermion fields incur an additional minus sign. Thus what we are interested in is the transformation (accounting for minus sign for our fermion fields):

$$(\Gamma^a)[\Gamma^a] = -\frac{1}{16} Tr(\Gamma^a \Gamma_c \Gamma^a \Gamma_c)(\Gamma^c)[\Gamma^c] \tag{A.12}$$

or conversely if we redefine which is the "diagonal" basis.

$$(\Gamma^a)[\Gamma^a] = -\frac{1}{16} Tr(\Gamma^a \Gamma_c \Gamma^a \Gamma_c)(\Gamma^c)[\Gamma^c] \tag{A.13}$$

Thus determining the above transformation matrix will determine the basis transformations we are looking for. We find

$$-\frac{1}{4}\begin{pmatrix} 1 & 1 & -1 & -1 & 1 \\ 4 & -2 & 0 & -2 & -4 \\ -6 & 0 & -2 & 0 & -6 \\ -4 & -2 & 0 & -2 & 4 \\ 1 & -1 & -1 & 1 & 1 \end{pmatrix} \tag{A.14}$$

which gives the Fierz Transformed elements

$$(S \otimes S)^F = (-1/4)((S \otimes S) + (V \otimes V) - (T \otimes T) - (A \otimes A) + (P \otimes P))$$

$$(V \otimes V)^F = (-1/4)(4(S \otimes S) - 2(V \otimes V) - 2(A \otimes A) - 4(P \otimes P))$$

$$(T \otimes T)^F = (-1/4)(-6(S \otimes S) - 2(T \otimes T) - 6(P \otimes P)) \tag{A.15}$$

$$(A \otimes A)^F = (-1/4)(-4(S \otimes S) - 2(V \otimes V) - 2(A \otimes A) + 4(P \otimes P))$$

$$(P \otimes P)^F = (-1/4)((S \otimes S) - (V \otimes V) - (T \otimes T) + (A \otimes A) + (P \otimes P)).$$

Specifically, for our color mixed operators we are interested in the basis transformations:

$$(V \otimes V)^F - (A \otimes A)^F = -2 * ((S \otimes S) - (P \otimes P))$$

$$2 * ((S \otimes S)^F + (P \otimes P)^F) = -((S \otimes S) + (P \otimes P) - (T \otimes T))$$

A.2.2 Color Diagonal Basis

The goal is to examine the relationship between the common dimension six four quark basis (A.16), and the P conserving $0\nu\beta\beta$ basis (A.17), which is used in reference Phys-RevD.68.034016,Nicholson:2016byl,Nicholson:2018mwc among others. A simpler, but

121

related basis is used to renormalize BSM Kaon physics for example [146, 254]

$$Q_1 = (\bar{\psi}_1 \gamma_\mu (1 - \gamma_5) \psi_2)(\bar{\psi}_1 \gamma_\mu (1 - \gamma_5) \psi_2)$$

$$Q_2 = (\bar{\psi}_1 \gamma_\mu (1 - \gamma_5) \psi_2)(\bar{\psi}_1 \gamma_\mu (1 + \gamma_5) \psi_2)$$

$$Q_3 = (\bar{\psi}_1 (1 - \gamma_5) \psi_2)(\bar{\psi}_1 (1 + \gamma_5) \psi_2) \qquad \text{(A.16)}$$

$$Q_4 = (\bar{\psi}_1 (1 - \gamma_5) \psi_2)(\bar{\psi}_1 (1 - \gamma_5) \psi_2)$$

$$Q_5 = (1/4)(\bar{\psi}_1 \sigma_{\mu\nu} (1 - \gamma_5) \psi_2)(\bar{\psi}_1 \sigma_{\mu\nu} (1 - \gamma_5) \psi_2).$$

Expanding out the parenthesis of (A.16) and keeping the parity conserving part (Ie. P operating on odd product γ_5 is odd under P.) leads to the basis (respectively) VV + AA, VV - AA, SS - PP, SS + PP, TT. In $SU(3)$ chiral perturbation theory,

- Q_1 renormalizes multiplicatively (27,1),

- Q_2, Q_3 are both (8,8) and mix together,

- Q_4, Q_8 are $(6, \bar{6})$ and mix together.

Thus if chiral symmetry is exact on the lattice, the renormalization matrix is block diagonal.

A.2.3 $0\nu\beta\beta$ **Basis**

Takahashi notation allows us to replace the matrix indices by parenthesis and brackets () [], that represent operator indices in an unambiguous way. For example, the Fierz type identity derived from the completeness relation of any fundamental representation of SU(N) algebra $\{T^a\}$ satisfying $\text{tr}[T^a T^b] = C\delta^{ab}$ is given as:

$$\frac{1}{C}(T_a)_{ij}(T_a)_{kl} + \frac{1}{N}\delta_{ij}\delta_{kl} = \delta_{il}\delta_{kj} \rightarrow \frac{1}{C}(T_a)[T_a] + \frac{1}{N}(\ )[\ ] = (\ ][\ )$$

in Takahashi notation[255, 256]. We will use this notation in defining the color mixed basis for $0\nu\beta\beta$.

Using Chiral EFT, the short range $0\nu\beta\beta$ interactions are characterized by contact operators between pions and nucleons [257]. Integrating out the heavy physics induces quark-lepton contact operators which induce at leading order:$\pi\pi ee$, $NN\pi ee$, and the $NNNNee$ contact interaction[165]. We focus on a subset of these operators.

Here $q = (u\ d)^T$, $\tau^+ = \tau^1 + i\tau^2$ is the isospin raising operator, and$\vec{\tau} = (1/2)\vec{\sigma}$ where $\vec{\sigma}$ is the vector of Pauli matrices. The brackets/parenthesis are in Takahashi notation and denote which indices are contracted together.

$$O_{1+}^{++} = (\bar{q}_L\tau^+\gamma^\mu q_L)[\bar{q}_R\tau^+\gamma_\mu q_R]$$

$$O_{2+}^{++} = (\bar{q}_R\tau^+ q_L)[\bar{q}_R\tau^+ q_L] + (\bar{q}_L\tau^+ q_R)[\bar{q}_L\tau^+ q_R]$$

$$O_{3+}^{++} = (\bar{q}_L\tau^+\gamma^\mu q_L)[\bar{q}_L\tau^+\gamma_\mu q_L] + (\bar{q}_R\tau^+\gamma^\mu q_R)[\bar{q}_R\tau^+\gamma_\mu q_R] \qquad \text{(A.17)}$$

$$O_{1+}'^{++} = (\bar{q}_L\tau^+\gamma^\mu q_L][\bar{q}_R\tau^+\gamma_\mu q_R)$$

$$O_{2+}'^{++} = (\bar{q}_R\tau^+ q_L][\bar{q}_R\tau^+ q_L) + (\bar{q}_L\tau^+ q_R][\bar{q}_L\tau^+ q_R)$$

Expanding out the isospin operators, making indices explicit, and rearranging things to look more like (A.16), we find

$$O_{1+}^{++} = (1/4)(\bar{u}_a^\alpha(\gamma^\mu(1-\gamma_5))_{\alpha\beta}\delta^{ab}d_b^\beta)[\bar{u}_c^\gamma(\gamma_\mu(1+\gamma_5))_{\gamma\delta}\delta^{cd}d_d^\delta]$$

$$O_{2+}^{++} = (1/4)\{(\bar{u}_a^\alpha(1-\gamma_5)_{\alpha\beta}\delta^{ab}d_b^\beta)[\bar{u}_c^\gamma(1-\gamma_5)_{\gamma\delta}\delta^{cd}d_d^\delta] + ...$$
$$... + (\bar{u}_a^\alpha(1+\gamma_5)_{\alpha\beta}\delta^{ab}d_b^\beta)[\bar{u}_c^\gamma(1+\gamma_5)_{\gamma\delta}\delta^{cd}d_d^\delta]\}$$

$$O_{3+}^{++} = (1/4)\{(\bar{u}_a^\alpha(\gamma^\mu(1-\gamma_5))_{\alpha\beta}\delta^{ab}d_b^\beta)[\ \bar{u}_c^\gamma(\gamma_\mu(1-\gamma_5))_{\gamma\delta}\delta^{cd}d_d^\delta] + ...$$
$$... + (\bar{u}_a^\alpha(\gamma^\mu(1+\gamma_5))_{\alpha\beta}\delta^{ab}d_b^\beta)[\ \bar{u}_c^\gamma(\gamma_\mu(1+\gamma_5))_{\gamma\delta}\delta^{cd}d_d^\delta]\}$$

$$O_{1+}'^{++} = (1/4)(\bar{u}_a^\alpha(\gamma^\mu(1-\gamma_5))_{\alpha\beta}\delta^{bc}d_b^\beta)[\bar{u}_c^\gamma(\gamma_\mu(1+\gamma_5))_{\gamma\delta}\delta^{ad}d_d^\delta)$$

$$O_{2+}'^{++} = ((1/4)\{(\bar{u}_a^\alpha(1-\gamma_5)_{\alpha\beta}\delta^{bc}d_b^\beta)[\bar{u}_c^\gamma(1-\gamma_5)_{\gamma\delta}\delta^{ad}d_d^\delta) + ...$$
$$... + (\bar{u}_a^\alpha(1+\gamma_5)_{\alpha\beta}\delta^{bc}d_b^\beta)[\bar{u}_c^\gamma(1+\gamma_5)_{\gamma\delta}\delta^{ad}d_d^\delta)\},$$

$$\text{(A.18)}$$

where Greek indices denote spin space elements, Roman indices denote color space elements, and μ denotes spacetime index. Upon comparison of (A.16) with (A.18), keeping

in mind we are only interested in parity conserving contributions, we find for the unmixed operators:

$$O_{1+}^{++} = (1/4) * (VV - AA) = (1/4) * Q_2$$

$$O_{2+}^{++} = (1/4) * 2 * (SS + PP) = (1/4) * 2 * Q_4$$

$$O_{3+}^{++} = (1/4) * 2 * (VV + AA) = (1/4) * 2 * Q_1$$

.

Following the notation of chapter ch:Renormalization, we denote the spin and color changing components of the basis element Γ, e.g.

$$O_{1+}^{++} = (1/4)(\bar{u}_a^\alpha \Gamma_{\alpha\beta}^{(1)ab} d_b^\beta)[\bar{u}_c^\gamma \Gamma_{\gamma\delta}^{(2)cd} d_d^\delta] \tag{A.19}$$

where for this basis element

$$\Gamma_{\alpha\beta}^{(1)ab} = (\gamma^\mu(1 - \gamma_5))_{\alpha\beta}\delta^{ab}. \tag{A.20}$$

The mixed operators, for example, give

$$\Gamma_{1+}^{'++(1)} \otimes \Gamma_{1+}^{'++(2)} = (\gamma^\mu(1 - \gamma_5))_{\alpha\beta}\delta^{bc} \otimes (\gamma_\mu(1 + \gamma_5))_{\gamma\delta}\delta^{ad}, \tag{A.21}$$

which can be related to color unmixed operators using the Fierz Identities. Noting the anti-symmetry of the Fermionic field operators, we arrive at

$$
\begin{aligned}
(\bar{u}_a^\alpha(\gamma^\mu(1 &- \gamma_5))_{\alpha\beta}\delta^{bc}d_b^\beta][\bar{u}_c^\gamma(\gamma_\mu(1 + \gamma_5))_{\gamma\delta}\delta^{ad}d_d^\delta) \\
&= -2(\bar{u}_a^\alpha(1 + \gamma_5)_{\alpha\delta}\delta^{bc}d_d^\delta][\bar{u}_c^\gamma(1 - \gamma_5)_{\gamma\beta}\delta^{ad}d_b^\beta) \\
&= -2(\bar{u}_a^\alpha(1 + \gamma_5)_{\alpha\delta}\delta^{ad}d_d^\delta][\bar{u}_c^\gamma(1 - \gamma_5)_{\gamma\beta}\delta^{bc}d_b^\beta) \\
&= -2(\bar{u}(1 + \gamma_5)d)[\bar{u}(1 - \gamma_5)d],
\end{aligned} \tag{A.22}
$$

yielding the color mixed operator

$$O_{1+}^{'++} = -(1/4) * 2 * (SS - PP) = -(1/4) * 2 * Q_3.$$

Likewise for the second color mixed operator, we have

$$O_{2+}^{'++} = -(1/4) * 2 * (SS^F + PP^F) = -(1/4) * (SS + PP - TT) = -(1/4) * (Q_4 - Q_5).$$

Putting things together, the color mixed basis is a linear combination of the color unmixed basis. The transformation is

$$O_{1+}^{++} = (1/4) * Q_2$$
$$O_{2+}^{++} = (1/4) * 2 * Q_4$$
$$O_{3+}^{++} = (1/4) * 2 * Q_1 \qquad \text{(A.23)}$$
$$O_{1+}^{'++} = -(1/4) * 2 * Q_3$$
$$O_{2+}^{'++} = -(1/4) * (Q_4 - Q_5),$$

which agrees with the transformation derived in reference [146, 254].

Appendix B

B.1 Extended Results for Renormalization Project

B.1.1 Numerical Results

The renormalization factors at 3 GeV may be found by applying the step scaling matrix $\sigma\,[3\,\text{GeV}, 2\,\text{GeV}]$ to the interpolated values at 2 GeV in the chiral limit. For the bilinear and four quark operators in both schemes, we present the 2 GeV results, the continuum step scaling matrix, and the factors at 3 GeV.

B.1.1.1 Wave Function and Quark Mass Renormalization

	$\slashed{q}$-scheme		γ-scheme	
scale	Z_q^a [2 GeV]	Z_m^a [2 GeV]	Z_q^a [2 GeV]	Z_m^a [2 GeV]
a15	1.0965(61)	0.9833(28)	1.0340(58)	1.0461(36)
a12	1.0951(82)	1.0068(15)	1.0168(30)	1.0753(53)
a09	1.0852(42)	1.0349(28)	1.0114(39)	1.1123(29)

Table B.1: Chiral limit values of the quark mass and wave function renormalization in $\slashed{q}$ and γ-schemes at $\mu =$ 2 GeV.

$$\begin{aligned}
\sigma_q^{\slashed{q}}\,[3\,\text{GeV}, 2\,\text{GeV}] &= 0.95303(82) & \sigma_m^{\slashed{q}}\,[3\,\text{GeV}, 2\,\text{GeV}] &= 0.9438(58) \\
\sigma_q^{\gamma}\,[3\,\text{GeV}, 2\,\text{GeV}] &= 0.98822(69) & \sigma_m^{\gamma}\,[3\,\text{GeV}, 2\,\text{GeV}] &= 0.9058(49)
\end{aligned} \tag{B.1}$$

	$\not{q}$-scheme		γ-scheme	
scale	Z_q^a [3 GeV]	Z_m^a [3 GeV]	Z_q^a [3 GeV]	Z_m^a [3 GeV]
a15	1.0450(58)	0.9280(58)	1.0218(57)	0.9476(50)
a12	1.0437(80)	0.9502(61)	1.0048(30)	0.9740(74)
a09	1.0342(41)	0.9767(63)	0.9995(39)	1.0076(59)

Table B.2: Chiral limit values of the quark mass and wave function renormalization in $\not{q}$ and γ-schemes at $\mu = 3$ GeV.

B.1.1.2   Scalar, Pseudoscalar, and Tensor

	$\not{q}$-scheme			γ-scheme		
scale	Z_S^a [2 GeV]	Z_P^a [2 GeV]	Z_T^a [2 GeV]	Z_S^a [2 GeV]	Z_P^a [2 GeV]	Z_T^a [2 GeV]
a15	1.0216(44)	1.0155(50)	1.0693(66)	0.9665(37)	0.9608(44)	1.0092(62)
a12	1.0111(29)	1.0136(45)	1.0847(26)	0.9498(27)	0.9521(42)	1.0192(37)
a09	0.9933(35)	0.9851(44)	1.1031(25)	0.9250(31)	0.9174(40))	1.0299(45)

Table B.3: Chiral limit values of the scalar, pseudoscalar, and tensor renormalization factors in $\not{q}$ and γ-schemes at $\mu = 2$ GeV.

$$
\begin{aligned}
\sigma_S^{\not{q}}[3\text{ GeV}, 2\text{ GeV}] &= 1.023(20) & \sigma_S^{\gamma}[3\text{ GeV}, 2\text{ GeV}] &= 1.054(25) \\
\sigma_P^{\not{q}}[3\text{ GeV}, 2\text{ GeV}] &= 1.057(31) & \sigma_P^{\gamma}[3\text{ GeV}, 2\text{ GeV}] &= 1.095(35) \\
\sigma_T^{\not{q}}[3\text{ GeV}, 2\text{ GeV}] &= 0.9392(14) & \sigma_T^{\gamma}[3\text{ GeV}, 2\text{ GeV}] &= 0.97813(29)
\end{aligned}
\tag{B.2}
$$

	$\not{q}$-scheme			γ-scheme		
scale	Z_S^a	Z_P^a	Z_T^a	Z_S^a	Z_P^a	Z_T^a
a15	1.045(21)	1.073(31)	1.0043(64)	1.018(25)	1.052(34)	0.9871(61)
a12	1.035(20)	1.071(31)	1.0187(30)	1.001(24)	1.042(34)	0.9969(37)
a09	1.016(20)	1.041(30)	1.0360(28)	0.975(24)	1.004(32)	1.0074(44)

Table B.4: Chiral limit values of the scalar, pseudoscalar, and tensor renormalization factors in $\not{q}$ and γ-schemes at $\mu = 3$ GeV. The scalar and pseudoscalar factors have an added systematic.

B.1.1.3 Color Diagonal Four Quark Basis

$$
Z^{\gamma,\mathsf{a}15}(\mu = 2\,\mathrm{GeV}) =
\begin{pmatrix}
0.9215(61) & 0 & 0 & 0 & 0 \\
0 & 0.9895(65) & 0.1328(10) & 0 & 0 \\
0 & 0.01902(19) & 0.9140(60) & 0 & 0 \\
0 & 0 & 0 & 0.9268(61) & -0.01661(26) \\
0 & 0 & 0 & -0.11493(91) & 0.9764(65)
\end{pmatrix}
\tag{B.3}
$$

$$
Z^{\gamma,\mathsf{a}12}(\mu = 2\,\mathrm{GeV}) =
\begin{pmatrix}
0.8931(41) & 0 & 0 & 0 & 0 \\
0 & 0.9589(44) & 0.13140(84) & 0 & 0 \\
0 & 0.01523(14) & 0.8621(40) & 0 & 0 \\
0 & 0 & 0 & 0.8750(40) & -0.01300(17) \\
0 & 0 & 0 & -0.11766(72) & 0.9543(44)
\end{pmatrix}
\tag{B.4}
$$

$$
Z^{\gamma,\mathsf{a}09}(\mu = 2\,\mathrm{GeV}) =
\begin{pmatrix}
0.8833(36) & 0 & 0 & 0 & 0 \\
0 & 0.9534(39) & 0.15333(72) & 0 & 0 \\
0 & 0.01312(10) & 0.8142(34) & 0 & 0 \\
0 & 0 & 0 & 0.8328(35) & -0.010705(75) \\
0 & 0 & 0 & -0.14153(67) & 0.9632(40)
\end{pmatrix}
\tag{B.5}
$$

We use two methods of constructing the continuum step scaling matrix. The first method parameterizes the running and lattice spacing dependence of the three lattice step scaling matrices, while the other takes the continuum limit momentum point by momentum point. We take half the difference between the two continuum results as a systematic. In equation (B.6), the first error being statistical, and the second systematic.

$$
\sigma^\gamma\,[3\,\mathrm{GeV}, 2\,\mathrm{GeV}] =
\begin{pmatrix}
1.02091(57)(54) & 0 & 0 & 0 & 0 \\
0 & 0.99634(69)(87) & -0.1216(25)(3) & 0 & 0 \\
0 & -0.00348(70)(37) & 1.1514(34)(2) & 0 & 0 \\
0 & 0 & 0 & 1.1194(35) & 0.00084(62)(60) \\
0 & 0 & 0 & 0.1064(30)(34) & 0.95844(78)(174)
\end{pmatrix}
\tag{B.6}
$$

The final 3 GeV γ-scheme matrices are

$$
Z^{\gamma,\mathsf{a}15}(\mu = 3\,\mathrm{GeV}) =
\begin{pmatrix}
0.9408(63) & 0 & 0 & 0 & 0 \\
0 & 0.9835(68) & 0.0212(30) & 0 & 0 \\
0 & 0.0185(20) & 1.0519(81) & 0 & 0 \\
0 & 0 & 0 & 1.037(11) & -0.0178(34) \\
0 & 0 & 0 & -0.0115(83) & 0.9341(75)
\end{pmatrix}
\tag{B.7}
$$

$$
Z^{\gamma,\mathsf{a}12}(\mu = 3\,\mathrm{GeV}) =
\begin{pmatrix}
0.9118(43) & 0 & 0 & 0 & 0 \\
0 & 0.9535(48) & 0.0261(29)) & 0 & 0 \\
0 & 0.0142(20) & 0.9922(61) & 0 & 0 \\
0 & 0 & 0 & 0.9794(92) & -0.0137(34) \\
0 & 0 & 0 & -0.0197(81) & 0.9132(60)
\end{pmatrix}
\tag{B.8}
$$

$$
Z^{\gamma,\mathsf{a}09}(\mu = 3\,\mathrm{GeV}) =
\begin{pmatrix}
0.9018(39) & 0 & 0 & 0 & 0 \\
0 & 0.9483(44) & 0.0538(28) & 0 & 0 \\
0 & 0.0118(20) & 0.9369(55) & 0 & 0 \\
0 & 0 & 0 & 0.9321(86) & -0.0112(34) \\
0 & 0 & 0 & -0.0470(78) & 0.9220(57)
\end{pmatrix}.
\tag{B.9}
$$

The $\not{q}$-scheme matrices are found in an exactly analogous manner. The step scaling matrix is awaiting final independent verification, so no systematic is given.

$$Z^{\not{q},\text{a15}}(\mu = 2\,\text{GeV}) = \begin{pmatrix} 0.9761(61) & 0 & 0 & 0 & 0 \\ 0 & 1.0040(63) & 0.13635(99) & 0 & 0 \\ 0 & 0.03564(36) & 1.0215(65) & 0 & 0 \\ 0 & 0 & 0 & 1.0512(81) & -0.0188(13) \\ 0 & 0 & 0 & -0.1989(30) & 1.1215(72) \end{pmatrix} \tag{B.10}$$

$$Z^{\not{q},\text{a12}}(\mu = 2\,\text{GeV}) = \begin{pmatrix} 0.9439(39) & 0 & 0 & 0 & 0 \\ 0 & 0.9690(40) & 0.15882(96) & 0 & 0 \\ 0 & 0.03415(25) & 0.9404(39) & 0 & 0 \\ 0 & 0 & 0 & 0.9707(41) & -0.01675(25) \\ 0 & 0 & 0 & -0.1953(18) & 1.1216(47) \end{pmatrix} \tag{B.11}$$

$$Z^{\not{q},a09}(\mu = 2\,\text{GeV}) = \begin{pmatrix} 0.9481(43) & 0 & 0 & 0 & 0 \\ 0 & 0.9735(44) & 0.1366(10) & 0 & 0 \\ 0 & 0.03314(28) & 0.9755(45) & 0 & 0 \\ 0 & 0 & 0 & 1.0009(47) & -0.01870(38) \\ 0 & 0 & 0 & -0.1801(13) & 1.0973(50) \end{pmatrix}, \tag{B.12}$$

$$\sigma^{\not{q}}[3\,\text{GeV}, 2\,\text{GeV}] = \begin{pmatrix} 0.98564(32) & 0 & 0 & 0 & 0 \\ 0 & 0.98919(66) & -0.1106(32) & 0 & 0 \\ 0 & -0.0168(11) & 1.0679(26) & 0 & 0 \\ 0 & 0 & 0 & 1.0319(49) & 0.00176(33) \\ 0 & 0 & 0 & 0.0993(36) & 0.8842(17) \end{pmatrix}. \tag{B.13}$$

The 3 GeV matrices are

$$Z^{\not{q},\text{a15}}(\mu = 3\,\text{GeV}) = \begin{pmatrix} 0.9620(61) & 0 & 0 & 0 & 0 \\ 0 & 0.9892(63) & 0.0219(33) & 0 & 0 \\ 0 & 0.0211(11) & 1.0886(74) & 0 & 0 \\ 0 & 0 & 0 & 1.0844(98) & -0.0174(14) \\ 0 & 0 & 0 & -0.0714(44) & 0.9897(66) \end{pmatrix} \tag{B.14}$$

$$Z^{\not{q},\text{a12}}(\mu = 3\,\text{GeV}) = \begin{pmatrix} 0.9345(43) & 0 & 0 & 0 & 0 \\ 0 & 0.9594(44) & 0.0272(32) & 0 & 0 \\ 0 & 0.0190(11) & 1.0394(54) & 0 & 0 \\ 0 & 0 & 0 & 1.0325(69) & -0.01736(54) \\ 0 & 0 & 0 & -0.0598(37) & 0.9684(48) \end{pmatrix} \tag{B.15}$$

$$Z^{\not{q},a09}(\mu = 3\,\text{GeV}) = \begin{pmatrix} 0.9304(38) & 0 & 0 & 0 & 0 \\ 0 & 0.9547(40) & 0.0531(31) & 0 & 0 \\ 0 & 0.0201(11) & 1.0016(48) & 0 & 0 \\ 0 & 0 & 0 & 1.0013(64) & -0.01530(46) \\ 0 & 0 & 0 & -0.0763(38) & 0.9900(45) \end{pmatrix}. \tag{B.16}$$

B.1.2   Figures

In this section we collect all of the figures showing the momentum interpolation, chiral extrapolation, and step scaling continuum extrapolation, for the results presented in chapter 4.
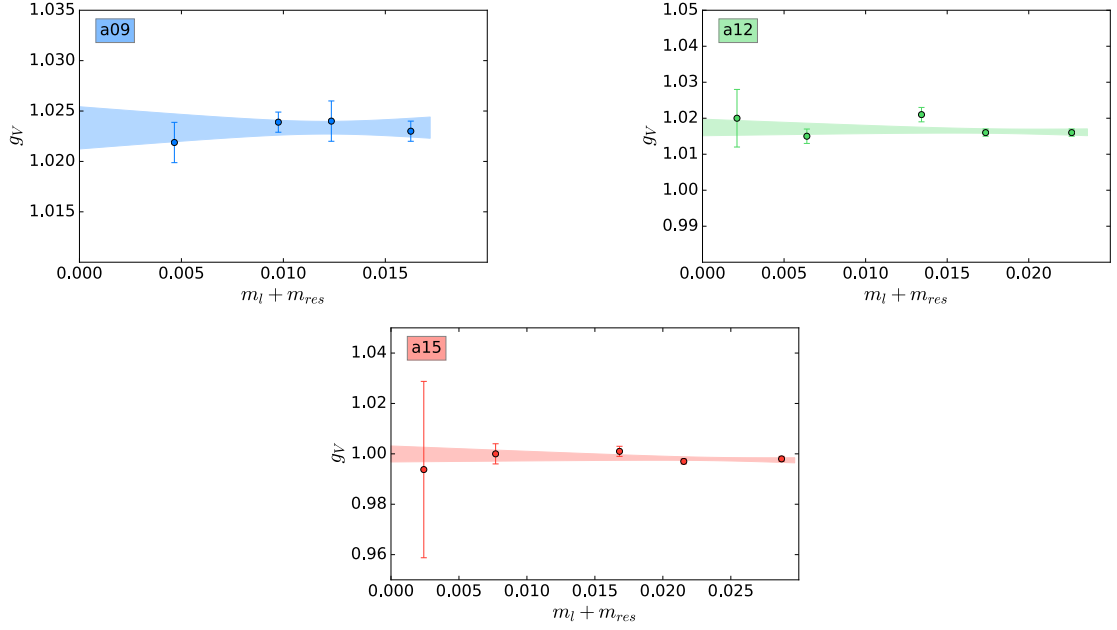
Figure B.1: Chiral extrapolation of Z_V.
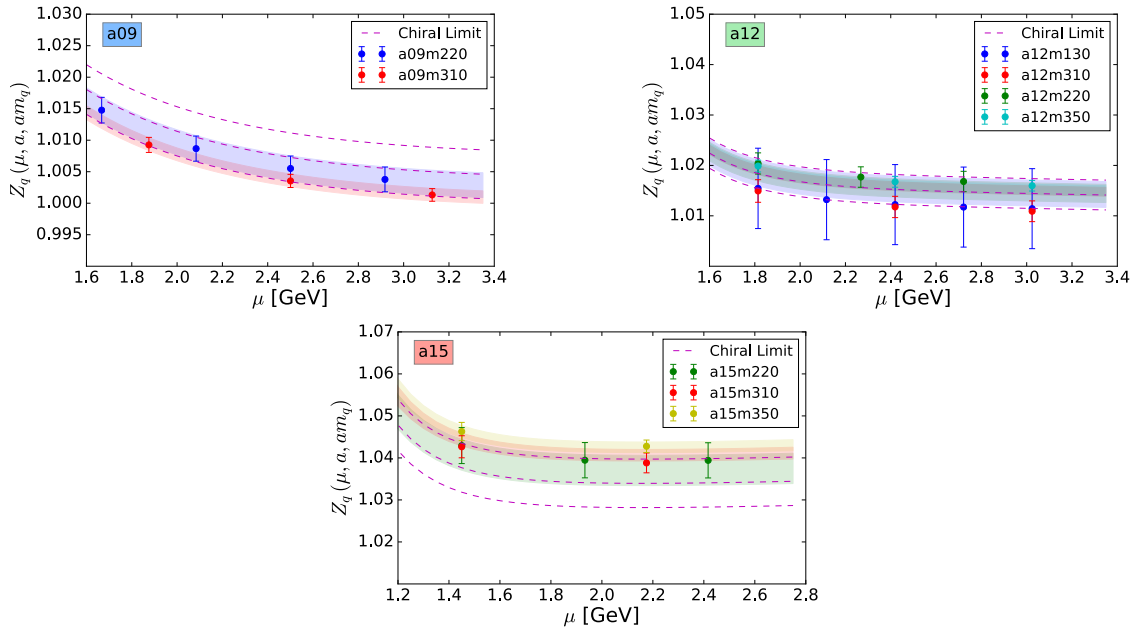
Figure B.2: SMOM γ wave function renormalization.
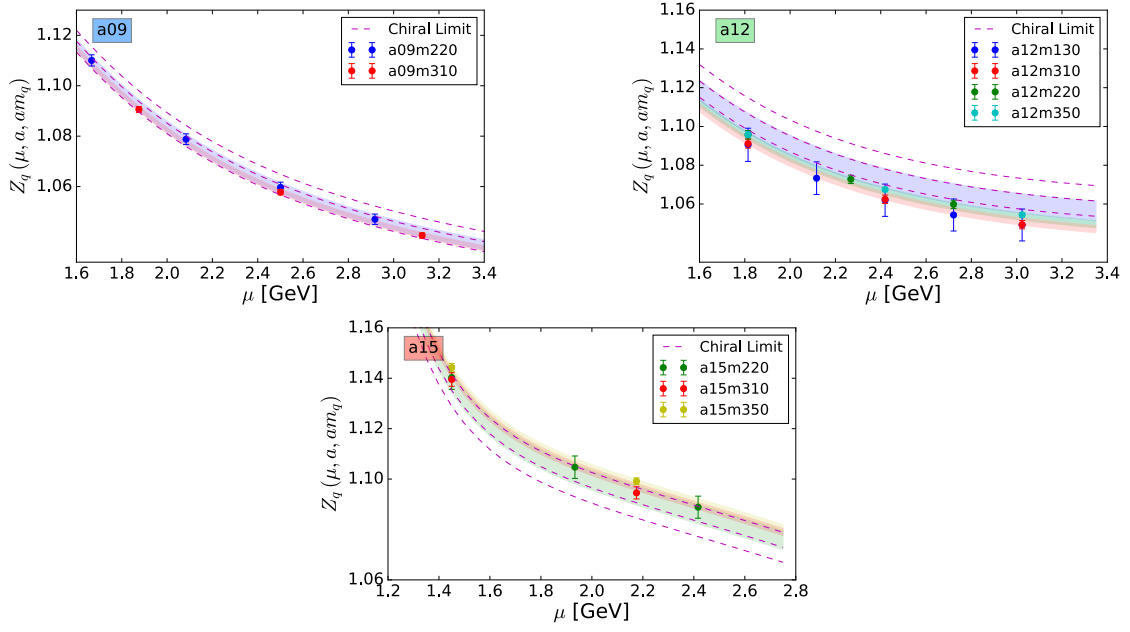
Figure B.3: SMOM $\not{q}$ wave function renormalization.
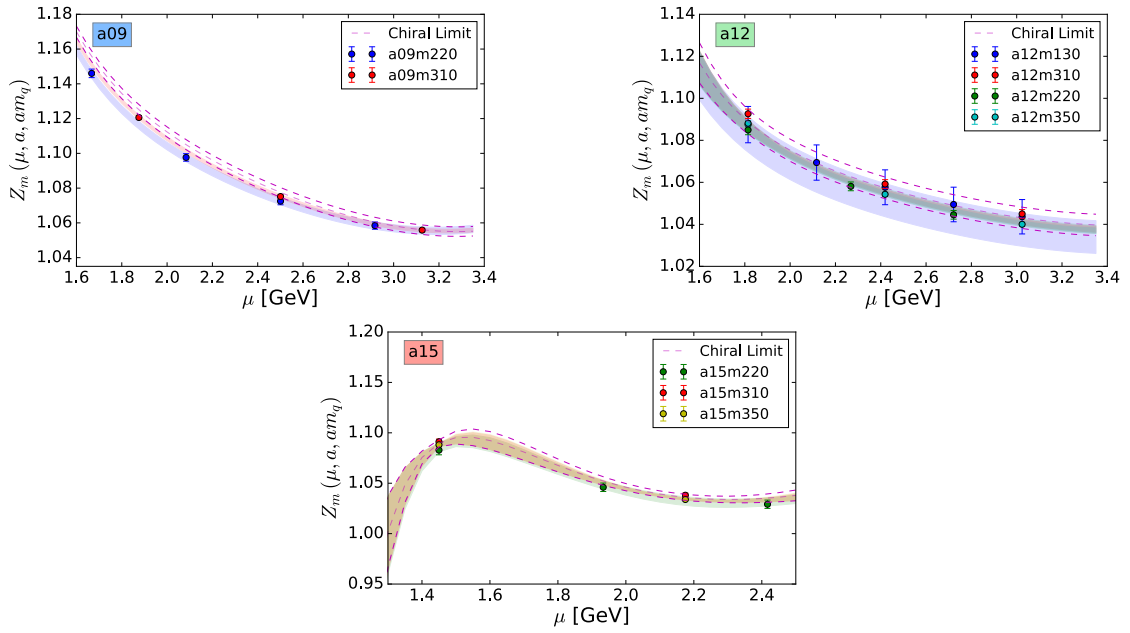
Figure B.4: SMOM γ quark mass renormalization.
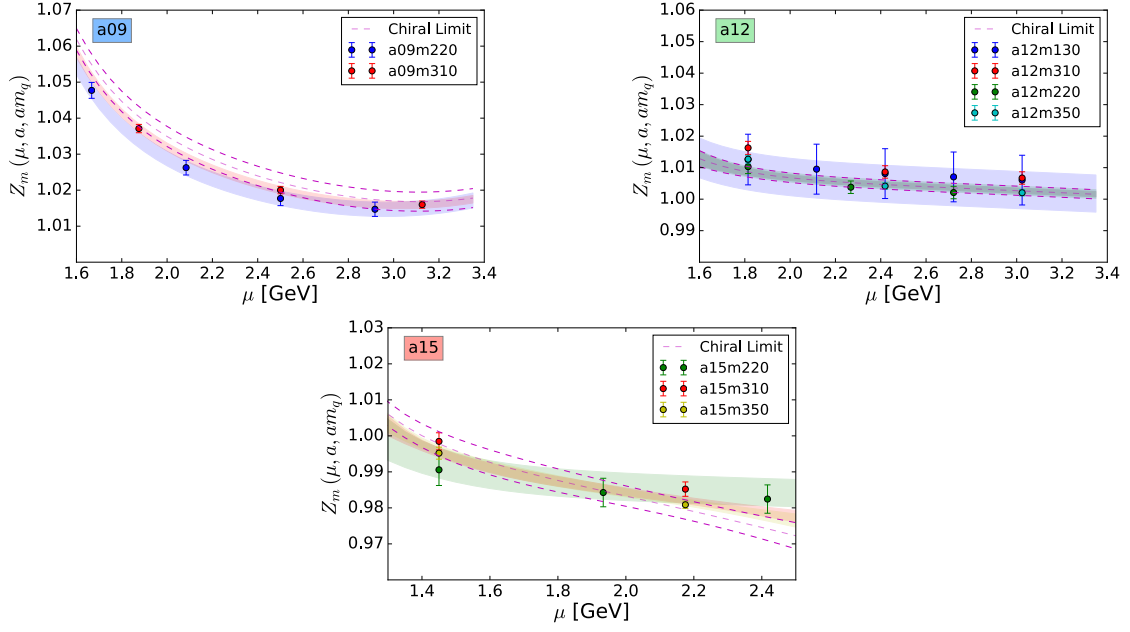
Figure B.5: SMOM $\displaystyle{\not}q$ quark mass renormalization.
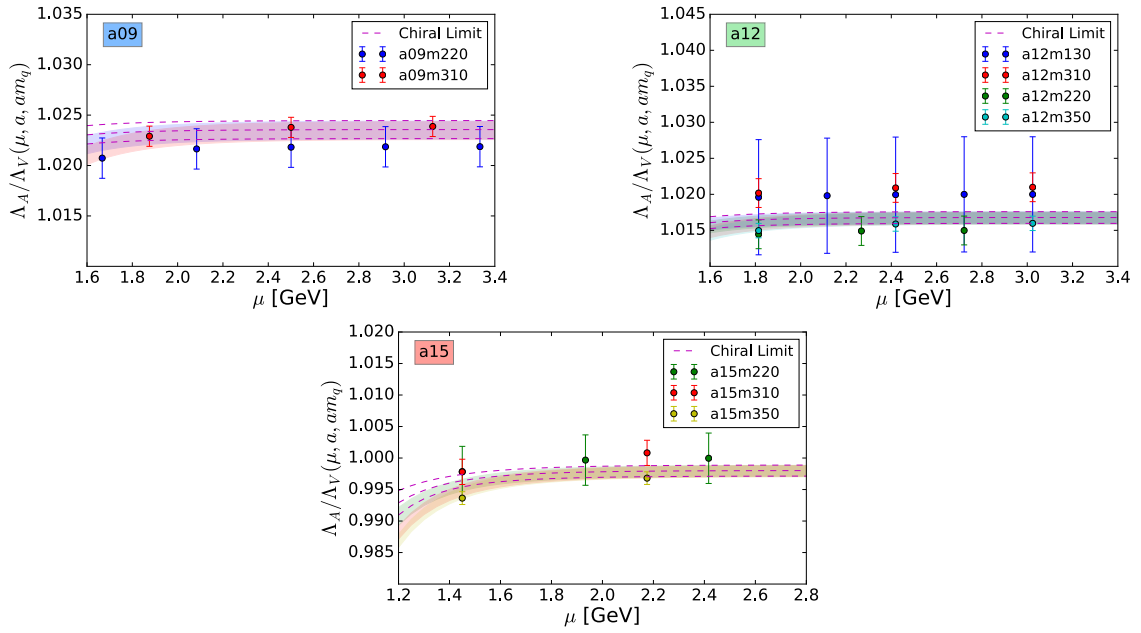
Figure B.6: SMOM γ axial renormalization.
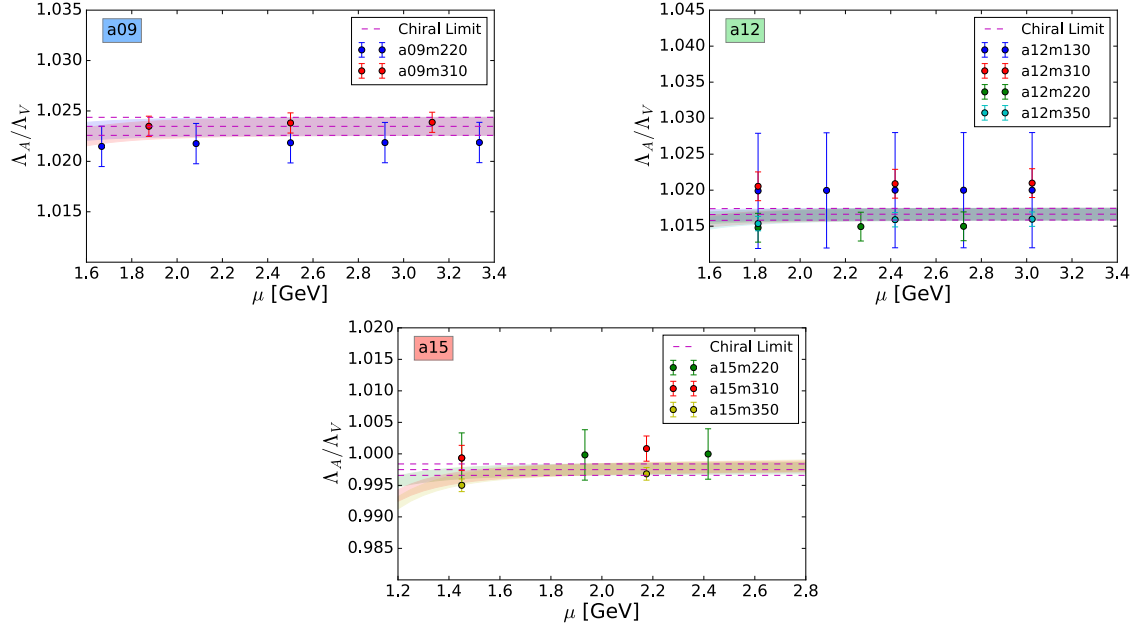
Figure B.7: SMOM $\not{q}$ axial renormalization.
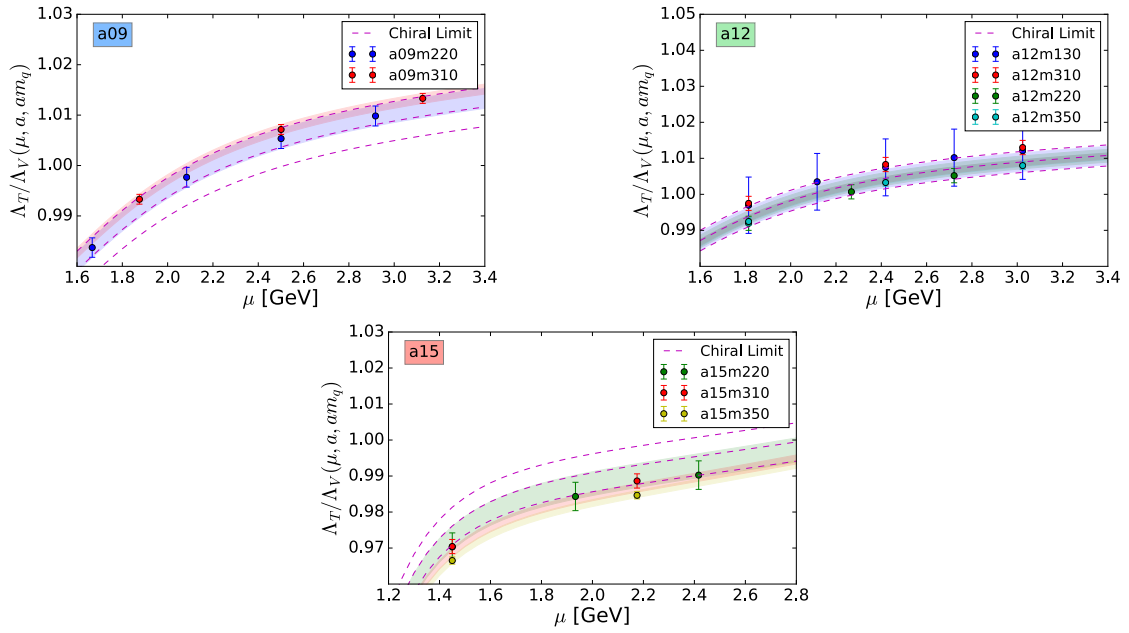
Figure B.8: SMOM γ tensor renormalization.
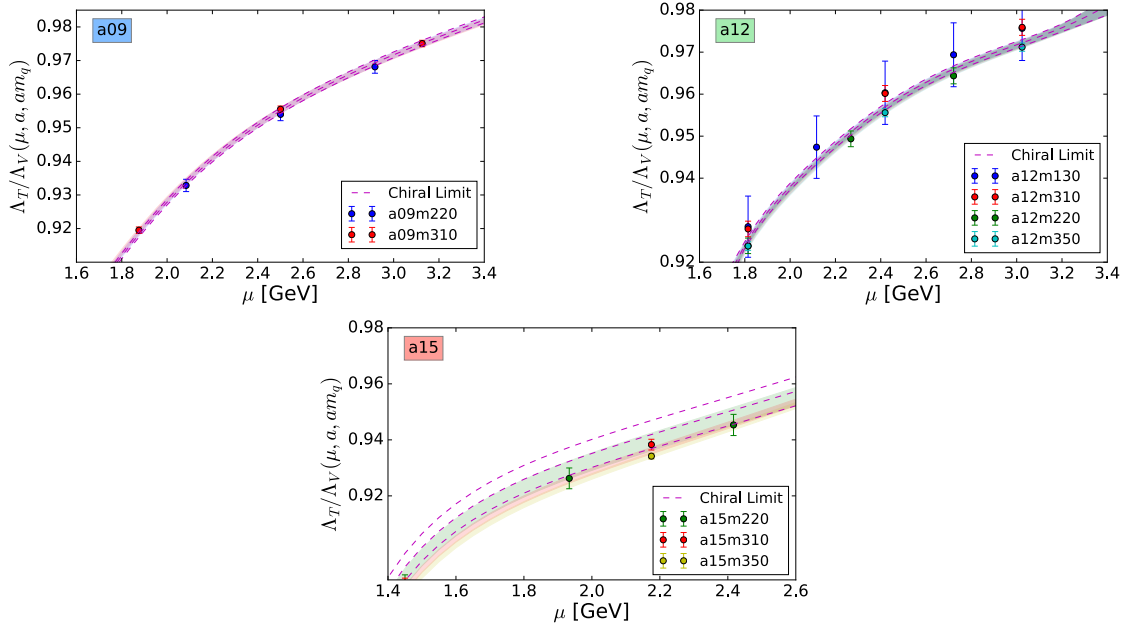
Figure B.9: SMOM $\not{q}$ tensor renormalization.
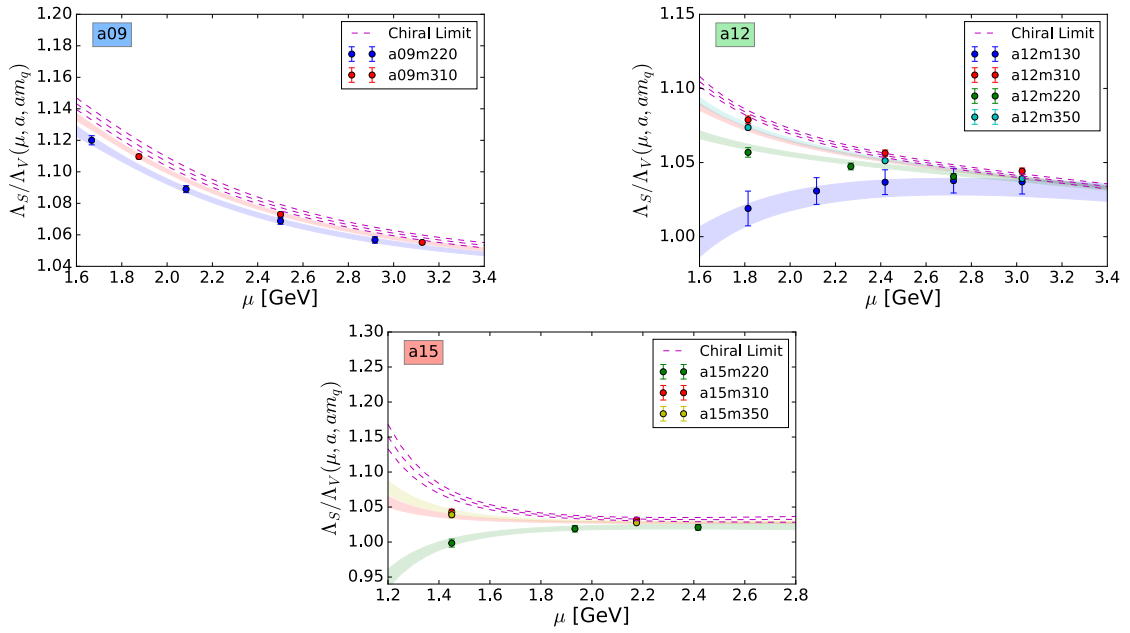
Figure B.10: SMOM γ scalar renormalization.
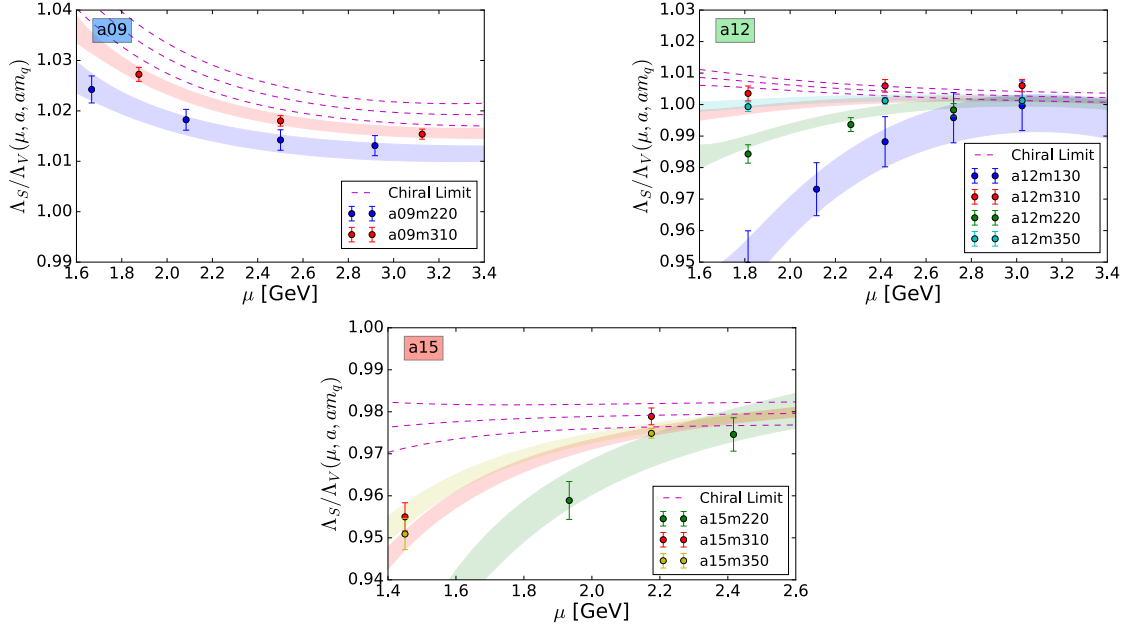
Figure B.11: SMOM $\not q$ tensor renormalization.
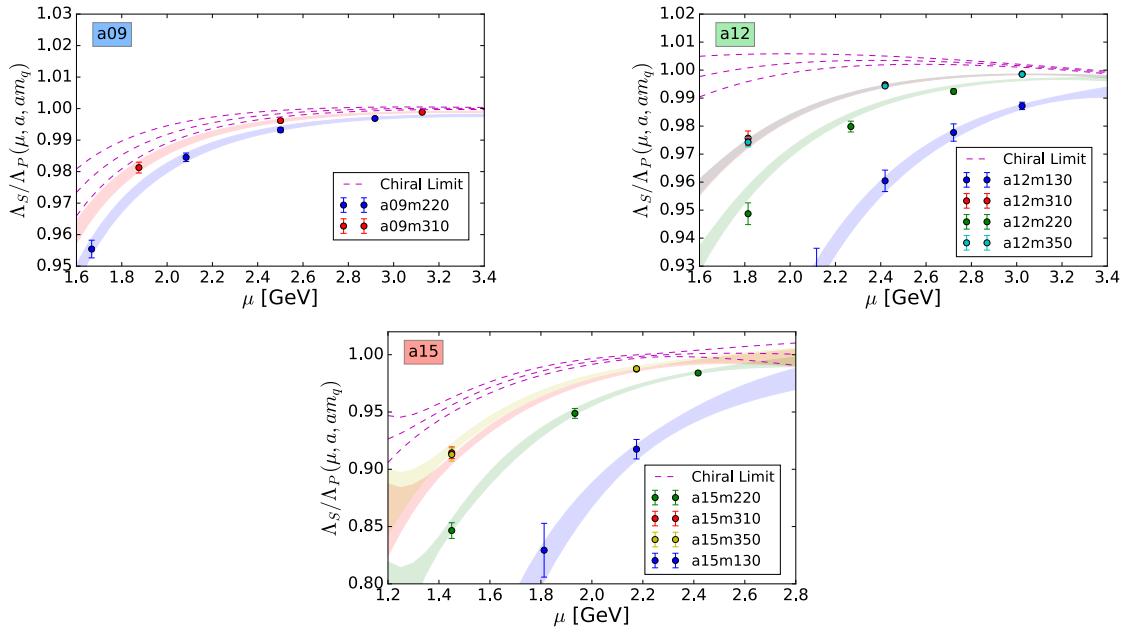
Figure B.12: SMOM $\not q$ axial renormalization.
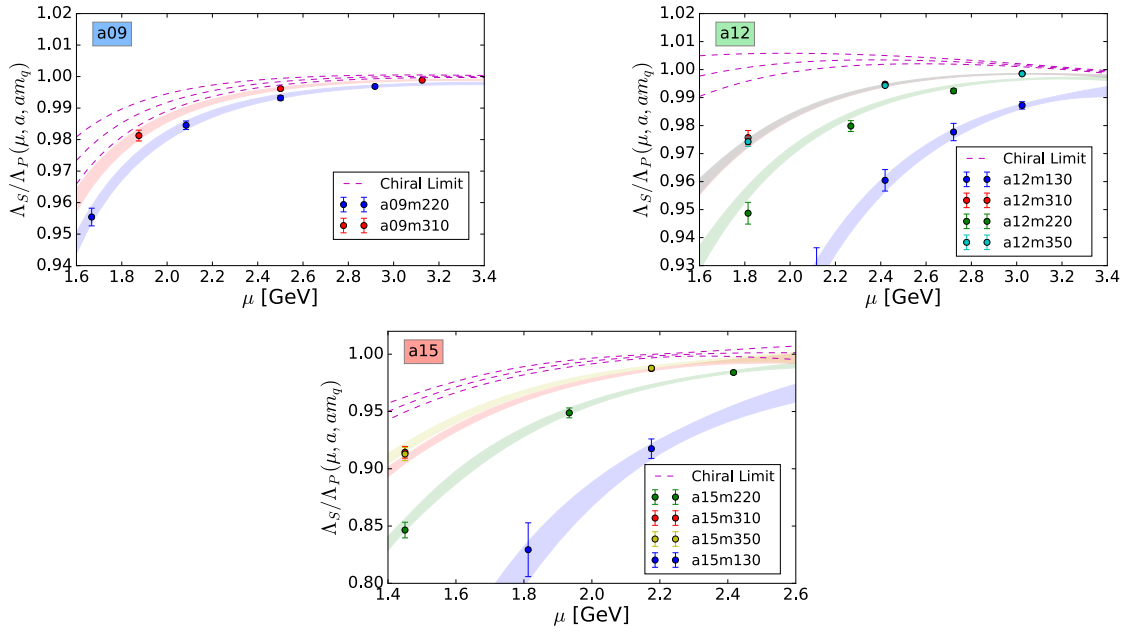
Figure B.13: SMOM $\displaystyle{\not}q$ axial renormalization.
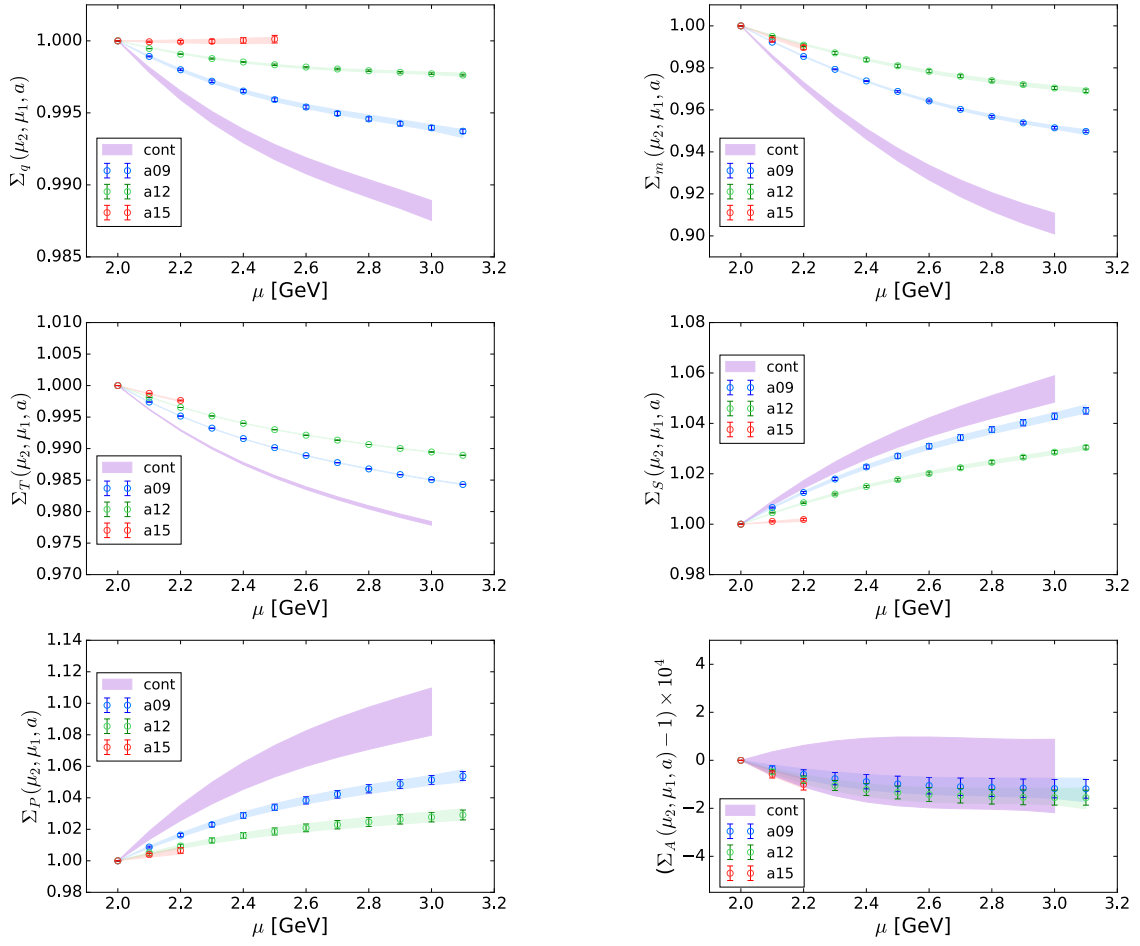
Figure B.14: SMOM γ step scaling functions.
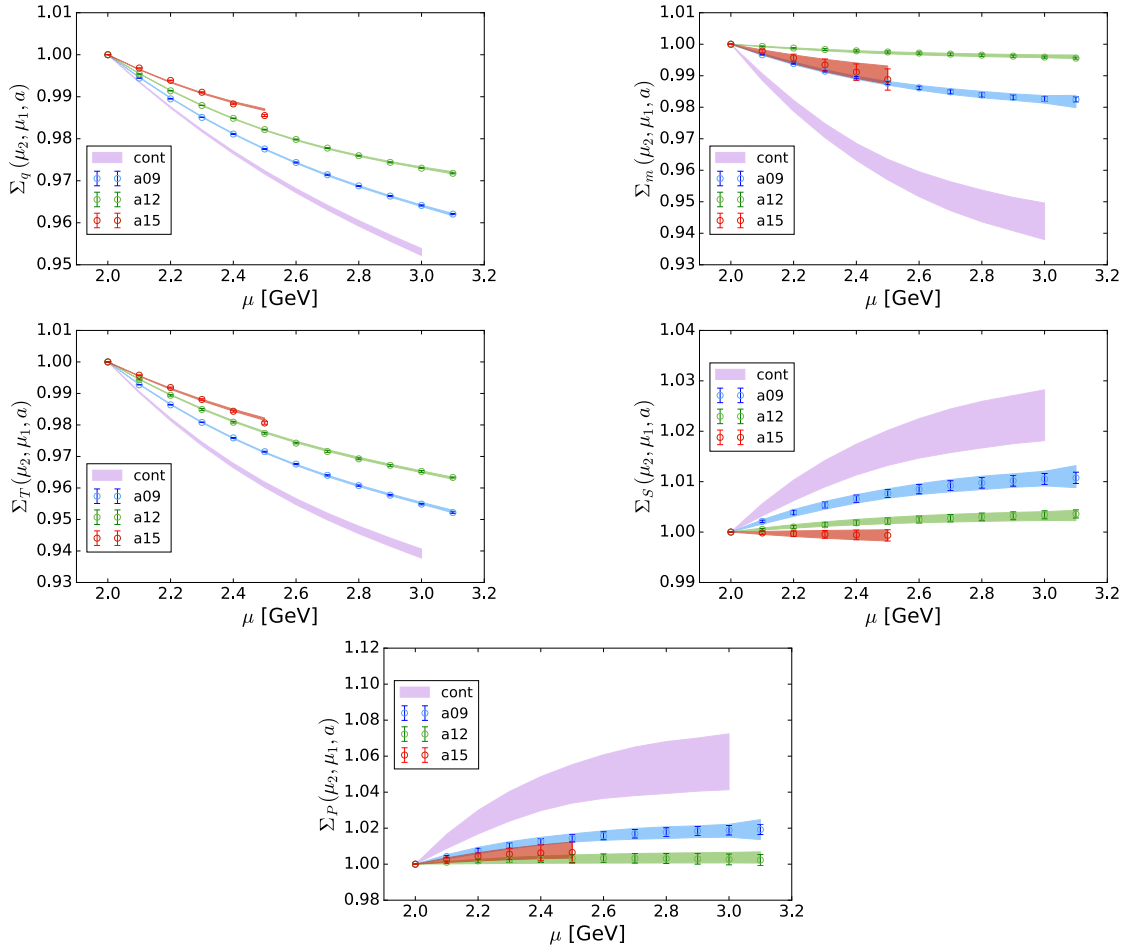
Figure B.15: SMOM $\displaystyle{\not}q$ step scaling functions.
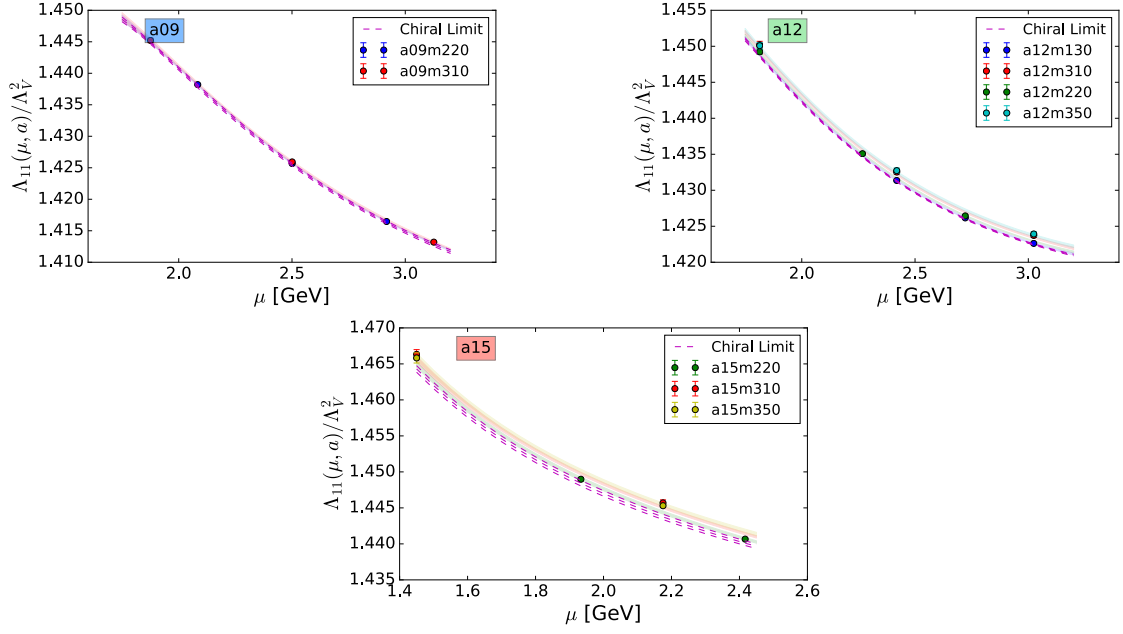
Figure B.16: SMOM γ Λ_{11}/Λ_V^2 renormalization.
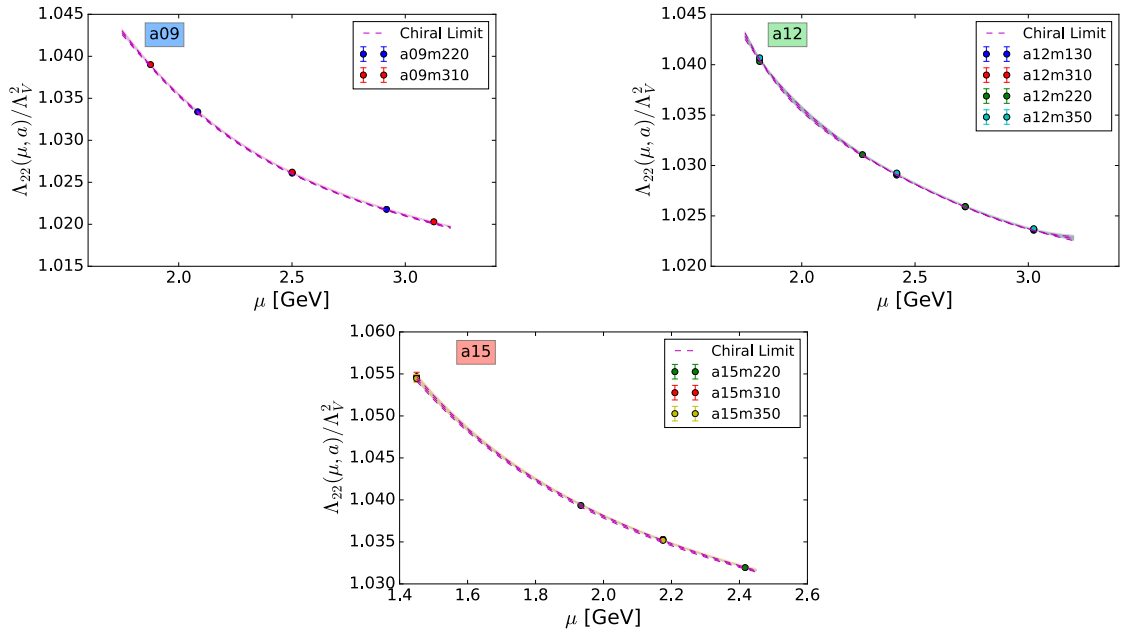
Figure B.17: SMOM γ Λ_{22}/Λ_V^2 renormalization.
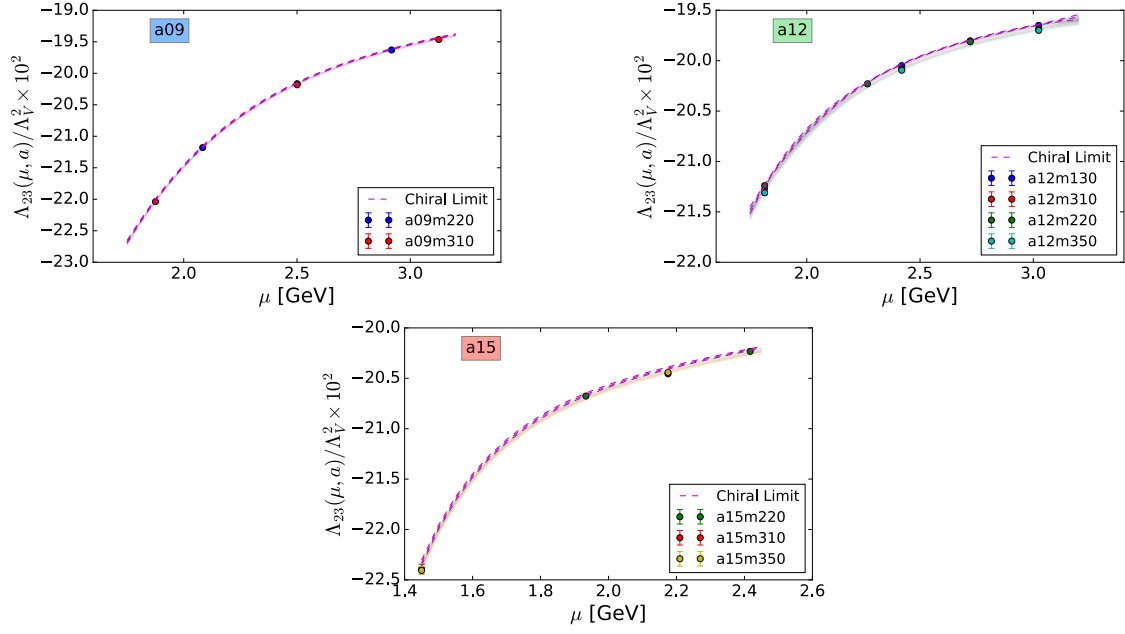
Figure B.18: SMOM γ Λ_{23}/Λ_V^2 renormalization.
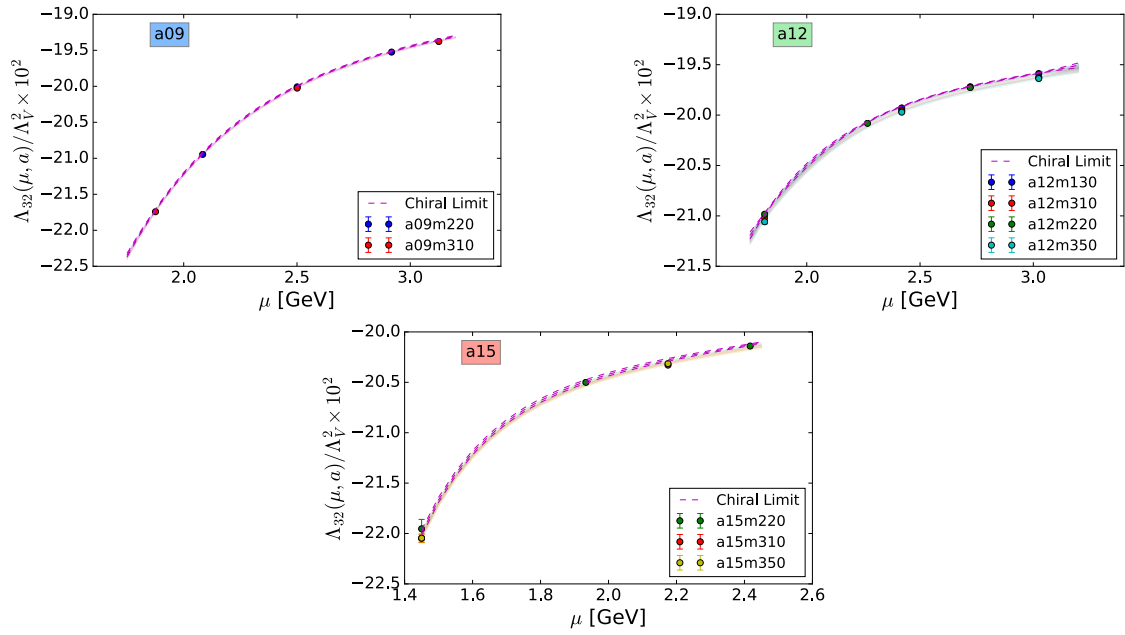
Figure B.19: SMOM γ Λ_{32}/Λ_V^2 renormalization.
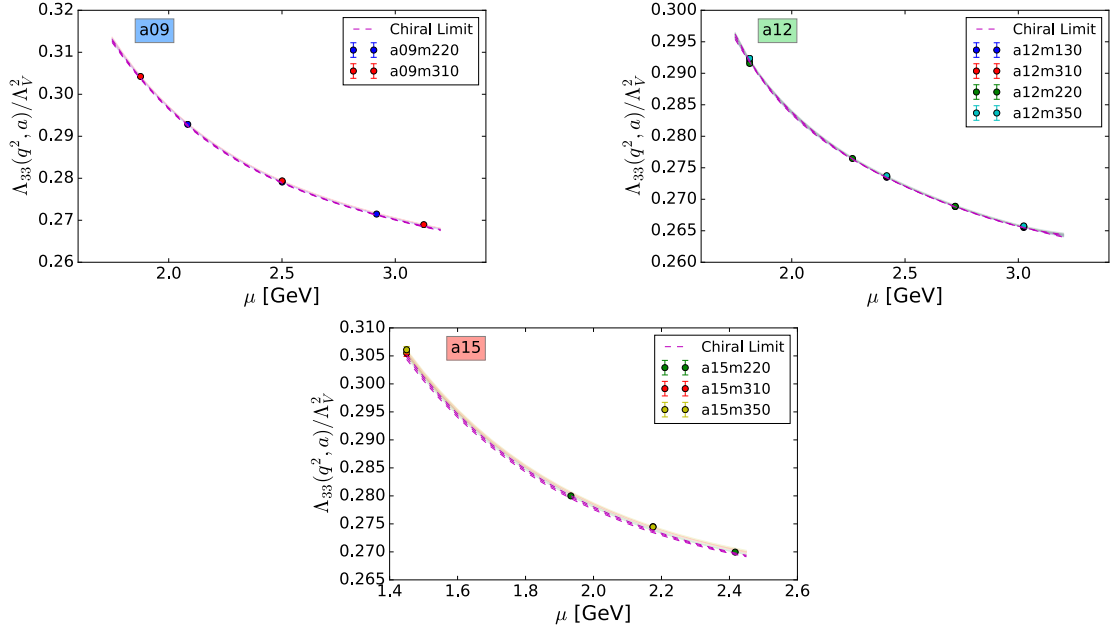
Figure B.20: SMOM γ Λ_{33}/Λ_V^2 renormalization.
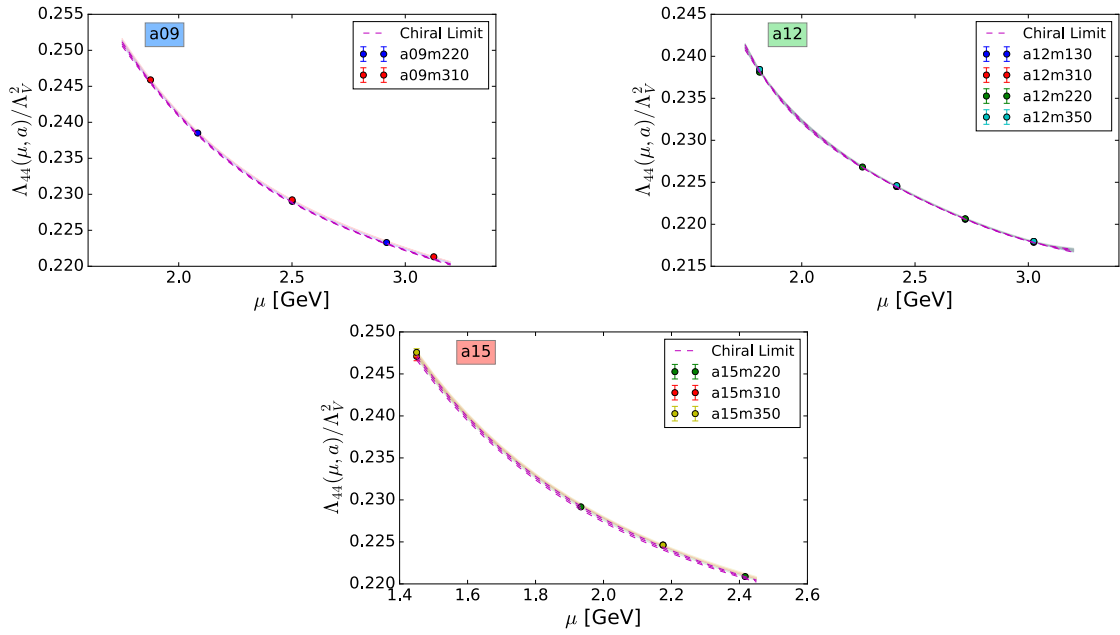
Figure B.21: SMOM γ Λ_{44}/Λ_V^2 renormalization.
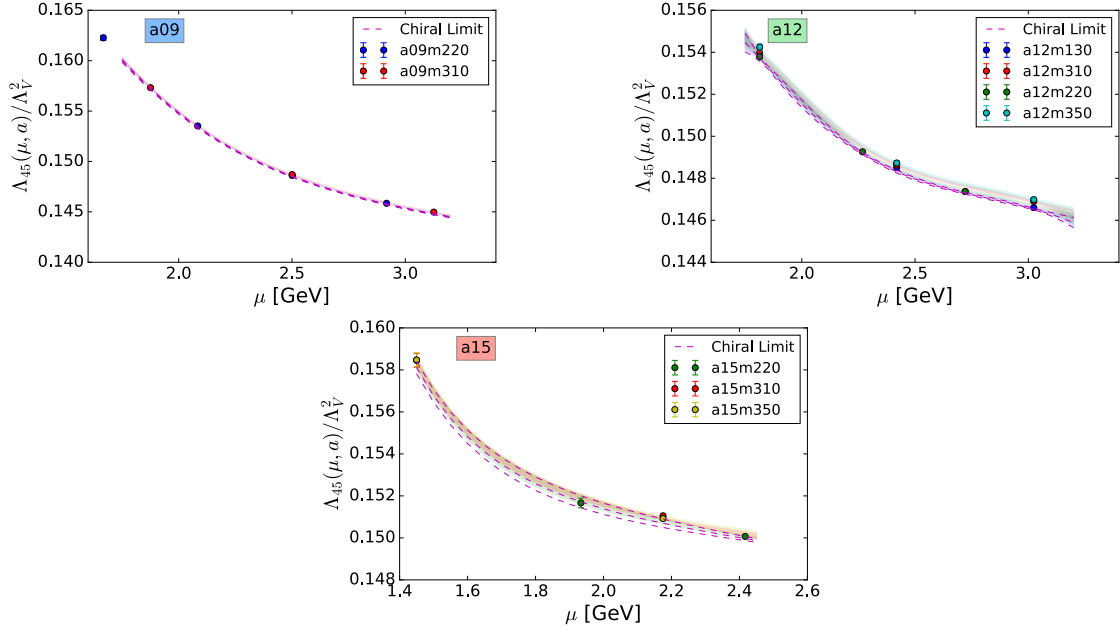
Figure B.22: SMOM γ Λ_{45}/Λ_V^2 renormalization.
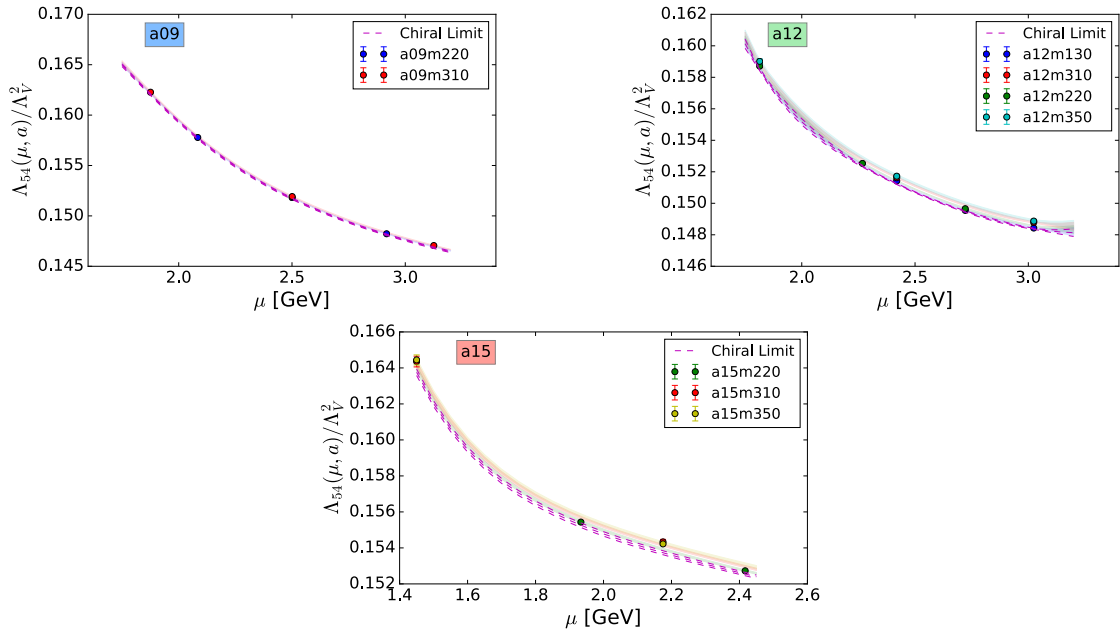
Figure B.23: SMOM γ Λ_{54}/Λ_V^2 renormalization.
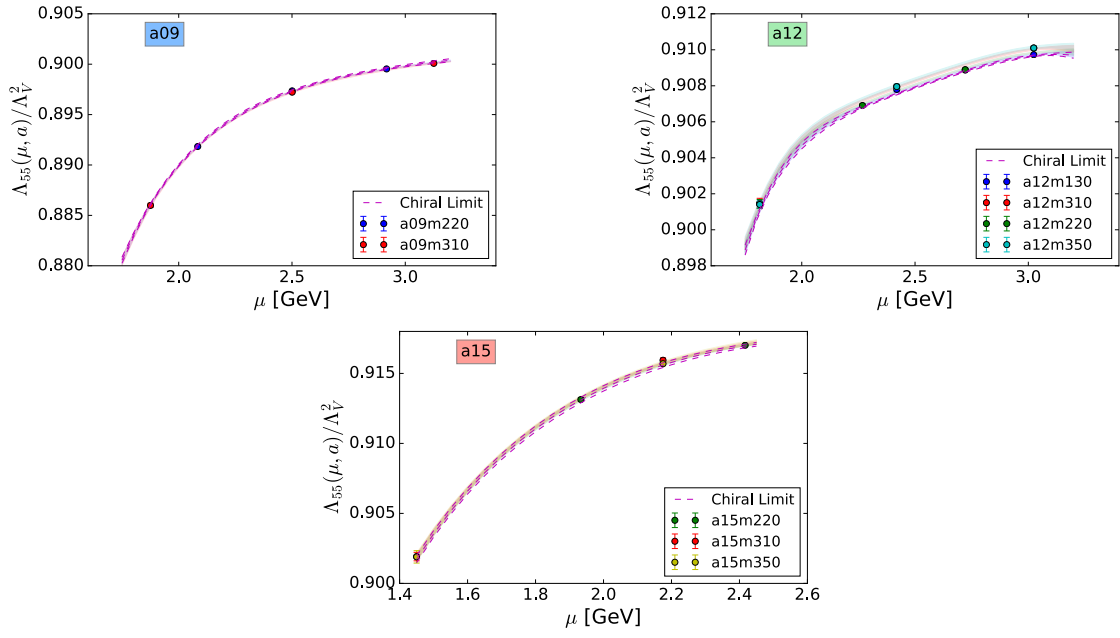
Figure B.24: SMOM $\gamma\ \Lambda_{55}/\Lambda_V^2$ renormalization.
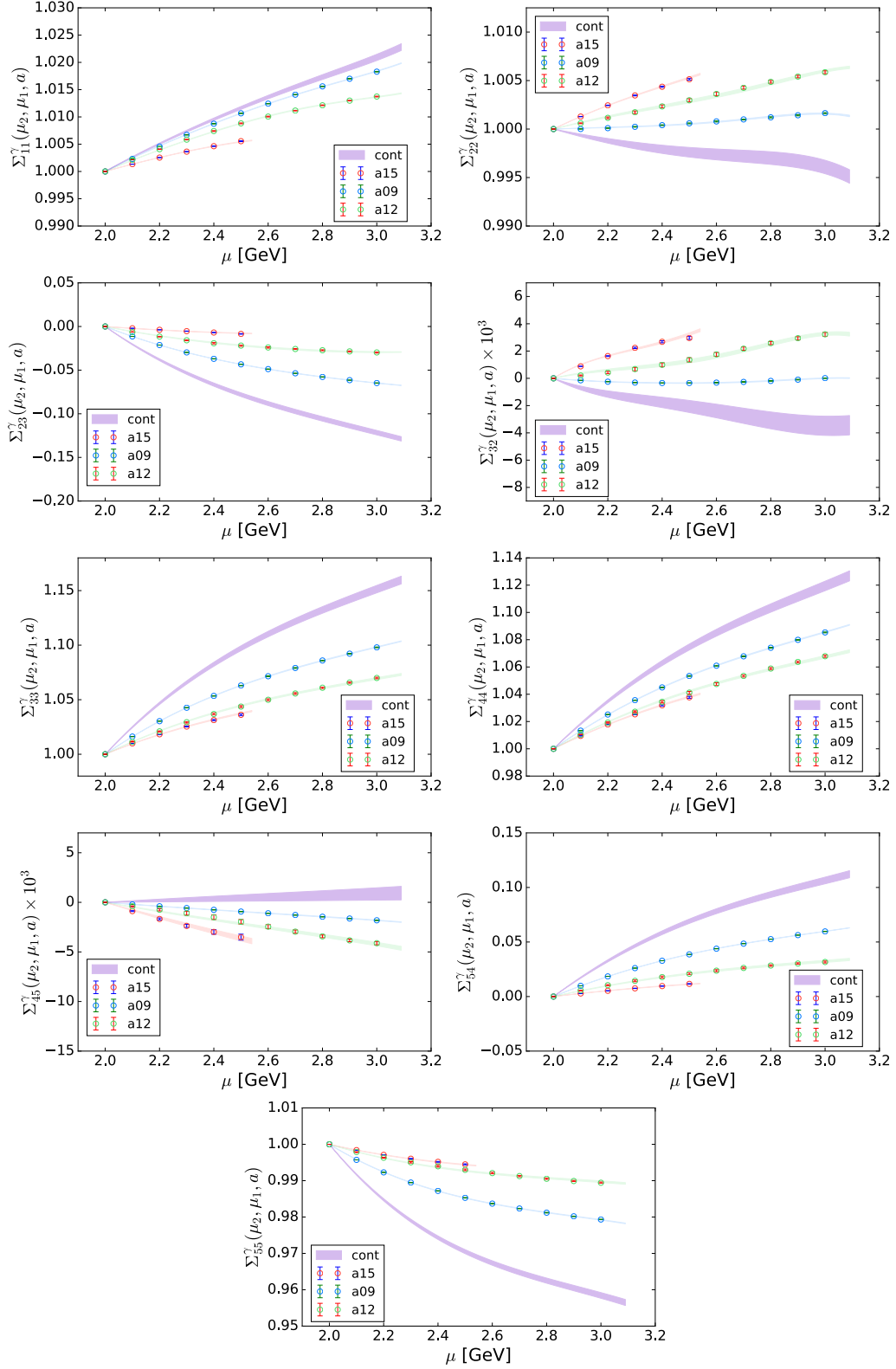
Figure B.25: SMOM γ step scaling functions. $\mu_1 = 2$ GeV.
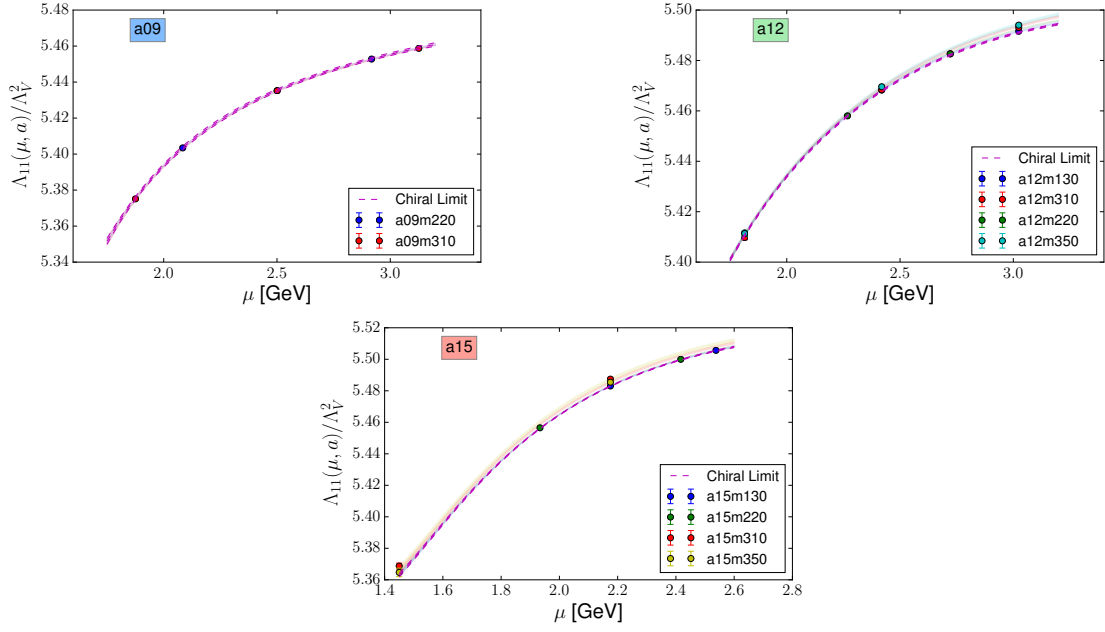
Figure B.26: SMOM $\displaystyle{\not}q$ Λ_{11}/Λ_V^2 renormalization.
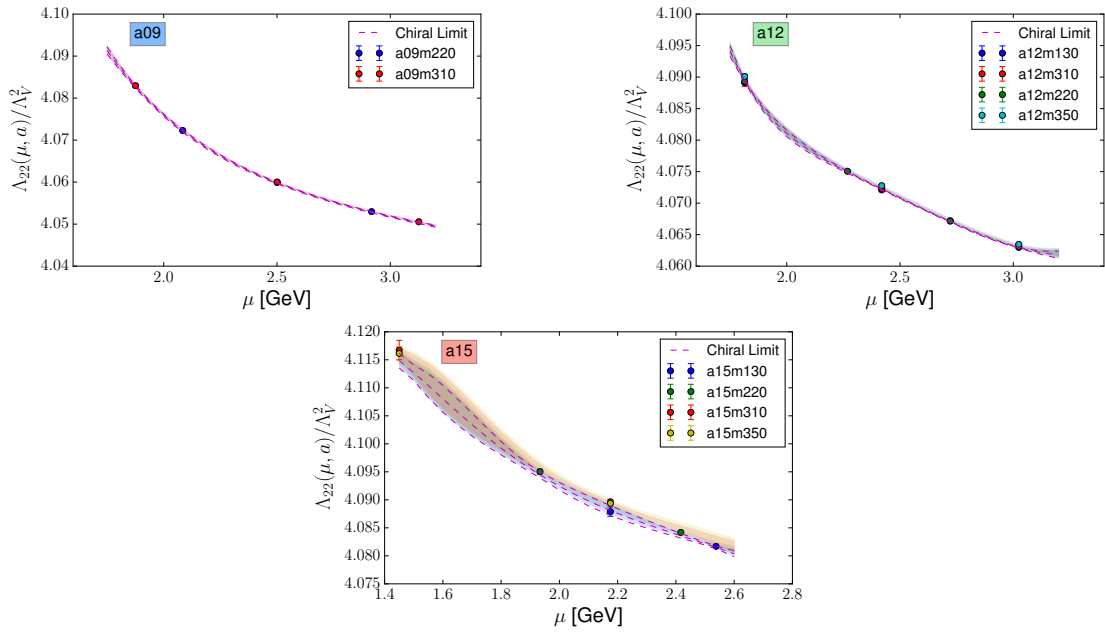
Figure B.27: SMOM $\displaystyle{\not}q$ Λ_{22}/Λ_V^2 renormalization.
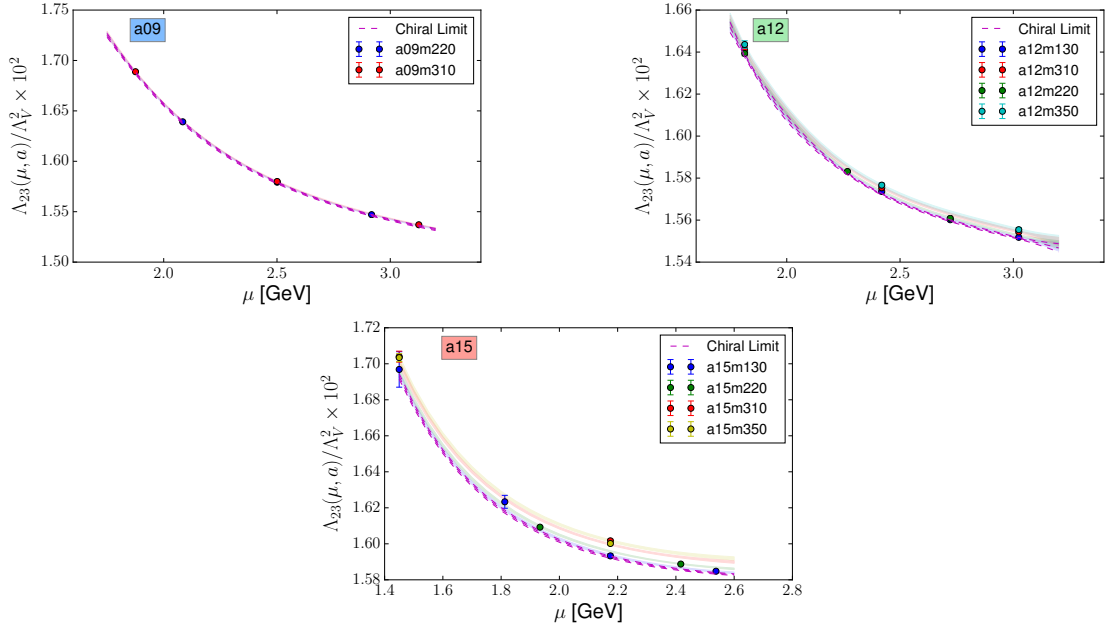
Figure B.28: SMOM $\not q$ Λ_{23}/Λ_V^2 renormalization.
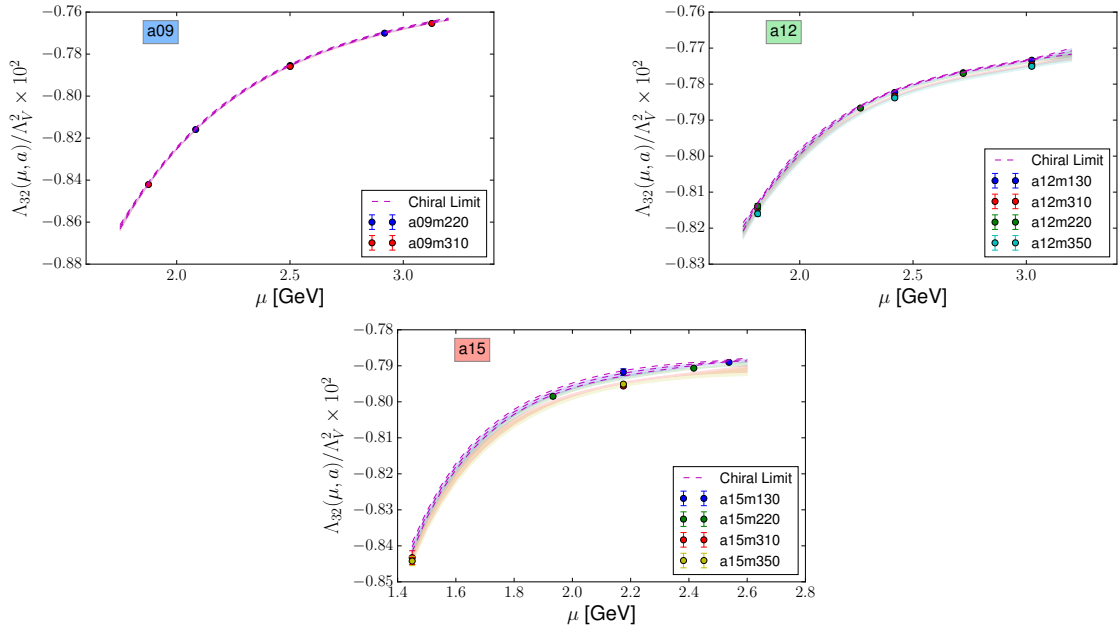
Figure B.29: SMOM $\not q$ Λ_{32}/Λ_V^2 renormalization.
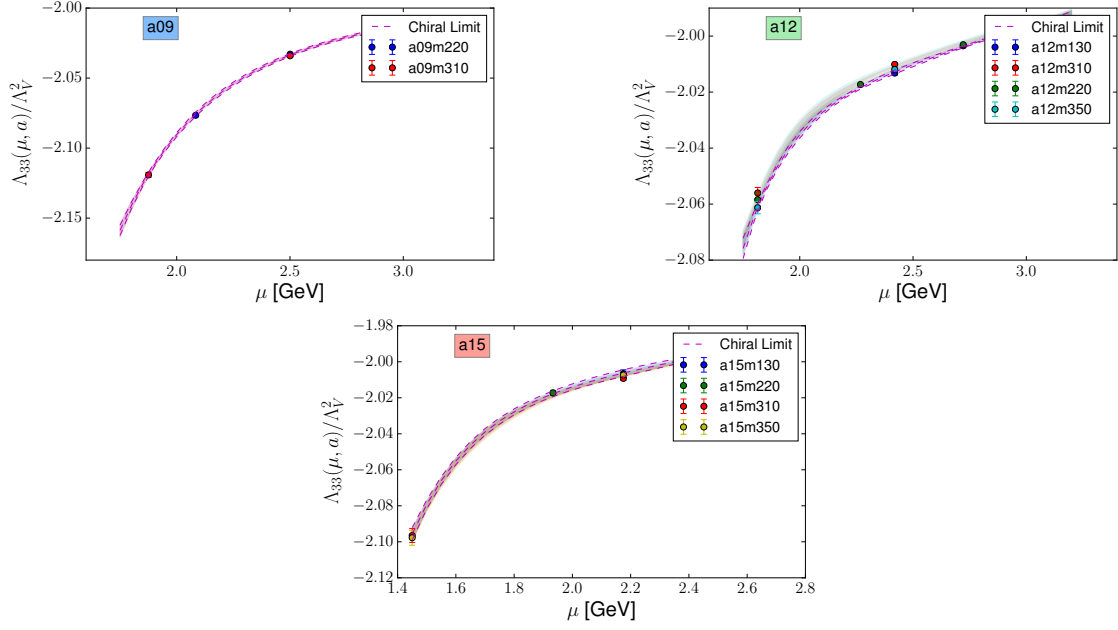
Figure B.30: SMOM $\displaystyle{\not}q$ Λ_{33}/Λ_V^2 renormalization.
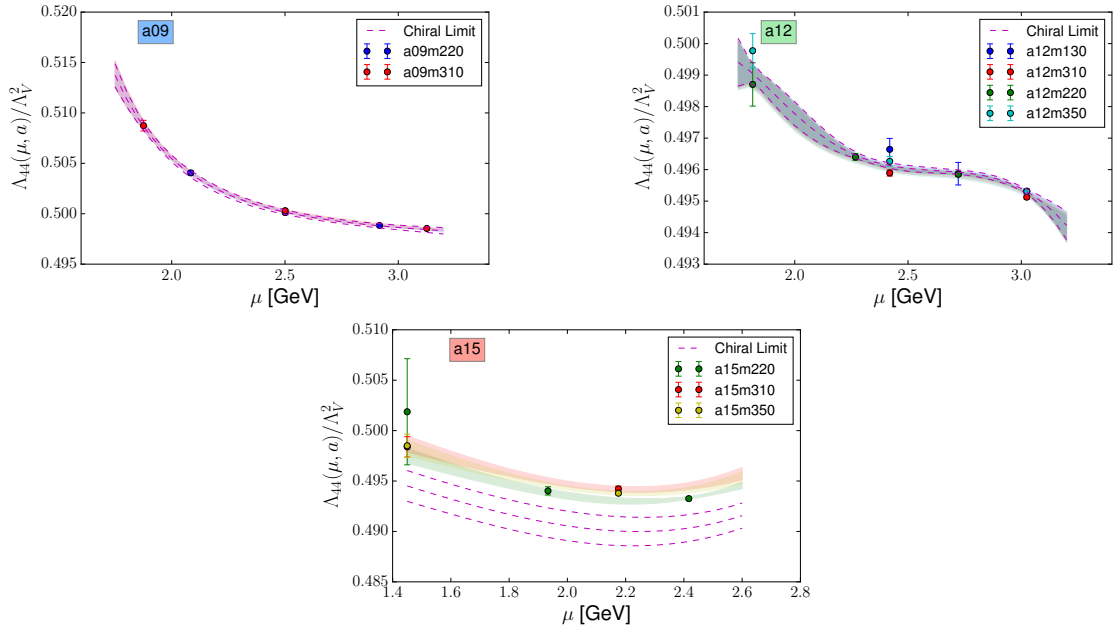
Figure B.31: SMOM $\displaystyle{\not}q$ Λ_{44}/Λ_V^2 renormalization.
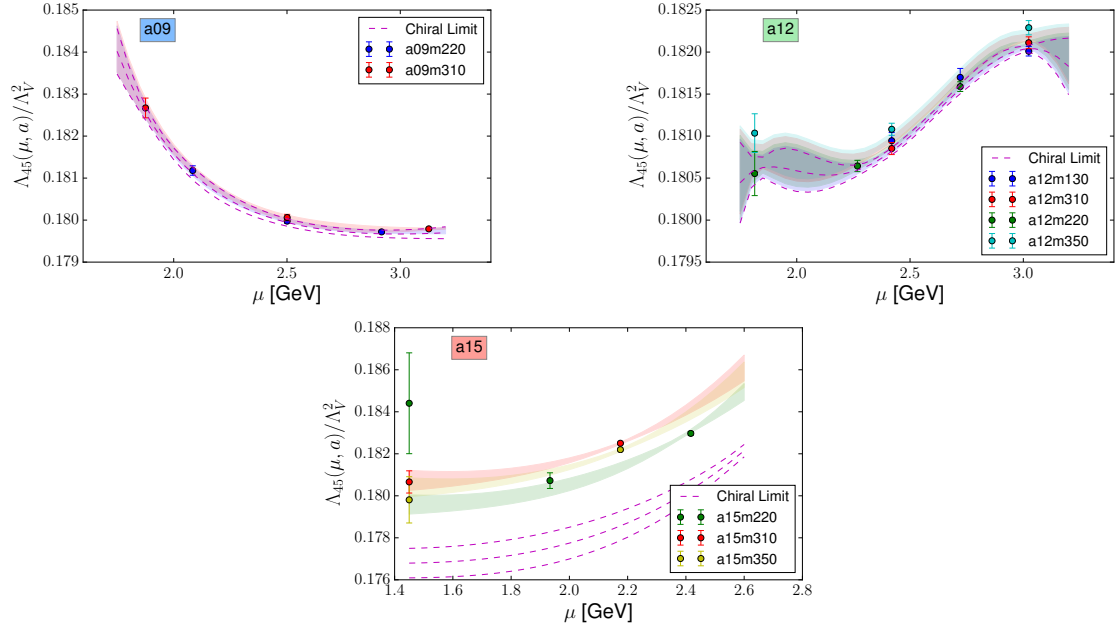
Figure B.32: SMOM $\displaystyle{\not}q$ Λ_{45}/Λ_V^2 renormalization.
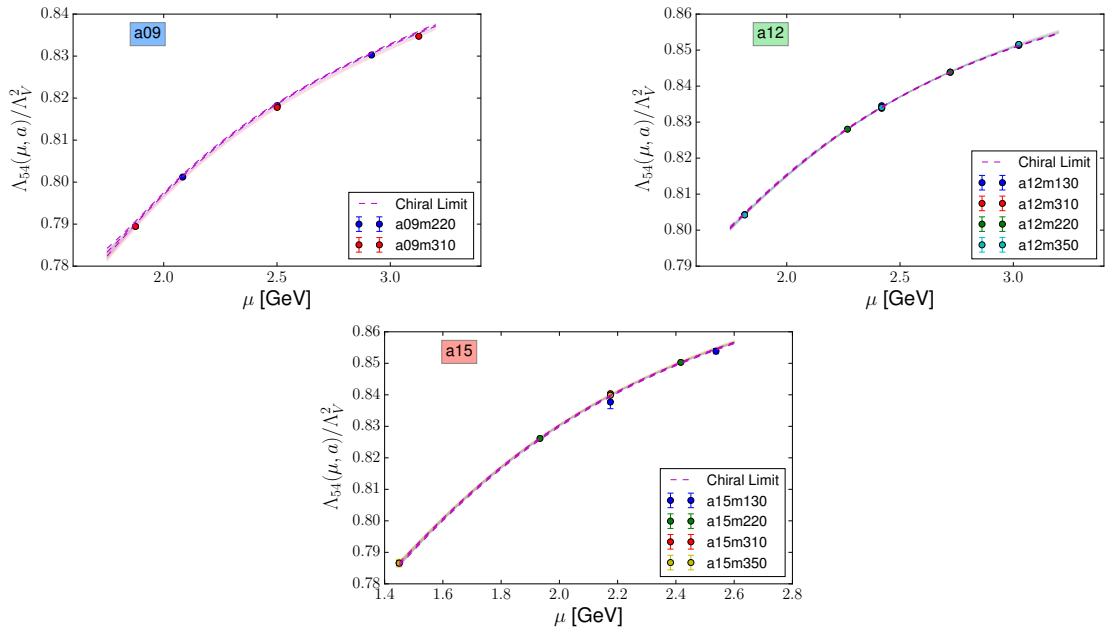
Figure B.33: SMOM $\displaystyle{\not}q$ Λ_{54}/Λ_V^2 renormalization.
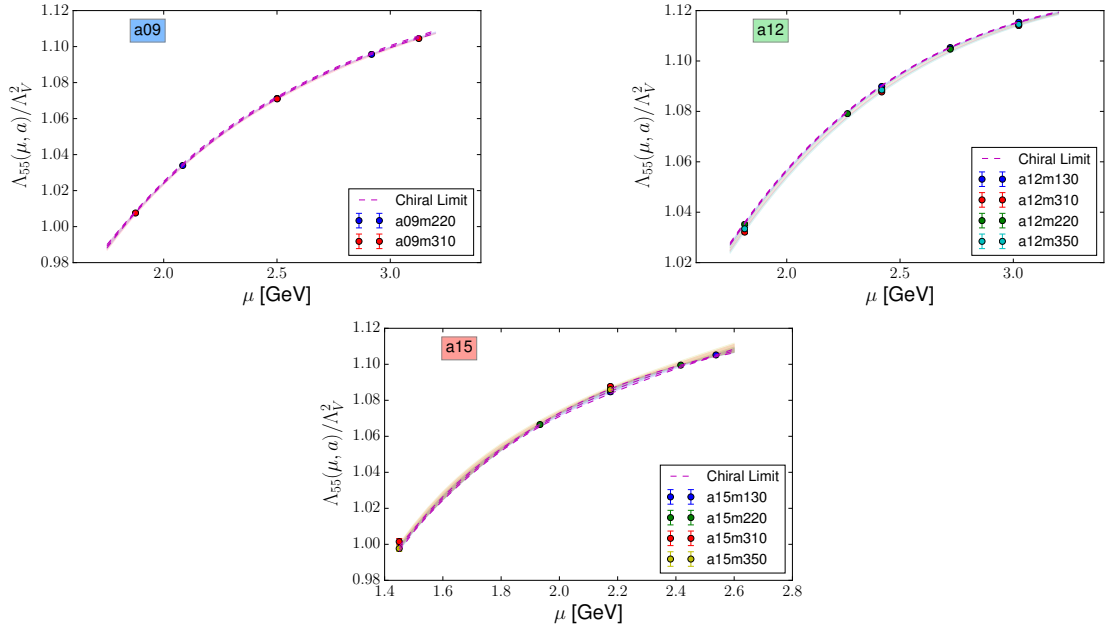
Figure B.34: SMOM $\not{q}$ Λ_{55}/Λ_V^2 renormalization.
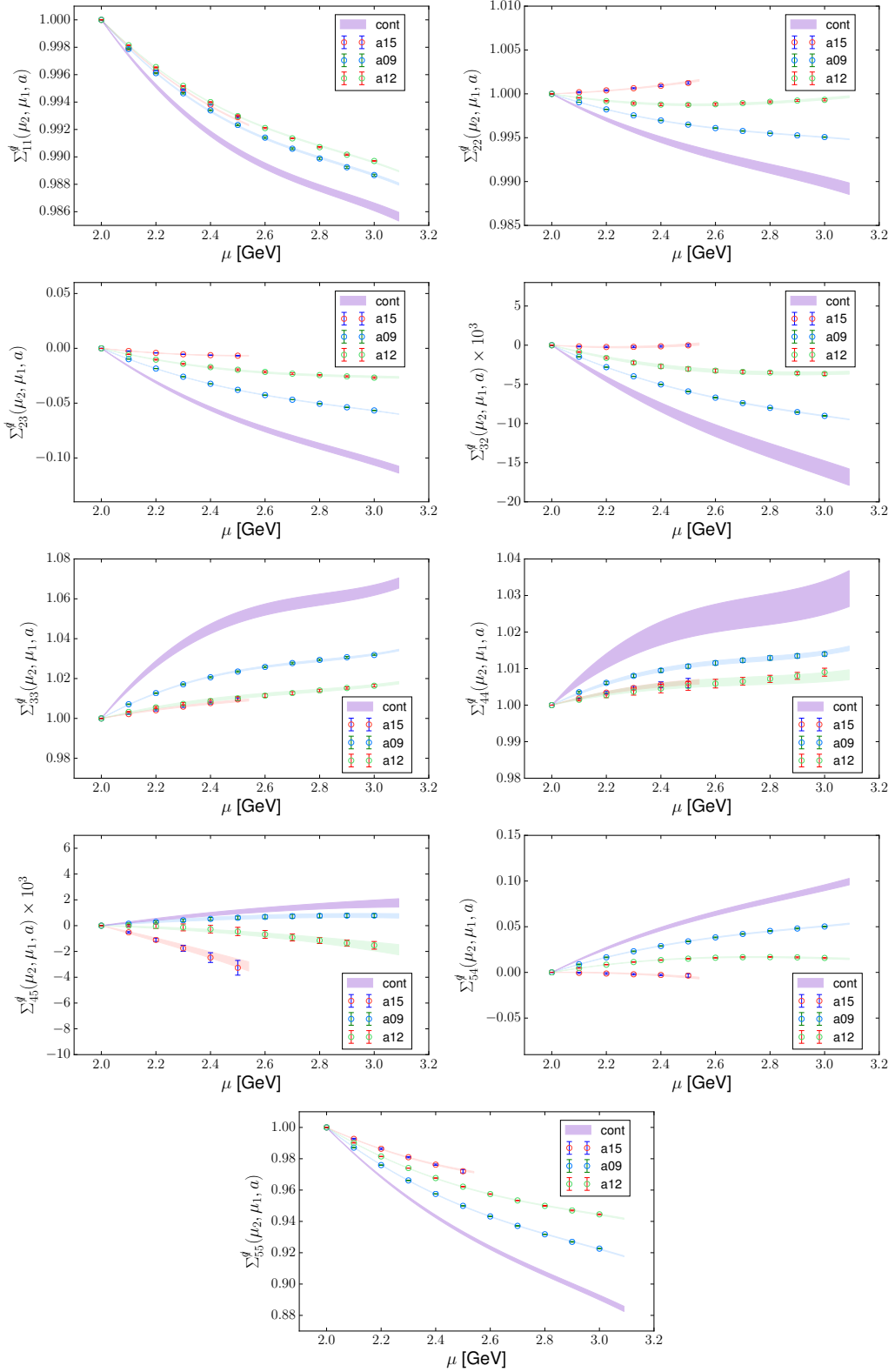
Figure B.35: SMOM $\not{q}$ step scaling functions. $\mu_1 = 2$ GeV.

Appendix C

C.1 Extended Results for CPV Couplings Project

We collect the relevant figures illustrating the analysis of the two and three point correlation functions for the four matrix elements (5.14).

C.1.1 m_{eff}
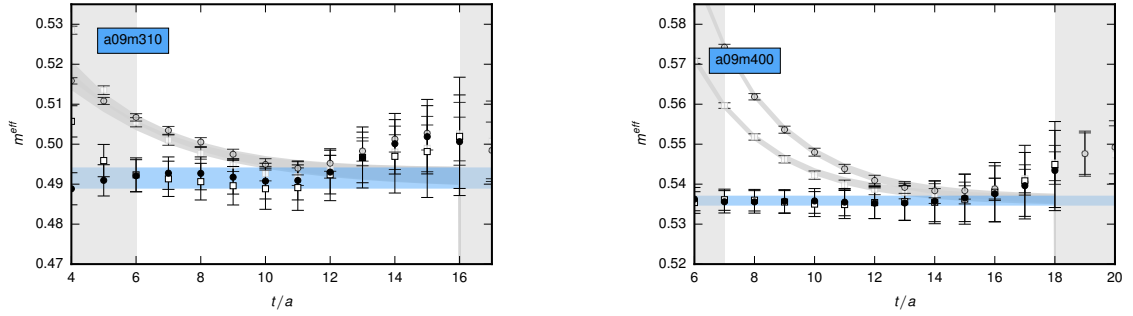
Figure C.1: m_{eff} for the a09 ensembles.
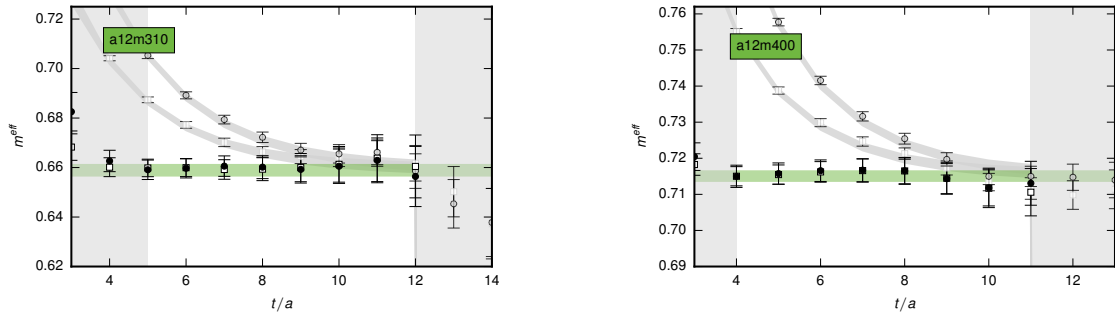
Figure C.2: m_{eff} for the a12 ensembles.
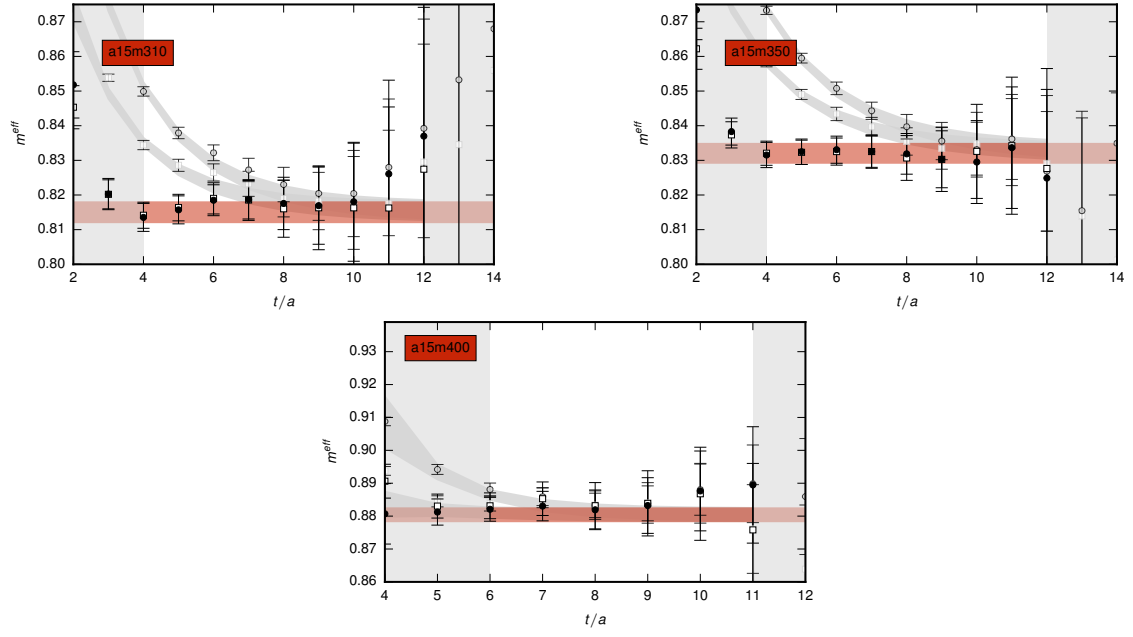
Figure C.3: m_{eff} for the a15 ensembles.
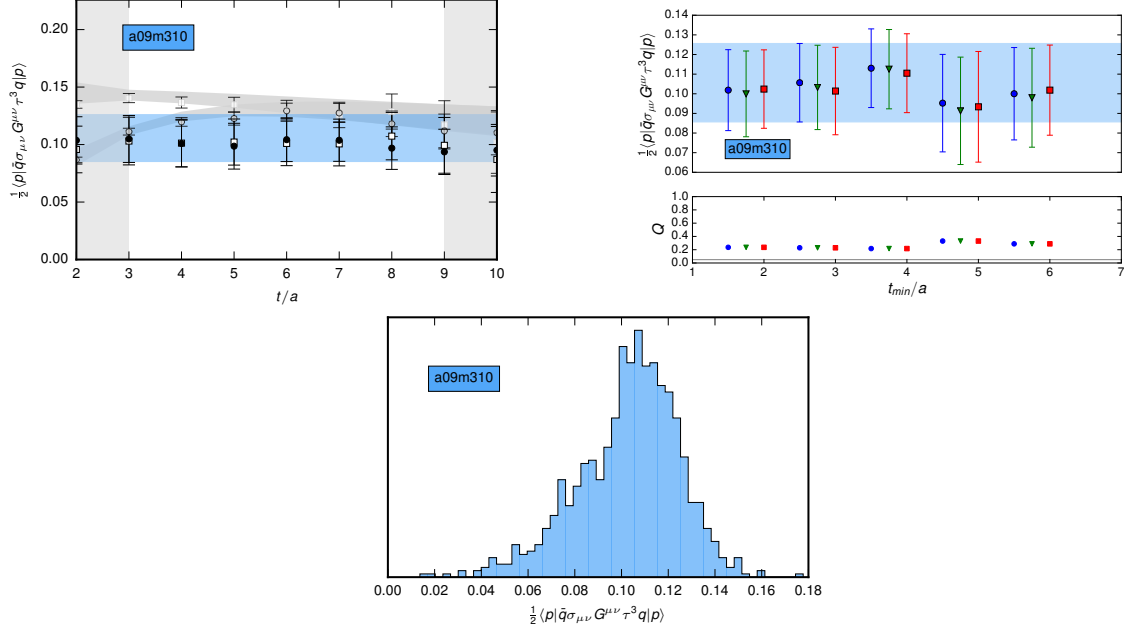
Figure C.4: Analysis of the a09m310 iso-vector qCMDM operator.
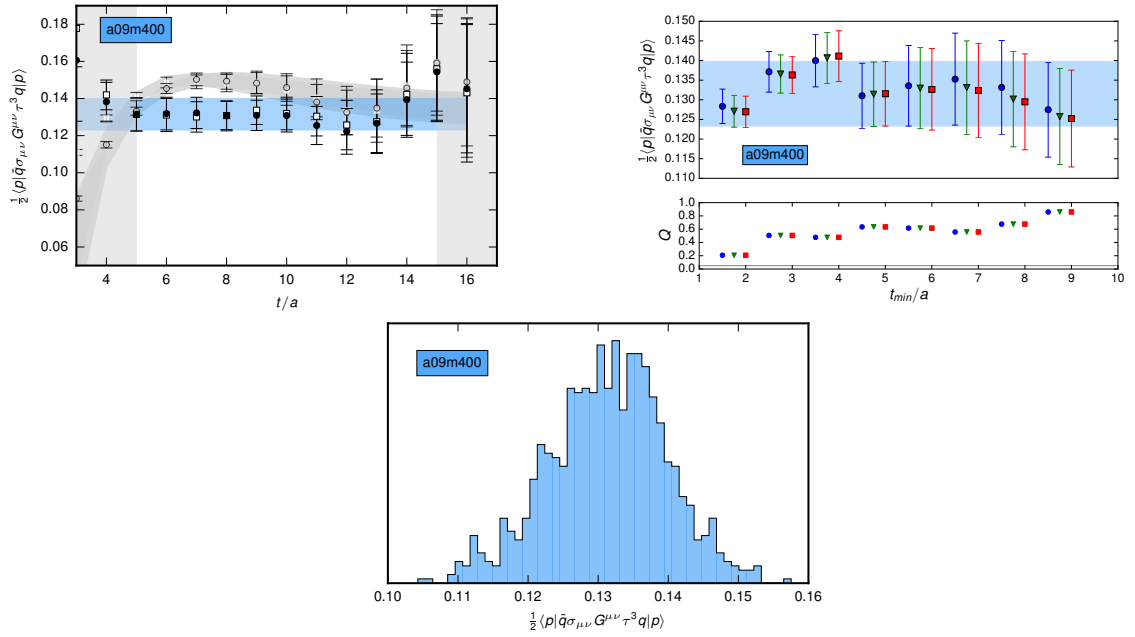
Figure C.5: Analysis of the a09m400 iso-vector qCMDM operator.
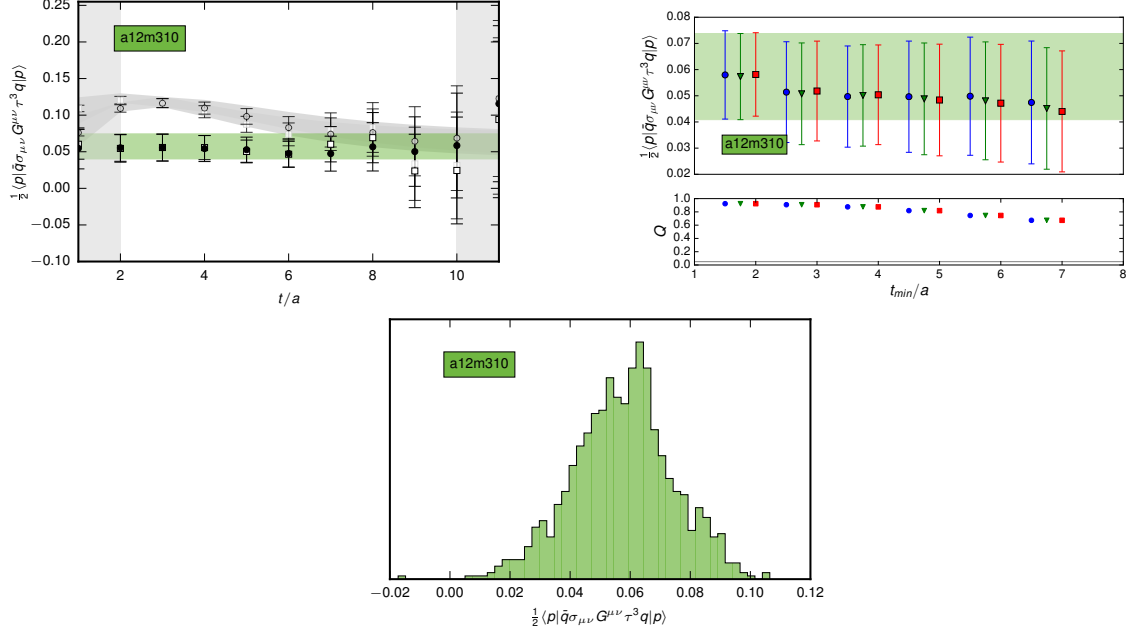
Figure C.6: Analysis of the a12m310 iso-vector qCMDM operator.
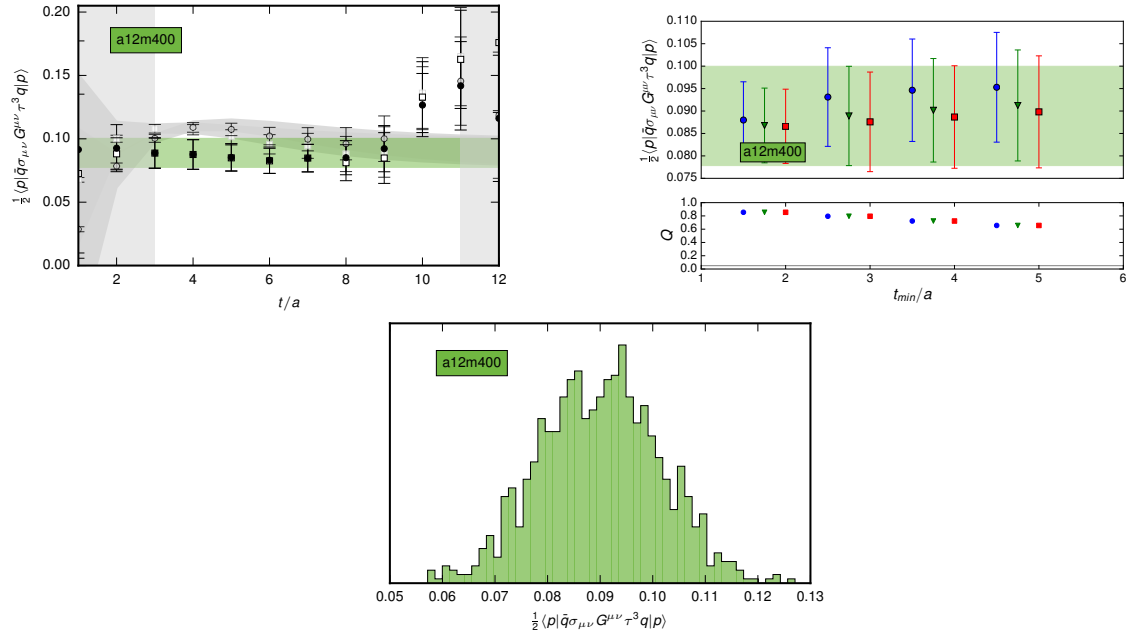
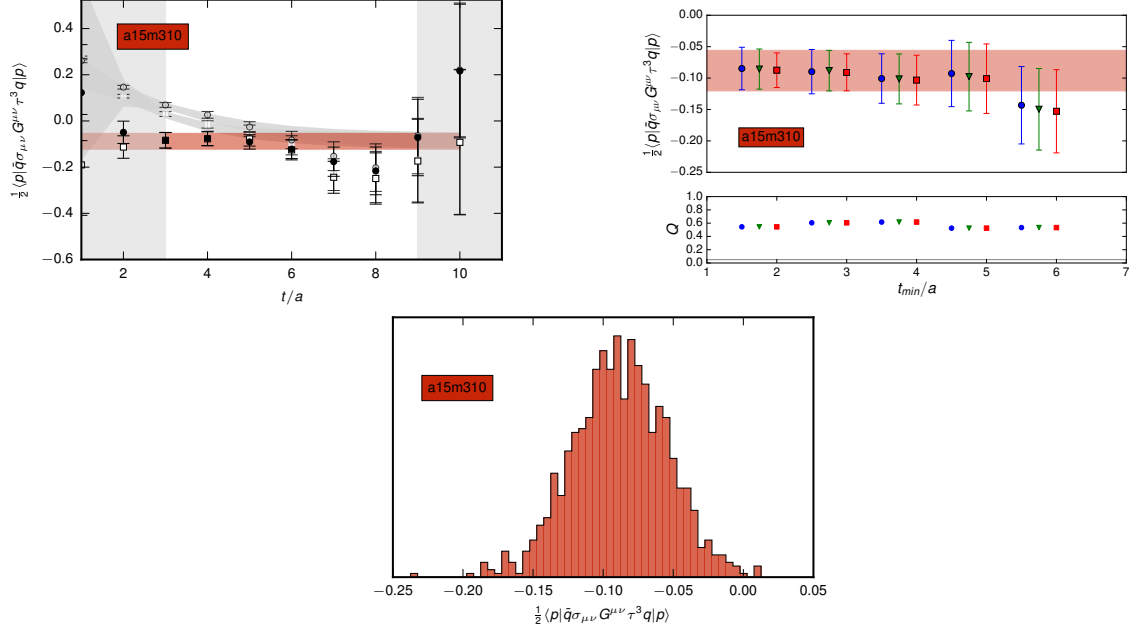**Figure C.7**: Analysis of the a12m400 iso-vector qCMDM operator.

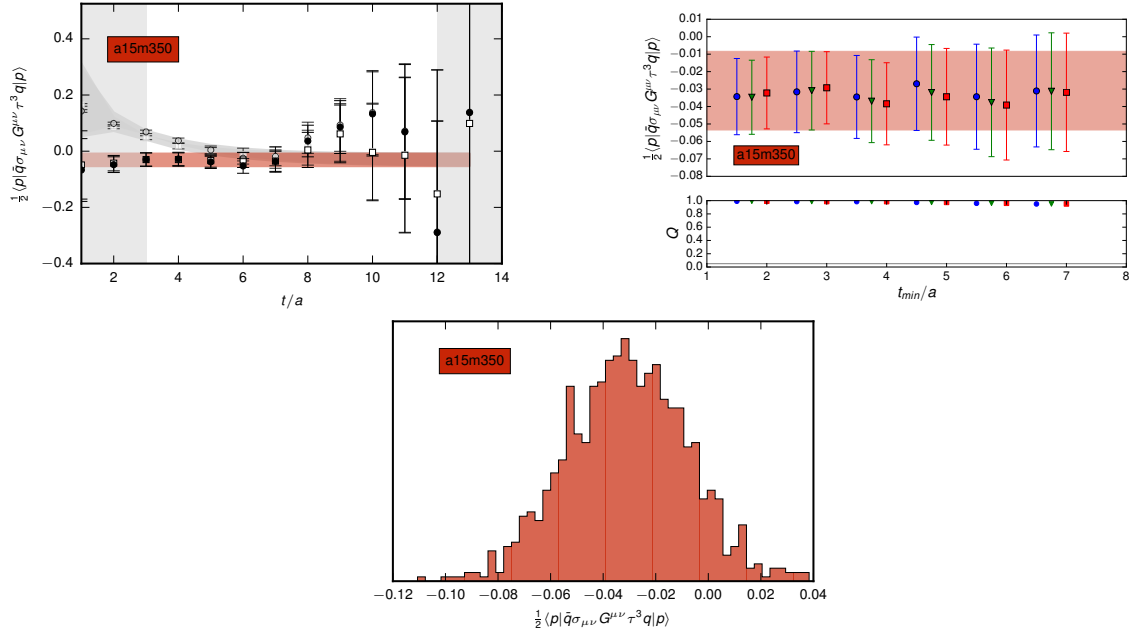**Figure C.8**: Analysis of the a15m310 iso-vector qCMDM operator.

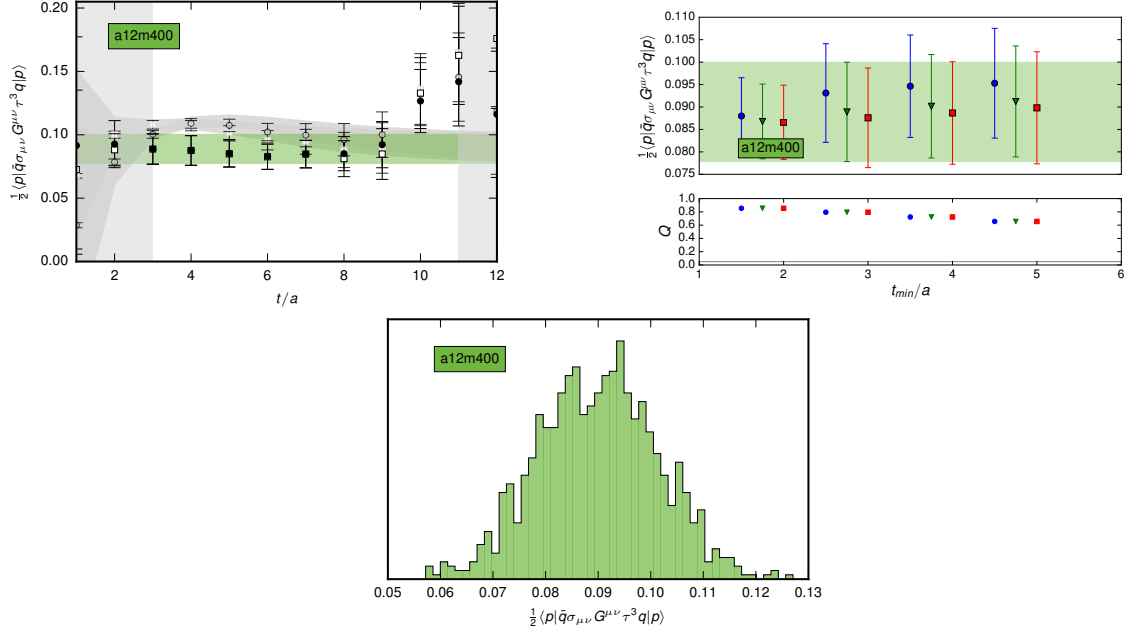**Figure C.9**: Analysis of the a15m350 iso-vector qCMDM operator.

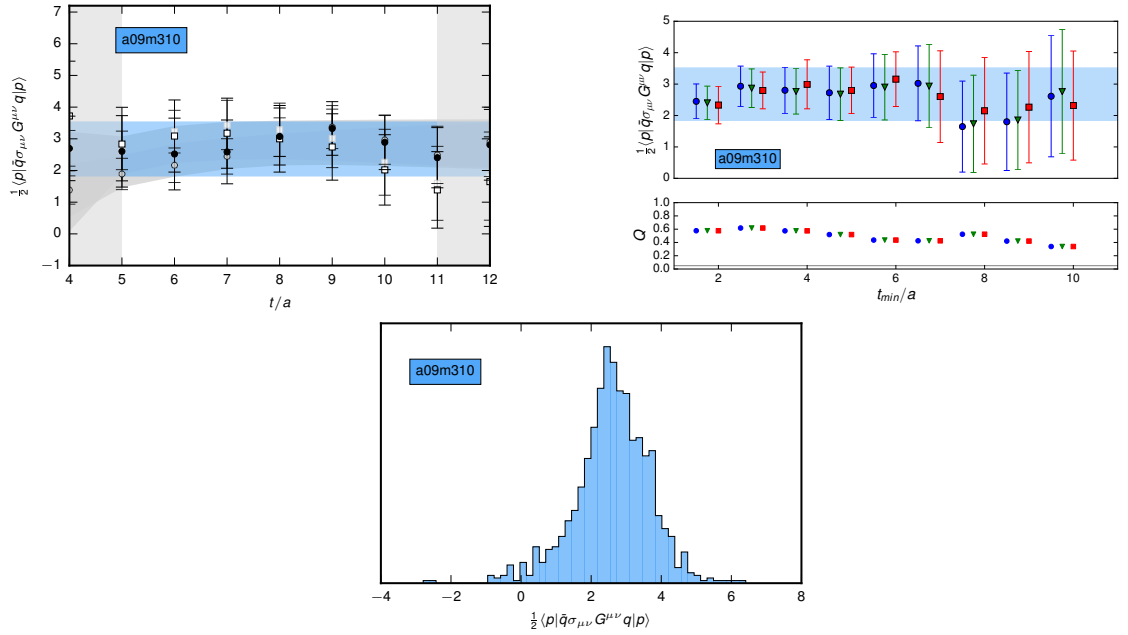**Figure C.10**: Analysis of the a15m400 iso-vector qCMDM operator.

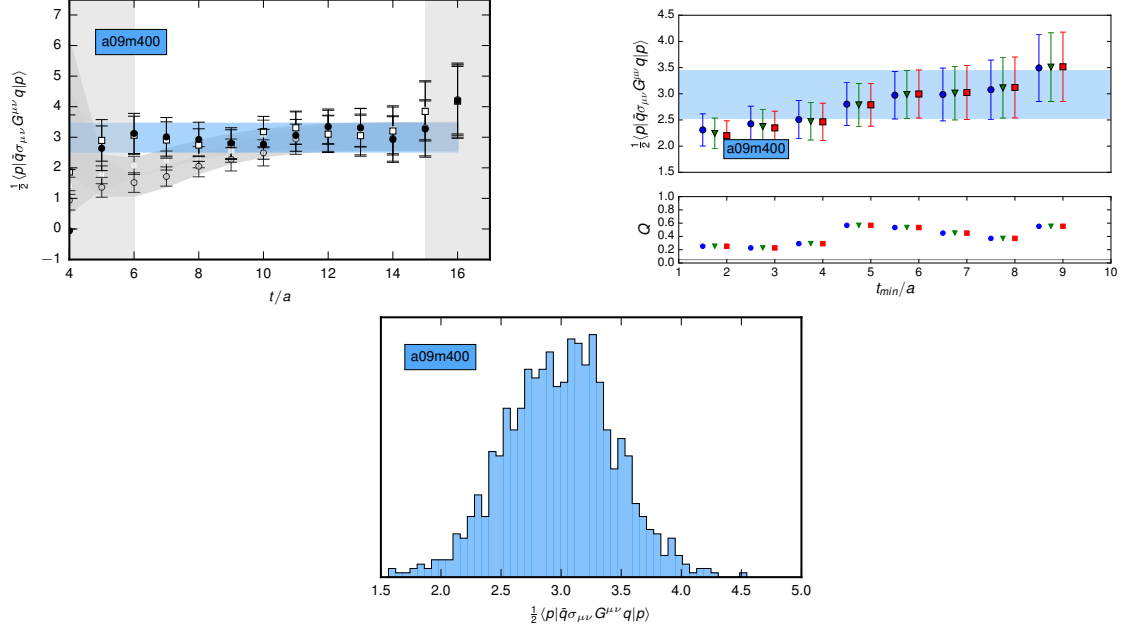**Figure C.11**: Analysis of the a09m310 iso-scalar qCMDM operator.

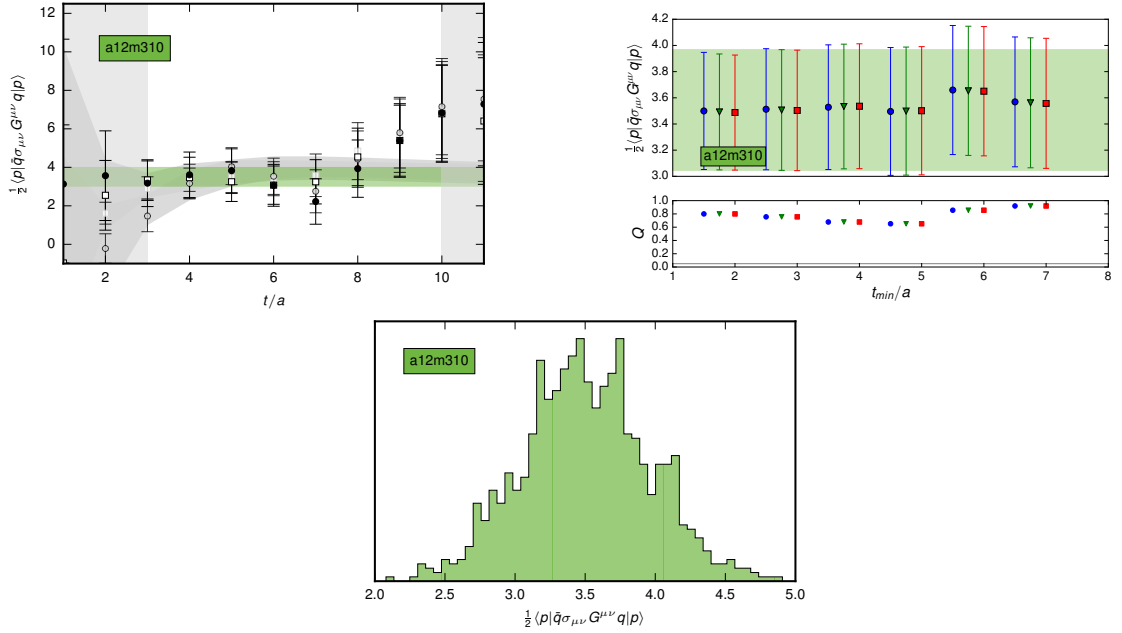**Figure C.12**: Analysis of the a09m400 iso-scalar qCMDM operator.

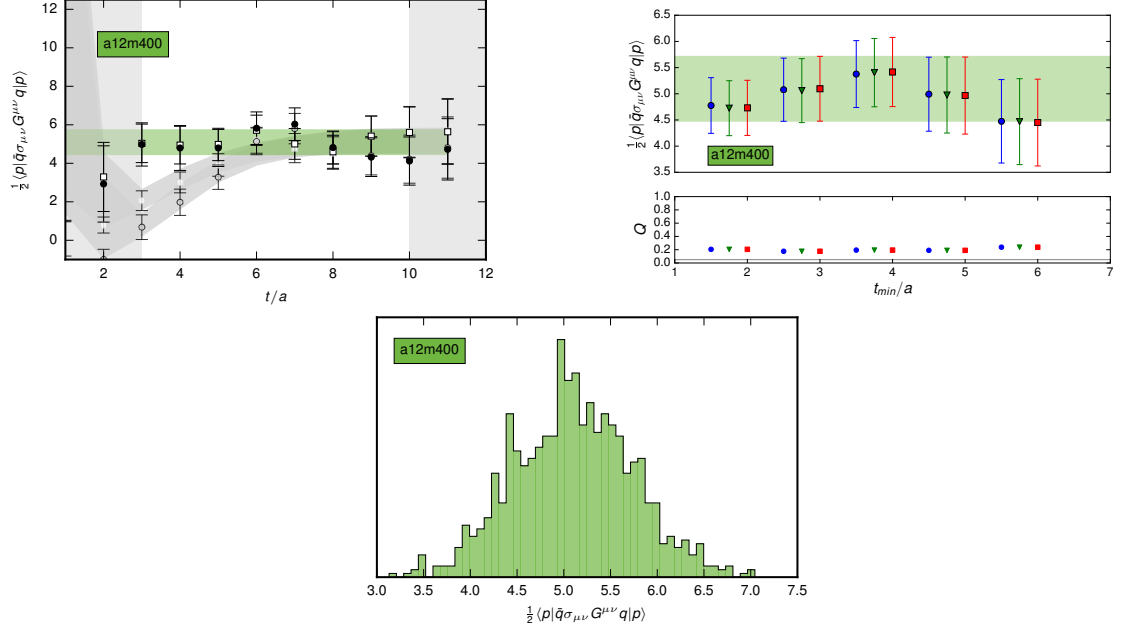**Figure C.13**: Analysis of the a12m310 iso-scalar qCMDM operator.

Figure C.14: Analysis of the a12m400 iso-scalar qCMDM operator.

Figure C.15: Analysis of the a15m310 iso-scalar qCMDM operator.

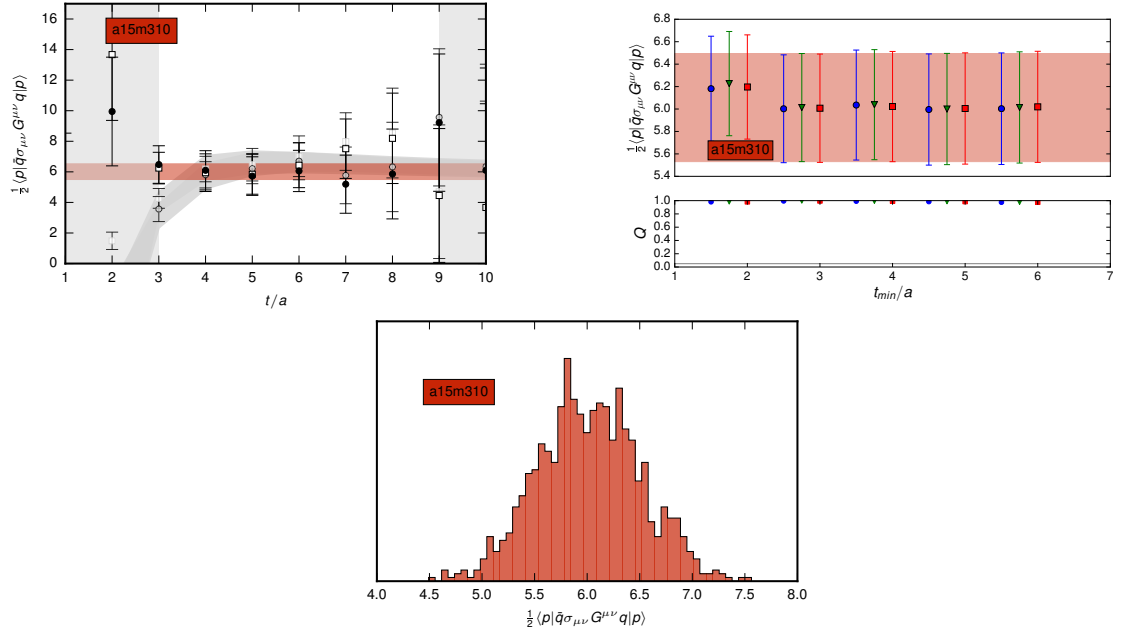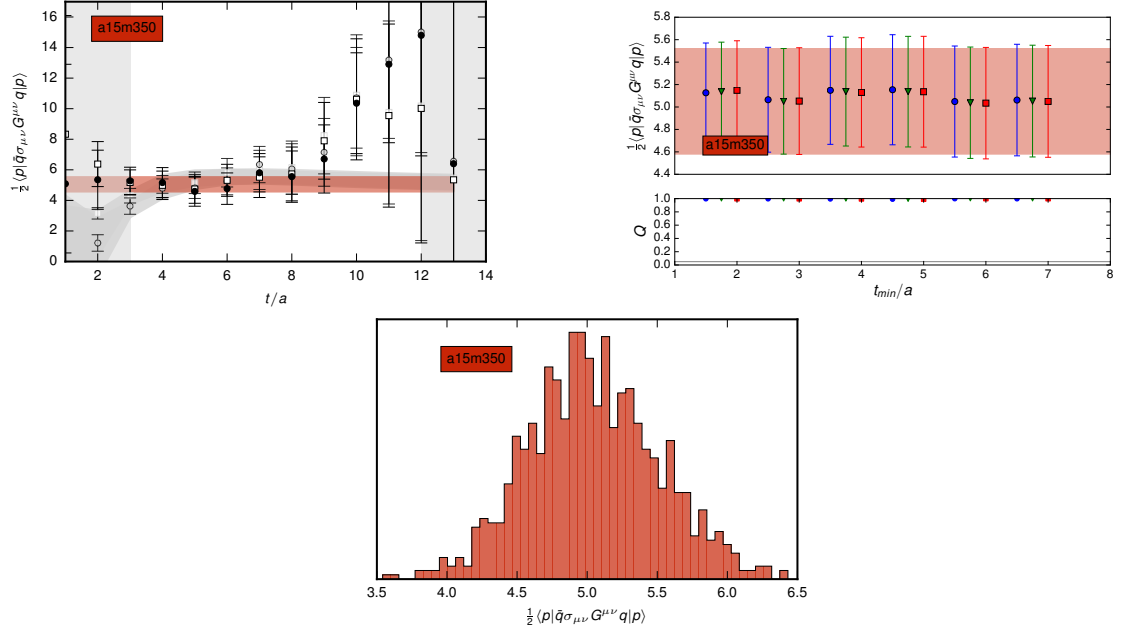**Figure C.16**: Analysis of the a15m350 iso-scalar qCMDM operator.
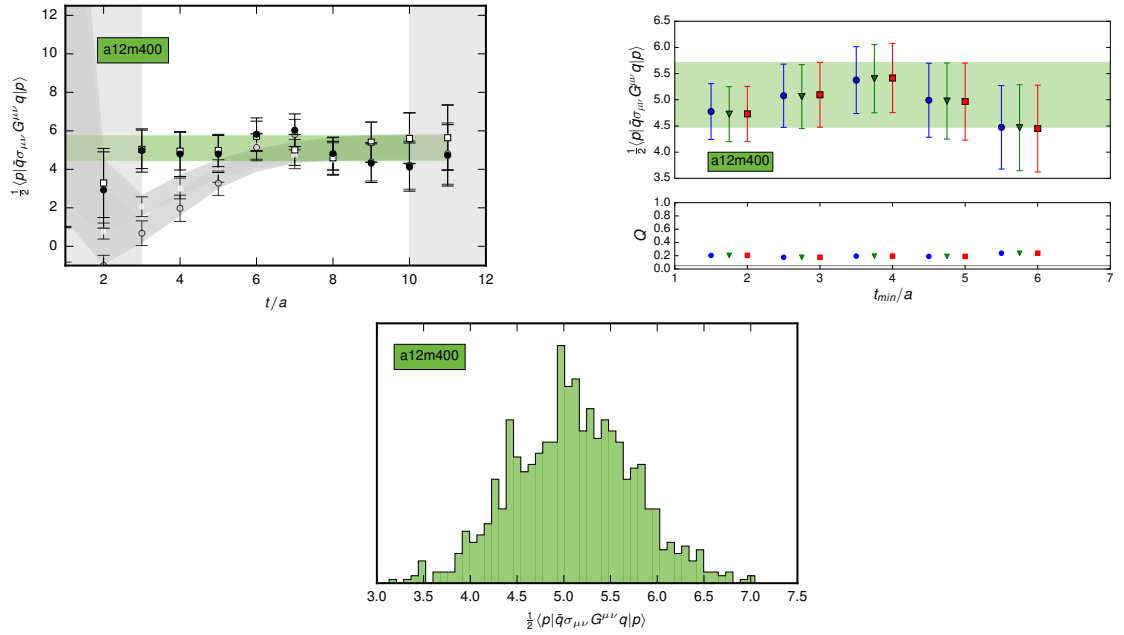
Figure C.17: Analysis of the a15m400 iso-scalar qCMDM operator.

Figure C.18: Analysis of the a09m310 iso-vector scalar operator.
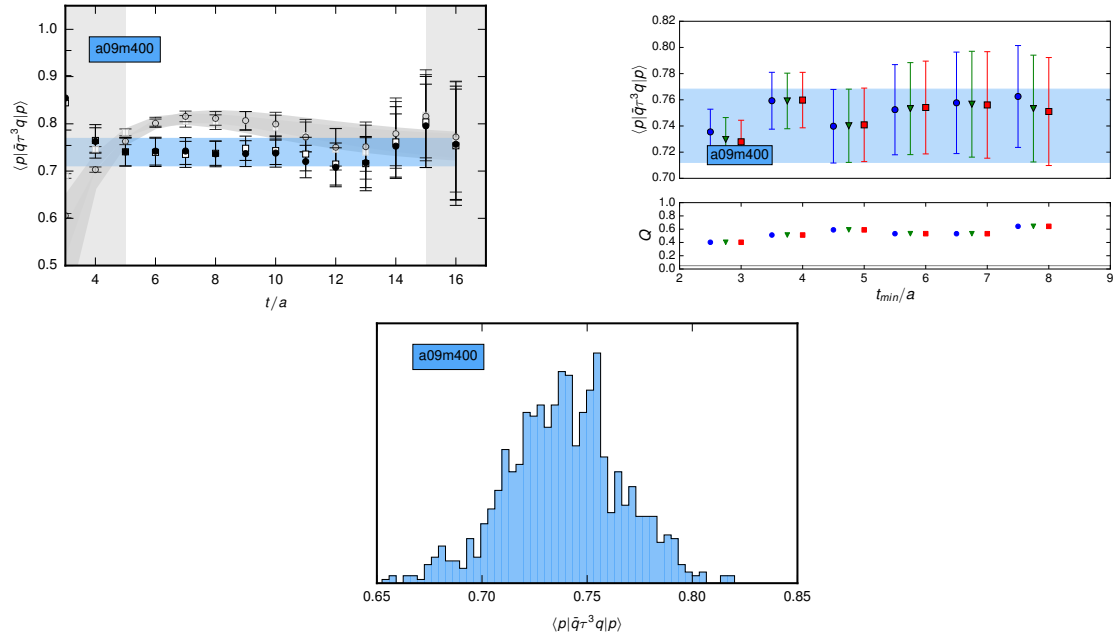
Figure C.19: Analysis of the a09m400 iso-vector scalar operator.

Figure C.20: Analysis of the a12m310 iso-vector scalar operator.

Figure C.21: Analysis of the a12m400 iso-vector scalar operator.

Figure C.22: Analysis of the a15m310 iso-vector scalar operator.

Figure C.23: Analysis of the a15m350 iso-vector scalar operator.

Figure C.24: Analysis of the a15m400 iso-vector scalar operator.

Figure C.25: Analysis of the a09m310 iso-scalar scalar operator.

Figure C.26: Analysis of the a09m400 iso-scalar scalar operator.
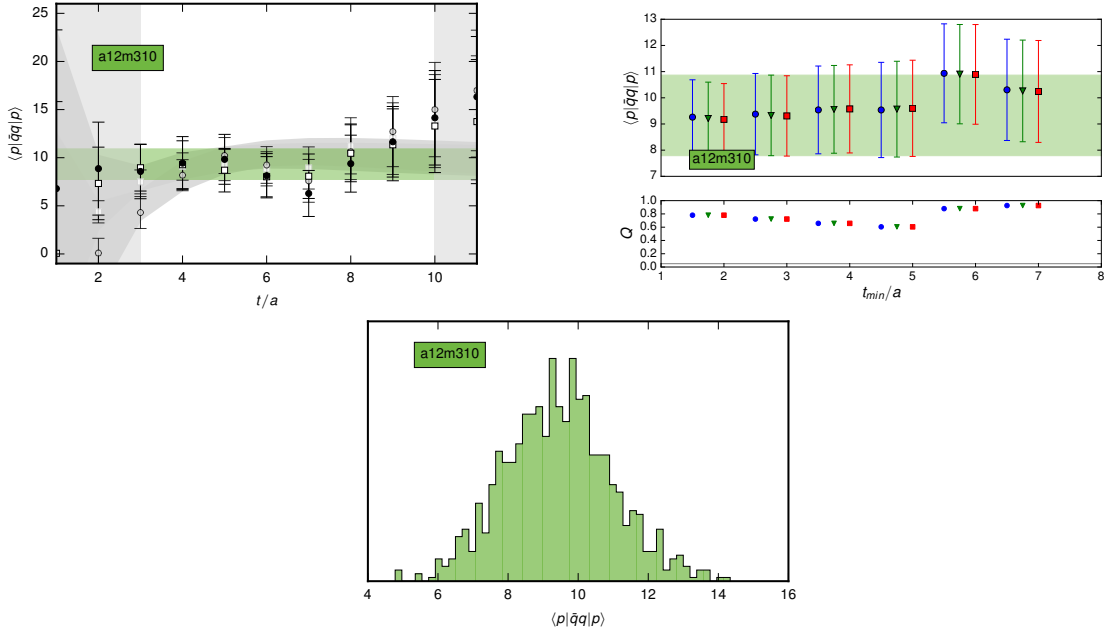
Figure C.27: Analysis of the a12m310 iso-scalar scalar operator.
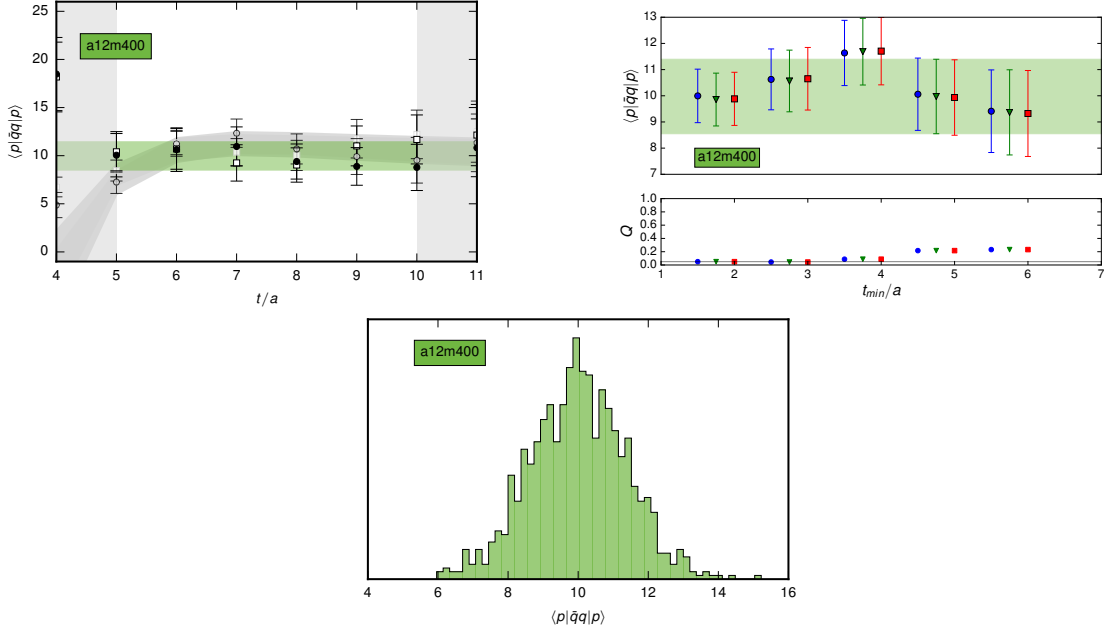
Figure C.28: Analysis of the a12m400 iso-scalar scalar operator.
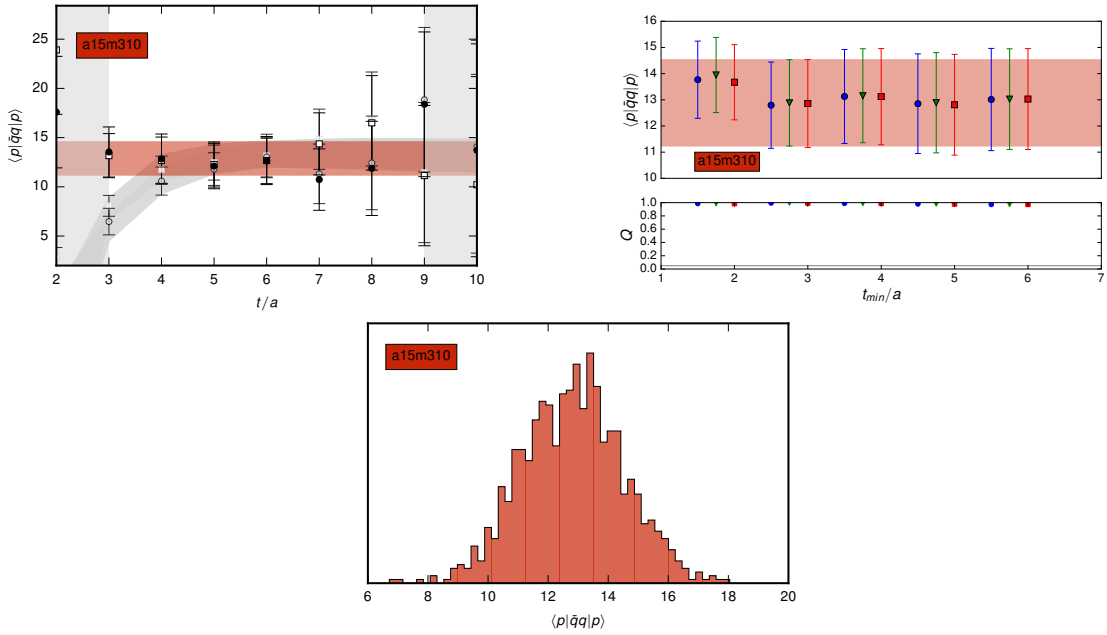
Figure C.29: Analysis of the a15m310 iso-scalar scalar operator.

165
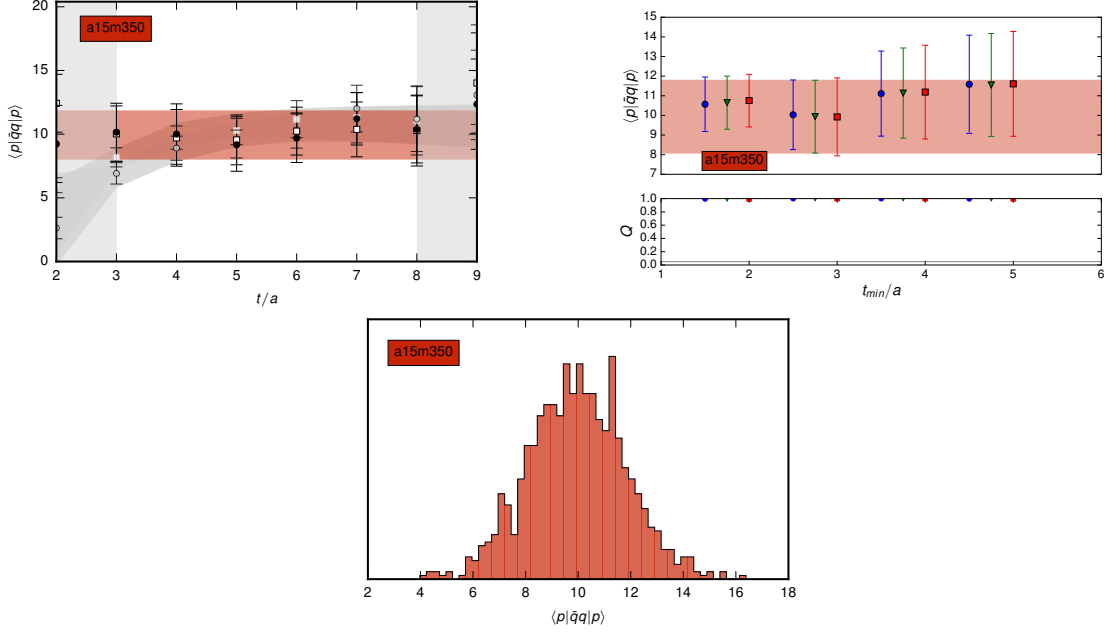
Figure C.30: Analysis of the a15m350 iso-scalar scalar operator.
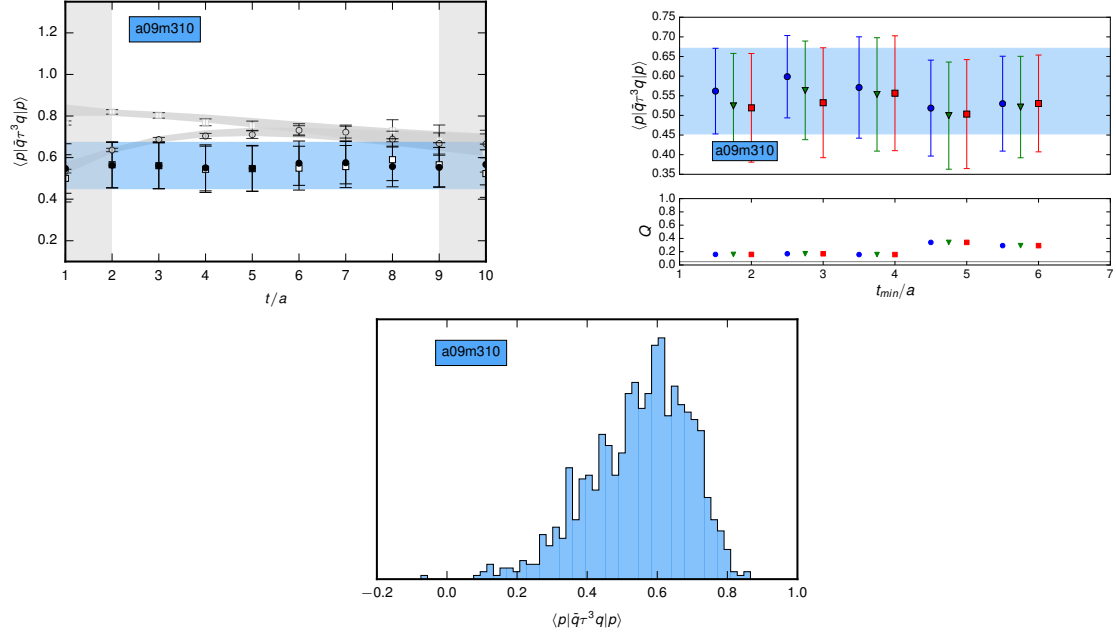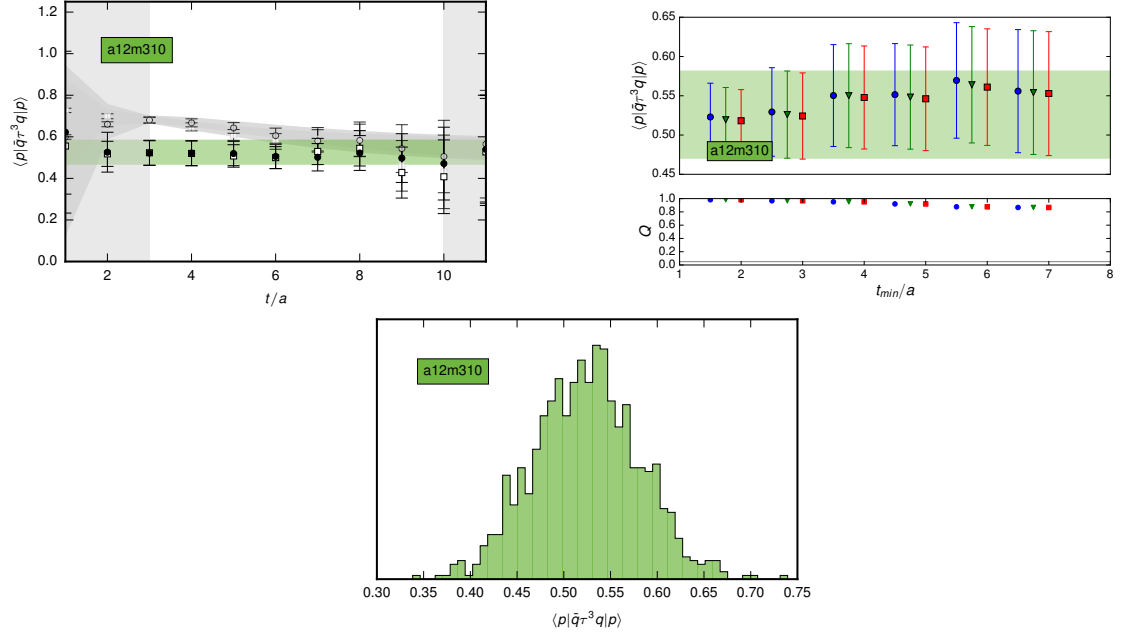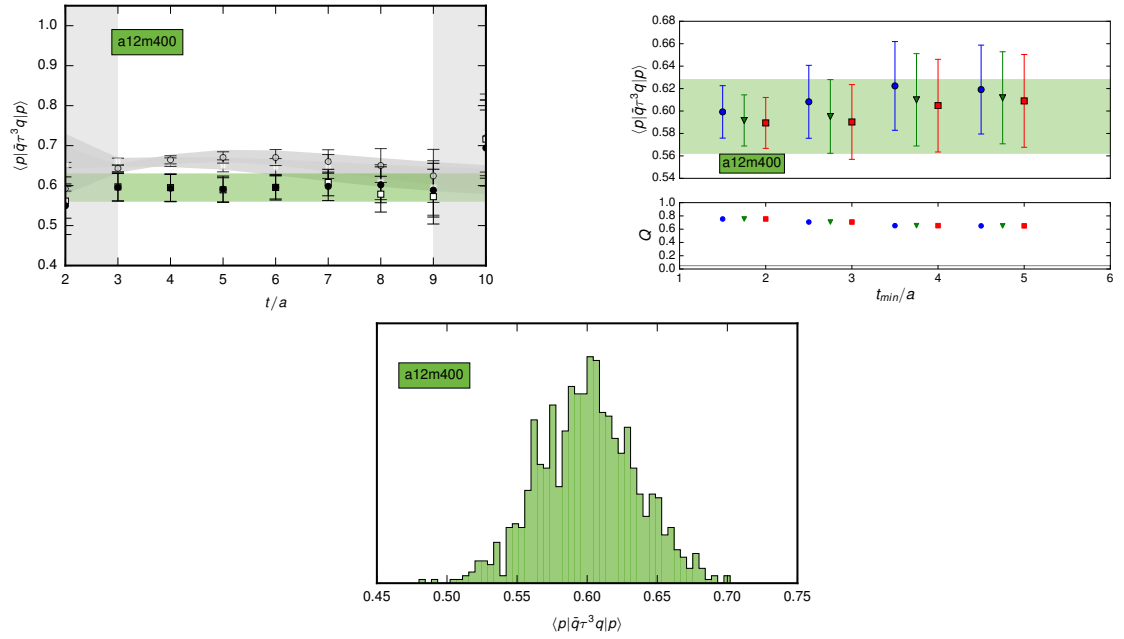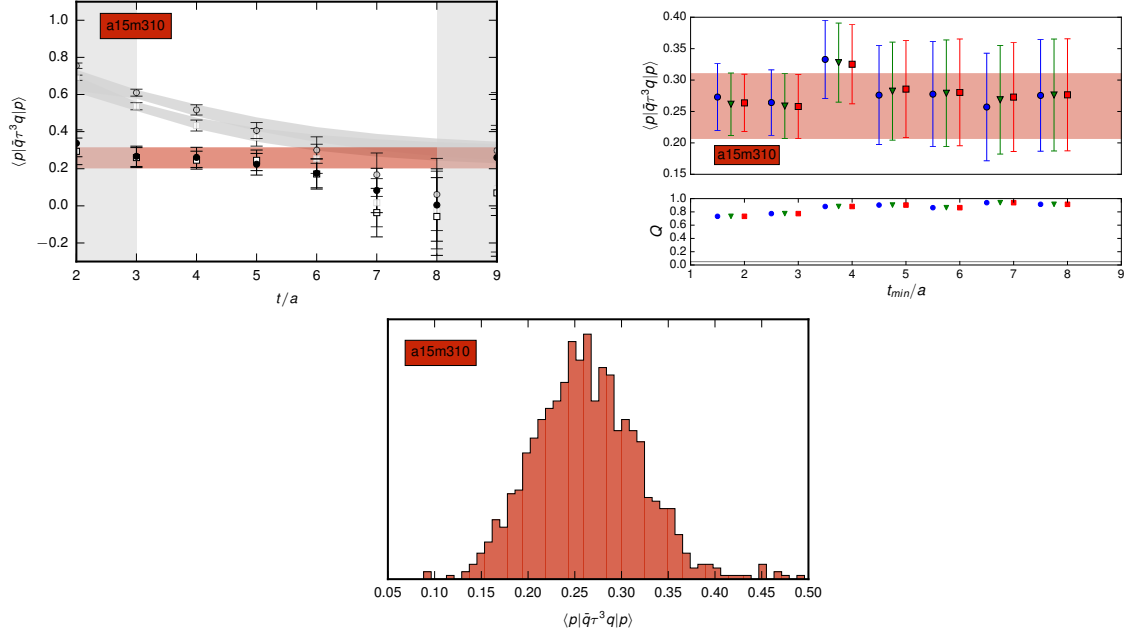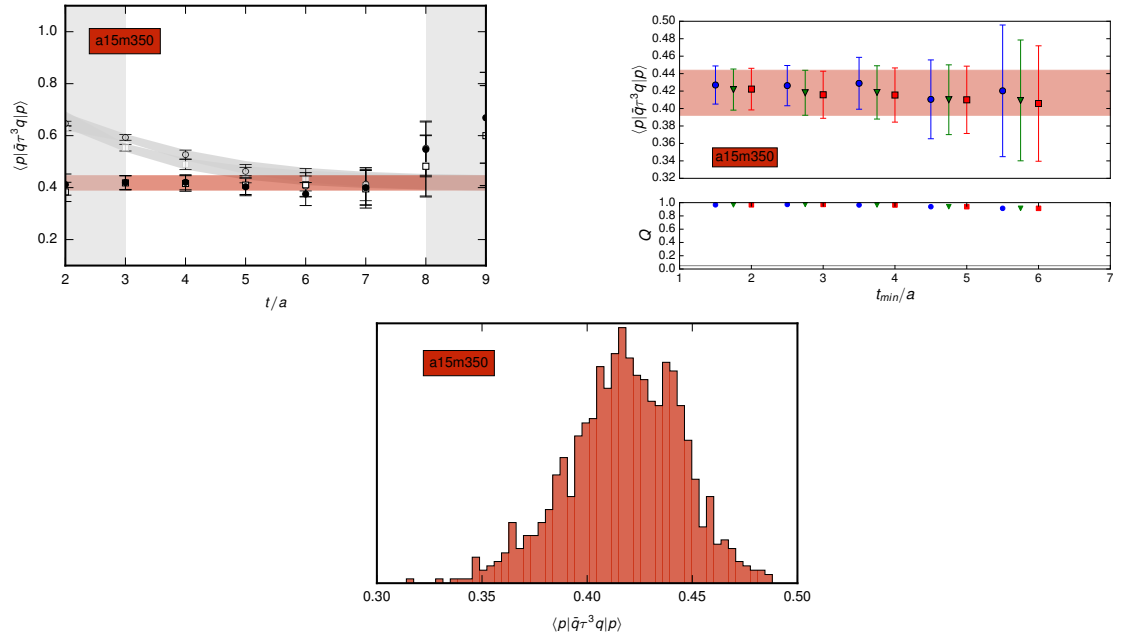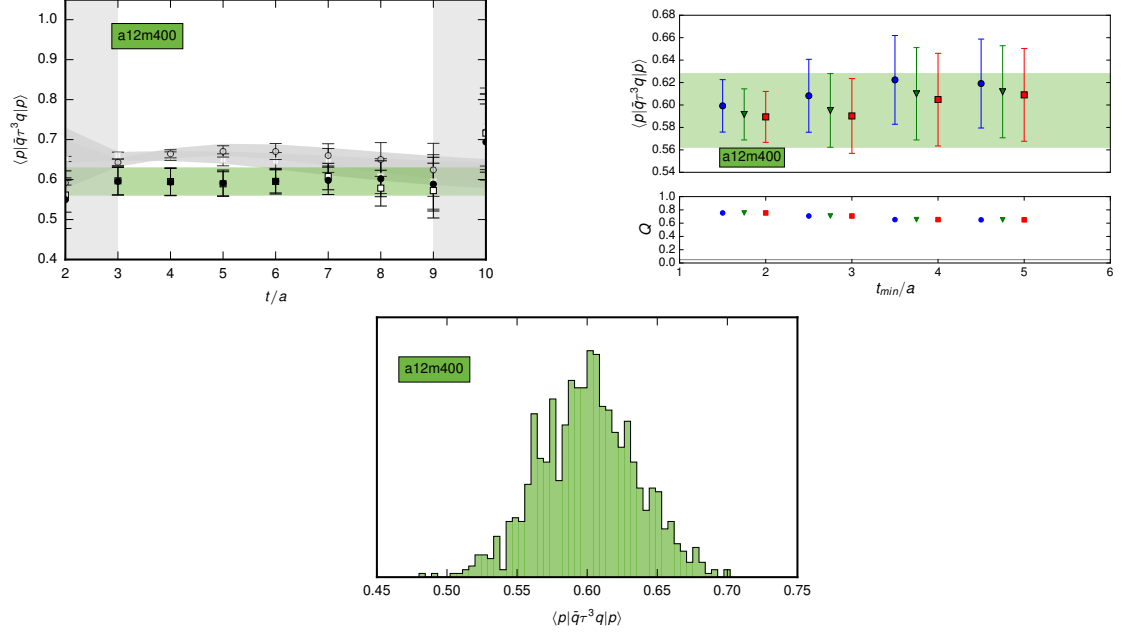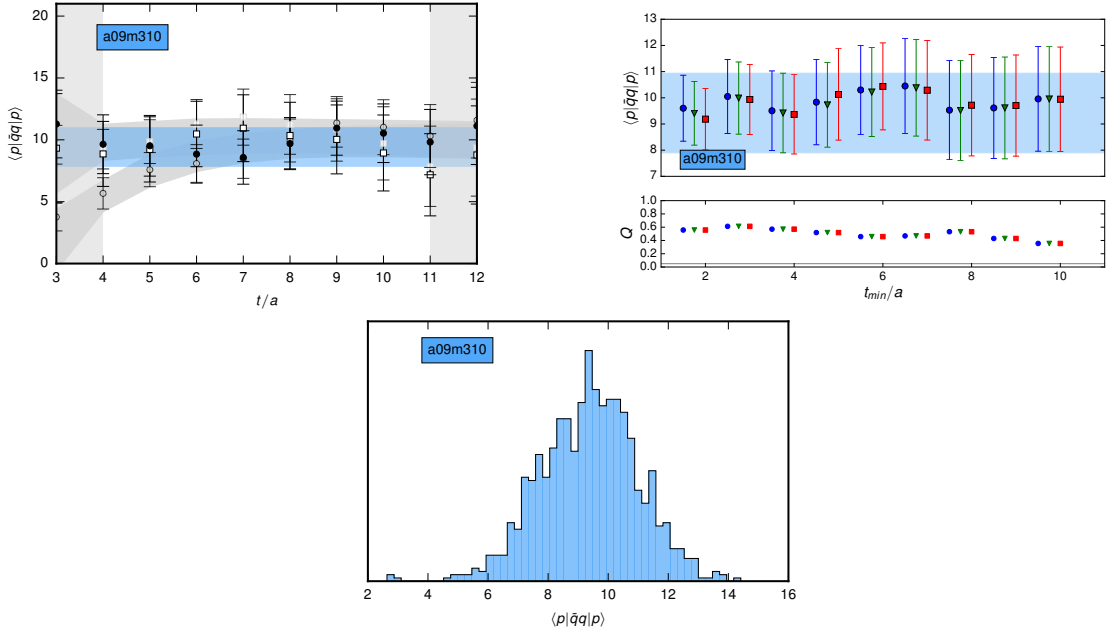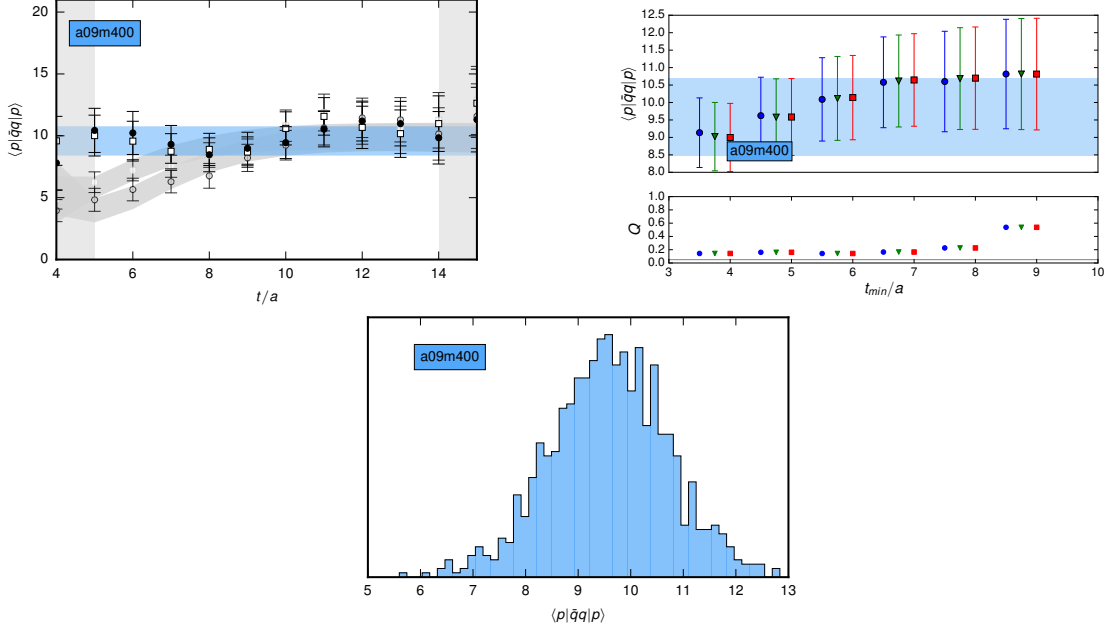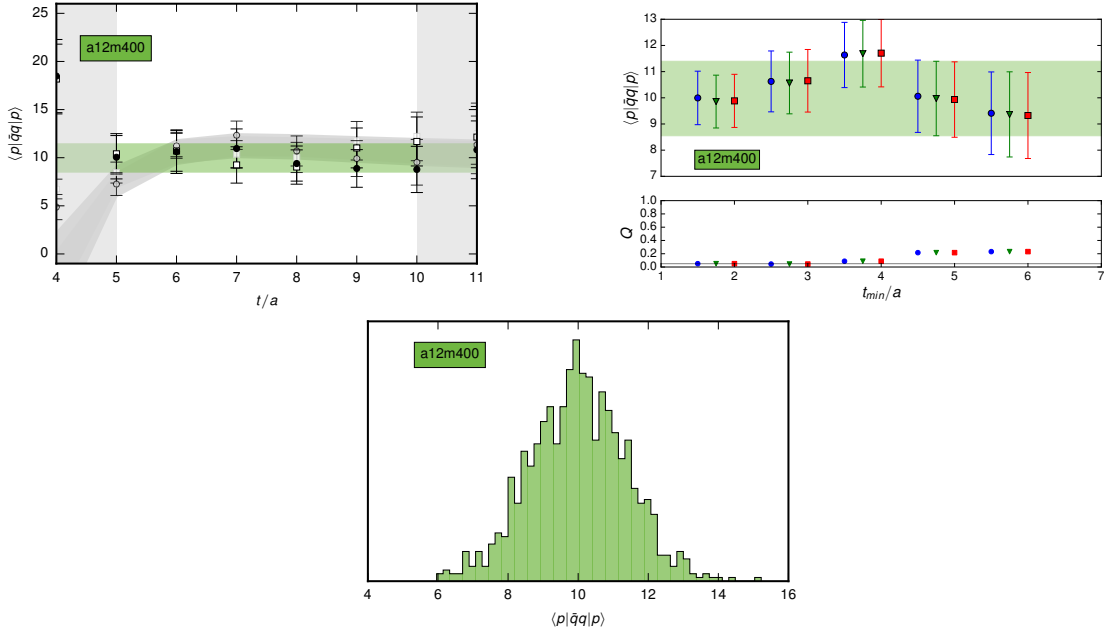

Figure C.31: Analysis of the a15m400 iso-scalar scalar operator.

Bibliography

[1] S. Weinberg. *Cosmology*. Cosmology. OUP Oxford, 2008.

[2] M. Aguilar et al. First Result from the Alpha Magnetic Spectrometer on the International Space Station: Precision Measurement of the Positron Fraction in Primary Cosmic Rays of 0.50 GeV. *Phys. Rev. Lett.*, 110:141102, 2013.

[3] M. Aguilar et al. The Alpha Magnetic Spectrometer (AMS) on the International Space Station. I: Results from the test flight on the space shuttle. *Phys. Rept.*, 366:331–405, 2002. [Erratum: Phys. Rept.380,97(2003)].

[4] C. L. Bennett et al. Nine-Year Wilkinson Microwave Anisotropy Probe (WMAP) Observations: Final Maps and Results. *Astrophys. J. Suppl.*, 208:20, 2013.

[5] P. A. R. Ade et al. Planck 2015 results. XIII. Cosmological parameters. *Astron. Astrophys.*, 594:A13, 2016.

[6] C. Patrignani et al. Review of Particle Physics. *Chin. Phys.*, C40(10):100001, 2016.

[7] A. D. Sakharov. Violation of CP Invariance, c Asymmetry, and Baryon Asymmetry of the Universe. *Pisma Zh. Eksp. Teor. Fiz.*, 5:32–35, 1967. [Usp. Fiz. Nauk161,61(1991)].

[8] R. D. Peccei. Physics at the interface of particle physics and cosmology. 1998.

[9] David E. Morrissey and Michael J. Ramsey-Musolf. Electroweak baryogenesis. *New J. Phys.*, 14:125003, 2012.

[10] Patrick Huet and Eric Sather. Electroweak baryogenesis and standard model CP violation. *Phys. Rev.*, D51:379–394, 1995.

[11] M. B. Gavela, P. Hernandez, J. Orloff, O. Pene, and C. Quimbay. Standard model CP violation and baryon asymmetry. Part 2: Finite temperature. *Nucl. Phys.*, B430:382–426, 1994.

[12] Sacha Davidson, Enrico Nardi, and Yosef Nir. Leptogenesis. *Phys. Rept.*, 466:105–177, 2008.

[13] S. T. Petcov. The Nature of Massive Neutrinos. *Adv. High Energy Phys.*, 2013:852987, 2013.

[14] S. V. Cao. Latest results from T2K. In *53rd Rencontres de Moriond on Electroweak Interactions and Unified Theories (Moriond EW 2018) La Thuile, Italy, March 10-17, 2018*, 2018.

[15] F. Capozzi, E. Lisi, A. Marrone, and A. Palazzo. Current unknowns in the three neutrino framework. 2018.

[16] G. L. Fogli, E. Lisi, A. Marrone, D. Montanino, A. Palazzo, and A. M. Rotunno. Global analysis of neutrino masses, mixings and phases: entering the era of leptonic CP violation searches. *Phys. Rev.*, D86:013012, 2012.

[17] K. Abe et al. Search for CP violation in Neutrino and Antineutrino Oscillations by the T2K experiment with 2.2×10^{21} protons on target. 2018.

[18] M. A. Acero et al. New constraints on oscillation parameters from ν_e appearance and ν_μ disappearance in the NOvA experiment. 2018.

[19] Dominic Brailsford. DUNE: Status and Perspectives. In *Prospects in Neutrino Physics (NuPhys2017) London, United Kingdom, December 20-22, 2017*, 2018.

[20] Peter Ballett, Stephen F. King, Silvia Pascoli, Nick W. Prouse, and TseChun Wang. Sensitivities and synergies of DUNE and T2HK. *Phys. Rev.*, D96(3):033003, 2017.

[21] W. Buchmuller, R. D. Peccei, and T. Yanagida. Leptogenesis as the origin of matter. *Ann. Rev. Nucl. Part. Sci.*, 55:311–355, 2005.

[22] Steven Weinberg. Phenomenological Lagrangians. *Physica*, A96(1-2):327–340, 1979.

[23] Timothy Chupp, Peter Fierlinger, Michael Ramsey-Musolf, and Jaideep Singh. Electric Dipole Moments of the Atoms, Molecules, Nuclei and Particles. 2017.

[24] J. M. Pendlebury et al. Revised experimental upper limit on the electric dipole moment of the neutron. *Phys. Rev.*, D92(9):092003, 2015.

[25] R. D. Peccei and Helen R. Quinn. CP Conservation in the Presence of Instantons. *Phys. Rev. Lett.*, 38:1440–1443, 1977. [,328(1977)].

[26] R. D. Peccei and Helen R. Quinn. Constraints Imposed by CP Conservation in the Presence of Instantons. *Phys. Rev.*, D16:1791–1797, 1977.

[27] R. D. Peccei. The Strong CP problem and axions. *Lect. Notes Phys.*, 741:3–17, 2008. [,3(2006)].

[28] Yoichiro Nambu. Quasiparticles and Gauge Invariance in the Theory of Superconductivity. *Phys. Rev.*, 117:648–663, 1960. [,132(1960)].

[29] Jeffrey Goldstone, Abdus Salam, and Steven Weinberg. Broken Symmetries. *Phys. Rev.*, 127:965–970, 1962.

[30] Pierre Sikivie. Axion Cosmology. *Lect. Notes Phys.*, 741:19–50, 2008. [,19(2006)].

[31] G. M. Prosperi, M. Raciti, and C. Simolo. On the running coupling constant in QCD. *Prog. Part. Nucl. Phys.*, 58:387–438, 2007.

[32] Arthur M. Jaffe and Edward Witten. Quantum Yang-Mills theory. 2000.

[33] Christof Gattringer, M. Gockeler, Philipp Huber, and C. B. Lang. Renormalization of bilinear quark operators for the chirally improved lattice Dirac operator. *Nucl. Phys.*, B694:170–186, 2004.

[34] J. Greensite. The Confinement problem in lattice gauge theory. *Prog. Part. Nucl. Phys.*, 51:1, 2003.

[35] Hans Gunter Dosch and Yu. A. Simonov. The Area Law of the Wilson Loop and Vacuum Field Correlators. *Phys. Lett.*, B205:339–344, 1988.

[36] S. Aoki et al. The Static quark potential in full QCD. *Nucl. Phys. Proc. Suppl.*, 73:216–218, 1999. [,216(1998)].

[37] Stanley J. Brodsky, Hans-Christian Pauli, and Stephen S. Pinsky. Quantum chromodynamics and other field theories on the light cone. *Phys. Rept.*, 301:299–486, 1998.

[38] Joshua Erlich, Emanuel Katz, Dam T. Son, and Mikhail A. Stephanov. QCD and a holographic model of hadrons. *Phys. Rev. Lett.*, 95:261602, 2005.

[39] Pietro Colangelo and Alexander Khodjamirian. QCD sum rules, a modern perspective. 2000.

[40] S. Aoki et al. Review of lattice results concerning low-energy particle physics. 2016.

[41] Paul A. M. Dirac. The Lagrangian in quantum mechanics. *Phys. Z. Sowjetunion*, 3:64–72, 1933.

[42] Richard Phillips Feynman. *The principle of least action in quantum mechanics*. PhD thesis, Princeton U., 1942.

[43] R. P. Feynman. Space-time approach to nonrelativistic quantum mechanics. *Rev. Mod. Phys.*, 20:367–387, 1948.

[44] Kenneth G. Wilson. Confinement of Quarks. *Phys. Rev.*, D10:2445–2459, 1974. [,319(1974)].

[45] G. Peter Lepage and Paul B. Mackenzie. On the viability of lattice perturbation theory. *Phys. Rev.*, D48:2250–2264, 1993.

[46] P. Hasenfratz and F. Karsch. Chemical Potential on the Lattice. *Phys. Lett.*, 125B:308–310, 1983.

[47] Owe Philipsen. Lattice QCD at finite temperature and density. *Eur. Phys. J. ST*, 152:29–60, 2007.

[48] F. K. Guo, R. Horsley, U. G. Meissner, Y. Nakamura, H. Perlt, P. E. L. Rakow, G. Schierholz, A. Schiller, and J. M. Zanotti. The electric dipole moment of the neutron from 2+1 flavor lattice QCD. *Phys. Rev. Lett.*, 115(6):062001, 2015.

[49] A. D. Kennedy. Algorithms for lattice QCD with dynamical fermions. *Nucl. Phys. Proc. Suppl.*, 140:190–203, 2005. [,190(2004)].

[50] M. A. Clark. The Rational Hybrid Monte Carlo Algorithm. *PoS*, LAT2006:004, 2006.

[51] Norman Christ and Chulwoo Jung. Computational requirements of the rational hybrid Monte Carlo algorithm. *PoS*, LATTICE2007:028, 2007.

[52] H. Goldstein, C.P. Poole, and J.L. Safko. *Classical Mechanics*. Addison Wesley, 2002.

[53] A. Bazavov et al. Up-, down-, strange-, charm-, and bottom-quark masses from four-flavor lattice QCD. 2018.

[54] Stefan Scherer. Introduction to chiral perturbation theory. *Adv. Nucl. Phys.*, 27:277, 2003. [,277(2002)].

[55] R. Machleidt and D. R. Entem. Chiral effective field theory and nuclear forces. *Phys. Rept.*, 503:1–75, 2011.

[56] C. Vafa and Edward Witten. Restrictions on Symmetry Breaking in Vector-Like Gauge Theories. *Nucl. Phys.*, B234:173–188, 1984.

[57] J. Gasser and H. Leutwyler. Chiral Perturbation Theory to One Loop. *Annals Phys.*, 158:142, 1984.

[58] J. Gasser and H. Leutwyler. Chiral Perturbation Theory: Expansions in the Mass of the Strange Quark. *Nucl. Phys.*, B250:465–516, 1985.

[59] Steven Weinberg. A Model of Leptons. *Phys. Rev. Lett.*, 19:1264–1266, 1967.

[60] Ian Low and Zhewei Yin. The Infrared Structure of Nambu-Goldstone Bosons. *Submitted to: JHEP*, 2018.

[61] Stefan Scherer. Chiral perturbation theory: Success and challenge. *Eur. Phys. J.*, A28:59–70, 2006.

[62] H. W. Fearing and S. Scherer. Extension of the chiral perturbation theory meson Lagrangian to order p(6). *Phys. Rev.*, D53:315–348, 1996.

[63] Elizabeth Ellen Jenkins and Aneesh V. Manohar. Baryon chiral perturbation theory using a heavy fermion Lagrangian. *Phys. Lett.*, B255:558–562, 1991.

[64] G. Ecker. Chiral symmetry. *Lect. Notes Phys.*, 521:83–129, 1999.

[65] J. Gasser, M. E. Sainio, and A. Svarc. Nucleons with Chiral Loops. *Nucl. Phys.*, B307:779–853, 1988.

[66] Thomas R. Hemmert, Barry R. Holstein, and Joachim Kambor. Systematic 1/M expansion for spin 3/2 particles in baryon chiral perturbation theory. *Phys. Lett.*, B395:89–95, 1997.

[67] Brian C. Tiburzi and Andre Walker-Loud. Strong isospin breaking in the nucleon and Delta masses. *Nucl. Phys.*, A764:274–302, 2006.

[68] David A. Brantley, Balint Joo, Ekaterina V. Mastropas, Emanuele Mereghetti, Henry Monge-Camacho, Brian C. Tiburzi, and Andre Walker-Loud. Strong isospin violation and chiral logarithms in the baryon spectrum. 2016.

[69] Andreas S. Kronfeld. Twenty-first Century Lattice Gauge Theory: Results from the QCD Lagrangian. *Ann. Rev. Nucl. Part. Sci.*, 62:265–284, 2012.

[70] Matthew Heffernan, Projjwal Banerjee, and Andre Walker-Loud. Quantifying the sensitivity of Big Bang Nucleosynthesis to isospin breaking with input from lattice QCD. 2017.

[71] Gerald A. Miller, Allena K. Opper, and Edward J. Stephenson. Charge symmetry breaking and QCD. *Ann. Rev. Nucl. Part. Sci.*, 56:253–292, 2006.

[72] Paul Langacker and Heinz Pagels. Chiral perturbation theory. *Phys. Rev.*, D8:4595–4619, 1973.

[73] H. Leutwyler. On the foundations of chiral perturbation theory. *Annals Phys.*, 235:165–203, 1994.

[74] Dürr, Stephan and others. Lattice QCD at the physical point meets SU(2) chiral perturbation theory. *Phys. Rev.*, D90(11):114504, 2014.

[75] Elizabeth Ellen Jenkins and Aneesh V. Manohar. Chiral corrections to the baryon axial currents. *Phys. Lett.*, B259:353–358, 1991.

[76] Howard Georgi. An Effective Field Theory for Heavy Quarks at Low-energies. *Phys. Lett.*, B240:447–450, 1990.

[77] S. Aoki et al. 2+1 Flavor Lattice QCD toward the Physical Point. *Phys. Rev.*, D79:034503, 2009.

[78] B. Colquhoun, R. J. Dowdall, J. Koponen, C. T. H. Davies, and G. P. Lepage. B $\rightarrow \pi l \nu$ at zero recoil from lattice QCD with physical u/d quarks. *Phys. Rev.*, D93(3):034502, 2016.

[79] William Detmold, C. J. David Lin, and Stefan Meinel. Calculation of the heavy-hadron axial couplings g_1, g_2 and g_3 using lattice QCD. *Phys. Rev.*, D85:114508, 2012.

[80] Andre Walker-Loud. Evidence for non-analytic light quark mass dependence in the baryon spectrum. *Phys. Rev.*, D86:074509, 2012.

[81] Robert G. Edwards, Balint Joo, and Huey-Wen Lin. Tuning for Three-flavors of Anisotropic Clover Fermions with Stout-link Smearing. *Phys. Rev.*, D78:054501, 2008.

[82] Huey-Wen Lin et al. First results from 2+1 dynamical quark flavors on an anisotropic lattice: Light-hadron spectroscopy and setting the strange-quark mass. *Phys.Rev.*, D79:034502, 2009.

[83] Colin J. Morningstar and Mike J. Peardon. Efficient glueball simulations on anisotropic lattices. *Phys. Rev.*, D56:4043–4061, 1997.

[84] B. Sheikholeslami and R. Wohlert. Improved Continuum Limit Lattice Action for QCD with Wilson Fermions. *Nucl. Phys.*, B259:572, 1985.

[85] Colin Morningstar and Mike J. Peardon. Analytic smearing of SU(3) link variables in lattice QCD. *Phys. Rev.*, D69:054501, 2004.

[86] Simon Duane, A. D. Kennedy, Brian J. Pendleton, and Duncan Roweth. Hybrid monte carlo. *Physics Letters B*, 195(2):216 – 222, 1987.

[87] Robert G. Edwards and Balint Joo. The Chroma software system for lattice QCD. *Nucl. Phys. Proc. Suppl.*, 140:832, 2005. [,832(2004)].

[88] M. A. Clark and A. D. Kennedy. Accelerating dynamical-fermion computations using the rational hybrid monte carlo algorithm with multiple pseudofermion fields. *Phys. Rev. Lett.*, 98:051601, Jan 2007.

[89] C. Urbach, K. Jansen, A. Shindler, and U. Wenger. HMC algorithm with multiple time scale integration and mass preconditioning. *Comput. Phys. Commun.*, 174:87–98, 2006.

[90] Tetsuya Takaishi and Philippe de Forcrand. Testing and tuning new symplectic integrators for hybrid Monte Carlo algorithm in lattice QCD. *Phys. Rev.*, E73:036706, 2006.

[91] I.P. Omelyan, I.M. Mryglod, and R. Folk. Symplectic analytically integrable decomposition algorithms: classification, derivation, and application to molecular dynamics, quantum and celestial mechanics simulations. *Computer Physics Communications*, 151(3):272 – 314, 2003.

[92] Andreas Frommer, Bertold Nockel, Stephan Gusken, Thomas Lippert, and Klaus Schilling. Many masses on one stroke: Economic computation of quark propagators. *Int. J. Mod. Phys.*, C6:627–638, 1995.

[93] Silas R. Beane, William Detmold, Thomas C. Luu, Kostas Orginos, Assumpta Parreno, Martin J. Savage, Aaron Torok, and Andre Walker-Loud. High Statistics Analysis using Anisotropic Clover Lattices: (I) Single Hadron Correlation Functions. *Phys. Rev.*, D79:114502, 2009.

[94] Andreas Stathopoulos and Kostas Orginos. Computing and deflating eigenvalues while solving multiple right hand side linear systems in quantum chromodynamics. *SIAM J. Sci. Comput.*, 32:439–462, 2010.

[95] M. A. Clark, R. Babich, K. Barros, R. C. Brower, and C. Rebbi. Solving Lattice QCD systems of equations using mixed precision solvers on GPUs. *Comput. Phys. Commun.*, 181:1517–1528, 2010.

[96] R. Babich, M. A. Clark, B. Joo, G. Shi, R. C. Brower, and S. Gottlieb. Scaling Lattice QCD beyond 100 GPUs. In *SC11 International Conference for High Performance Computing, Networking, Storage and Analysis Seattle, Washington, November 12-18, 2011*, 2011.

[97] Andre Walker-Loud. Strong isospin breaking with twisted mass lattice QCD. 2009.

[98] Claude W. Bernard and Maarten F. L. Golterman. Partially quenched gauge theories and an application to staggered fermions. *Phys. Rev.*, D49:486–494, 1994.

[99] Stephen R. Sharpe. Enhanced chiral logarithms in partially quenched QCD. *Phys. Rev.*, D56:7052–7058, 1997. [Erratum: Phys. Rev.D62,099901(2000)].

[100] Stephen R. Sharpe and N. Shoresh. Partially quenched QCD with nondegenerate dynamical quarks. *Nucl. Phys. Proc. Suppl.*, 83:968–970, 2000.

[101] Stephen R. Sharpe and Noam Shoresh. Partially quenched chiral perturbation theory without Phi0. *Phys. Rev.*, D64:114510, 2001.

[102] Jiunn-Wei Chen and Martin J. Savage. Baryons in partially quenched chiral perturbation theory. *Phys. Rev.*, D65:094001, 2002.

[103] Silas R. Beane and Martin J. Savage. Nucleons in two flavor partially quenched chiral perturbation theory. *Nucl. Phys.*, A709:319–344, 2002.

[104] Stephen R. Sharpe and Ruth S. Van de Water. Unphysical operators in partially quenched QCD. *Phys. Rev.*, D69:054027, 2004.

[105] Parikshit Junnarkar and Andre Walker-Loud. Scalar strange content of the nucleon from lattice QCD. *Phys. Rev.*, D87:114510, 2013.

[106] Brian C. Tiburzi and Andre Walker-Loud. Hyperons in Two Flavor Chiral Perturbation Theory. *Phys. Lett.*, B669:246–253, 2008.

[107] Brian C. Tiburzi and Andre Walker-Loud. Decuplet baryon masses in partially quenched chiral perturbation theory. *Nucl. Phys.*, A748:513–536, 2005.

[108] Johan Bijnens and Joaquim Prades. Electromagnetic corrections for pions and kaons: Masses and polarizabilities. *Nucl. Phys.*, B490:239–271, 1997.

[109] Andre Walker-Loud. Octet baryon masses in partially quenched chiral perturbation theory. *Nucl. Phys.*, A747:476–507, 2005.

[110] Sara Collins. Hadron Structure (plenary presentation), 2016. PoS LATTICE2016.

[111] A. Walker-Loud et al. Light hadron spectroscopy using domain wall valence quarks on an Asqtad sea. *Phys. Rev.*, D79:054502, 2009.

[112] Andre Walker-Loud. New lessons from the nucleon mass, lattice QCD and heavy baryon chiral perturbation theory. *PoS*, LATTICE2008:005, 2008.

[113] Walker-Loud, André. Baryons in/and Lattice QCD. *PoS*, CD12:017, 2013.

[114] Silas R. Beane, Kostas Orginos, and Martin J. Savage. Strong-isospin violation in the neutron-proton mass difference from fully-dynamical lattice QCD and PQQCD. *Nucl. Phys.*, B768:38–50, 2007.

[115] T. Blum, R. Zhou, T. Doi, M. Hayakawa, T. Izubuchi, S. Uno, and N. Yamada. Electromagnetic mass splittings of the low lying hadrons and quark masses from 2+1 flavor lattice QCD+QED. *Phys. Rev.*, D82:094508, 2010.

[116] R. Horsley, J. Najjar, Y. Nakamura, D. Pleiter, P. E. L. Rakow, G. Schierholz, and J. M. Zanotti. Isospin breaking in octet baryon mass splittings. *Phys. Rev.*, D86:114511, 2012.

[117] G. M. de Divitiis, R. Frezzotti, V. Lubicz, G. Martinelli, R. Petronzio, G. C. Rossi, F. Sanfilippo, S. Simula, and N. Tantalo. Leading isospin breaking effects on the lattice. *Phys. Rev.*, D87(11):114505, 2013.

[118] Sz. Borsanyi et al. Isospin splittings in the light baryon octet from lattice QCD and QED. *Phys. Rev. Lett.*, 111(25):252001, 2013.

[119] Sz. Borsanyi et al. Ab initio calculation of the neutron-proton mass difference. *Science*, 347:1452–1455, 2015.

[120] R. Horsley et al. Isospin splittings of meson and baryon masses from three-flavor lattice QCD + QED. *J. Phys.*, G43(10):10LT02, 2016.

[121] Roger F. Dashen, Elizabeth Ellen Jenkins, and Aneesh V. Manohar. Spin flavor structure of large N(c) baryons. *Phys. Rev.*, D51:3697–3727, 1995.

[122] Elizabeth Ellen Jenkins. Chiral Lagrangian for baryons in the 1/n(c) expansion. *Phys. Rev.*, D53:2625–2644, 1996.

[123] Matthias R. Schindler and Daniel R. Phillips. Bayesian Methods for Parameter Estimation in Effective Field Theories. *Annals Phys.*, 324:682–708, 2009. [Erratum: Annals Phys.324,2051(2009)].

[124] R. J. Furnstahl, D. R. Phillips, and S. Wesolowski. A recipe for EFT uncertainty quantification in nuclear physics. *J. Phys.*, G42(3):034028, 2015.

[125] R. J. Furnstahl, N. Klco, D. R. Phillips, and S. Wesolowski. Quantifying truncation errors in effective field theory. *Phys. Rev.*, C92(2):024005, 2015.

[126] S. Wesolowski, N. Klco, R. J. Furnstahl, D. R. Phillips, and A. Thapaliya. Bayesian parameter estimation for effective field theories. *J. Phys.*, G43(7):074001, 2016.

[127] Jordy de Vries, Emanuele Mereghetti, and Andre Walker-Loud. Baryon mass splittings and strong CP violation in SU(3) Chiral Perturbation Theory. *Phys. Rev.*, C92(4):045201, 2015.

[128] Gerard 't Hooft. Symmetry Breaking Through Bell-Jackiw Anomalies. *Phys. Rev. Lett.*, 37:8–11, 1976.

[129] Varouzhan Baluni. CP Violating Effects in QCD. *Phys. Rev.*, D19:2227–2230, 1979.

[130] R. J. Crewther, P. Di Vecchia, G. Veneziano, and Edward Witten. Chiral Estimate of the Electric Dipole Moment of the Neutron in Quantum Chromodynamics. *Phys. Lett.*, 88B:123, 1979. [Erratum: Phys. Lett.91B,487(1980)].

[131] E. Mereghetti, W. H. Hockings, and U. van Kolck. The Effective Chiral Lagrangian From the Theta Term. *Annals Phys.*, 325:2363–2409, 2010.

[132] W. H. Hockings and U. van Kolck. The Electric dipole form factor of the nucleon. *Phys. Lett.*, B605:273–278, 2005.

[133] E. Mereghetti, J. de Vries, W. H. Hockings, C. M. Maekawa, and U. van Kolck. The Electric Dipole Form Factor of the Nucleon in Chiral Perturbation Theory to Sub-leading Order. *Phys. Lett.*, B696:97–102, 2011.

[134] Feng-Kun Guo and Ulf-G. Meissner. Baryon electric dipole moments from strong CP violation. *JHEP*, 12:097, 2012.

[135] Eigo Shintani, Thomas Blum, Taku Izubuchi, and Amarjit Soni. Neutron and proton electric dipole moments from $N_f = 2 + 1$ domain-wall fermion lattice QCD. *Phys. Rev.*, D93(9):094503, 2016.

[136] Andrea Shindler, Thomas Luu, and Jordy de Vries. Nucleon electric dipole moment with the gradient flow: The θ-term contribution. *Phys. Rev.*, D92(9):094518, 2015.

[137] A. Nicholson et al. Heavy physics contributions to neutrinoless double beta decay from QCD. 2018.

[138] Evan Berkowitz et al. Möbius domain wall fermions on gradient-flowed dynamical HISQ ensembles. *Phys. Rev.*, D96(5):054513, 2017.

[139] G. Martinelli, C. Pittori, Christopher T. Sachrajda, M. Testa, and A. Vladikas. A General method for nonperturbative renormalization of lattice operators. *Nucl. Phys.*, B445:81–108, 1995.

[140] Y. Aoki et al. Non-perturbative renormalization of quark bilinear operators and B(K) using domain wall fermions. *Phys. Rev.*, D78:054510, 2008.

[141] Yujiang Bi, Hao Cai, Ying Chen, Ming Gong, Keh-Fei Liu, Zhaofeng Liu, and Yi-Bo Yang. RI/MOM and RI/SMOM renormalization of overlap quark bilinears on domain wall fermion configurations. *Phys. Rev.*, D97(9):094501, 2018.

[142] Jangho Kim, Jongjeong Kim, Weonjong Lee, and Boram Yoon. Non-perturbative Renormalization of Bilinear Operators with Improved Staggered Quarks. *PoS*, LAT-TICE2013:308, 2014.

[143] Philipp Huber. Renormalization factors of quark bilinears using the DCI operator with dynamical quarks. *JHEP*, 11:107, 2010.

[144] C. Sturm, Y. Aoki, N. H. Christ, T. Izubuchi, C. T. C. Sachrajda, and A. Soni. Renormalization of quark bilinear operators in a momentum-subtraction scheme with a nonexceptional subtraction point. *Phys. Rev.*, D80:014501, 2009.

[145] J. Noaki, T. W. Chiu, H. Fukaya, S. Hashimoto, H. Matsufuru, T. Onogi, E. Shintani, and N. Yamada. Non-perturbative renormalization of bilinear operators with dynamical overlap fermions. *Phys. Rev.*, D81:034502, 2010.

[146] Peter A. Boyle, Nicolas Garron, Renwick J. Hudspith, Christoph Lehner, and Andrew T. Lytle. Neutral kaon mixing beyond the Standard Model with n$_f$ = 2 + 1 chiral fermions. Part 2: non perturbative renormalisation of the $\Delta F = 2$ four-quark operators. *JHEP*, 10:054, 2017.

[147] Petros Dimopoulos, Gregorio Herdoíza, Mauro Papinutto, Carlos Pena, David Preti, and Anastasioss Vladikas. Non-Perturbative Renormalisation and Running of BSM Four-Quark Operators in $N_f = 2$ QCD. 2018.

[148] Chia Cheng Chang et al. Nucleon axial coupling from Lattice QCD. *EPJ Web Conf.*, 175:01008, 2018.

[149] C. C. Chang et al. A per-cent-level determination of the nucleon axial coupling from quantum chromodynamics. *Nature*, 558(7708):91–94, 2018.

[150] M. Gockeler, R. Horsley, H. Oelrich, H. Perlt, D. Petters, Paul E. L. Rakow, A. Schafer, G. Schierholz, and A. Schiller. Nonperturbative renormalization of composite operators in lattice QCD. *Nucl. Phys.*, B544:699–733, 1999.

[151] Jean-Rene Cudell, A. Le Yaouanc, and Carlotta Pittori. Pseudoscalar vertex, Goldstone boson and quark masses on the lattice. *Phys. Lett.*, B454:105–114, 1999.

[152] R. Arthur, P. A. Boyle, S. Hashimoto, and R. Hudspith. Note on Rome-Southampton renormalization with smeared gauge fields. *Phys. Rev.*, D88(11):114506, 2013.

[153] R. Arthur and P. A. Boyle. Step Scaling with off-shell renormalisation. *Phys. Rev.*, D83:114511, 2011.

[154] Mauro Papinutto, Carlos Pena, and David Preti. On the perturbative renormalization of four-quark operators for new physics. *Eur. Phys. J.*, C77(6):376, 2017. [Erratum: Eur. Phys. J.C78,no.1,21(2018)].

[155] Sinya Aoki and Oliver Bar. The Vector and axial vector current in Wilson ChPT. *PoS*, LATTICE2007:062, 2007.

[156] A. Bazavov et al. Gradient flow and scale setting on MILC HISQ ensembles. *Phys. Rev.*, D93(9):094510, 2016.

[157] Christof Gattringer and Christian B. Lang. Quantum chromodynamics on the lattice. *Lect. Notes Phys.*, 788:1–343, 2010.

[158] V. N. Gribov. Quantization of Nonabelian Gauge Theories. *Nucl. Phys.*, B139:1, 1978. [,1(1977)].

[159] T. P. Killingback. The Gribov Ambiguity in Gauge Theories on the 4 Torus. *Phys. Lett.*, 138B:87–90, 1984.

[160] Enzo Marinari, Claudio Parrinello, and Roberto Ricci. Evidence for the existence of Gribov copies in Landau gauge lattice QCD. *Nucl. Phys.*, B362:487–497, 1991.

[161] O. Oliveira and P. J. Silva. An Algorithm for Landau gauge fixing in lattice QCD. *Comput. Phys. Commun.*, 158:73–88, 2004.

[162] N. Vandersickel and Daniel Zwanziger. The Gribov problem and QCD dynamics. *Phys. Rept.*, 520:175–251, 2012.

[163] Paolo Marenzoni and Pietro Rossi. Gribov copies in lattice QCD. *Phys. Lett.*, B311:219–222, 1993.

[164] Leonardo Giusti, M. L. Paciello, C. Parrinello, S. Petrarca, and B. Taglienti. Problems on lattice gauge fixing. *Int. J. Mod. Phys.*, A16:3487–3534, 2001.

[165] Gary Prezeau, M. Ramsey-Musolf, and Petr Vogel. Neutrinoless double beta decay and effective field theory. *Phys. Rev.*, D68:034016, 2003.

[166] D. Becirevic, V. Gimenez, V. Lubicz, G. Martinelli, M. Papinutto, and J. Reyes. Renormalization constants of quark operators for the nonperturbatively improved Wilson action. *JHEP*, 08:022, 2004.

[167] Nicolas Garron, Peter A Boyle, Renwick J Hudspith, and Andrew T Lytle. Weak Matrix Elements of Beyond the Standard Model $\Delta s = 2$ four-quark operators from nf=2+1 Domain-Wall fermions. *PoS*, LATTICE2012:108, 2012.

[168] P. A. Boyle. Conserved currents for Mobius Domain Wall Fermions. 2014.

[169] P. Hasenfratz, S. Hauswirth, T. Jorg, F. Niedermayer, and K. Holland. Testing the fixed point QCD action and the construction of chiral currents. *Nucl. Phys.*, B643:280–320, 2002.

[170] Jordy de Vries, Emanuele Mereghetti, Chien-Yeah Seng, and Andre Walker-Loud. Lattice QCD spectroscopy for hadronic CP violation. *Phys. Lett.*, B766:254–262, 2017.

[171] E. Mereghetti and U. van Kolck. Effective Field Theory and Time-Reversal Violation in Light Nuclei. *Ann. Rev. Nucl. Part. Sci.*, 65:215–243, 2015.

[172] Chris Bouchard, Chia Cheng Chang, Thorsten Kurth, Kostas Orginos, and Andre Walker-Loud. On the Feynman-Hellmann Theorem in Quantum Field Theory and the Calculation of Matrix Elements. *Phys. Rev.*, D96(1):014504, 2017.

[173] Shahida Dar. The Neutron EDM in the SM: A Review. 2000.

[174] Maxim Pospelov and Adam Ritz. Electric dipole moments as probes of new physics. *Annals Phys.*, 318:119–169, 2005.

[175] Jonathan Engel, Michael J. Ramsey-Musolf, and U. van Kolck. Electric Dipole Moments of Nucleons, Nuclei, and Atoms: The Standard Model and Beyond. *Prog. Part. Nucl. Phys.*, 71:21–74, 2013.

[176] J. de Vries, R. Higa, C. P. Liu, E. Mereghetti, I. Stetcu, R. G. E. Timmermans, and U. van Kolck. Electric Dipole Moments of Light Nuclei From Chiral Effective Field Theory. *Phys. Rev.*, C84:065501, 2011.

[177] J. de Vries, E. Mereghetti, R. G. E. Timmermans, and U. van Kolck. The Effective Chiral Lagrangian From Dimension-Six Parity and Time-Reversal Violation. *Annals Phys.*, 338:50–96, 2013.

[178] S. Dinter, V. Drach, and K. Jansen. Dark matter search and the scalar quark contents of the nucleon. *Int. J. Mod. Phys.*, E20:110–117, 2011.

[179] Simon Dinter, Vincent Drach, Roberto Frezzotti, Gregorio Herdoiza, Karl Jansen, and Giancarlo Rossi. Sigma terms and strangeness content of the nucleon with $N_f = 2 + 1 + 1$ twisted mass fermions. *JHEP*, 08:037, 2012.

[180] S. Durr et al. Lattice computation of the nucleon scalar quark contents at the physical point. *Phys. Rev. Lett.*, 116(17):172001, 2016.

[181] Constantia Alexandrou, Martha Constantinou, Kyriakos Hadjiyiannakou, Christos Kallidonis, Giannis Koutsou, Karl Jansen, Christian Wiese, and Alejandro Vaquero AvilCasco. Nucleon spin and quark content at the physical point. *PoS*, LATTICE2016:153, 2016.

[182] A. Abdel-Rehim, C. Alexandrou, M. Constantinou, K. Hadjiyiannakou, K. Jansen, Ch. Kallidonis, G. Koutsou, and A. Vaquero Aviles-Casco. Direct Evaluation of the Quark Content of Nucleons from Lattice QCD at the Physical Point. *Phys. Rev. Lett.*, 116(25):252001, 2016.

[183] Boram Yoon, Tanmoy Bhattacharya, and Rajan Gupta. Neutron Electric Dipole Moment on the Lattice. *EPJ Web Conf.*, 175:01014, 2018.

[184] Michael Abramczyk, Sinya Aoki, Tom Blum, Taku Izubuchi, Hiroshi Ohki, and Sergey Syritsyn. Computing nucleon EDM on a lattice. *EPJ Web Conf.*, 175:06027, 2018.

[185] M. Abramczyk, S. Aoki, T. Blum, T. Izubuchi, H. Ohki, and S. Syritsyn. Lattice calculation of electric dipole moments and form factors of the nucleon. *Phys. Rev.*, D96(1):014501, 2017.

[186] M. Constantinou, M. Costa, R. Frezzotti, V. Lubicz, G. Martinelli, D. Meloni, H. Panagopoulos, and S. Simula. $K \to \pi$ matrix elements of the chromomagnetic operator on the lattice. *Phys. Rev.*, D97(7):074501, 2018.

[187] Gerhart Luders. On the Equivalence of Invariance under Time Reversal and under Particle-Antiparticle Conjugation for Relativistic Field Theories. *Kong. Dan. Vid. Sel. Mat. Fys. Med.*, 28N5(5):1–17, 1954.

[188] C. Hamzaoui and M. E. Pospelov. Electric dipole moment of neutron in the Kobayashi-Maskawa model with four generations of quarks. *Phys. Lett.*, B357:616–623, 1995.

[189] Apostolos Pilaftsis. CP violation and baryogenesis due to heavy Majorana neutrinos. *Phys. Rev.*, D56:5431–5451, 1997.

[190] V. V. Flambaum, I. B. Khriplovich, and O. P. Sushkov. On the Possibility to Study P Odd and T Odd Nuclear Forces in Atomic and Molecular Experiments. *Sov. Phys. JETP*, 60:873, 1984.

[191] V. Spevak, N. Auerbach, and V. V. Flambaum. Enhanced t-odd, p-odd electromagnetic moments in reflection asymmetric nuclei. *Phys. Rev. C*, 56:1357–1369, Sep 1997.

[192] J. Dobaczewski and J. Engel. Nuclear time-reversal violation and the Schiff moment of Ra-225. *Phys. Rev. Lett.*, 94:232502, 2005.

[193] R. H. Parker et al. First Measurement of the Atomic Electric Dipole Moment of ^{225}Ra. *Phys. Rev. Lett.*, 114(23):233002, 2015.

[194] J. de Vries, E. Mereghetti, R. G. E. Timmermans, and U. van Kolck. Parity- and Time-Reversal-Violating Form Factors of the Deuteron. *Phys. Rev. Lett.*, 107:091804, 2011.

[195] Jack Dragos, Thomas Luu, Andrea Shindler, and Jordy de Vries. Electric Dipole Moment Results from lattice QCD. *EPJ Web Conf.*, 175:06018, 2018.

[196] J. Bsaisou, Ulf-G. Meißner, A. Nogga, and A. Wirzba. P- and T-Violating Lagrangians in Chiral Effective Field Theory and Nuclear Electric Dipole Moments. *Annals Phys.*, 359:317–370, 2015.

[197] B. Bunk, K. H. Mutter, and K. Schilling. LATTICE GAUGE THEORY. A CHALLENGE IN LARGE SCALE COMPUTING. PROCEEDINGS, NATO WORKSHOP, WUPPERTAL, F.R. GERMANY, NOVEMBER 5-7, 1985. *NATO Sci. Ser. B*, 140:pp.1–334, 1986.

[198] G. W. Kilcup, Stephen R. Sharpe, Rajan Gupta, G. Guralnik, A. Patel, and T. Warnock. ϵ Beyond the Naive Mass Spectrum. *Phys. Lett.*, 164B:347–355, 1985.

[199] G. Parisi. The Strategy for Computing the Hadronic Mass Spectrum. *Phys. Rept.*, 103:203–211, 1984.

[200] G. Peter Lepage. The Analysis of Algorithms for Lattice Field Theory. In *Boulder ASI 1989:97-120*, pages 97–120, 1989.

[201] C. Carl, D. Brantley, H.J. Monge, and A. Walker-Loud. Meson Feynman-Hellmann. *X*, X:X, X.

[202] Jeffrey E. Mandula, George Zweig, and Jan Govaerts. COVARIANT LATTICE GLUEBALL FIELDS. *Nucl. Phys.*, B228:109–121, 1983.

[203] E. Gabrielli, G. Martinelli, C. Pittori, G. Heatlie, and Christopher T. Sachrajda. Renormalization of lattice two fermion operators with improved nearest neighbor action. *Nucl. Phys.*, B362:475–486, 1991.

[204] Andre Walker-Loud. *Topics in effective field theory for lattice QCD*. PhD thesis, Washington U., Seattle, 2006.

[205] M. Lujan, A. Alexandru, Y. Chen, T. Draper, W. Freeman, M. Gong, F. X. Lee, A. Li, K. F. Liu, and N. Mathur. The Δ_{mix} parameter in the overlap on domain-wall mixed action. *Phys. Rev.*, D86:014501, 2012.

[206] Richard C. Brower, Hartmut Neff, and Kostas Orginos. Möbius fermions: Improved domain wall chiral fermions. *Nucl. Phys. Proc. Suppl.*, 140:686–688, 2005. [,686(2004)].

[207] R. C. Brower, H. Neff, and K. Orginos. Mø"bius fermions. *Nucl. Phys. Proc. Suppl.*, 153:191–198, 2006.

[208] Richard C. Brower, Harmut Neff, and Kostas Orginos. The Möbius domain wall fermion algorithm. *Comput. Phys. Commun.*, 220:1–19, 2017.

[209] A. Bazavov et al. Scaling studies of QCD with the dynamical HISQ action. *Phys. Rev.*, D82:074501, 2010.

[210] A. Bazavov et al. Lattice QCD ensembles with four flavors of highly improved staggered quarks. *Phys. Rev.*, D87(5):054505, 2013.

[211] Eduardo Follana, Quentin Mason, Christine Davies, Kent Hornbostel, Peter Lepage, and Howard Trottier. Further improvements to staggered quarks. *Nucl. Phys. Proc. Suppl.*, 129:447–449, 2004. [,447(2003)].

[212] E. Follana, Q. Mason, C. Davies, K. Hornbostel, G. P. Lepage, J. Shigemitsu, H. Trottier, and K. Wong. Highly improved staggered quarks on the lattice, with applications to charm physics. *Phys. Rev.*, D75:054502, 2007.

[213] A. Bazavov et al. Nonperturbative QCD Simulations with 2+1 Flavors of Improved Staggered Quarks. *Rev. Mod. Phys.*, 82:1349–1417, 2010.

[214] Jiunn-Wei Chen, Donal O'Connell, and Andre Walker-Loud. Universality of mixed action extrapolation formulae. *JHEP*, 04:090, 2009.

[215] David B. Kaplan. A Method for simulating chiral fermions on the lattice. *Phys. Lett.*, B288:342–347, 1992.

[216] Yigal Shamir. The Euclidean spectrum of Kaplan's lattice chiral fermions. *Phys. Lett.*, B305:357–365, 1993.

[217] Yigal Shamir. Chiral fermions from lattice boundaries. *Nucl. Phys.*, B406:90–106, 1993.

[218] Martin Luscher. Chiral symmetry and the Yang–Mills gradient flow. *JHEP*, 04:123, 2013.

[219] R. Narayanan and H. Neuberger. Infinite N phase transitions in continuum Wilson loop operators. *JHEP*, 03:064, 2006.

[220] G. P. Lepage, B. Clark, C. T. H. Davies, K. Hornbostel, P. B. Mackenzie, C. Morningstar, and H. Trottier. Constrained curve fitting. *Nucl. Phys. Proc. Suppl.*, 106:12–20, 2002.

[221] Ronald R. Horgan, Zhaofeng Liu, Stefan Meinel, and Matthew Wingate. Lattice QCD calculation of form factors describing the rare decays $B \to K^* \ell^+ \ell^-$ and $B_s \to \phi \ell^+ \ell^-$. *Phys. Rev.*, D89(9):094501, 2014.

[222] G. Peter Lepage. Lsqfit Python Package. .

[223] Costas Bekas, Alessandro Curioni, and Irina Fedulova. Low cost high performance uncertainty quantification, 01 2009.

[224] Arjun Singh Gambhir, Andreas Stathopoulos, and Kostas Orginos. Deflation as a Method of Variance Reduction for Estimating the Trace of a Matrix Inverse. *SIAM J. Sci. Comput.*, 39:A532–A558, 2017.

[225] Lingfei Wu, Jesse Laeuchli, Vassilis Kalantzis, Andreas Stathopoulos, and Efstratios Gallopoulos. Estimating the trace of the matrix inverse by interpolating from the diagonal of an approximate inverse. *Journal of Computational Physics*, 326:828 – 844, 2016.

[226] Arjun Singh Gambhir, Andreas Stathopoulos, Kostas Orginos, Boram Yoon, Rajan Gupta, and Sergey Syritsyn. Algorithms for Disconnected Diagrams in Lattice QCD. *PoS*, LATTICE2016:265, 2016.

[227] Andreas Stathopoulos, Jesse Laeuchli, and Kostas Orginos. Hierarchical probing for estimating the trace of the matrix inverse on toroidal lattices. 2013.

[228] M.F. Hutchinson. A stochastic estimator of the trace of the influence matrix for laplacian smoothing splines. 18:1059–1076, 01 1989.

[229] Shao-Jing Dong and Keh-Fei Liu. Stochastic estimation with Z(2) noise. *Phys. Lett.*, B328:130–136, 1994.

[230] Rajamani Narayanan and Herbert Neuberger. Infinitely many regulator fields for chiral fermions. *Phys. Lett.*, B302:62–69, 1993.

[231] Rajamani Narayanan and Herbert Neuberger. Chiral fermions on the lattice. *Phys. Rev. Lett.*, 71(20):3251, 1993.

[232] Rajamani Narayanan and Herbert Neuberger. Chiral determinant as an overlap of two vacua. *Nucl. Phys.*, B412:574–606, 1994.

[233] Rajamani Narayanan and Herbert Neuberger. A Construction of lattice chiral gauge theories. *Nucl. Phys.*, B443:305–385, 1995.

[234] Herbert Neuberger. More about exactly massless quarks on the lattice. *Phys. Lett.*, B427:353–355, 1998.

[235] Tanmoy Bhattacharya, Vincenzo Cirigliano, Rajan Gupta, Emanuele Mereghetti, and Boram Yoon. Dimension-5 CP-odd operators: QCD mixing and renormalization. *Phys. Rev.*, D92(11):114026, 2015.

[236] M. Constantinou, M. Costa, R. Frezzotti, V. Lubicz, G. Martinelli, D. Meloni, H. Panagopoulos, and S. Simula. Renormalization of the chromomagnetic operator on the lattice. *Phys. Rev.*, D92(3):034505, 2015.

[237] G. Martinelli, G. C. Rossi, Christopher T. Sachrajda, Stephen R. Sharpe, M. Talevi, and M. Testa. Nonperturbative improvement of composite operators with Wilson fermions. *Phys. Lett.*, B411:141–151, 1997.

[238] V. Gimenez, Leonardo Giusti, S. Guerriero, V. Lubicz, G. Martinelli, S. Petrarca, J. Reyes, B. Taglienti, and E. Trevigne. Nonperturbative renormalization in coordinate space. *Nucl. Phys. Proc. Suppl.*, 129:411–413, 2004. [,411(2003)].

[239] V. Gimenez, Leonardo Giusti, S. Guerriero, V. Lubicz, G. Martinelli, S. Petrarca, J. Reyes, B. Taglienti, and E. Trevigne. Non-perturbative renormalization of lattice operators in coordinate space. *Phys. Lett.*, B598:227–236, 2004.

[240] M. Tomii, G. Cossu, B. Fahy, H. Fukaya, S. Hashimoto, T. Kaneko, and J. Noaki. Renormalization of domain-wall bilinear operators with short-distance current correlators. *Phys. Rev.*, D94(5):054504, 2016.

[241] M. Tomii, G. Cossu, S. Hashimoto, and J. Noaki. Non-perturbative renormalization of bilinear operators with Möbius domain-wall fermions in the coordinate space. *PoS*, LATTICE2014:287, 2014.

[242] Krzysztof Cichy, Karl Jansen, and Piotr Korcyl. Step scaling in coordinate space: running of the quark mass. *PoS*, LATTICE2016:186, 2016.

[243] Krzysztof Cichy, Karl Jansen, and Piotr Korcyl. Non-perturbative running of renormalization constants from correlators in coordinate space using step scaling. *Nucl. Phys.*, B913:278–300, 2016.

[244] K. G. Chetyrkin. Correlator of the quark scalar currents and Gamma(tot) (H —> hadrons) at O (alpha-s**3) in pQCD. *Phys. Lett.*, B390:309–317, 1997.

[245] Teresa MarrodUndagoitia and Ludwig Rauch. Dark matter direct-detection experiments. *J. Phys.*, G43(1):013001, 2016.

[246] E. Aprile et al. First Dark Matter Search Results from the XENON1T Experiment. *Phys. Rev. Lett.*, 119(18):181301, 2017.

[247] D. G. Phillips, II et al. The Majorana experiment: an ultra-low background search for neutrinoless double-beta decay. *J. Phys. Conf. Ser.*, 381:012044, 2012.

[248] M. Agostini et al. Background-free search for neutrinoless double-β decay of ^{76}Ge with GERDA. 2017. [Nature544,47(2017)].

[249] J. B. Albert et al. Sensitivity and Discovery Potential of nEXO to Neutrinoless Double Beta Decay. *Phys. Rev.*, C97(6):065503, 2018.

[250] Ruediger Picker. How the minuscule can contribute to the big picture: the neutron electric dipole moment project at TRIUMF. *JPS Conf. Proc.*, 13:010005, 2017.

[251] M. G. D. van der Grinten et al. CryoEDM: A cryogenic experiment to measure the neutron electric dipole moment. *Nucl. Instrum. Meth.*, A611:129–132, 2009.

[252] E. P. Tsentalovich. The nEDM experiment at the SNS. *Phys. Part. Nucl.*, 45:249–250, 2014.

[253] Frank Wilczek. What qcd tells us about nature and why we should listen. *Nuclear Physics A*, 663-664:3c – 20c, 2000.

[254] Nicolas Garron. Fierz transformations and renormalization schemes for fourquark operators. *EPJ Web Conf.*, 175:10005, 2018.

[255] C. C. Nishi. Simple derivation of general Fierz-like identities. *Am. J. Phys.*, 73:1160–1163, 2005.

[256] Y. Takahashi. THE FIERZ IDENTITIES. 1987.

[257] G. Prézeau, M. Ramsey-Musolf, and Petr Vogel. Neutrinoless double β decay and effective field theory. *Phys. Rev. D*, 68:034016, Aug 2003.